Abstract

Critical Temperature Dependence of High Frequency Electron Dynamics in Superconducting Hot-Electron Bolometer Mixers

Irfan Siddiqi

May, 2002

Superconducting diffusion-cooled hot-electron bolometer (HEB) mixers are ideal candidates for use in terahertz heterodyne spectroscopy (THz). This thesis investigates mixer performance as a function of the superconducting transition temperature (T_c). In the present work, three different materials systems have been used to obtain devices with T_c between 1 and 5.5 K – Al, Nb in a magnetic field, and Nb-Au. The mixing measurements were conducted in a 30 GHz microwave setup with the mixer block at T = 0.22K. Microwave measurements are used to understand the underlying physics of the HEB mixer, and are a guide for the future development of THz receivers. The mixer noise temperature is found to be equal to approximately 25 times T_c, and the dominant noise is assumed to be thermal fluctuations. The LO power is found to equal (0.7 nW/K^2) $\cdot$ T_c^2 when the HEB is cooled to well below T_c. As for saturation effects, input saturation is expected when the incident noise power is greater than (0.14 nW/K^2) $\cdot$ T_c^2, and output saturation should result for incident power greater than (27 pW/K^2) $\cdot$ T_c^2. Additional performance limitations are observed in Al devices which have a long coherence length. Superconductivity is suppressed in the ends of the microbridge due to the proximity effect. This results in a minimum bridge length of ~ 6-7 $\xi(0)$ for superconductivity to be observed, therefore imposing an upper limit for the IF bandwidth of approximately (8 GHz/K) $\cdot$ T_c for N-S-N HEB structures. Output saturation is also more likely in Al devices with normal ends. Nb-Au mixers perform the best and are very convenient with their tunable T_c. A mixer T_c of 2 K is predicted to be optimum for many applications. Such devices should have lower noise than Nb and should not exhibit saturation effects.

Critical Temperature Dependence of High Frequency Electron Dynamics in Superconducting Hot-Electron Bolometer Mixers

A Dissertation

Presented to the Faculty of the Graduate School

of

Yale University

in Candidacy for the Degree of

Doctor of Philosophy

By

Irfan Siddiqi

Dissertation Director: Professor Daniel E. Prober

May, 2002

Acknowledgements

Upon the completion of this manuscript I am grateful to many. I thank God Almighty for giving me strength and bestowing upon me many favors along this journey. I owe a debt which cannot be repaid to my parents, who have cultivated and constantly nurtured a love for the acquisition of knowledge, and without whose support I would not be writing this preamble. Their selfless sacrifice and the prayers of my entire family have culminated in this thesis.

I am deeply grateful for the guidance, support, and care shown to me by my advisor Professor Daniel Prober. He has never faltered in his enthusiasm for this work, and has taught me many valuable lessons. I am happy to have had the opportunity to explore the world of physics under his direction, and I value his friendship. I am thankful to the entire faculty of the applied physics department who have always been willing to help in matters small and large, especially Professor Robert Schoelkopf and Professor Michel Devoret. I want to acknowledge Dr. Aleksandr Verevkin who helped with the initial aluminum bolometer measurements. I am thankful to Dr. Alexay Kozhevnikov and Dr. Christopher Wilson for many things, including assistance with device fabrication.

I want to thank Dr. William R. McGrath and all the members of his group at JPL for providing some of the devices measured in this work, and for their technical expertise and guidance, especially Dr. Boris S. Karasik and Dr. Anders Skalare. I have enjoyed working with them on this project.

I have made many friends in Becton Center over the years, and I thank them all for their friendship and assistance. For a complete set of acknowledgements, many pages would be needed as the number of people who have assisted me is large. I apologize to those I have not mentioned above in the interest of brevity. Your help has not gone unappreciated, and my well wishes are with you.

February 20, 2002

Contents

List of Figures

List of Tables

List of Symbols

A	Cross-sectional area
α_0	Electro-thermal feedback parameter, no IF load
α	Electro-thermal feedback parameter, with IF load
c	Specific heat
C	Heat capacity
d	Device thickness
D	Diffusion constant
2Δ	Superconducting energy gap
ΔT_c	Superconducting transition width
DSB	Double side band
e	Electron charge
Φ	Heat flux
G	Thermal conductance
GHz	Gigahertz (10^9 Hz)
HEB	Hot-electron bolometer
I	DC current
IF	Intermediate frequency
K	Thermal conductivity
L	Device length
$\mathscr{L}$	Lorenz number

LO	Local oscillator
η	Conversion efficiency
η_{IF}	IF coupling efficiency
η_{RF}	RF coupling efficiency
P	Power
R	Resistance (V/I)
ρ	Electrical resistivity
RF	Radio frequency
R_L	IF load resistance
R_N	Normal state resistance
σ	Electrical conductivity
SIS	Superconducting-insulating-superconducting (tunnel junction)
SSB	Single side band
T_b	Bath temperature
T_c	Superconducting transition temperature
τ_{diff}	Diffusion time
τ_{eff}	Effective thermal time constant
$\tau_{e\text{-}e}$	Electron-electron inelastic time
$\tau_{e\text{-}ph}$	Electron-phonon inelastic time
θ	Electron temperature
THz	Terahertz (10^{12} Hz)
T_M	Mixer noise temperature

$\mathbf{T_M^{TF}}$	Mixer noise due to thermal fluctuations
$\mathbf{T_M^{J}}$	Mixer noise due to Johnson noise
$\mathbf{T_{output}}$	Output noise temperature
$\mathbf{T_R}$	Receiver noise temperature
$\mathbf{T_{amp}}$	IF amplifier input noise temperature
τ_θ	Inelastic relaxation time of the electron temperature
V	DC voltage
W	Device width
ξ	superconducting coherence length
Z	Impedance

Chapter I: Introduction

Electromagnetic radiation is a sensitive probe for determining the nature of matter. Its absorption and emission provide important information relating to the composition of matter and the underlying mechanisms of physical processes. The energy associated with a particular process determines the associated photon frequency. Over the years, specialized spectroscopic techniques and equipment have been developed to study different portions of the electromagnetic spectrum such as the visible and microwave ranges. One frequency window that has not yet been studied extensively is the terahertz (THz) band (~ 10^{12} – 10^{13} Hz). Equipment for conducting THz studies is still under development. This fact, along with strong atmospheric absorption, is in part why THz measurements are challenging, and relatively few measurements have been conducted.

Though there are a wide variety of applications for THz measurements in biology, chemistry and other disciplines, the focus of the current work is the development of ultra-sensitive detectors for remote-sensing applications in astronomy and stratospheric chemistry. By accurately measuring the frequency of the radiation emitted from cold objects in space – molecular gas clouds for example – or from gases in the Earth's atmosphere, it is possible to identify their chemical composition. The emission frequency corresponding to transitions between rotational and vibrational states in various light molecules and radicals such as CO, OH^-, and HCN lie within the THz band. Additionally, the radiation intensity is a measure of the abundance. The linewidth relates information about the temperature. Any Doppler shifts in the center frequency of the

emission line can be used to describe motion of the object under study. The relevance of these quantities to astrophysics is discussed below.

The effectiveness of emission spectroscopy to accurately identify different chemical species relies on the ability to precisely resolve the frequency of the emitted radiation. To this end, the heterodyne technique is used. Two sources of photons – a known local oscillator (LO) and the unknown signal to be studied – are focused on the heterodyne detector, often simply referred to as a mixer. A non-linear element, the mixer combines the two input waveforms and generates various frequency harmonics and sum and difference frequencies at its output. Typically, the component with frequency equal to the difference of the two input signal frequencies is studied. This difference frequency is called the beat or intermediate frequency (IF; $IF = |f_S - f_{LO}|$). Here f_s is the frequency of the signal being studied and f_{LO} is that of the LO source. The LO signal is controllable, and its properties are well characterized. Thus, the unknown input signal can be reconstructed from the LO and IF waveforms.

Two common heterodyne detectors used in astronomical observations at frequencies of ~ 0.3-3 THz are superconductor-insulator-superconductor (SIS) tunnel junctions and Schottky diodes (Tucker and Feldman, 1985; Blundell and Tong, 1992). Both mixers make use of a sharp non-linearity in their current-voltage characteristic. SIS mixers have very high sensitivity, but currently only up to f ~ 1.2 THz since their operation is based on physics relating to the superconducting energy gap of the materials used (Kawamura et al., 1999). For applications above 1 THz, semiconductor based Schottky diodes have traditionally been used. Schottky mixers are typically 20-100 times

noisier than SIS mixers, and thus are not ideal for detecting the faintest sources. Schottly mixers also require large LO power which is not readily available at THz frequencies.

As an alternative to both SIS and Schottky mixers, we have studied hot-electron bolometer (HEB) mixers for THz astronomy applications. HEB mixers do not have operating frequency limitations as SIS mixers do, and have far greater sensitivity than Schottky mixers. The HEB device is a thermal mixer. Electrons in the mixer are heated by the input power. The thermal response time of the electrons is not short enough to allow the electron temperature to vary at either the LO or signal frequencies, both of which in proposed applications are f ~ THz. However, the electron temperature can be modulated at the IF which can be of order 10^9 Hz (GHz). The HEB is constructed from a superconductor so that, when biased appropriately, the device resistance varies sharply with the electron temperature. The device resistance thus modulates at the IF, and provides a readout mechanism for the mixer.

Nb and NbN HEB mixers have been studied in the last decade and are excellent candidates for THz spectroscopy applications. The primary goal of this work is to examine the behavior of the superconducting HEB mixer as a function of its critical temperature (T_c). Improvements in mixer performance are predicted when T_c is lowered. For example, when certain conditions are met, mixer noise is predicted to decrease linearly with a reduction in T_c. Additionally, the required LO power is also predicted to decrease. In our work, HEB mixers with T_c between 1-5 K have been investigated both experimentally and through numerical simulations. Mixers in which the hot electrons are cooled by diffusion rather than phonon emission are studied because the speed of diffusion-cooled HEBs is fast and is independent of T_c. The particular set of

measurements described is carried out using a microwave frequency LO. The motivation behind these low frequency studies, instead of THz studies, is that the operation of the HEB does not directly depend on the whether the frequency of the incident radiation is above or below the superconducting energy gap frequency, as discussed later. Microwave mixing experiments allow for a more rapid and systematic survey of HEB performance than involved THz measurements. The details of the physics relating to HEB operation obtained through microwave studies is intended to be a guide for the future development of THz mixers.

1.1 Motivation: HEB mixers for astronomy

Over the past decade, interest in THz astronomy has greatly increased (Phillips and Keene, 1992; Blundell and Tong, 1992). Considerable effort is being made both by individual research groups and large government agencies to develop THz heterodyne receivers. There is a wealth of information about the nature of our universe that can be uniquely obtained through THz measurements (Waters, 1992). Proposed receivers currently envision the use of ground-based, airborne, and satellite observatories. The choice of observatory type depends on which part of the THz band is to be studied.

The study of THz radiation from extraterrestrial objects is a difficult task from Earth due to heavy atmospheric absorption. Some useful windows, at ~ 800 GHz for example, can be reached by observing from high altitudes where the water vapor content is low. Facilities such as the Caltech Sub-millimeter Observatory (CSO) on top of Mauna Kea, Hawaii and the AST/RO facility in Antartica are approximately 4 km above

sea level and are amongst the best ground-based observatories for measurements at and above 1 THz. Going to even higher altitudes further reduces the effects of atmospheric absorption, and thus aircraft equipped with THz receivers are also well suited for astronomical observation. The Kuiper Airborne Observatory (KAO) flew successfully for 21 years and was decommissioned in 1995 to be replaced the Stratospheric Observatory For Infrared Astronomy (SOFIA) which is scheduled for first light in 2004 (Becklin, 1997). Satellites are also under construction for THz astronomy. Observing from space avoids the effects of the terrestrial atmosphere completely, which is an advantage of satellite missions compared to aircraft observatories such as SOFIA, though it is not possible to change and upgrade instrumentation in the former. The Herschel/FIRST satellite is an European Space Agency project scheduled for launch in 2007 via Ariane-5 rocket (Pilbratt, 2000).

The missions described above have an immediate need for ultra-sensitive heterodyne detectors. HEB mixers are proposed for use at f ~ 1 THz and higher. For ground-based observation, single pixel and multi-pixel HEB receivers are being designed for SuperCam and TREND. SuperCam is a multi-pixel 810 GHz HEB camera proposed for use at the SMTO on Mt. Graham, Arizona and the AST/RO facility in Antartica (Groppi et al., 2001). The effort is a collaboration between the University of Arizona and Yale University, where the latest diffusion-cooled HEB technology is being developed. TREND, a collaboration between the University of Massachusetts at Amherst and the University of Arizona, is a single pixel f ~ 1.5 THz NbN receiver for use on AST/RO (Yngvesson, 2001). SOFIA, an airborne observatory, will have much wider spectral coverage than ground-based systems. SOFIA will span frequencies from a few hundred

GHz to 1000 THz. HEB mixers are being developed at NASA/JPL for the CASIMIR instrument on SOFIA, and similar mixers will undoubtedly be used on other future SOFIA instruments as well. Finally, the Herschel satellite will have receivers from 450 GHz – 3.75 THz. The HIFI instrument is a heterodyne module which will use HEB mixers in band 6 which covers 1.41 - 1.91 THz.

The success of the next generation of THz observatories promises to answer many fundamental scientific questions. Analyzing THz emission from space is key in understanding the dynamics of stellar and planetary evolution. Protostars, objects that eventually evolve into stars, are currently the topic of much research. The physical properties of the dense gas envelope in close proximity to star forming cores can be studied by observing transitions between high angular momentum states (eg. $J = 10 \rightarrow 9$, $9 \rightarrow 8$, ...) of CO, HCN, and HCO^+. Comparing the composition of gas clouds with and without star cores reveals the initial conditions needed for star formation and subsequent evolution (Ceccarelli et al., 1996). The molecules in gas clouds can be excited either through collisions or radiation. Collisions can occur between different kinematic components of the gas cloud and interactions with outflows from the protostar. Low angular momentum transition ($J=2\rightarrow1$ and $1\rightarrow0$) outflow studies at $f \sim$ a few hundred GHz might not accurately account for the CO mass, leading to an underestimate of the mechanical power. Looking at the higher frequency transitions, as proposed, is thus useful in describing protostar outflows. Radiative excitation can occur from photodissociation (PDR) fronts located at the illuminated surface of gas clouds. The details of PDR fronts give information relating to the ability of molecular gas clouds to shield themselves from interstellar radiation, and is thus indicative of their lifetime

(Kaufman et al., 1999). In addition to star formation, planetary development is currently being studied. Examining the disks of material surrounding young stars is necessary for verifying theories of planet formation. Vibrationally excited transitions in HCN that are close in frequency to pure rotational transitions can be used for probing circumstellar disks (Boonman et al., 2001).

Achieving a greater understanding of the origin and evolution of objects in our universe is possible through sensitive studies of THz emission from space. High quality heterodyne receivers are required for several missions currently being developed for astronomical study. The HEB mixer technology investigated in the present work has direct relevance to THz astronomy as these devices are excellent candidates for spectroscopy above 1 THz, and moreover they are proposed for future use on these missions.

1.2 Heterodyne Detection

For applications where it is necessary to precisely measure the frequency of the input signal (typically $\Delta f/f < 10^{-6}$), heterodyne detection is often used. The general detection scheme typically used for astronomy is illustrated in Figure 1.1. The faint, unknown signal to be detected is simply termed "RF signal". The RF signal is combined with a much stronger signal of known frequency, the local oscillator. The heterodyne element "mixes" the RF and LO signals and at the detector output are signals at various combinations of the input signal frequencies. In heterodyne mode, the output at the IF, the difference of the RF and LO frequencies, is analyzed. The IF signal is first amplified

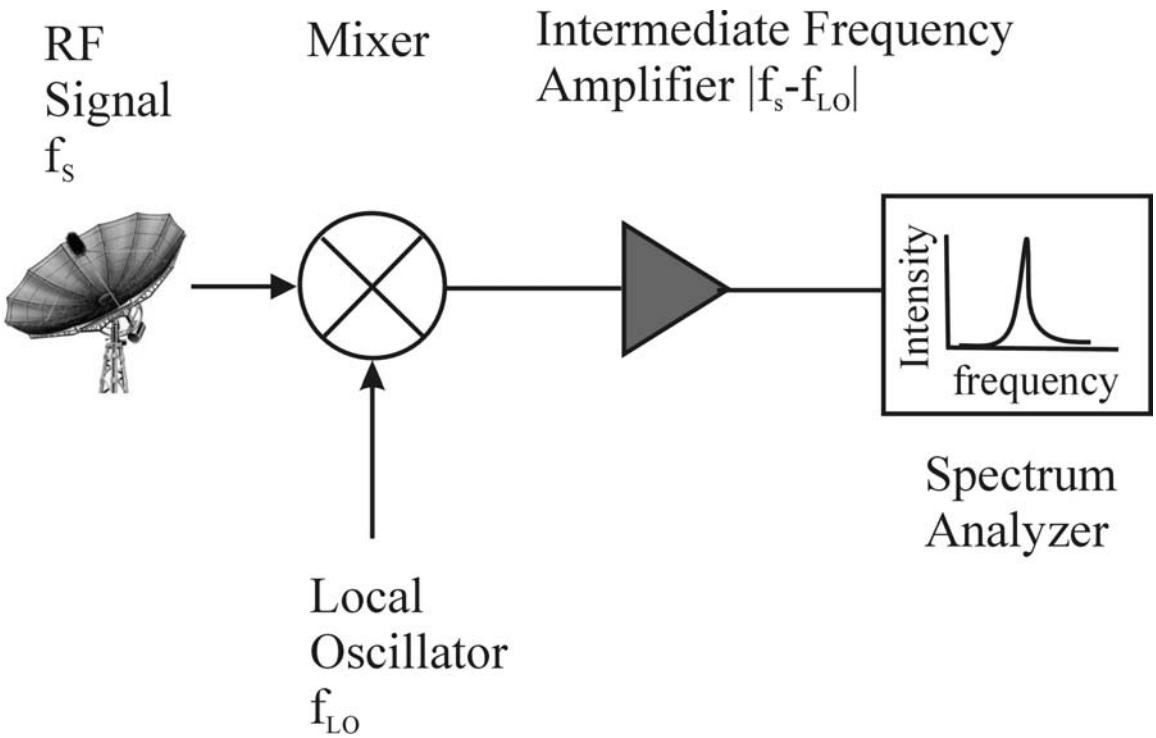

Figure 1.1: Block diagram of a typical heterodyne receiver used in astronomy.

by way of a cooled high-electron mobility transistor (HEMT) amplifier and then analyzed by a spectrum analyzer.

The mixer in essence is used as a device to down-convert a high frequency RF signal to a much lower frequency IF signal which can be characterized directly, typically with some associated conversion loss. Similar to AM radio, the RF signal is amplitude modulated and the frequency of the envelope is detected. The ratio of output power at the mixer IF to the available input RF signal power is called the mixer conversion efficiency (η),

$$\eta = P_{RF} / P_{IF}. \qquad 1.1$$

The mixer conversion efficiency depends on several parameters such as the LO power and the IF. For a given mixer, there is a value of P_{LO} which yields the optimum value of η. The conversion efficiency decreases as the IF is increased, and the value of the IF where the conversion efficiency drops by 3 dB (a factor of 2) is called the IF conversion bandwidth, or simply the IF bandwidth.

In addition to P_{LO} and the IF bandwidth, the receiver noise is an important parameter which describes the sensitivity of the complete heterodyne detector. The noise is taken to be the input RF power per unit bandwidth which results in a unity signal to noise ratio at the IF output. This power is commonly expressed as the temperature of a matched Johnson resistor that radiates, in the Rayleigh-Jeans regime, a power kT per bandwidth. The receiver noise temperature (T_R) has contributions from the noise of the mixer element itself and the noise of the IF amplifier. Also, any losses in coupling efficiency due to impedance mismatches and imperfections in the coupling hardware (lenses, cables, etc.) at the RF input or IF output increases T_R. T_R can be expressed as

$$T_R = \frac{T_{output}}{\eta_{RF}\eta} + \frac{1}{\eta_{RF}\eta_{IF}\eta} T_{amp} \qquad 1.2$$

where T_{output} is the noise the mixer itself generates at the IF output, T_{amp} is the input noise temperature of the IF amplifier, η_{RF} and η_{IF} are the respective RF and IF coupling efficiencies. In well designed receivers, these coupling losses can be made of order unity. Low noise GaAs HEMT IF amplifiers at IF ~ 1-2 GHz can have a noise temperature of a few Kelvin. Thus, to make a sensitive receiver, after the losses have

been minimized, the task is to minimize the mixer noise temperature. The mixer noise temperature is used a benchmark to compare the noise of different mixing elements. It can be expressed in terms of the output noise and conversion efficiency as

$$T_M = T_{output} / \eta. \qquad 1.3$$

If η is the single sideband (SSB) conversion efficiency, Equation 1.3 is the single sideband mixer noise temperature. If the noise is distributed into two sidebands arising from contributions to the IF signal from input RF signals at $f = f_{LO} + IF$ and one at $f = f_{LO} - IF$, then the double sideband (DSB) noise temperature is equal to half the value given in Equation 1.3, assuming the sensitivity is the same for both RF sidebands. There is a lower bound on the mixer noise temperature set by quantum mechanical constraints. At a given frequency,

$$T_M \geq n\,(h/k)\,f \qquad 1.4$$

where n is a number of order unity which depends on the precise definition of the noise temperature (Caves, 1981). This limit comes about due to a combination of quantum mechanical fluctuations in the input radiation and the mixer element itself.

Very sensitive mixers are typically also susceptible to saturation effects. Heterodyne detectors can saturate due to excess input RF radiation. This input radiation can be due to the monochromatic signal being studied or due to broadband noise. There are two modes of saturation that are usually observed. Input saturation or saturation at

the RF port occurs when the input power becomes comparable to the LO power. Saturation can also occur at the mixer output or IF port when the down-converted radiation generates a voltage large enough to shift the mixer out of the linear operation regime.

These are the basic parameters that will be used to describe the operation of THz mixers. The mixer noise temperature is a measure of the mixer sensitivity. Along with the sensitivity, the saturation power needs to be known. This sets the operating range of the mixer. Finally, the optimum LO power and the IF bandwidth are important in determining what type of LO source is needed for a given mixer. The specific requirements for practical astronomical receivers are discussed next.

1.3 THz Mixers for Astronomy

The desired parameters for THz mixers for astronomical applications are primarily set by sensitivity requirements and the type of LO sources available. In general, in terms of sensitivity, the lower the noise temperature the better. The Herschel mission has a design goal of T_R = 650 K (DSB) for band 6 which covers 1.41-1.91 THz. We can roughly estimate the required mixer noise temperature needed to achieve this goal using Equation 1.2 and typical values of the coupling losses and IF amplifier parameters. Expressing the required mixer noise temperature in terms of a temperature, one finds that $T_M \sim 5$ hf/k is needed. Two types of LO sources, solid state and laser, are commonly used. Solid state sources consist of a Gunn diode which generates radiation at f ~ 100 GHz with subsequent power amplifiers and frequency multipliers. The resulting

output is of order μW at ~ 1.5 THz for the best systems, and considerably smaller at higher frequencies. THz molecular laser systems typically consist of a CO_2 pump laser which excites a far infrared laser (eg. methanol). Until very recently, laser LO systems have been very bulky and unreliable. New commercial laser LO systems have greatly improved stability (Mueller et al., 2000), though they may not be deployable in all observational setups due to size and power requirements. Thus, it is still desirable for a THz mixer to have a small LO power requirement, for example μW or less, especially for multiple element array applications. Additionally, the LO sources mentioned are not widely tunable in a continuous fashion. Consequently, the mixer IF bandwidth needs to be ~ several GHz for practical applications. A large IF bandwidth also makes efficient use of limited observing time since typical acousto-optical spectrometers (AOS) that are used to record the IF output of the mixer record simultaneously across their band. Generating an emission spectrum by recording a MHz bin for a certain integration time and then sweeping the IF is much less efficient.

SIS mixers fulfill all the requirements of sensitivity, LO power, and IF bandwidth discussed for a good heterodyne detector. However, they currently cannot operate at frequencies much larger than about 1.2 THz with the required sensitivity (Kawamura et al., 1999). Schottky mixers have been the alternative to SIS for operation above a THz, though at the expense of greatly reduced sensitivity and large (~ mW) required LO power. HEB mixers, in contrast, promise to be an order of magnitude more sensitive then the best Schottky mixers with only nW of required LO power. Each of these technologies is briefly described in the subsequent sections.

1.3.1 SIS Mixers

SIS mixers operate on quantum mechanical tunneling. The mixer consists of two superconducting electrodes separated by a thin insulating layer. At T=0 there are no thermally excited quasiparticles; the Cooper pairs are at the Fermi energy. In the semiconductor model of the quasiparticles, between the pairs and occupied single particles states below the Fermi energy and empty single particle states above it there exists an energy gap Δ. No quasiparticles can tunnel across the insulating barrier at T=0 in the absence of an external bias voltage; see Figure 1.2a. When a bias voltage $V \geq 2\Delta/e$ is applied to the SIS device, quasiparticles in one superconductor can tunnel through the insulator to a very large number of empty states at the gap edge on the other superconductor, see Figure 1.2b. The onset of tunneling results in a sharp non-linearity in the current-voltage (I-V) characteristic (see Figure 1.3) which gives rise to mixing, in the classical sense. A fully quantum mechanical theory for SIS mixers exists which uses the formalism of photon assisted tunneling. These details are omitted here for simplicity. For finite temperature, an exponentially small population of thermally excited quasiparticles exists above the Fermi energy, and small currents are observed at finite voltages below the gap voltage.

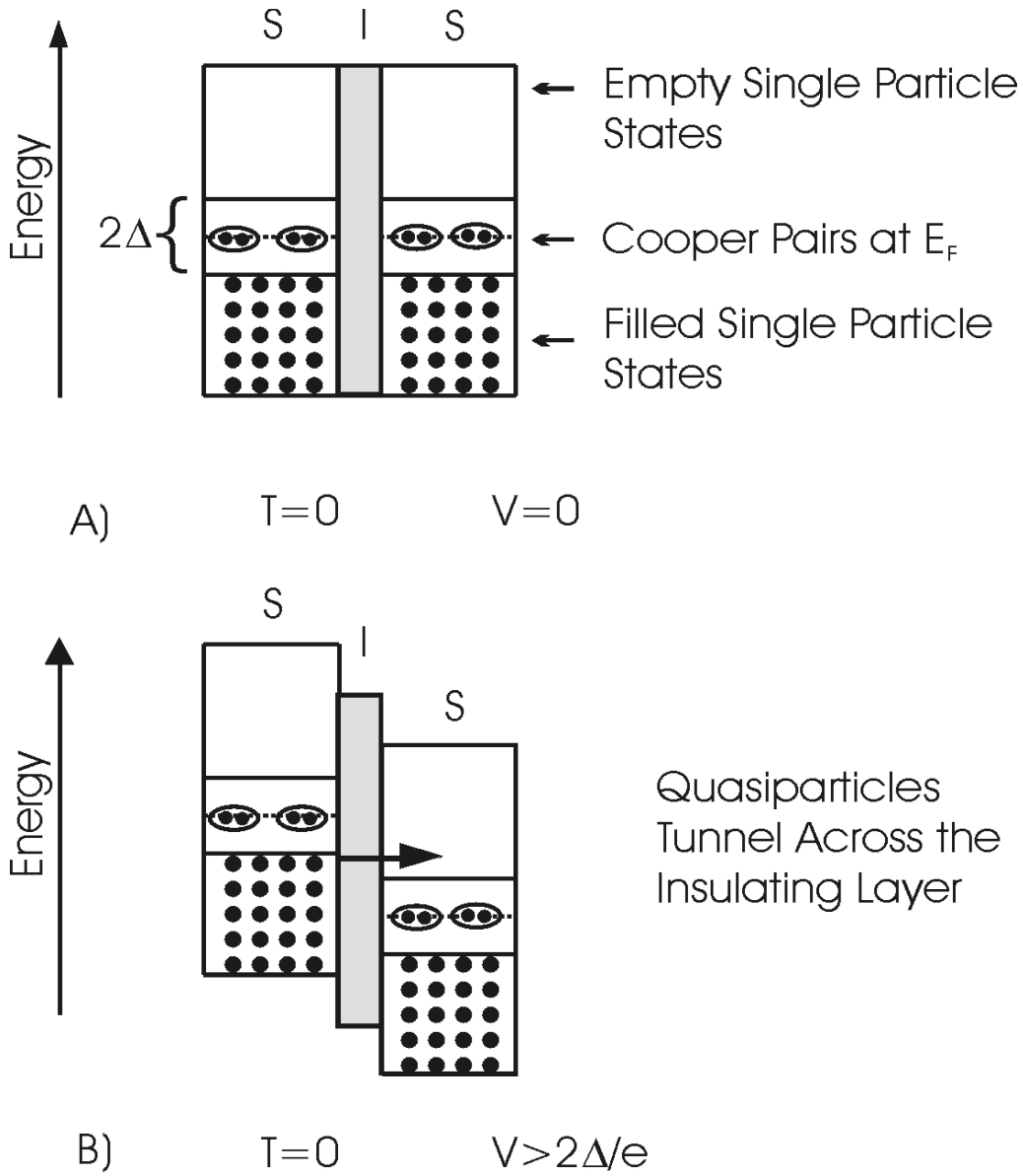

Figure 1.2a: Semiconductor representation of a SIS tunnel junction at T=0 and V=0; no tunneling is present.

Figure 1.2b: The junction at T=0 and V slightly greater than 2Δ/e; tunneling is present.

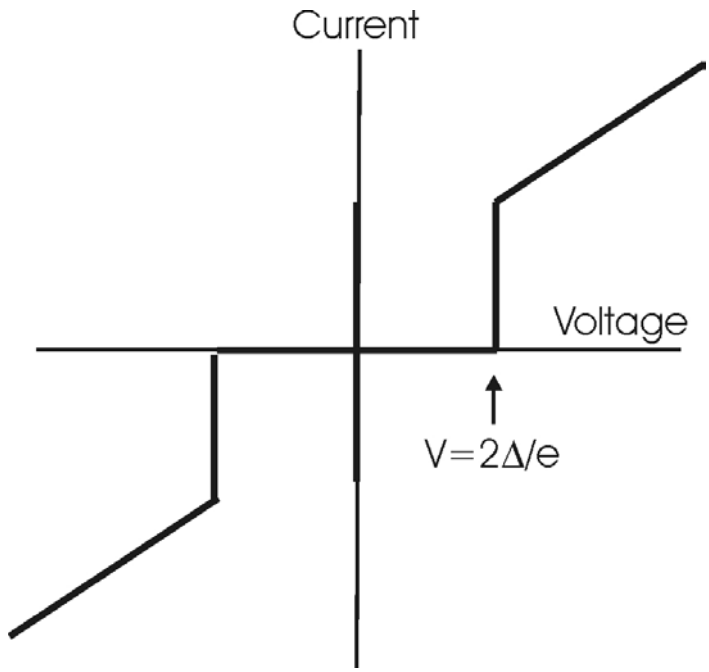

Figure 1.3: I-V characteristic for an ideal SIS junction at T=0 with no magnetic field applied.

The general operation of the mixer, however, is qualitatively the same. In SIS mixers, it is necessary to suppress the tunneling of Cooper pairs at zero bias voltage (DC Josephson effect, see Figure 1.3 at V=0). This is accomplished through the application of a magnetic field, typically of order 0.01 T. The field strengths required to suppress the pair current are small, although for array applications it may be difficult to apply the same field to every element. Different pixels might therefore have different mixer properties.

A more serious limitation with SIS mixers results from the fact that the superconducting energy gap frequency ($f_{gap} = 2\Delta/h$) for typical low temperature superconductors is ~ 1 THz or less. Bulk Nb, for example, has a gap frequency of 740 GHz. Mixer performance begins to degrade when the input radiation frequency is above the gap frequency due to film RF losses. The performance is significantly worse above 2

times the gap frequency since the SIS I-V curve is symmetric and the non-linearity spans a voltage $4\Delta/e$. Additionally, SIS devices have a capacitance, C, associated with them which results in an intrinsic inverse RC time of ~ 100 GHz. This ~ 100 GHz bandwidth can be utilized at a higher frequency if inductive elements are used. These inductive elements use superconducting materials to minimize resistive losses. Above the gap frequency of the superconducting inductors, they are poor conductors and considerably degrade mixer performance. Several materials have been used to solve this problem, including high conductivity normal metals and higher T_c superconductors such as NbN and NbTiN. NbTiN (T_c ~ 14K) has been the most promising and is currently used to extend the operating range of SIS mixers to ~ 1.2 THz (Kawamura et al., 1999; Jackson et al., 2000). Very high sensitivity SIS mixers based on high-T_c materials have not yet been demonstrated.

Thus, SIS mixers are currently the preferred mixer technology to frequencies ~ 1.2 THz. Below ~ 0.7 THz, a few groups have demonstrated mixer noise temperatures approaching a few times the quantum limit. The LO power requirements can be satisfied with convenient solid-state sources. However, due to fundamental limitations arising from the energy gap frequency, SIS mixers are currently not suitable for applications above 1.4 THz.

1.3.2 Schottky Diode Mixers

Schottky diode mixers are semiconductor devices, typically made of GaAs. The non-linear diode I-V results in mixing. Considerable work has been done in the past

decade to improve diode mixer technology, including making better contacts and shrinking the diode size. Some of the best Schottky mixers have been fabricated for use on NASA's EOS/AURA satellite. Receiver measurements at room temperature have yielded $T_R = 9000$ K (DSB) with the mixer noise temperature estimated to be $T_M = 3500$K (DSB) at a LO frequency of 2.5 THz (Gaidis et al., 2000). The required LO power is 5 mW, and a molecular laser LO is used in these measurements. The dominant noise sources are thermal noise from the series resistance of the diode and shot noise from carrier emission across the p-n junction. Though Schottky mixers are robust devices that work above 1 THz, it is desired to have a mixer with considerably lower noise temperature and smaller LO power requirements.

1.3.3 Hot-Electron Bolometer (HEB) Mixers

The HEB mixer consists of a thin, narrow superconducting microbridge that is contacted with thick normal-metal banks, see Figure 1.4. HEB mixers, like all

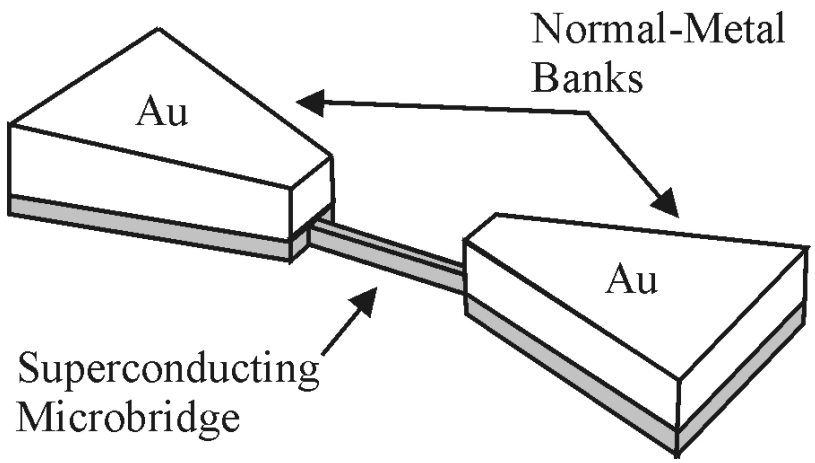

Figure 1.4: Typical geometry of a HEB mixer.

bolometers, are thermal detectors. Radiation incident on the HEB raises its temperature, which is inferred by a change in the highly temperature-dependent resistance. The temperature rise in the detector is proportional to the input power. The HEB is operated in the vicinity of the superconducting transition at $T = T_c$, see Figure 1.5a, so that dR/dT is very large

The I-V has two branches: the superconducting branch and the resistive branch. At zero voltage, the microbridge is superconducting and has zero resistance. When the critical current (I_c) is exceeded, the I-V switches to the resistive branch of the I-V curve. Typically one biases an HEB mixer by starting with a large bias voltage in which case the microbridge is almost fully normal. The one steadily decreases the voltage until the conversion efficiency peaks. At low enough bias voltages, the I-V switches to the superconducting branch, this is often called the "drop-back" point. The region in which best performance is observed is on the resistive branch just above the drop-back point, indicated in Figure 1.5b with a circle. In this region, the resistance is a sensitive function of the input power. The change in the DC resistance R of the HEB can be expressed as,

$$\delta R = \frac{dR}{dT}\ \delta T \propto P_{input} \propto V^2 \qquad 1.5$$

where V is the RF input voltage. The input voltage has two contributions, one from the signal and the other from the LO. Modeling each as a simple sinusoidal input, the following expression is obtained:

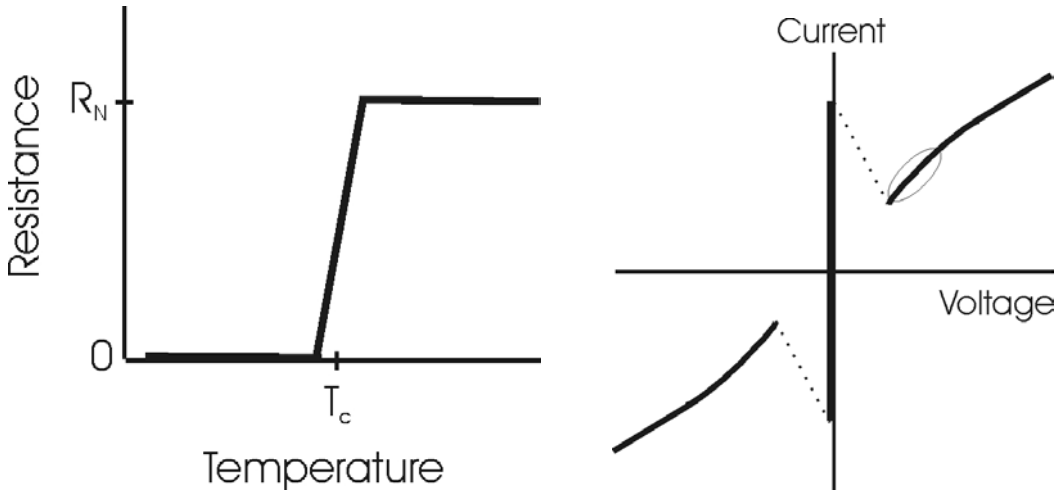

(a) (b)

Figure 1.5a & b: (left) R vs. T and (right) I-V characteristic with LO power applied for a typical HEB mixer with $T < T_c$.

$$P_{input} = \frac{(V_s\cos(\omega_s t) + V_{LO}\cos(\omega_{LO} t))^2}{R}, \qquad 1.6$$

which using trigonometric identities simplifies to,

$$\frac{V_s^2\cos^2(\omega_s t)}{R} + \frac{V_{LO}^2\cos^2(\omega_{LO} t)}{R} + \frac{V_s V_{LO}\cos([\omega_s + \omega_{LO}]t)}{R} + \frac{V_s V_{LO}\cos([\omega_s - \omega_{LO}]t)}{R}. \qquad 1.7$$

If the response time of the mixer were very short, the temperature of the HEB would modulate at four frequencies corresponding to each of the above four terms. However, this is not the case. In a HEB mixer, the electron temperature can be raised above the lattice temperature since the escape time for phonon is much shorter than the phonon-

electron scattering time. The time it takes for electrons heated by the external power to cool back down is called the thermal relaxation time τ_θ. The inverse of this time determines the maximum frequency at which the electron temperature, and hence the device resistance, can be modulated (Prober, 1993). In a THz HEB mixer, the only oscillatory component of the device resistance is at the difference frequency (term #4 in Eq. 1.7) since

$$\frac{1}{\tau_\theta} << \omega_s\,,\ \ \omega_{LO}\,. \qquad 1.8$$

Two processes govern the thermal relaxation time of hot-electrons in the HEB microbridge: diffusion of hot electrons to the cold contact pads and phonon emission. One of these processes will dominate, depending on the material and geometry. Both diffusion-cooled and phonon-cooled HEB mixers can have IF bandwidths in the GHz range, though as will be discussed in the next section, optimized diffusion-cooled devices should have greater sensitivity.

The sensitivity of HEB mixers at f ~ a few THz is limited by thermal fluctuation noise. The electron temperature of the HEB fluctuates causing a fluctuation in the resistance. The magnitude of the thermal fluctuations should decrease as the temperature is lowered. More precisely, since the operating point of the mixer is in the vicinity of T_c, the device noise should decrease with a reduction in T_c. Johnson noise is also present in HEB mixers, and will also decrease by lowering T_c, although its magnitude is smaller than that of thermal fluctuation noise when the HEB is optimized for best performance.

In Nb HEBs, the mixer noise has been shown to be a few hundred K, which is much lower than that of Schottky mixers.

In addition to having lower noise than Schottky mixers, HEBs require considerably less LO power. The HEB is cooled to a temperature T_b below T_c and then heated by a combination of RF and DC power to the vicinity of T_c. The LO power is roughly the power needed to heat the device from T_b to T_c. For a device with $T_c = 5$ K, this can be tens of nW. Devices with lower T_c require smaller LO power.

HEB mixers are promising for use in THz astronomy. They are very sensitive and fulfill the requirements for a practical receiver. Coupling is easy and broadband both at the RF input and the IF output. Unlike SIS mixers, HEBs should work well at several THz. The upper frequency limitation in these devices is set by the elastic scattering time, which is of order 10^{-15} s in dirty metallic films. Nb films have been shown to absorb RF power uniformly from 10 GHz to 1000 THz (Gershenzon et al., 1982). Another attractive feature is that the LO power is small and the IF bandwidth broad, making the device compatible with current solid-state sources.

1.4 Summary of Current Thesis

Nb diffusion-cooled and NbN phonon-cooled HEB mixers have been studied in various groups at different frequencies in laboratory experiments. NbN devices have also been used in actual observatory settings (Kawamura et al., 1998), and similar tests for Nb mixers are in progress. Receivers for use at 2.5 THz based on Nb devices have demonstrated a receiver noise temperature $T_R \sim 2000$ K (DSB), where it is estimated

from measurements on similar devices that the noise temperature of the mixing element is approximately 300-350 K (Wyss et al., 1999; Burke et al., 1999). For NbN, typical values of the receiver noise temperature also at 2.5 THz are comparable to the Nb result above with a mixer noise estimated to be on the order of 400 K (Cherednichenko et al., 2000). Both Nb and NbN mixers are still many times noisier than the quantum limit. The goal of this work is to improve the performance of diffusion-cooled bolometers. Since previous measurements made on Nb mixers at 20 GHz and at much higher frequencies have shown relatively good correspondence, microwave measurements ($f_{LO} \sim$ 26.5-40 GHz) have been employed here as well to systematically test several devices to discover the underlying physics. Testing many devices at THz frequencies is arduous and it is often difficult to separate the properties of the mixer itself from those of the entire receiver.

The path chosen to improve mixer performance has been to lower mixer T_c. Karasik and Elantiev (1996) have predicted that the mixer noise temperature should decrease linearly with T_c when the HEB is operated with high conversion efficiency, and thermal fluctuation noise dominates. This formulation is not quantum mechanical and does not take into account the lower limit on mixer noise temperature, quantum noise. However, the noise due to thermal fluctuations experimentally observed in Nb and NbN mixers is larger than "quantum noise" ($T_Q = hf/k$), even at 2.5 THz, and there should be performance improvements with lower T_c mixers. Also, the LO power for diffusion-cooled mixers is predicted to decrease as T_c^2 under normal operating conditions. The mixer noise temperature and LO power are proportional to T_c and T_c^2, respectively, since the thermal conductivity is proportional to T_c.

In diffusion-cooled HEB mixers it is possible to get lower noise and required LO power in lower T_c devices without sacrificing IF bandwidth. The IF bandwidth is essentially independent of T_c in diffusion-cooled devices since the cooling time for electrons only depends on the diffusivity and geometry. Phonon-cooled mixers constructed from conventional materials should also have improvements in noise and LO power but at the expense of much slower operation since the electron-phonon cooling rate decreases as T_c^p, with p typically 2-4. NbN, with $T_c \sim 8$-10 K, achieves an IF bandwidth of ~ 3 GHz, limited in part by the phonon escape time from the microbridge. With a similar material having $T_c = 2$ K, the largest IF bandwidth expected is ~ 0.1 GHz, much too small for any typical application. Also, such a material would need to be developed, a challenge in materials science.

Along with improvements in sensitivity, the tendency for HEB mixers to saturate also increases with lowering T_c. One of the goals of this work, in addition to verifying the scaling with T_c mentioned above, has been to study in detail the different modes of saturation and any other performance limiting effects of the HEB mixer as a function of T_c.

Experimentally, three different techniques are used for realizing lower T_c HEB mixers. First, Al based HEB mixers fabricated at NASA/JPL with $T_c \sim 1$-2 K have been thoroughly studied. Also, bilayer mixers constructed of Nb-Au have been fabricated and characterized at Yale. The T_c of these devices is tuned by adjusting the thickness of the Au layer in contact with the Nb. Finally, Nb devices fabricated at JPL and used in previous microwave mixer measurements (Burke, 1997) were tested again, however, now in the presence of a strong magnetic field to continuously lower T_c. To verify the

experimental results obtained, numerical calculations using computer code developed at JPL were carried out, and are shown to be in good agreement with the experimental results.

The predicted dependence of the mixer noise temperature and LO power on T_c has been verified. As for saturation effects, saturation at the input RF port typically dominates for diffusion-cooled devices with 6 K $\geq$ T_c $\geq$ 2 K. For Al devices with T_c ~ 1 K, saturation at the IF output is the problem. In these mixers, good performance is only observed for a narrow range of bias voltages which places a low threshold on the maximum voltage that can be generated at the IF. The voltage width over which mixer performance degrades decreases linearly with decreasing T_c. The observed IF bandwidth is inversely proportional to the diffusion time, as expected. Limitations of IF bandwidth arising from the normal-superconductor proximity effect are observed for the first time. These effects are seen in Al mixers that have a large superconducting coherence length (ξ). We have observed the minimum length of a N-S-N type HEB to be 6-7 ξ to observe superconductivity and even longer to observe sensitive detection. This minimum length places a limit on the IF bandwidth of ~ 8 GHz • T_c, which is independent of all other parameters.

Having mapped out the dependence on T_c, a balanced picture emerges for the gains and tradeoffs associated with lower T_c HEB mixers. Lower T_c devices are more sensitive and require less LO power, but are easier to saturate. The conditions necessary to observe a simple scaling of mixer performance with T_c are also discussed, specifically the requirements on the transition width. Upper limits on the IF bandwidth for typical N-S-N HEB mixers exist, though these limits are several GHz and do not present a problem

for any proposed applications. Now it is possible to estimate the optimum T_c required for a given receiver application based on the required minimum sensitivity, and the amount of radiation that will be incident on the detector. The latter consideration is necessary to ensure the mixer does not saturate.

Chapter II: Diffusion-Cooled HEB Theory

For a given HEB mixer, the device parameters that are typically 'designed' are the resistance R, length L, critical temperature T_c, and transition width ΔT_c. Within the present theory, the other material properties of the superconductor, such as the coherence length and inelastic time, do not play a direct role. The device resistance is chosen to optimize coupling efficiency of the HEB mixer with external components. In diffusion-cooled mixers, L determines the cooling time of the hot electrons and thus the IF bandwidth. The mixer noise temperature and required LO power are then determined primarily by T_c and ΔT_c. It will be shown that for narrow transition widths, the only device parameter that determines performance is T_c. For this reason, the central goal of this work is to improve HEB mixer performance through a reduction in mixer T_c. In this chapter, two different theoretical approaches are described which predict the dependence of key operating parameters on T_c.

To develop a theory for the operation of HEB mixers, it is necessary to understand how radiation interacts with the mixer. The size and geometry of the mixer as well as the scattering processes present at low temperatures are therefore important factors to consider. Diffusion-cooled HEB mixers consist essentially of two parts, the superconducting microbridge and the thick contact pads. The microbridge is a thin, narrow strip made of conventional low temperature superconducting material such as Nb ($T_c \sim 6$ K, thin film) or Al ($T_c \sim 1.4 - 2.5$ K, thin film). All dimensions of the microbridge -- width, length, and height -- are less than 1 μm. For the particular devices studied here, the width is W ~ 0.1 μm, and the length is varied from L ~ 0.1 – 1.0 μm.

The film thickness or microbridge height is d ~ 10-20 nm. At the ends of the microbridge are thick normal-metal contacts (d ~ 100 nm), typically made of Au, as described in the previous chapter in Figure 1.4.

The dimensions of the HEB mixer are much smaller than the wavelength of THz radiation. Typically, the HEB is coupled to either a planar antenna or a waveguide structure would be placed at the focus of an appropriate telescope. Quasioptical techniques using an on-chip antenna are currently preferred over waveguide coupling at frequencies above 1 THz (Narayanan, 1999), though this is set by electromagnetic engineering considerations. Required physical dimensions for THz components become very small (~ 10 μm), and are difficult to produce reliably. However, recent advances using laser micromachined silicon structures are promising and may extend the range of waveguide receivers to higher frequencies (Groppi et al., 2001).

For efficient coupling to either a planar antenna or a waveguide, the input impedance of the mixer should be Z ~ 50-100 Ω. HEBs are metallic structures with a real impedance and negligible capacitance. By appropriate choice of film resistivity and geometry, it is relatively easy to achieve the desired input impedance. At THz frequencies, the input impedance is mainly resistive. One way to 'explain' this is to examine the Drude formula for the electrical conductivity,

$$\sigma(\omega) = \sigma(0)\,\frac{1}{1 - i\omega\tau} \qquad (2.1)$$

where σ (0) is the DC Drude conductivity and τ is the elastic scattering time. Since the metallic film is very thin and has many impurities, the electron elastic scattering time is

very short, typically ~ 10^{-15} s. At frequencies much higher than $1/\tau$, the inductive component dominates, which makes it difficult to couple radiation efficiently. This upper frequency limit is ~ 100 THz and thus not a concern for any planned applications. For THz HEB devices, the radiation frequency is larger than the superconducting energy gap frequency ($2\Delta/h$). It is thus plausible that the incoming radiation is absorbed uniformly over the microbridge. Gershenzon et al. (1982) have verified that thin Nb films in a resistive state absorb radiation uniformly over a broad frequency range from roughly 10^{10} – 10^{15} Hz.

After radiation is absorbed in the mixer, inelastic processes result in a sharing of energy. At low temperatures and for electron excitation energies of order k_BT, inelastic scattering between electrons dominates over electron-phonon processes. For a two dimensional dirty metal, the inelastic electron-electron scattering rate can be estimated (Altshuler et al., 1983) from

$$\tau_{ee}^{-1} \approx \frac{1}{4\pi} \frac{R_{\square}}{\hbar/e^2} \frac{k_B\theta}{\hbar} \tag{2.2}$$

where $R_{\square}$ is the resistance per square and θ is the electron temperature. The electron-phonon inelastic scattering rate ($\tau^{-1}_{e\text{-}ph}$) and its temperature dependence varies from material to material. For Nb films with in the normal state at 6K with 30 $\Omega/\square$ sheet resistance, the electron phonon scattering time is ~ 1 ns, and is proportional to T^2 at temperatures below 10 K (Gershenzon et al., 1990). As a result, the electron-electron scattering rate is ~ 17 times larger than the electron-phonon scattering rate. For Al at 1.5

K with comparable film parameters the electron-phonon scattering time is approximately 20 ns with a T^3 dependence (Santhanam and Prober, 1984). The electron-electron scattering rate is about 100 larger than the electron-phonon rate. Thus, after the electrons in the HEB absorb power, energy is shared amongst them rapidly via electron-electron interaction. After the electrons are heated, they eventually cool down. There is energy relaxation in a time τ_θ over which the hot electrons lose their excess energy and cool back down to the lattice temperature. In short microbridges, typical of the devices studied in this thesis, τ_θ is determined by the diffusion time (τ_{diff}) of hot electrons to the contact pads that are at fixed temperature T_b. In longer bridges, hot electrons emit phonons before being able to diffuse out of the bridge and in this case $\tau_\theta \approx \tau_{e\text{-}ph}$. The cooling time for hot electrons τ_θ is referred to the thermalization time τ_{th} in some works. However, in some other literature the thermalization time is used synonymously with the electron-phonon time. To avoid any such confusion and to be consistent with several works on HEB theory, τ_θ is used to define the relaxation time of the electron temperature, which in this thesis will always be comparable to τ_{diff}.

Thus $1/\tau_\theta$ determines how fast the electron temperature can be modulated in a HEB. Times as fast as 10-20 ps have been experimentally verified (Burke et al., 1999; Wyss et al., 1999). The fact that the HEB is a very fast bolometer makes it useful as a mixer and not just a direct detector. In the HEB mixer, the two THz input signals do not modulate the electron temperature at their respective frequencies, nor at twice their frequencies, nor at their sum. Rather, the electron temperature is modulated at the difference frequency. The difference frequency can be as large as several GHz. The

upper limit depends of course on $1/\tau_\theta$ (Section 2.2). The electron temperature is inferred from the resistance versus temperature characteristic, schematically represented in Figure 1.5a. As power heats up electrons in the microbridge, a temperature distribution along the length of the microbridge is established, as long as the bridge is long enough to have electron-electron inelastic scattering. Because of their high thermal conductivity, the thick Au contacts can be considered fixed at a temperature T_b. The center of the microbridge is the hottest since electrons there have to diffuse the furthest to reach the contacts. With sufficient applied power, the electron temperature at the center of the microbridge exceeds T_c of the film and a 'hot spot' forms, see Figure 2.1. In the 'hot spot', the film is in the normal state and thus has resistance. Outside the 'hot spot', the DC resistance is zero. The fractional length of the 'hot spot' relative to the total microbridge length gives the instantaneous DC resistance of the device. The profile of the electron temperature oscillates at the IF and so does the size of the 'hot spot'.

A partial theory for HEB mixer performance based on the 'hot spot' model has been developed over the last few years (Floet et al., 1998). This theory predicts the R vs. T characteristic, the I-V curve, and the conversion efficiency as a function of bias voltage. Numerical agreement is reasonably good for the R vs. T characteristic; but further work is needed to accurately model the conversion efficiency. Additionally, the mixer noise needs to be calculated. As such, currently there is no complete analytic theory of diffusion-cooled HEB mixer performance that takes into account the spatially dependent temperature profile of the device. Further, all models, including the theory described here, use at best, a local temperature dependent resistivity and ignore non-equilibrium

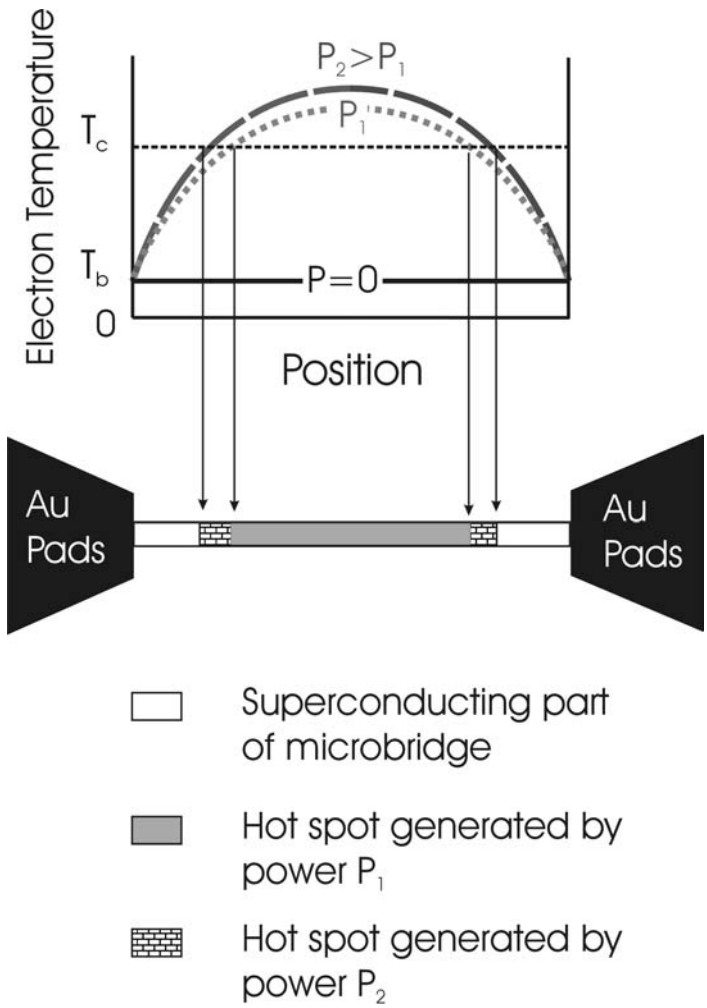

Figure 2.1: The top diagram illustrates the electron temperature profile as a function of position along the microbridge. For no input power, the electron temperature is equal to the bath temperature T_b along the microbridge. For large enough input power P_1, a 'hot spot' is formed in the center of the bridge where the local electron temperature exceeds T_c and the film in the center is in the normal state. Areas adjacent to the 'hot spot' remain superconducting since the local electron temperature is below the film T_c. For larger input power, the size of the resistive 'hot spot' grows, as shown in the lower part of the figure.

superconductivity physics. There is therefore a need for future theoretical work in this area.

For the present, we have adopted two approaches to predict HEB mixer performance as a function of T_c. In the first approach, the lumped element calculation presented by Karasik and Elantiev (1995, 1996) is utilized. This model (Section 2.3) treats the case of a bolometer with a single thermal conductance. To more accurately model a HEB, an effective thermal conductance which takes into account the electron temperature profile across the microbridge, calculated by Burke (1997), is substituted (Section 2.1). This approach allows us to predict that the mixer noise temperature is proportional to T_c and the LO power is proportional to T_c^2 for certain operating regimes. Second, we have used a numerical technique developed by Skalare et al. (1999[a,b]) to make distributed element predictions of all mixer quantities (Section 2.4). The numerical method is powerful because it allows for the easy calculation of mixer properties under different operating conditions. In addition to the mixer noise temperature and LO power, the numerical simulations are used to calculate the conversion efficiency and noise temperature as a function of bias voltage. How sharply these quantities depend on bias voltage determine how the mixer is affected by noise voltages generated at the IF by background radiation. This leads directly to predictions of the output saturation power of the mixer, and its dependence on T_c. Finally, the dependence of mixer performance on the transition width ΔT_c is investigated. From the analytic calculation, for very narrow transitions, we find that the noise temperature does not depend on ΔT_c. With the numerical calculations, it possible to quantitatively estimate how wide the transition can be before performance begins to degrade.

2.1 Temperature Profile and Effective Thermal Conductance

In this section, the position-dependent electron temperature in the microbridge is calculated as a function of input power. The calculation described here is taken from Burke (1997). The result is then used to calculate the effective thermal conductance. This is a steady state derivation which treats the microbridge as a fully normal strip of metal. In reality, there is a small energy gap in the superconducting areas adjacent to the 'hot spot' located at the center of the microbridge. However, in typical operation, the size of the 'hot spot' is fairly close to the full bridge length. Additionally, the gap at the ends is significantly reduced since the local electron temperature is in the vicinity of T_c. Thus approximating the structure as a normal-metal is reasonable.

Determining the temperature as a function of position requires solving the one-dimensional heat flow equation. The geometry being treated is that shown in Figure 2.1, where the ends of the bolometer are fixed at a temperature T_b. At any given point along the microbridge, the heat flux Φ is given by

$$\Phi = -K \frac{\partial \theta}{\partial x} \tag{2.3}$$

where K is the thermal conductivity. The heat flow is governed by

$$c \frac{\partial \theta}{\partial t} = \nabla \Phi + p_{input} \tag{2.4}$$

where p_{input} is the total input power per unit volume (radiation and DC) and c is the specific heat. Heat flow through phonon emission has been neglected. In the steady

state, the left hand side equals zero. We can relate the thermal conductivity to the electrical conductivity and electron temperature by way of the Wiedemann-Franz relation. The thermal conductivity K is equal to

$$K = \mathscr{L}\,\theta\,\sigma \tag{2.5}$$

where $\mathscr{L}$ is the Lorenz constant and σ is the electrical conductivity. Here we have used the normal state value of K. Defining capital P_{input} as the input power and expressing the electrical conductivity in terms of the bridge geometry and resistance R, Equation 2.4 simplifies for the one dimensional case to

$$\frac{P_{input}}{AL} + \frac{d}{dx}\left[\frac{\mathscr{L}\,\theta L}{RA}\frac{d\theta}{dx}\right] = 0 \tag{2.6}$$

in which A is cross-section area and L is the length of the microbridge. P_{input} is assumed to the be uniformly dissipated in the microbridge. In reality, this is not true for DC power and RF power with a frequency much smaller than the superconducting energy gap frequency. The non-uniform DC dissipation is actually accounted for in the numerical calculations discussed later. Equation 2.6 upon further simplification yields,

$$\left(\frac{d\theta}{dx}\right)^2 + \theta\frac{d^2\theta}{dx^2} + \frac{P_{input}R}{\mathscr{L}L^2} = 0\,. \tag{2.7}$$

This differential equation has to be solved with the boundary conditions that $\theta = T_b$ at x=0, L. DeJong (1995) relates the following solution,

$$\theta(x) = T_b \sqrt{1 + \frac{x}{L}\left(1 - \frac{x}{L}\right)\frac{P_{input} R}{T_b^2 \mathscr{L}}} \,. \tag{2.8}$$

The highest electron temperature is in the center of the microbridge as expected. The electron temperature at the center is

$$\theta\left(x = \frac{L}{2}\right) = T_b \sqrt{1 + \frac{P_{input} R}{4 \mathscr{L} T_b^2}} \,. \tag{2.9}$$

Simpler forms can be obtained by delineating two different operating regimes based on the magnitude of the input power P. If $P < (\mathscr{L} T_b^2/R)$, this is called the weak heating limit. Conversely, for $P > (\mathscr{L} T_b^2/R)$, we have strong heating. In these two regimes, the electron temperature is

$$\theta(x) = T_b \left[1 + \frac{x}{2L}\left(1 - \frac{x}{L}\right)\frac{P_{input} R}{\mathscr{L} T_b^2}\right] \quad \text{for weak heating} \tag{2.10}$$

and

$$\theta(x) = T_b \sqrt{\frac{x}{L}\left(1 - \frac{x}{L}\right)\frac{P_{input} R}{\mathscr{L} T_b^2}} \quad \text{for strong heating}\,. \tag{2.11}$$

To obtain Equation 2.10 the expansion $(1+x)^n \approx (1+nx)$ for $x << 1$ has been used. Additionally, one can now define the average temperature rise across the microbridge for a given input power using

$$\langle\theta\rangle_x = \frac{1}{L}\int_0^L \theta(x)\,dx \quad . \tag{2.12}$$

This yields,

$$\langle\theta\rangle_x = T_b\left[1+\frac{P_{input}R}{12\mathscr{L}T_b^2}\right] \quad \text{for weak heating} \tag{2.13}$$

and

$$\langle\theta\rangle_x = T_b\left[\frac{\pi}{8}\sqrt{\frac{P_{input}R}{\mathscr{L}T_b^2}}\right] \quad \text{for strong heating}\,. \tag{2.14}$$

From the average electron temperature, it is then possible to define the average thermal conductance using,

$$\langle G\rangle_x = \frac{\partial P_{input}}{\partial\langle\theta\rangle_x}\,. \tag{2.15}$$

For the two heating regimes, this yields

$$\langle G\rangle_x = \frac{12\mathscr{L}T_b}{R} \quad \text{for weak heating} \tag{2.16}$$

and

$$\langle G \rangle_x = \frac{2^7}{\pi^2} \frac{\mathscr{L} \langle \theta \rangle_x}{R} \quad \text{for strong heating .} \tag{2.17}$$

For a HEB mixer, we want to generate a 'hot spot' in the center so that the resistance modulates at the IF. This means that the center temperature must be greater than or equal to T_c. Consequently, the power needed to raise the electron temperature at the center of the microbridge to T_c is then approximately the total input power needed for mixing. Using Equation 2.9, this input power is

$$P_{operation} = \frac{4\mathscr{L}}{R}\left(T_c^2 - T_b^2\right) \quad \text{such that } \theta(\tfrac{L}{2}) = T_c \,. \tag{2.18}$$

The average electron temperature for this input power is $(\pi/4)\ T_c$. It will be shown in subsequent sections that the best mixer performance is achieved when $T_b << T_c$. Using the result in Equation 2.18 and this condition on the bath temperature, it is clear that the HEB operates in the strong heating limit. The average thermal conductance in the strong heating limit with an input power given by Equation 2.18 is

$$\langle G \rangle_x = \frac{2^5}{\pi} \frac{\mathscr{L} T_c}{R} \,. \tag{2.19}$$

This is an important result that will be used in the later sections. We observe that this average conductance is larger than that of a point source at temperature T_c located a distance L from the thermal reservoir at temperature T_b. In the above derivation we have treated the case of uniform power injection across the microbridge rather than heat

injection at the center. Hot electrons near the ends of the microbridge have a shorter distance to travel, enhancing the average conductance. Uniform power injection resembles more accurately the actual heat dissipation in HEB mixers. For a THz mixer, the LO frequency is much larger that the energy gap frequency and uniform power dissipation is expected. Also, the bias current used is larger than the critical current so approximating the DC dissipation as uniform is a reasonable simplification. Mather (1982) has treated the case of a bolometer with a position dependent heat conductivity, but with heat injection at a single point a distance L from the thermal reservoir.

2.2 Intermediate Frequency Bandwidth

To compute the IF bandwidth of the HEB mixer, it is necessary to compute the average diffusion time of hot electrons from the microbridge. This yields the intermediate frequency at which the conversion efficiency drops by 3dB from its IF = 0 value,

$$f_{-3dB} = \frac{1}{2\pi\tau_\theta} = \frac{1}{2\pi\tau_{diff}} . \tag{2.20}$$

The approach is to solve Equation 2.4 but without making the steady state approximation in which the time derivative of the electron temperature is taken to be zero. The input power is then time dependent and is represented by the following Fourier expansion,

$$P_{input}(t) = \sum_\omega P_\omega \, e^{i\omega t} \tag{2.21}$$

Burke (1997) finds the solution for the general time dependent equation, following the treatment in Carslaw and Jaeger (1959), to be

$$\theta(x,t) = T_b + \frac{4L^2}{\pi^2 \frac{K}{c}} \sum_{\omega} \sum_{n=0}^{\infty} \frac{(-1)^n}{(2n+1)^3} \cos\left[\frac{(2n+1)\pi x}{L}\right] \frac{P_\omega}{1+i\omega\tau_n} \left(e^{i\omega t} + e^{-t/\tau_n}\right) \quad (2.22)$$

with

$$\tau_n = \frac{L^2}{\pi^2 D\,(2n+1)^2} \quad (2.23)$$

where D is the diffusion constant, given here as the ratio of the thermal conductivity to the specific heat. In the HEB, the input power can be further simplified to include a constant term and only one oscillating term. With this simplification the time dependence of 2.22 simplifies to $1/(1+i\omega\tau_n)$. Furthermore, it can be shown that the n=0 term dominates the series expansion. As such, the IF bandwidth is set by a single time constant,

$$\tau_{diff} = \frac{L^2}{\pi^2 D}. \quad (2.24)$$

It is to be noted that in actual operation, the observed bolometer time constant may differ slightly from this form due to electro-thermal feedback effects, as will be discussed later in this chapter. Deviations from Equation 2.24 are typically seen when biasing at very high voltages, though this is not the usual mode of operation of the mixer as the conversion efficiency drops significantly at these higher voltages.

2.3 Mixer Noise Temperature

In this section the derivation of the mixer noise temperature given in the point bolometer model of Karasik and Elantiev (1995, 1996) is presented. The first step is to derive the frequency dependent bolometer impedance, following the original treatment of Mather (1984). Using this, the voltage responsivity, $S(\omega)$, is derived which is used to obtain the mixer conversion efficiency. Finally, the output noise power is calculated. Using the conversion efficiency and the output noise, the mixer input noise temperature is calculated.

2.3.1 HEB Impedance

A DC current bias is assumed in this derivation. The voltage across the HEB is then a function of the electron temperature and the bias current. A differential change in voltage is then,

$$dV = \frac{\partial V}{\partial \theta}\frac{d\theta}{dI}dI + \frac{\partial V}{\partial I}dI. \tag{2.25}$$

Often the assumption is made that the partial derivative of the voltage with respect to the current is equal to the device resistance. The rationale behind this is that at frequencies $>> 1/\tau_\theta$, the first term in Equation 2.25 is zero because $d\theta/dI = 0$ and thus a differential change in the voltage is equal to the resistance multiplied by a differential change in the current. In this derivation, the term $\partial V/\partial I$ is set equal to $Z(\omega=\infty)$ for generality. This

allows one to include effects of vortex flow or other high frequency effects that might add to the resistivity.

The DC impedance is defined as,

$$Z(\omega = 0) \equiv \frac{dV}{dI} = \frac{\partial V}{\partial \theta}\frac{d\theta}{dI} + Z(\omega = \infty)\,. \tag{2.26}$$

The resistance R is equal to V/I. Equation 2.26 simplifies to,

$$= I\frac{\partial R}{\partial \theta}\frac{d\theta}{dI} + Z(\infty)\,. \tag{2.27}$$

To make the frequency dependence of $d\theta/dI$ explicit, this quantity is defined as $M(\omega)$. $M(\omega)$ tends to zero at high frequencies. Thus the frequency dependent impedance is equal to,

$$Z(\omega) = I\frac{\partial R}{\partial \theta}M(\omega) + Z(\infty)\,. \tag{2.28}$$

To express the impedance in terms of quantities of physical interest, let's calculate the effect of a small change in current on the electron temperature. The variation in current is approximated by

$$\Delta I = \Delta I_0 e^{i\omega t} \tag{2.29}$$

which results in a change in electron temperature

$$\Delta\theta = \Delta\theta_0 e^{i\omega t}. \tag{2.30}$$

The relationship between these two variations is set by the heat balance Equation 2.4 which can be written as,

$$C\frac{d\theta}{dt} = -P_{outflow} + IV + P_{rad} \tag{2.31}$$

where C is the heat capacity, $P_{outflow}$ is heat that is carried out of the microbridge by diffusion, and P_{rad} is the total coupled input radiation power. In the small signal formalism, Equation 2.31 with no applied radiation power yields,

$$C\frac{\partial\Delta\theta}{\partial t} = -\underbrace{\frac{dP_{outflow}}{d\theta}}_{G(\theta)}\frac{d\theta}{dI}\Delta I + I\Delta V - V\Delta I \quad . \tag{2.32}$$

Substituting the form of dV given in Equation 2.25 and matching terms in Equation 2.28 gives the following,

$$i\omega CM(\omega) = -GM(\omega) + V + IZ(\omega). \tag{2.33}$$

Defining the ratio C/G as the thermal time constant τ_θ, the impedance equals,

$$Z(\omega) = \frac{\frac{I\left(\frac{\partial R}{\partial \theta}\right)R}{G} + Z(\infty)}{1 - I^2 \frac{\partial R}{\partial \theta}\frac{1}{G}} \frac{1 + i\omega \frac{\tau_\theta Z(\infty)}{Z(\infty) + I^2 \frac{\partial R}{\partial \theta}\frac{1}{G}}}{1 + i\omega \frac{\tau_\theta}{1 - I^2 \frac{\partial R}{\partial \theta}\frac{1}{G}}}. \tag{2.34}$$

At this point, we can define the self heating parameter α_0 as

$$\alpha_0 = \frac{I^2}{G}\frac{\partial R}{\partial \theta}. \tag{2.35}$$

This parameter describes the thermal response of the bolometer to a small change in electrical power. The parameter itself is basically the ratio of a differential change in DC power with a current bias to the associated change in thermal power. Consider the following scenario. A small change in resistance causes the power dissipated in the bolometer to increase under a current bias. The increase in power causes the electron temperature to increase. If $\partial R/\partial\theta > 0$, the resistance further increases and positive feedback is established. The quantity α_0 characterizes the strength of this feedback. For α_0=1, there is thermal runaway in which case the temperature continues to rise until $\partial R/\partial\theta$ finally goes to zero as the superconducting transition temperature is exceeded. With a voltage bias, the system is actually stabilized since the power decreases with increasing resistance. The parameter α_0 will be used in the later sections to characterize the operating regimes of the HEB mixer. The impedance calculated above can be expressed in terms of α_0 as,

$$Z(\omega) = \frac{\alpha_0 R + Z(\infty)}{1-\alpha_0} \frac{1 + i\omega \dfrac{\tau_\theta Z(\infty)}{Z(\infty) + \alpha_0 R}}{1 + i\omega \dfrac{\tau_\theta}{1-\alpha_0}}$$

$$\Downarrow \qquad . \qquad (2.36)$$

$$Z(0)$$

2.3.2 Voltage Responsivity

Another important quantity in describing the operation of a bolometer is its responsivity to radiation. The responsivity of the HEB is a function of the IF, and is defined as

$$S(\omega) = \frac{dV}{dP_{rad}}. \qquad (2.37)$$

The starting point in the derivation involves making the small signal approximation again (see Equations 2.29, 2.30), but this time the radiation term in Equation 2.31 is not set to zero. This yields the following equation,

$$(i\omega C + G)\Delta\theta = V\Delta I + I\Delta V + P_{rad}. \qquad (2.38)$$

The output circuitry of the HEB must be specified to correctly define the responsivity. The bolometer is assumed to be connected in parallel to a load resistance R_L. The change in current is then simply

$$\Delta I = \frac{-\Delta V}{R_L}. \qquad (2.39)$$

The change in voltage is obtained by substituting into Equation 2.25,

$$\Delta V = I\,\Delta\theta \frac{\partial R}{\partial \theta}\left(1+\frac{Z(\infty)}{R_L}\right)^{-1} . \tag{2.40}$$

This equation can be used to eliminate $\Delta\theta$ from Equation 2.38, resulting in

$$(i\omega C + G)\frac{\Delta V}{I\dfrac{\partial R}{\partial \theta}}\left(1+\frac{Z(\infty)}{R_L}\right) = -V\frac{\Delta V}{R_L} + I\Delta V + \Delta P_{rad} . \tag{2.41}$$

Dividing both side of the equation by ΔP_{rad} gives the voltage responsivity,

$$S(\omega) = \frac{1}{I}\left[\frac{(i\omega C + G)}{I^2\dfrac{\partial R}{\partial \theta}}\left(1+\frac{Z(\infty)}{R_L}\right) + \frac{Z(\infty)}{R_L} - 1\right]^{-1} . \tag{2.42}$$

After many algebraic transformations, Equation 2.42 can be expressed in the following form,

$$S(\omega) = S(0)\frac{1}{1+i\omega\tau_{eff}} \qquad \text{where}$$

$$S(0) = \frac{1}{I}\frac{\alpha_0}{1+\alpha_0\dfrac{R-R_L}{R_L+Z(\infty)}}\frac{R_L}{Z(\infty)+R_L} \qquad \text{and} \tag{2.43}$$

$$\tau_{eff} = \frac{\tau_\theta}{1+\alpha_0\dfrac{R-R_L}{R_L+Z(\infty)}} .$$

From Equation 2.43 the effect of electro-thermal feedback on the speed of the bolometer can be seen. If there is considerable electro-thermal feedback, the parameter $\alpha_0 \sim 1$ and the effective time constant observed differs from the thermal relaxation time of the hot electrons. However, there is also a stabilizing effect from the load resistor. The load resistor establishes a passive voltage bias at the IF and thus the effect of electro-thermal feedback on the device speed is minimized. In fact, the effective time constant is equal to the thermal time constant if the device resistance is equal to the load resistance.

2.3.3 Mixer Conversion Efficiency

The voltage at the IF can be calculated from the responsivity derived in the previous section,

$$V_{IF} = \frac{dV}{dP} P_{ac\ input} . \tag{2.44}$$

In the HEB, the only oscillatory component of the input power that is detected is at the IF. Using the expression for the incident power at the IF given in Equation 1.7, the output voltage of the HEB at the IF is

$$V_{IF} = 2S(\omega)\sqrt{P_s P_{LO}}\, e^{i(\omega t+\varphi)} , \tag{2.45}$$

where ϕ is an arbitrary phase factor inserted for generality. Assuming this voltage is coupled to a matched load, the detected voltage on the load resistor is ½ the value in Equation 2.45. The conversion efficiency is the ratio of output power at the IF and input signal power, and is then equal to

$$\begin{aligned}\eta(\omega) &= \frac{2|S(\omega)|^2}{R_L} P_{LO} \\ &= 2\alpha_0^2 \frac{R_L R}{(Z(\infty)+R_L)^2} \frac{P_{LO}}{P_{DC}} \frac{1}{\left(1+\alpha_0 \frac{R-R_L}{Z(\infty)+R_L}\right)^2} \frac{1}{1+(\omega\tau_{eff})^2}\end{aligned} \quad . \qquad (2.46)$$

To obtain the highest conversion efficiency, working in the regime where $\alpha_0 \sim 1$ is best. It is possible to get high conversion efficiency without a reduction in IF bandwidth if $R_L \sim R$.

2.3.4 Thermal Fluctuation Noise

Thermal fluctuation noise exists due to a random exchange of heat carriers between the bolometer and the bath. In the point bolometer calculation we only consider fluctuations of a single electron temperature connected to a thermal reservoir at temperature T_b. The average fluctuation of the electron temperature can be shown to equal,

$$\langle \Delta\theta \rangle = \sqrt{\frac{4k_b\theta^2}{G}} \frac{1}{1+i\omega\tau_\theta} . \qquad (2.47)$$

The frequency dependence of the temperature fluctuations can be understood in a simple way. The electron temperature cannot fluctuate at a frequency greater than that set by the thermal relaxation rate of hot electrons. Fluctuations in the electron temperature generate fluctuations in the device resistance, which finally result in voltage fluctuations at the HEB output in the case of a current bias.

To derive how thermal fluctuations couple to the mixer output, an equivalent circuit representation is needed. Mather (1982) introduced an inductive circuit to model the reactance of the HEB. Karasik and Elantiev (1995) have generalized Mather's results by letting the high frequency impedance of the bolometer be $Z(\infty)$ instead of R. This equivalent circuit is shown in Figure 2.2. To match the results derived above for the impedance and responsivity, the following parameters are chosen for the equivalent circuit,

$$R_1 = \frac{Z(0)Z(\infty)}{Z(\infty) - Z(0)}$$

$$L = \frac{-\tau_\theta}{\alpha_0} \frac{Z(\infty)^2}{R + Z(\infty)} \tag{2.48}$$

$$V_1 = \frac{-P_{LO}}{I} \frac{Z(\infty)}{R + Z(\infty)}.$$

This definition of V_1 corresponds to the voltage generated at the IF by the mixer. To calculate the effect of thermal fluctuation noise, V_1 is now replaced by the noise voltage generated by thermal fluctuations,

$$-G\langle\Delta\theta\rangle\frac{Z(\infty)}{I(Z(\infty)+R)}. \tag{2.49}$$

G is the thermal conductivity. The noise voltage across the load resistor is

$$V_{Noise}^{TF}=\frac{\sqrt{4k_b\theta^2G}}{I}\frac{\alpha_0}{1+\alpha_0\frac{R-R_L}{Z(\infty)+R_L}}\frac{R_L}{Z(\infty)+R_L}\frac{1}{1+i\omega\tau_{eff}}. \tag{2.50}$$

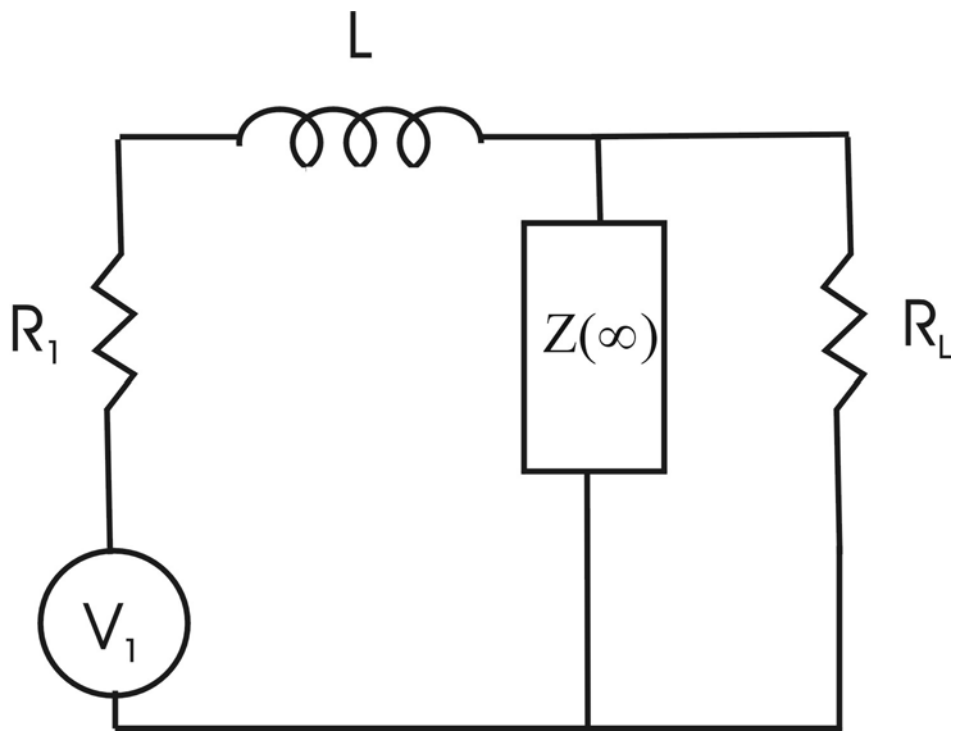

Figure 2.2: Electrical equivalent circuit representation for the HEB used in the analytical lumped bolometer model. The definitions of V_1, R_1, and L given in Equation 2.48 are chosen so as to yield the conversion efficiency given in Equation 2.46.

The output noise temperature (T_{output}) due to thermal fluctuation is defined as the output noise power divided by Boltzman's constant. This noise temperature can be referred to the mixer input by dividing by the conversion efficiency; this is $T_M^{TF}=T_{output}/(2\eta)$. In fact, we divide by twice the conversion efficiency to obtain the DSB mixer noise temperature due to thermal fluctuations, and obtain

$$T_M^{TF} = \frac{\theta^2 G}{P_{LO}}. \tag{2.51}$$

This noise temperature is independent of IF since both the conversion efficiency and the noise spectral density have the same frequency dependence. At high frequencies, a smaller quantity of noise is generated at the output, but by the same token the conversion efficiency is low so the thermal fluctuation noise, referred to the input, is frequency independent.

2.3.5 Johnson Noise

The HEB, like any resistor, generates Johnson noise. In addition to the classical Johnson noise voltage generated across a resistor, it is necessary to include the self-detection of the Johnson noise power by the bolometer. Since the bolometer has a finite thermal conductance, the bias current does work on the source of Johnson noise which

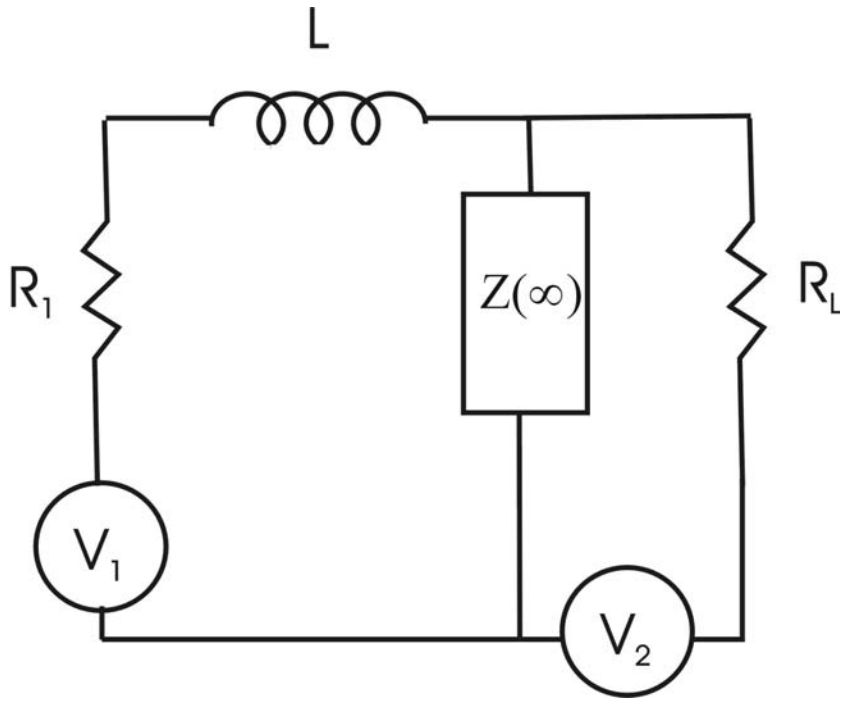

Figure 2.3: Electrical equivalent circuit representation for the HEB used for modeling Johnson noise with electro-thermal feedback in the analytical lumped bolometer model. V_1 and V_2 are now both noise voltages used to model Johnson noise. V_1 models the usual contribution of the Johnson noise of a resistor, while V_2 takes into account the self-detection of Johnson present when the thermal conductance is finite.

can be detected by the bolometer. Two noise generators are included in the equivalent circuit for Johnson noise, as shown in Figure 2.3 (Mather, 1982). The Johnson noise of the bolometer in the absence of electro-thermal feedback is approximated with the expression for simple resistors. V_1 represents this usual contribution of Johnson noise,

$$V_1 = \sqrt{4k_b Z(\infty)\theta}\,. \tag{2.52}$$

The second noise voltage source V_2 takes into account the detection of Johnson noise by the bolometer,

$$V_2 = -\sqrt{4k_b Z(\infty)\theta}\,\frac{Z(\infty)}{Z(\infty)+R}\,. \tag{2.53}$$

The total noise voltage across the load resistor is then,

$$V_{\text{Noise}}^{J} = \sqrt{4k_b Z(\infty)\theta}\,\frac{Z(0)+R}{Z(0)+R_L}\frac{R_L}{R+Z(\infty)}\frac{1+i\omega\tau_\theta}{1+i\omega\tau_{\text{eff}}}\,. \tag{2.54}$$

Expressing this voltage as an input noise temperature as was done with thermal fluctuation noise in the previous sections gives the following relation for the DSB mixer noise temperature (at the input) due to Johnson noise,

$$T_M^J = \frac{\theta}{\alpha_0^2}\frac{P_{DC}}{P_{LO}}\frac{Z(\infty)}{R}\left[1+(\omega\tau_\theta)^2\right]. \tag{2.55}$$

Unlike thermal fluctuation noise, the Johnson noise contribution to the mixer noise does have a frequency dependence. This is because Johnson noise is almost frequency

independent and the conversion efficiency has a roll off set by the thermal time constant. Additionally, we note that electro-thermal feedback, which increases α_0, suppresses Johnson noise.

2.3.6 Noise Bandwidth

The noise bandwidth of the hot electron bolometer mixer is the frequency range over which the mixer noise temperature increases by a factor of 2. The noise temperature is twice the IF=0 value at a frequency,

$$f_{Noise} = \frac{1}{2\pi\tau_\theta}\sqrt{1+\frac{T_M^{TF}}{T_M^J(\omega=0)}} \tag{2.56}$$

The noise bandwidth is thus larger than the conversion bandwidth by a factor related to the ratio of the magnitude of the thermal fluctuation noise to the IF=0 Johnson noise.

2.3.7 Broken Line Transition Model

The results for the noise temperature derived in the point bolometer model above can be simplified for a resistive transition in which the resistance drops linearly from the normal state value to zero in a temperature interval ΔT_c centered on T_c. In this model, the assumption is that the HEB is biased in the middle of the transition through a combination of DC and LO power. Thus the resistance R (=V/I) is ½ the normal state resistance R_N. The electron temperature at the middle of the transition is T_c. For the rest

of this section we approximate the electron temperature of the HEB to be T_c. Thus the derivative of the resistance with electron temperature is equal to

$$\frac{\partial R}{\partial \theta} = \frac{R_N}{\Delta T_c} = \frac{2R}{\Delta T_c} \tag{2.57}$$

where ΔT_c is the width of the superconducting transition. Using Equation 2.19 for the average thermal conductance and Equation 2.57 above, the self heating parameter simplifies to

$$\alpha_0 = \frac{\pi P_{DC} R}{16 \mathscr{L} T_c \Delta T_c} . \tag{2.58}$$

The DC power can thus be expressed as a function of the self-heating parameter. The total input power needed to raise the electron temperature in the center of the bolometer to T_c is given by Equation 2.9. Heat balance then gives,

$$\frac{4\mathscr{L}}{R}\left(T_c^2 - T_b^2\right) = P_{DC} + P_{LO} \tag{2.59}$$

Therefore,

$$\begin{aligned} P_{DC} &= \frac{16\mathscr{L}\, T_c \Delta T_c \alpha_0}{\pi R} \\ P_{LO} &= \frac{4\mathscr{L}}{R}\left(T_c^2 - T_b^2 - \frac{4}{\pi} T_c \Delta T_c \alpha_0\right). \end{aligned} \tag{2.60}$$

The mixer noise temperature due to thermal fluctuation noise and Johnson noise can be simplified by substituting Equation 2.19 for the average thermal conductance and the above result for the LO power into Equations 2.51 and 2.55,

$$T_M^{TF} = \frac{2^3}{\pi} \frac{T_c^3}{\left(T_c^2 - T_b^2 - \frac{4}{\pi} T_c \Delta T_c \alpha_0 \right)}$$

$$T_M^{J} = \frac{4}{\pi \alpha_0} \frac{T_c^2 \Delta T_c}{\left(T_c^2 - T_b^2 - \frac{4}{\pi} T_c \Delta T_c \alpha_0 \right)} \left[1 + (\omega \tau_\theta)^2 \right]. \tag{2.61}$$

To derive the expression for the Johnson noise, $Z(\infty)$ was set to the device resistance R. For good conversion efficiency, T_b must be << T_c. For $T_b \sim T_c$, the required LO power becomes very small and thus the conversion efficiency does as well, since it is proportional to P_{LO}. In the limit of a very narrow transition and T_b << T_c, the noise temperature is given by

$$T_M^{TF} = \frac{8T_c}{\pi} \propto T_c$$

$$T_M^{J} = \frac{4}{\pi \alpha_0} \Delta T_c \left[1 + (\omega \tau_\theta)^2 \right]. \tag{2.62}$$

The LO power simplifies to

$$P_{LO} = \frac{4\mathscr{L}}{R} T_c^2 \propto T_c^2 . \tag{2.63}$$

2.3.8 Summary of Analytical Results

When the HEB mixer is optimized and operated with good conversion efficiency, the parameter α_0 is maximized. In this regime, with a narrow superconducting transition width, the thermal fluctuation noise dominates over the Johnson noise. As a result, the mixer noise temperature should be a few times T_c. For wide transition widths, the conversion efficiency decreases since $\partial R/\partial\theta$ decreases. When operating with poor conversion efficiency, Johnson noise begins to dominate. The noise temperature is then not a priori proportional to T_c. Thus for an HEB operating with high conversion efficiency and with a narrow transitions, the noise temperature is dominated by thermal fluctuations, and is predicted to be proportional to T_c.

An important point has to be noted regarding the noise temperature calculated in this section. The theory presented does not consider any quantum mechanical limitations to the mixer noise. The minimum noise temperature for a heterodyne mixer is ~ hf/k, which is 48 K/THz (Kerr et al., 1997). The calculations presented only consider thermal fluctuation noise and Johnson noise. The contribution of thermal fluctuations to the mixer noise scales linearly with T_c. The total noise temperature will scale linearly with T_c only if thermal fluctuations dominate, which is the case when the conversion efficiency is maximized. When operating with poor conversion efficiency, the Johnson noise is not negligible compared to thermal fluctuation noise and a linear dependence of T_M on T_c is not necessarily expected. If quantum noise is larger than thermal fluctuation noise, the mixer noise temperature will only be minimally affected by lowering T_c. Measurements of Nb devices at 20 GHz show that the thermal component of the mixer noise is larger than 100 K. Therefore, even in a 2.5 THz receiver where the quantum

noise is ~ 150K, thermal fluctuations will still be a significant contribution to the total noise and lowering mixer T_c should reduce the total noise.

The LO power is predicted to be proportional to T_c^2. It is important to note the decreasing the LO power by operating the mixer with $T_b \sim T_c$ is not useful since the conversion efficiency degrades in this regime. The reason for this is that the conversion efficiency is proportional to P_{LO}/G^2 and G is proportional to T_c. Decreasing the LO power by increasing the bath temperature leaves the conductance unaffected and hence conversion decreases. Lowering T_c on the other hand, lowers the thermal conductance and the LO power simultaneously, and thus does not degrade the conversion efficiency.

2.4 Numerical Simulations

In order to study HEB performance as a function of T_c and other parameters in greater detail, numerical simulations have been employed. The technique involves discretizing the microbridge into many segments and then applying classical heat flow equations to each segment. The method and the computer code were developed by Skalare (1999[a,b]). R. Jahn (2001) carried out the simulations. There are several advantages of using numerical calculations. With this method, the I-V curves can be calculated from first principles. From the I-V curves, the conversion efficiency and other parameters can be calculated. In the analytical approach, the self-heating parameter (or $\partial R/\partial\theta$) has to be specified at the operating point. The self-heating parameter can be estimated using the experimental I-V curve, but cannot be predicted accurately without the help of experimental data. With the numerical model, it is possible to study

quantitatively the mixer performance under a wide range of operating conditions: high/low conversion efficiency, wide/narrow superconducting transition, uniform/non-uniform R vs. T across the bridge length, etc. The critical temperature dependence in these different conditions can then be extracted. In this section the numerical method is described. First, a steady state model is used to calculate the I-V curves. Then a small signal model is used to calculate the conversion efficiency and mixer noise due to thermal fluctuations. Johnson noise is not treated, as it is assumed the mixer will be operated in a regime where thermal fluctuation noise dominates.

2.4.1 Large Signal Model: I-V Curves

The model involves dividing the microbridge into 2N segments, each of width Δx. Each segment has a local electron temperature and thermal conductivity associated with it, see Figure 2.4. The thermal conductivity is assumed to follow the Wiedemann-Franz relation, and the heat flow at a given point is,

$$\Phi = -G(\theta)\nabla\theta = -\frac{G_0}{\theta_0}\theta\nabla\theta \tag{2.64}$$

where G_0 is the thermal conductivity at a reference temperature θ_0. The thermal conductivity is thus a linear function of the electron temperature and its magnitude is defined by a user specified parameter G_0/θ_0. Similar to the analytic calculation, uniform dissipation of the radiation power is assumed. DC power in only dissipated where the local electron temperature is greater than T_c. The center of the bolometer is taken to be the origin and the bridge extends to a length $N\Delta x$ on each side of the origin. Invoking

symmetry arguments, only half of the bolometer has to be considered. At a given distance x from the center of the HEB, a steady state heat flow condition is enforced. This gives,

$$-\frac{G_0}{\theta_0}\theta\frac{d\theta}{dx}=\frac{P_{rad}}{wdL}x+\frac{I_0^2}{w^2d^2}\int_0^x\rho(x',\theta(x'))dx' \tag{2.65}$$

where the left hand side of the equation is the heat flowing out by diffusion, the first term on the right hand side is the RF power dissipated in the fraction of the microbridge from the origin to the point x, and the last term is the DC power dissipated. W is the microbridge width and d is the thickness. The resistivity is a non-linear function of the temperature and this differential equation does not, in general, have a closed-form solution. To formulate a numerical solution, the term $\theta\frac{d\theta}{dx}$ is written as $\frac{1}{2}\frac{d\theta^2}{dx}$. The finite difference formalism with an index k running from 1 to N can then be used to write equation 2.65 as,

$$-\frac{1}{2}\frac{G_0}{\theta_0}\frac{\theta_k^2-\theta_{k-1}^2}{\Delta x}=\frac{P_{rad}}{w\,d\,L}\Delta x\,(k-1)+\frac{I_0^2}{w^2d^2}\Delta x\,U_k\,. \tag{2.66}$$

The integral in Equation 2.65 has been approximated by $\Delta x\,U_k$. The function U_k is the average resistivity in the kth segment,

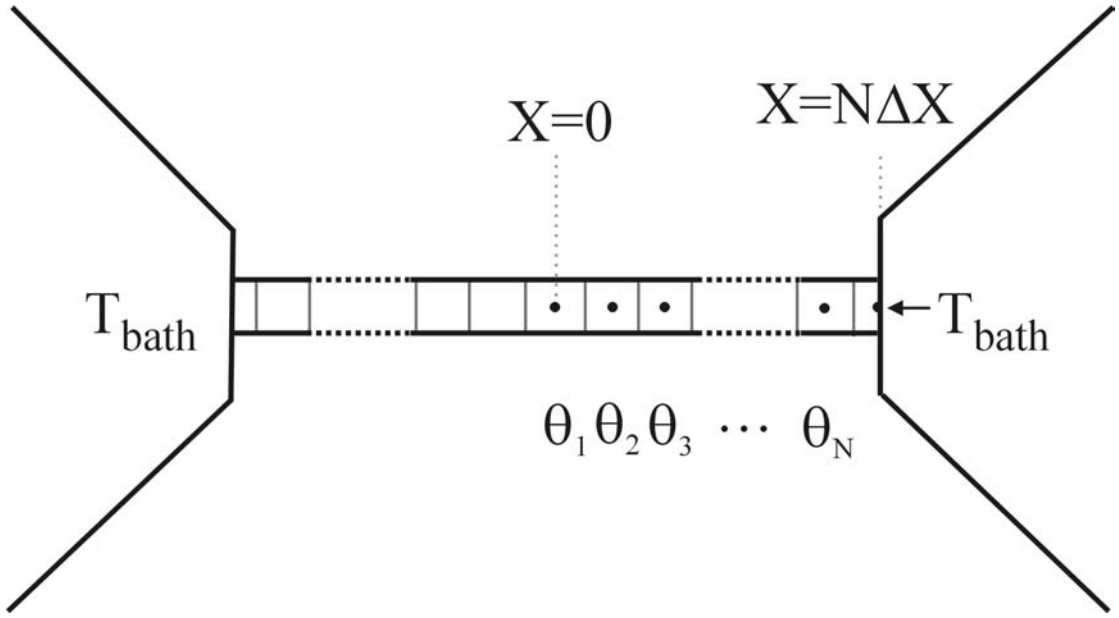

Figure 2.4: Scheme used to discretize the HEB in the numerical calculations.

$$U_1 = 0,\ U_2 = \rho_1,\ U_k = \frac{1}{2}\rho_1 + \sum_{m=2}^{k-1}\rho_m + \frac{1}{2}\rho_{k-1} \text{ for } k = 3, 4...N\,. \qquad (2.67)$$

A DC current bias with current I_0 is assumed and wdL is the volume of the microbridge. The local resistivity is given by ρ_k. In the simulation, the resistance versus electron temperature characteristic is specified for points along the bridge. In the simplest case, each point x has the same R vs. θ. If the critical temperature of the ends of the microbridge is suppressed due to close proximity to the normal contacts, this effect can be included in the model by specifying a different R vs. θ for the bridge ends. This effect will be discussed in detail in Chapter IV. Each value of the center temperature thus specifies a particular point on the IV curve. For a given value of the center temperature and radiation power, the bias current is adjusted until the temperature of the microbridge

ends is the bath temperature T_b. Stepping through a range of center temperatures thus generates the I-V curve.

2.4.2 Small Signal Model: Conversion Efficiency

Each segment along the microbridge is modeled as having a power dissipation ΔP_k and a heat capacity C_k. Between segments, there is a heat conductance G_k, and a temperature difference $\Delta\theta_k$. Analogous to electrical systems, a thermal equivalent circuit is shown in Figure 2.5. Each temperature difference along the microbridge can be related to the dissipated power through a matrix A, $\Delta\theta_k = \sum_m A_{km}\,\Delta P_l$. The matrix A is given by

$$A^{-1} = \begin{pmatrix} (i\omega C_1 + G_1) & -G_1 & 0 & \dots \\ -G_1 & (i\omega C_2 + G_1 + G_2) & -G_2 & \dots \\ 0 & -G_2 & \dots & \dots \\ \dots & \dots & \dots & \dots \end{pmatrix}. \tag{2.68}$$

To calculate the change in resistance from the change in temperature and finally the conversion efficiency, an equivalent electrical circuit for the bolometer is needed and is shown in Figure 2.6. R_0 and I_0 are the large signal resistance and current calculated in Section 2.4.1, and ΔR and ΔI are the respective modulations. R_L is the load resistor to which the IF output signal is coupled and I_L is the externally applied DC bias. Simple circuit analysis gives formulas for the IF current (ΔI) and voltage (ΔV),

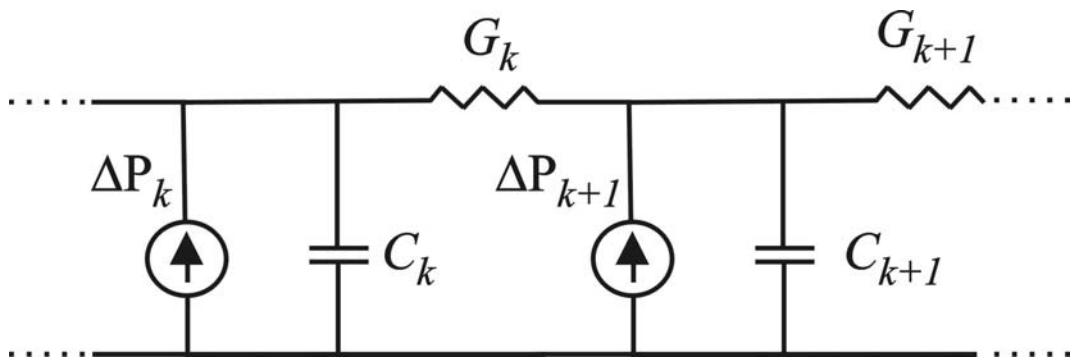

Figure 2.5: Thermal equivalent circuit used to calculate the conversion efficiency in the numerical calculations. The sources represent power dissipation in each segment of the bolomter.

$$\Delta I = -\frac{I_0}{R_0 + R_L}\Delta R$$
$$\Delta V = -R_L \Delta I \tag{2.69}$$

with

$$I_0 = \frac{I_L R_L}{R_0 + R_L}.$$

The power dissipated in each element is a combination of DC and radiation power, and keeping only the first order terms is given by,

$$\Delta P_k = \Delta P_{rad,k} + \Delta P_{bias,k} = \Delta P_{rad,k} + 2R_{0,k} I_0 \Delta I + I_0^2 \Delta R_k . \tag{2.70}$$

The contribution to the total IF resistance modulation in each segment is ΔR_k. Each segment contributes $R_{0,k}$ to the total large signal resistance R_0. ΔR_k can be expressed in terms of the temperature difference as,

$$\Delta R_k = \frac{\partial R_k}{\partial \theta_k}\Delta\theta_k = \frac{\partial R_k}{\partial \theta_k}\sum_m A_{km}\left(\Delta P_{rad,m} + 2R_{0,m}I_0\Delta I_0 + I_0^2\Delta R_m\right). \tag{2.71}$$

The ratio of the total IF resistance modulation to the total input radiation power is used to define a parameter E for notational ease,

$$E \equiv \frac{\Delta R = \sum_k \Delta R_k}{\Delta P_{rad} = \sum_k \Delta P_{rad,k}}. \tag{2.72}$$

E in essence is obtained by matrix manipulations of Equation 2.71. Modeling the LO and RF signals as sinusoids (Equation 1.7), the radiation power at the IF is $\frac{V_{LO}V_S}{R_N}$ where R_N is the normal state resistance of the bolometer. The voltage at the IF output is thus,

$$\Delta V = \frac{R_L^2 I_L}{(R_0 + R_L)^2}\Delta R = \frac{R_L^2 I_L}{(R_0 + R_L)^2} E \frac{V_{LO}V_S}{R_N}. \tag{2.73}$$

The conversion efficiency is simply the ratio of the output power at the IF divided by the input signal power,

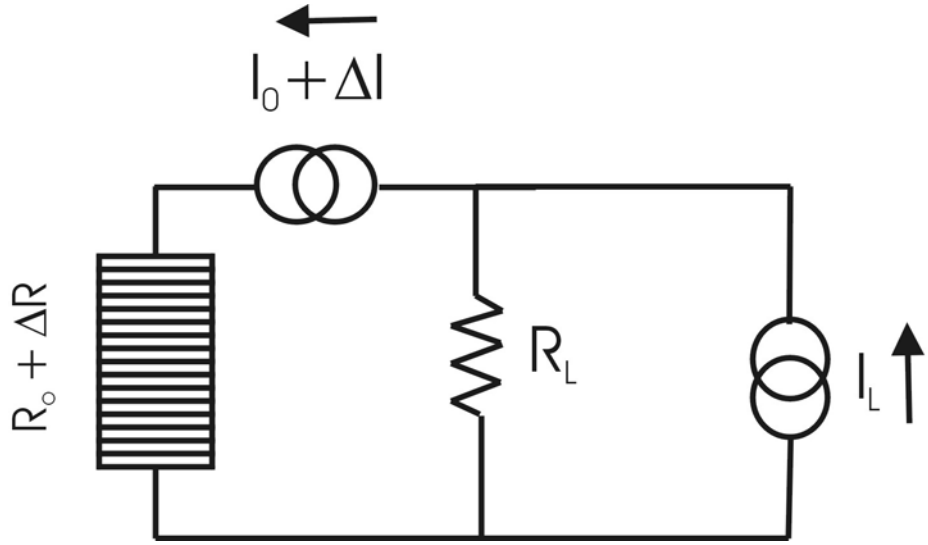

Figure 2.6: Electrical equivalent circuit used to represent the HEB in the numerical calculations. The bolometer is represented as a distributed element with a resistance $R_0 + \Delta R$. R_0 and I_0 are the steady state resistance and current of the HEB while ΔR and ΔI are the modulations at the IF. R_L is the IF load resistance and I_L the external bias current.

$$\eta = 2R_L P_{rad} \left| \frac{I_0 E}{R_0 + R_L} \right|^2 . \tag{2.74}$$

2.4.3 Small Signal Model: Thermal Fluctuation Noise Temperature

To calculate the effect of thermal fluctuations on the mixer noise, the equivalent circuit model shown in Figure 2.7 is used. The noise power sources Q_k represent energy exchange between different elements rather than dissipation. The noise sources are

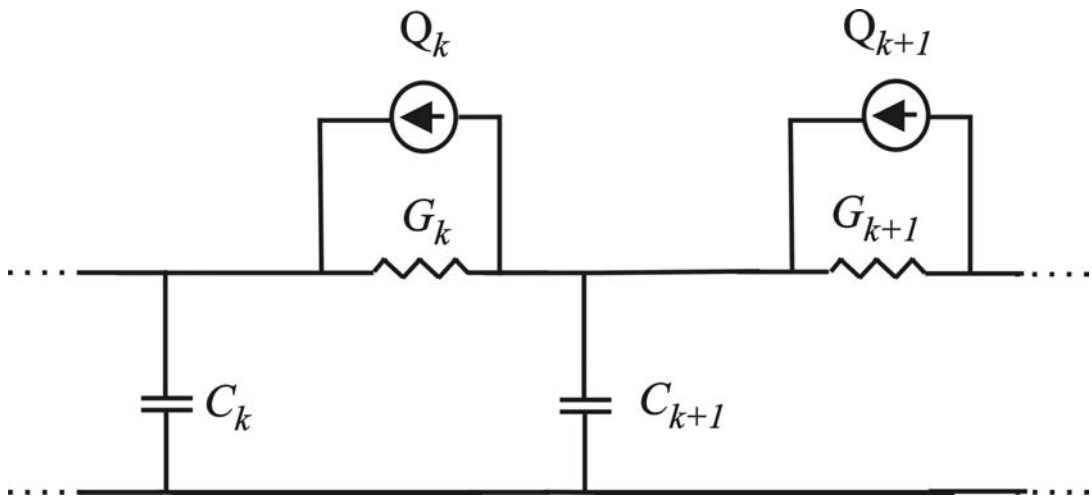

Figure 2.7: Equivalent circuit representation used to calculate thermal fluctuation noise in the numerical calculations.

assumed uncorrelated in time and with each other. Similar to the approach in the previous section, the temperature change in a bandwidth interval df is equal to,

$$\begin{aligned} \left|\Delta\theta_k\right|^2 \mathrm{df} &= \left|F_{km}\right|^2 \left|Q_m\right|^2 \mathrm{df} \\ F_{km} &= A_{kl}[\delta_{lm} - \delta_{l,m+1}]. \end{aligned} \tag{2.75}$$

In the actual calculation, all of the above quantities are cast into matrices and column vectors. To calculate the magnitude of the thermal noise sources, the following relation based on the Wiener-Khinchine theorem is used,

$$\int_0^\infty \left|\Delta\theta_k(f)\right|^2 \mathrm{df} = \left\langle \left|\Delta\theta_k(t)\right|^2 \right\rangle = \frac{k_b \theta_k^2}{C_k}. \tag{2.76}$$

After calculating the magnitude of the sources and appropriate algebraic manipulations, the noise power generated at the IF on the load resistor can be calculated. The details can be found in Skalare (1999[b]).

2.4.4 Summary of Numerical Calculations

The numerical simulations were first used to model mixing performance in the limit of $\Delta T_c << T_c$. In this regime, the predictions for the mixer noise temperature and LO power resemble those of the analytic theory. The mixer noise temperature is a few times the critical temperature, considering only the contribution of thermal fluctuations. Calculations for the conversion efficiency as a function of bias voltage agree well with experiment, and are useful in characterizing output saturation effects, especially if any suppression of superconductivity in seen in the ends of the microbridge. Finally, the scaling predictions were studied for HEBs with large transition widths. It will be shown that deviations from the predictions obtained for narrow transitions occur when $\Delta T_c > T_c / 3$, which is a relatively large transition width.

Chapter III: Devices

The goal of this work is to study the properties of superconducting diffusion-cooled HEB mixers with $T_c < 6$ K. Nb thin film HEB mixers with $T_c \sim 6$ K have previously been characterized, and the motivation for studying devices with lower T_c is to improve sensitivity and reduce local oscillator power. Two different approaches have been used in the present work to obtain HEB mixers with $T_c < 6$ K. The first method simply uses superconductors with $T_c < 6$ K such as Al and Nb-Au. The second method involves applying a strong magnetic field to Nb devices with $T_c \sim 6$ K in zero field to reduce T_c.

Al HEB mixers were the first devices to be studied. Bulk Al has $T_c \sim 1.2$ K; pure films 10 nm thick have $T_c \sim 1.4$ K. As the resistivity of Al is increased, T_c also increases. This trend is opposite to what is normally observed with most classic, low temperature superconductors, and has been well documented over the years. The thin Al films used to fabricate the HEBs in the present work have $T_c \sim 1.4 - 2.5$ K, depending on resistivity. Measurements on Al devices show that the mixer noise temperature and LO power decrease with T_c, as expected. Along with these improvements, however, many unexpected effects are also observed. Al has a long coherence length and very short HEB mixers are not superconducting due to a suppression of superconductivity from the large normal-metal contacts. Also, the increased sensitivity of the Al devices is accompanied by a small saturation power. The small saturation power of Al mixers is a limitation for many current applications. As such, it is desirable to study materials with T_c higher than

Al but still lower than Nb. Such devices would have less sensitivity than Al but would also be less prone to saturation effects.

Rather than try many different material systems, each of which would have their own specific characteristics, we then measured Nb devices in a perpendicular magnetic field. (Our new cryostat had this capability, with its 5 T magnet). At the onset, this seemed like an ideal way to test the dependence of mixer properties on T_c. A single device can be measured at many different values of T_c, thus eliminating any variations that might occur from device to device and from different choice of materials. This technique works well for lowering T_c down to about 3 K. For even lower values of T_c, complicated behavior is observed, and the mixers are only weakly superconducting; the critical currents are very low.

Producing Nb devices with lower T_c is a good idea, but we found that the use of a magnetic field is not the best way to achieve this goal. The final devices investigated in this thesis are HEBs with a bi-layer microbridge, consisting of superconducting Nb with a layer of normal Au on top. These devices have low T_c without a drastic decrease in critical current. Additionally, no magnetic field is needed to lower T_c. Good mixing performance is observed and these devices seem ideal for future applications.

In this chapter, the fabrication methods for the three different device types described above are detailed. The Al and Nb HEBs were fabricated at the Jet Propulsion Laboratory (JPL), NASA and the Nb-Au devices were fabricated at Yale. The geometry and film properties of the specific devices studied are also listed in each subsection.

3.1 Al HEB Mixers

The Al mixers were fabricated at the Micro-Devices Laboratory at JPL by P. Echternach (1999). Electron-beam lithography was used to expose a bi-layer poly-methyl methacrylate (PMMA) resist. A narrow channel is patterned in the upper resist layer with wide contacts on both ends. Al is subsequently deposited in an electron-beam evaporator. Without breaking vacuum, the substrate is tilted and the contact pad material is deposited. When depositing with the substrate tilted at an angle metal only strikes the wide contacts and does not land on top of the microbridge, see Figure 3.1. Such in-situ deposition of the contacts is necessary to ensure that no aluminum oxide insulating barrier forms between the microbridge and the contacts. Aluminum oxidizes very rapidly in the presence of oxygen, and the aluminum oxide insulator cannot be easily removed. The contact pads immediately on top of the microbridge are made of thicker Al rather than a typical normal metal such as Au, Ag, or Pt. Thick Al was chosen because in the JPL devices, it was observed that any type of heating in the processing steps after the microbridge deposition would cause the normal metal (eg. Au) in the contacts to diffuse into the microbridge. The contacts were finally chosen to be thicker Al (63nm), followed by Ti (28nm), and capped with Au (28nm).

The trilayer contact is itself superconducting, with a T_c lower than that of pure Al. The normal metals, Ti and Au, suppress T_c of the contacts down to ~ 0.6 K. A small (~ 0.01-0.1 T) perpendicular magnetic field is applied to drive the contacts into the normal state. The upper critical field of the microbridge is several times larger, and thus superconductivity in the microbridge is not significantly suppressed. With the magnetic field applied, these devices resemble the typical HEB geometry considered so far, normal-metal contacts with a superconducting microbridge (N-S-N). For 30 GHz

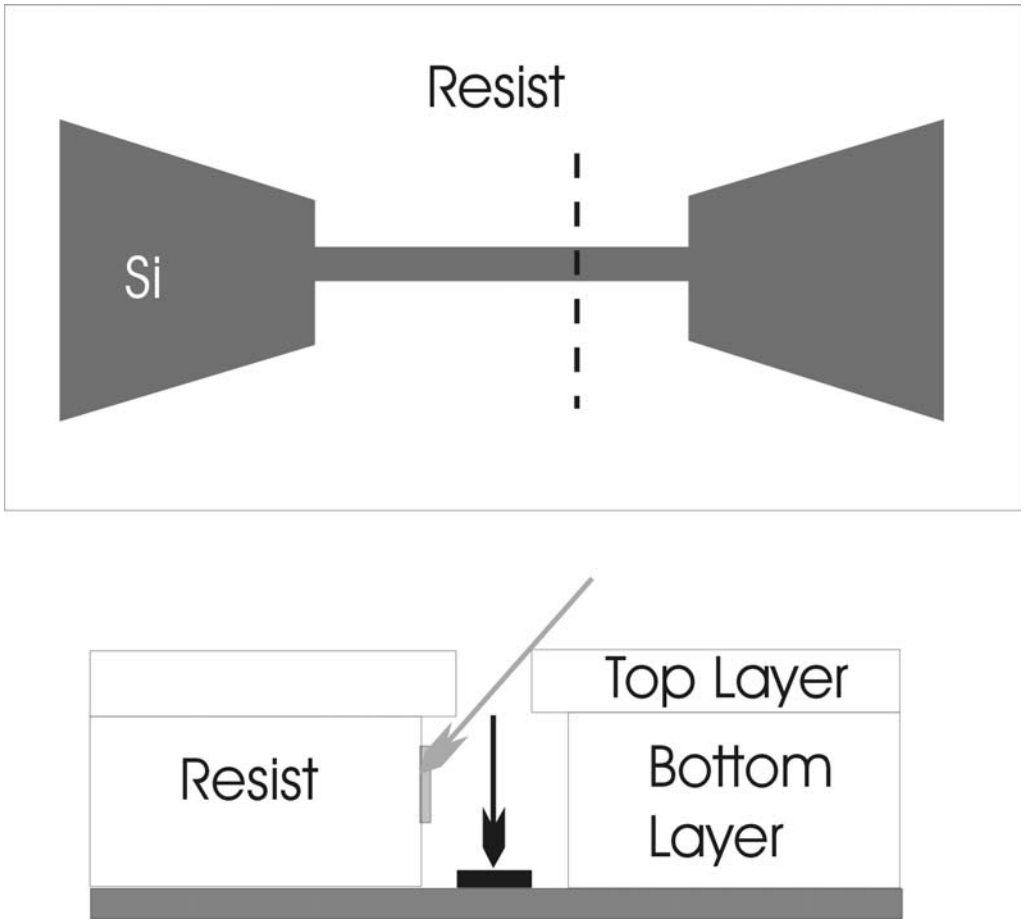

Figure 3.1: The upper figure is a top view looking down on a Si wafer coated with bilayer PMMA resist which has been pattered to define a microbridge and adjacent contact pads. The lower figure is a cross-sectional view taken through the dashed line on the upper figure. Metal (Al) deposited at normal incidence enters the trench and defines the microbridge. Metal deposited at an angle only deposits on the wide areas of the pattered sample and thus defines the contact pads.

measurements, it is crucial to suppress the contacts into the normal state. If a magnetic field is not used, we find that the device resembles a Josephson junction with two superconducting reservoirs and a constriction in between them. We observed Josephson mixing with high conversion efficiency but with significantly higher output noise, similar to previous observations made on Josephson mixers (Schoelkopf et al., 1995). The use of a small magnetic field could been avoided if devices with fully normal metal contacts are used. For example, devices with only thick Ti and Au on the ~ 10 nm Al microbridge layer would have normal contacts. HEBs with this geometry were fabricated and did indeed have normal contacts. However, this batch of mixers was damaged by electrostatic discharge before any high frequency measurements were made. DC measurements of these devices at JPL suggest that there is little difference between devices with Ti-Au normal contacts and devices with Al-Ti-Au superconducting contacts placed in a magnetic field.

The Al HEB mixers measured are listed in Table 3.1. These devices all have trilayer contacts and mixer measurements were made with and without a magnetic field applied. The width of all the Al HEB devices is 0.1μm. The device length and other properties are summarized in Table 3.1. The resistive transition of these devices has some remarkable features, and for this reason the value of the critical temperature is not listed here. In the next chapter, the R vs. T curves will be discussed in some detail. These devices are taken from several different batches, accounting for most of the variability in resistivity. Additional variability maybe due to partial oxidation of the microbridge due to exposure to atmosphere between the metal deposition and SiO passivation layer deposition. Thin, dirty Al films can increase in resistance over several

Al HEB Device	L (μm)	d (nm)	W (μm)	$R_{N\ (T=4K)}$ (Ω)	ρ ($\mu\Omega$-cm)
A	0.2	13	0.1	58	37.7
B	0.3	17	0.1	33	18.7
C	0.3	13	0.1	145	62.8
D	0.6	17	0.1	48	13.6
E	0.6	17	0.1	52	14.7
F	0.6	13	0.1	387	83.9
G	1.0	17	0.1	100	17.0
H	1.0	13	0.1	260	33.8
I	1.0	13	0.1	417	54.2

Table 3.1: Al HEB device parameters.

hours when exposed to air. This phenomenon was observed in initial Al HEBs fabricated at Yale. Cleaner films tend to be more stable, perhaps due to grain size effects, though this issue is not well understood.

3.2 Nb HEBs in a Magnetic Field

The Nb devices studied in a magnetic field were also fabricated at JPL. The device parameters for the two mixers characterized are listed in Table 3.2. These Nb

Nb HEB Device	L (μm)	d (nm)	W (μm)	$R_{N\ (T=4K)}$ (Ω)	ρ ($\mu\Omega$-cm)
J	0.16	10	0.08	90	45.0
K	0.24	10	0.08	110	36.6

Table 3.2: Nb HEB device parameters. Device J (K) is device B (C) in Burke's thesis.

devices were fabricated by B. Bumble, and the details can be found in Bumble and LeDuc (1997). The Nb is deposited by DC magnetron sputtering. The sheet resistance for 10 nm thick films with $T_c \sim 5.5$ K, in zero applied magnetic field, is ~ 30 Ω per square. The contacts are thick Au. Reactive ion etching is used to pattern the microbridge as opposed to angle evaporation and lift-off. These same devices were used in the 20 GHz Nb studied performed by Burke (1997). Two devices (Device B and Device C in Burke's thesis) were first measured in zero field, and Burke's original results were reproduced. Subsequently, perpendicular magnetic fields up to 2.5 T were used to reduce T_c from ~ 5.5 K to 1.4 K.

3.3 Nb-Au HEBs

The Nb-Au HEBs fabricated at Yale are produced by double-angle deposition and lift-off, similar to the Al HEBs produced at JPL. A PMMA bi-layer resist consisting of a 100 nm thick 100,000 molecular weight bottom layer and a 60 nm thick 950,000

molecular weight top layer is used. The bottom layer is spin coated at 3500 RPM for 60 sec and subsequently baked at 170 degrees Celsius for 10 min. Following the bottom layer bake, the top layer is spun on at a speed of 8000 RPM for 60 sec. The spinner is started at 3500 RPM and the speed is increased to 8000 RPM in about 5 sec. This procedure is used to reduce intermixing of the two layers since the same casting solvent is used for both layers. The top layer is then also baked for 10 min at 170 degrees Celsius. The short baking time is used to facilitate lift-off after metal deposition, with only a minor tradeoff in resolution (Kozhevnikov, 2001). Line widths of 100 nm are easily written in this 'soft baked' resist. Resist baked for several hours has better resolution but often requires hot acetone, ultrasonic agitation, etc. to complete the lift-off process.

After the resist is baked, electron-beam lithography using a JEOL 6400 scanning electron microscope (SEM) equipped with Nabity is used to define the microbridge and adjacent contact pads. The microbridge is written as a single pass line at a magnification of 1000 x and a beam current of 3.6 pA. Next to the bridge, small (~ 10 μm) pads are written with the same current. After this first write step, the magnification is reduced to 100 x and the beam current is increased to 10 nA to write mm sized contact pads. The exposed resist is developed in a solution of 3:1 isopropanol: methyl iso-butyl ketone (MIBK) for 30 sec, and then immediately rinsed in pure isopropanol for 30 sec.

Nb is first deposited at normal incidence using DC magnetron sputtering in a Kurt J. Lesker deposition system. The system base pressure is ~ $3x10^{-7}$ T, and an Ar pressure of 10 mT is used during the sputtering. The Nb deposition rate is about 1 nm/sec for 330 W (I ~ 1 A) of input power. After the Nb deposition, the sample is moved to a cluster of

sputtering guns tilted at 45 degrees without breaking vacuum. Au is then DC sputtered at an angle at a power of 100 W (I ~ 0.13 A) and a deposition rate of ~ 0.7 nm/sec. Approximately 10 nm of Nb is sputtered; 100 nm of Au is sputtered at an angle. No passivation layer is used. Nb films of comparable thickness without Au on top have T_c > 4.2 K. The Nb-Au bi-layer is formed when Au being deposited at an angle is not fully blocked from entering into the bridge area. This occurs due to a combination of thin resist and the non-directional transport of the metals during sputtering. The T_c of the Nb-Au film is 1.6 K. The presence of Au on top of the Nb film is confirmed by atomic force microscopy which reveals a total film thickness of 20 nm. Nb films of this thickness deposited in the Lesker system have T_c > 5 K. This method of fabrication was adequate for producing several test devices. However, a more robust fabrication technique is planned for future mass production of these devices.

After metal deposition, the devices are soaked in room temperature acetone for several hours. A syringe is then used to circulate the acetone over the chip and this is sufficient to complete the lift-off. An optical micrograph of the device is shown in Figure 3.2a. A zoomed in view of the microbridge area is shown in Figures 3.2b and c. These images were taken with an atomic force microscope (AFM) and scanning electron microscope (SEM), respectively.

The first batch of Nb-Au devices yielded more than 60% useful devices, all with nearly the same DC resistance. The devices were all ~ 0.48 μm long and 0.20 μm wide. Two of these devices were measured at low temperature, and had nearly identical behavior. Mixing measurements were not completed on the first measured device before

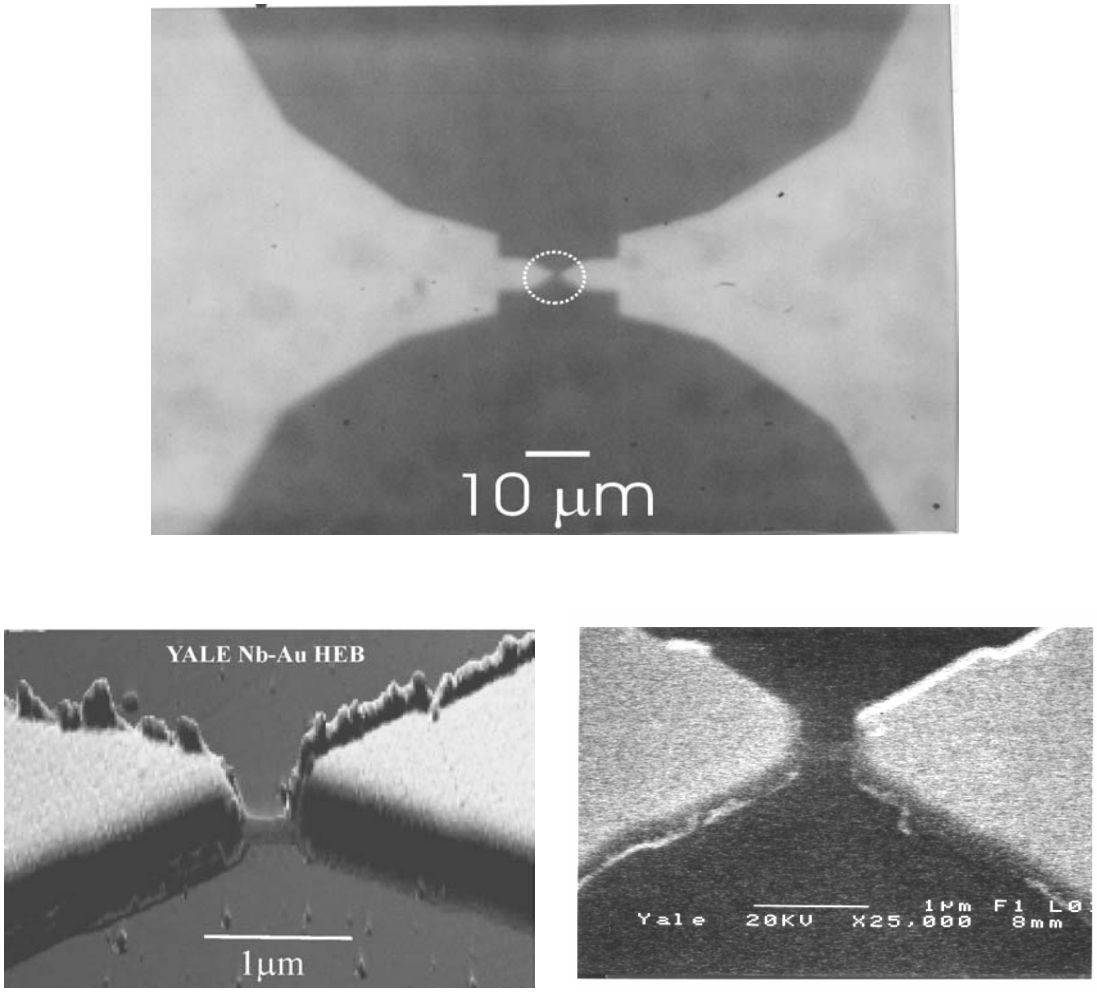

Figure 3.2: (a, top) Optical image of the Nb-Au HEB. The dark areas are Si and the light are Au. The central region marked by a circle is expanded in the two lower images. (b, bottom left) AFM image of Nb-Au device K. (c, bottom right) SEM image. The microbridge is a bilayer of Nb and Au, and the pads are thick Au. The little spikes on top of the Au pads visible in the lower left image are flakes of Au which adhered to the side wall of the resist and were not completely removed after lift-off. We believe they have no effect on performance, and that these spikes could be eliminated with a more concerted fabrication program.

Nb-Au HEB Device	L (μm)	d (nm)	W (μm)	$R_{N\ (T=4K)}$ (Ω)	ρ ($\mu\Omega$-cm)
L	0.48	20	0.20	85	70.0

Table 3.3: Nb-Au HEB device parameters.

it was damaged due to electrostatic discharge, a result of operator error A second device was then fully characterized, and the parameters of this device are listed in Table 3.3.

Chapter IV: Microwave Measurement Setup

In this thesis, diffusion-cooled HEB mixers are characterized at microwave frequencies. The HEB mixer is a thermal device. Radiation heats the mixer to a regime where the device resistance is sharp function of the electron temperature. The bolometer is thus sensitive to absorbed power, and this is the non-linearity which gives rise to mixing. The non-linear effect is therefore not directly linked to physics of the superconducting energy gap, as it is with SIS mixers. HEB mixers therefore can be operated at tens of GHz or tens of THz. What it slightly different is the device impedance at frequencies above and below the superconducting energy gap frequency. For frequencies well above the gap, high frequency radiation is uniformly absorbed in the HEB mixer. At microwave frequencies, this is not necessarily the case since the areas adjacent to the 'hot spot' in the microbridge are superconducting. However, these only comprise a small fraction of the total microbridge length, and since the local temperature in these areas is close to T_c, the gap is probably small in any case. Additionally, extensive measurements have been carried out on Nb HEB mixers at 20 GHz (Burke et al., 1999) and at 2.5 THz (Wyss et al., 1999), which is well above the Nb energy gap frequency. These measurements demonstrate that there is a general correspondence between low and high frequency measurements. The diffusion time of hot-electrons as inferred from the IF bandwidth as well as other properties are nearly the same at THz and microwave frequencies. Measurements of the mixer noise are comparable, though with sizable variations from device to device. Since it is difficult to accurately extract the

mixer noise temperature from the total receiver noise at 2.5 THz, a rigorous quantitative comparison with the 20 GHz measurements is not possible.

There are several reasons why microwave measurements are used to probe the underlying physics of HEB mixers. It is possible to determine the coupling losses with reasonable accuracy in a microwave setup, allowing for the determination of the noise of the mixer itself. This is useful in studying the dependence of mixer properties as a function of T_c. The coupling of the microwave system is also nearly unchanged from run to run allowing for systemic comparison of a batch of devices. Finally, the noise background can be made negligible by using calibrated cryogenic attenuators and filters. This is particularly useful in studying saturation effects.

In the microwave setup, a ~ 30 GHz LO and RF signal are fed into the cryostat via standard coaxial components. A directional coupler at 4.2 K is used to couple the high frequency signals into the mixer and couple the IF signal out to the first stage IF amplifier, which is also as 4.2 K. The IF signal is further amplified at room temperature and detected with a spectrum analyzer, or a Schottky diode detector in the case of noise measurements. The mixer block itself sits at ~ 0.22 K, and radiation is coupled to the device using a coaxial-coplanar waveguide transition. All the measurements are computer controlled using LabView.

In Figure 4.1, a block diagram is given of the entire measurement setup. In the remainder of this chapter, a detailed description of all the components in the block diagram is given. Additionally, the calibration procedures used to generate the mixer data presented in later chapters is also discussed.

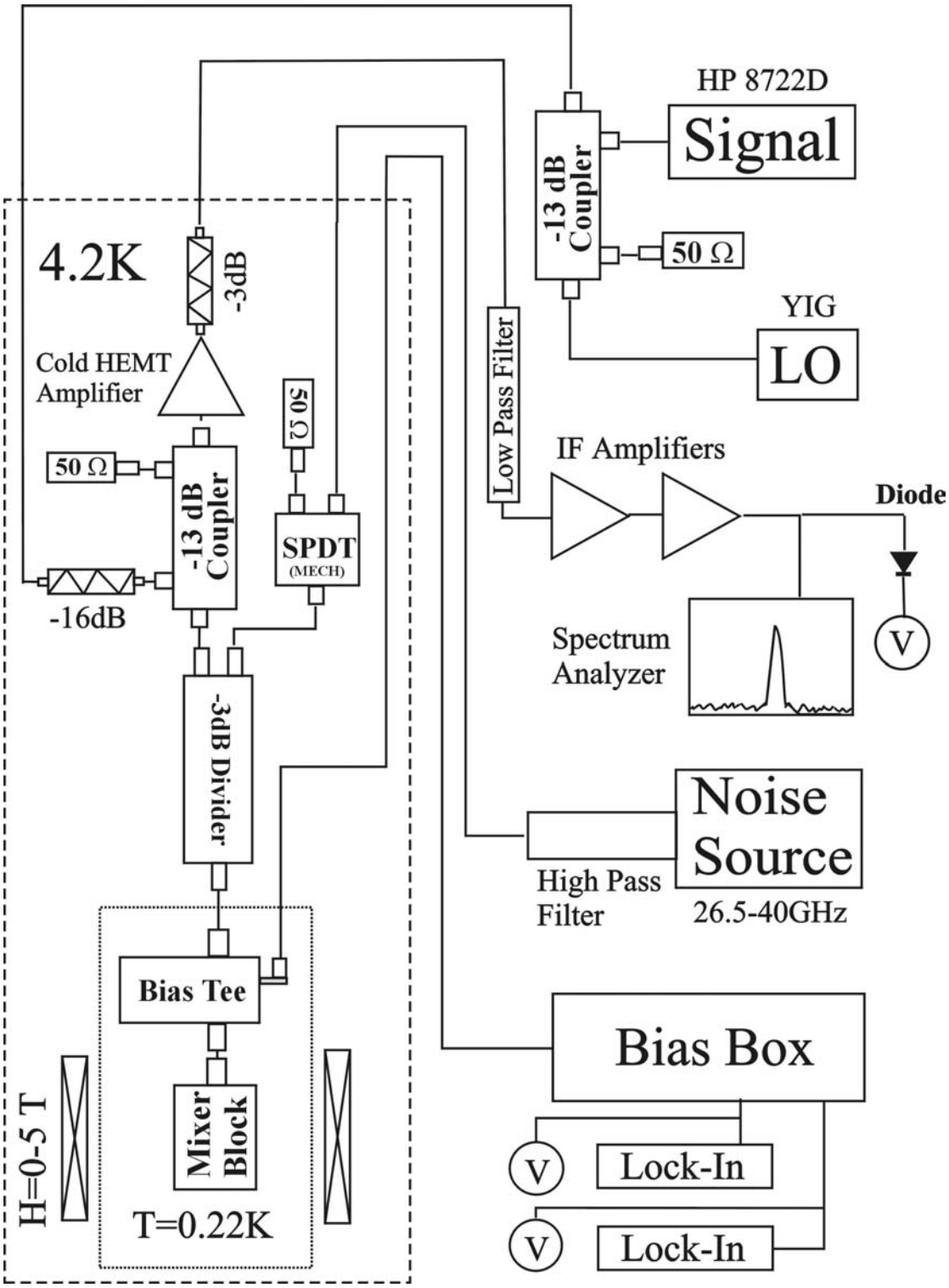

Figure 4.1: Block diagram of the microwave mixing setup.

4.1 Cryostat

The mixer measurements are made in an Oxford Instruments Heliox liquid ^{3}He cryostat. The base temperature of this particular unit is 210 mK. Base temperature can be sustained in a single ^{3}He condensation cycle for several days provided that the ^{4}He reservoir is kept filled. Recondensing the ^{3}He takes about 30 minutes, and thus the system can be run for several weeks without any difficulty. In Figure 4.2, a picture of the entire insert is shown. The insert is submerged into a liquid ^{4}He bath. Three temperature stages are available in this system. Components can be placed directly in the liquid ^{4}He bath for cooling down to 4.2 K. Inside the vacuum can is a small reservoir of pumped ^{4}He which cools to ~ 1.4 K. The main purpose of this '1K' stage is to cool the ^{3}He stage, also inside the vacuum can, below 4.2 K to allow ^{3}He gas to condense. Additionally, the '1K' stage cools the charcoal sorption pump that pumps on the liquid ^{3}He. Electrical components are heat sunk to the '1K' stage before being connected to the lowest temperature stage to in order obtain the lowest base temperature.

The cryostat has been modified significantly from it original design to allow for greater experimental access. Following the original design of Schoelkopf (2000), the inner vacuum can has been expanded to allow for a greater number of low temperature feed-throughs and for the placement of cryogenic microwave components. Electrical lines exit the top of the cryostat via a custom designed baffle set with standard KF type flanges. A commercial American Magnetics (Oak Ridge, TN) superconducting Nb-Ti magnet is suspended via fiberglass supports off a supporting plate on the main baffle stack.

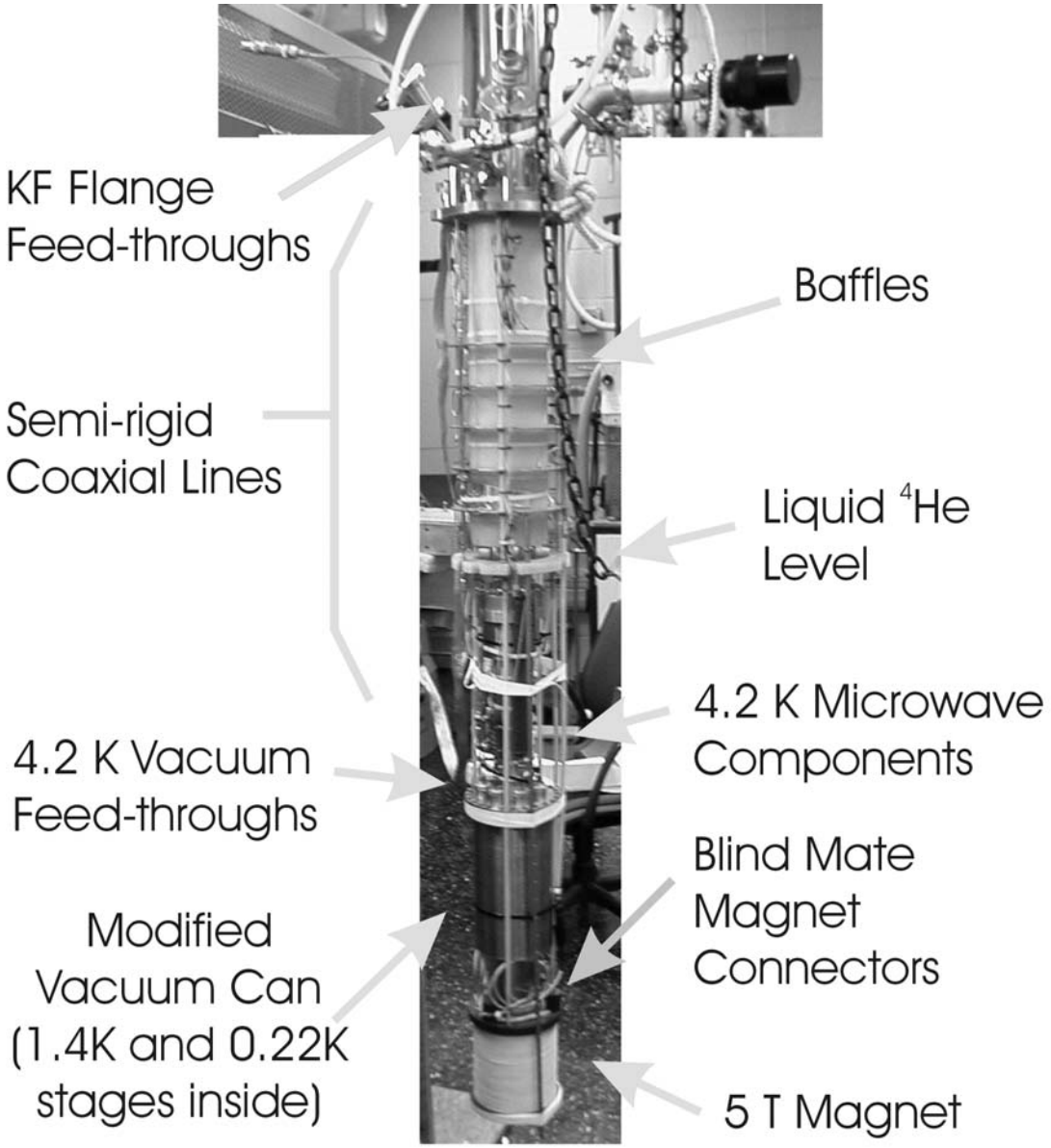

Figure 4.2: The ^{3}He cryostat insert which is inserted into a dewar filled with liquid ^{4}He. The maximum level of liquid ^{4}He is indicated along with the position of various components.

The maximum magnetic field is 5 T with an input current of 36 A. The magnet is equipped with custom designed blind mate connectors which allow it to be removed from the superconducting current leads in the baffle stack with ease. The connectors attach on one side to the Nb_3Sn busbar of the vapor-cooled leads and to Nb-Ti cable which connects to the magnet on the other side.

4.2 Microwave Setup

4.2.1 Cables and Connectors

Semi-rigid coaxial cable is used in all the microwave lines in the setup. The cable diameter is 0.085" with PTFE dielectric, manufactured by MicroCoax (Pottstown, PA). There are several different cable types used in the setup: (i) Cu outer conductor, silver plated copper weld (SPCW) inner conductor; (ii) 304 stainless steel outer conductor, SPCW inner conductor; and (iii) 304 stainless steel outer and inner conductor. In low temperature areas where a large thermal gradient is present, stainless cable (type ii or iii) is used to minimize heat conduction. From 300 K to the top of the baffle stack, Cu cable (type i) was used since it has the lowest RF loss of the three cable types and heat flow is not a significant problem. From the top of the baffles down to the liquid ^{4}He bath, stainless steel/SPCW (type ii) is used. This is a long length of cable. Type ii cable with stainless steel outer jacket has less attenuation than the pure stainless cable, and has significantly smaller thermal conductivity than Cu cable. Pure stainless cable (type iii) has significant attenuation (5.76 dB/ft at 20 GHz, Oxford Instruments specification). The

cables are heat sunk to the baffles using copper straps. To fasten the heat sinking straps to the coaxial cables, two copper plates are tightened around the cable with a sheet of indium foil between them. This is used rather than soldering so as to avoid any degradation in cable performance. For lines dedicated for low frequency use (DC - 10 GHz), the straps are directly soldered. Once in the liquid ^{4}He bath, Cu cables are used down to the feed-throughs on top of the vacuum can. Inside the vacuum can, stainless/SPCW cable is used from the feed-throughs to the '1K' stage. Pure stainless cable is not needed as the heat load from 4.2 K is negligible compared to the cooling power of the '1K' stage. From the '1K' stage to the coldest part, pure stainless steel cable is used to achieve the lowest base temperature. The base temperature after installation of all the microwave hardware increased ~ 2 mK, to 212 mK. Heat sinking of the inner conductor is achieved through contact with the outer conductor by way of the PTFE dielectric. To reduce the heat load on the ^{3}He stage, in-line microstrip structures could be used on the '1K' stage to reduce the heat load from the center conductor. Since the base temperature is practically unchanged with the present microwave setup, no additional parts are used to improve the heat sinking of the coaxial inner conductor. Any excess heat carried by the central conductor is transferred to the cold stage before reaching the device through the bias tee that is on the ^{3}He stage and a section of Au microstrip line that precedes the device.

The semi-rigid cables are connected with two types of connectors. Lines designated for use above 20 GHz are connected with M/A Com OS-50 (2.4 mm) connectors that are specified for use up to 50 GHz. On all the other lines SMA connectors manufactured by Applied Engineering Products (New Haven, CT) are used.

For connecting any 2.4 mm components with precision 2.9 mm components, K type connectors rated for use up to 40 GHz from C.W. Swift, Inc. (Van Nuys, CA) are used. Special procedures are used to minimize failure of the cables at cryogenic temperatures due to thermal expansion and contraction. Loops are added to cables going from sections at different temperatures to prevent migration of the inner conductor relative to the outer conductor. This is necessary because in the particular connectors used the inner conductor is not soldered to the captivated center pin of the connector. Additionally, the connectors are soldered using the following procedure, which has proven to be significant in the long-term stability of these cables upon repeated thermal cycling. First, the outer conductor is stripped to the specified trim code. Only a fraction of specified length of PTFE dielectric is removed. Both inner and outer conductors are coated with flux and tinned. A non-conductive organic flux (Superior Flux & Mfg. Co #30, Cleveland, OH) is used to contact Cu and SPCW while zinc chloride solution is necessary with 304 SS. The cable is then thoroughly cleaned with water followed by methanol, and dried to remove any residual flux. To prevent any flux from seeping into the space between the inner conductor and the dielectric, the cables are always soldered with the connector end pointing completely downward. During tinning, the dielectric expands plastically for some length and then stops. The dielectric is then cut to the proper length. Cutting the dielectric to the proper length after tinning serves two purposes. First, it prevents flux from seeping into the cable. Second, it ensures that the cable connector sits flush with the trimmed edge of the outer conductor. If on the other hand the connector is attached to the cable and then soldered from the outside, the dielectric expands and reduces the length of center pin contacting the inner conductor of the coaxial cable. This can often

result in the cable becoming disconnected at low temperature due to thermal contraction since the center pin is barely making contact at room temperature. Flux is used in soldering both the tinned Cu and stainless cables to ensure maximum structural integrity. Carefully following the above procedure provides adequate DC electrical isolation; all cables made with this technique have a DC resistance > 30 MΩ.

Different connector styles are employed in different locations. For straight lengths of cable, matching male and female connections are used to minimize the number of connectors used. Panel-mount OS-50 and hermetic glass seal SMA connectors are affixed to the top of the cryostat. Since OS-50 hermetic connectors are expensive and require great care in their assembly, panel-mount connectors are preferred at the room temperature feed-throughs, as these connect from the room air to the space for liquid ^{4}He. The panel-mount connectors were tested and appeared to hold rough vacuum. A small o-ring was placed around the connectors and a groove machined into the KF flange to produce a "semi-hermetic" connector. High vacuum is not necessary at the top of the cryostat, and it is sufficient that the connectors do not leak large quantities of water vapor that would eventually condense and freeze inside. At the vacuum can which is submerged in liquid ^{4}He, hermetic OS-50 and hermetic SMA glass bead feed-throughs are used. The OS-50 feed-throughs require machining of some ~ 3 mil thick ledges in the supporting flange to 1 mil accuracy. The feed-through was assembled and checked for any resonances using a network analyzer. If resonances were found, the flange was re-machined to bring it to the appropriate dimension.

4.2.2 Passive Components

Microwave signals are combined using directional couplers manufactured by Krytar (Sunnyvale, CA). These couplers are –13dB couplers, and are specified for use from 1-40 GHz. At room temperature, one of these couplers is used to weakly combine the RF signal with the LO signal. At 4.2 K, another coupler is used to couple in the RF/LO signal into the mixer and couple out the IF signal. This particular coupler has 2.4mm connectors on the –13 dB port and K type connectors on the through line, which are compatible with the SMA connectors on the IF components. The transmission and reflection characteristics of these couplers do not change at cryogenic temperature, and performance is not degraded upon thermal cycling. The terminations used on the couplers are also manufactured by Krytar and change in DC resistance by less than 1 Ω from room temperature to 4.2 K. When two signals need to be combined with the smallest possible attenuation, a broadband –3dB Krytar combiner/divider (0.5-36 GHz) is used. This device is used when combining the RF/LO signals with a broadband noise background. In the end, a high power room temperature noise source was used and a directional coupler could have been used here. The –3dB divider/combiner was originally designed for use with a cryogenic hot/cold load with limited power output. In between the 4.2 K microwave coupler and the mixer is a Anritsu K250 bias tee at 0.22K. This component combines a DC bias with the input microwave signals to be delivered to the mixer block.

In addition to passive components to combine signals, filters and attenuators are used to block undesired radiation. Two attenuators from INMET corporation (Ann Arbor, MI), 10 dB and 6 dB, are placed in the 4 K bath on the –13 dB port of the direction coupler to give a total of –29 dB of cold attenuation to block any 300 K

radiation from reaching the mixers. The INMET 2.4 mm attenuators maintain their room temperature characteristics at 4.2 K, per our tests. A 12 GHz multi-pole low pass filter from K&L microwave (Salisbury, MD) is used on the IF line at room temperature to prevent any reflected RF signals from the device from being amplified and detected. Two Ka band waveguide-coaxial transitions from Dorado microwave (Seattle, WA) are mated to form a high-pass filter. This filter is placed on the room temperature noise source to ensure no low frequency noise (DC and IF) reaches the device. Finally, a tunable 1-2 GHz 5% bandpass filter is used at the IF output when making output noise measurements to define a narrow, tunable bandwidth.

4.2.3 Chip Mount

The HEB mixer is housed in a co-planar waveguide (CPW) mixer block. CPW was chosen over microstrip to allow for wire bonds to be used as the interconnect between the planar transmission lines and the mixer chips. Previously with Nb HEBs fabricated on quartz substrates, the mixer chips were 'flip chipped' onto microstrip line. Connecting with wire bond introduced too much inductance and coupling was not broadband (Burke, 1997). Quartz being optically transparent allowed for easy alignment of the mixer contacts with the microstrip line. All the current devices are fabricated on Si, and the flip chip technique would require a complicated mounting procedure. It was conjectured that a CPW structure would be less sensitive to the details of the wire bonding.

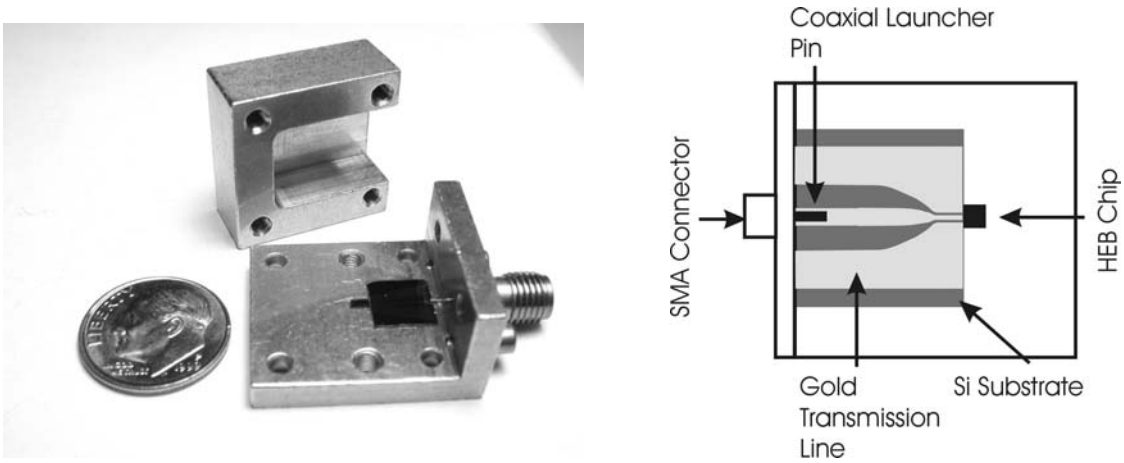

Figure 4.3: (a, left) The HEB mixer block with launcher structure and chip. (b, right) A diagram illustrating the transmission lines used in the lauching scheme. The mode excited by the coaxial connector is microstrip, and changes to CPW on the taper chip.

The block itself is constructed of gold plated copper and is shown in Figure 4.3a. A M/A Com coaxial connector is used launch the microwave signals from the coaxial port on the block to the planar transmission line structures inside. The transmission lines are pattered on a 0.012" thick 20,000 μΩ-cm TOPSIL (Gilbert, Az) Si wafer. High resistivity wafers are used to allow testing of the transmission line structures at room temperature without significant high frequency losses. Wafers of this resistivity have been shown to relatively loss free at frequencies higher than 40 GHz, which is the maximum used in the current experiments (McGrath, 1999). Due to the diameter of the coaxial launcher, it is not possible to launch directly onto CPW. As such, the initial transmission line that is coupled to the coaxial probe is microstrip. Then, over several mm, ground planes are brought into the proximity of the single microstrip line and the

mode is transformed into a co-planar one. The CPW is then finally tapered down to the required dimensions. A diagram of the launching structure is shown in Figure 4.3b. This transition is similar to the one tested in Sturdivant et al. (1996). At each point along the transition, the line impedance is calculated using Hewlett Packard's LineCalc. This procedure is used since the thickness of the Si substrate is not large enough to treat it as infinitely thick A 36x scale model was first used to test the transmission of two back to back tapers prior to fabrication of the actual structures using photo-lithography, and the results were satisfactory. The transmission vs. frequency has structure, but does not have deep repeated resonances, and is cleaner than that of microstrip structures connected with wire bonds. Recent work by Turek (2001) has shown that some of the structure seen in the transmission characteristic is related to the details of the contact between the coaxial probe and the launcher chip. Further work is needed to design a better transition structure, and modeling with a finite element simulator such as HP's HFSS would be useful. For the present work, the launchers described are sufficient. Additionally, since many coaxial connectors, many different cable segments and many passive components are used, the transmission of the full microwave setup is not perfectly flat, and particular calibration methods, describe later, are used to ensure that a constant microwave power is delivered to the device.

4.2.4 Signal Generators

The LO signal is generated using an Avantek K_a band YIG oscillator. The oscillator output can be tuned with a single external voltage from 26.5 GHz to 40 GHz,

with approximately a few mW of output power. A set of HP variable attenuators allow the output power to be changed in 1 dB steps. A section of waveguide is attached to the YIG output, and this servers as a 26.5 GHz high pass filter. The line width is typically much less than 1 MHz, and good frequency stability is observed once the unit has been running for a few hours. The RF signal to be detected is generated from the synthesizer of a HP 8722D network analyzer. For the saturation measurements, a broadband 50 Ω termination is placed on the input of a Quinstar (Torrance, CA) 26.5-40 GHz high gain (40 dB) broadband amplifier. Another set of HP variable attenuators regulates the output power. A commercial HP noise source was acquired after the initial measurements, but the output power of the termination/amplifier combination was more than sufficient for the Al experiments.

4.2.5 IF Amplifiers

Two different cryogenic IF amplifiers were used in the mixing setup. For IF bandwidth measurements, a broadband Miteq (Hauppauge, NY) 0.1-8 GHz cryogenic AFS amplifier is used. The amplifier is submersed in the liquid helium bath and dissipates ~ 480 mW with a 6 V bias. In previous studies (Burke, 1997), this amplifier had been biased at 3 V to minimize helium boil-off and increase the cryostat running time. In the present cryostat, 10 additional liters of liquid helium can be placed in a belly section of the dewar to add additional run time. As such, helium consumption is not a concern, and the Miteq amplifier is operated with a 6 V bias, greatly adding to its stability. The input noise temperature of this amplifier is ~ 22 K with ~ 33 dB gain, and

its characteristics have been described in detail in Burke (1997). To make narrow band noise measurements, a 1.1-1.9 GHz HEMT amplifier with an attached isolator is used. This device was obtained from Prof. Gol'tsman at Moscow State Pedagogical University. The noise temperature of the amplifier and isolator is ~ 4-7 K with ~ 34 dB of gain. The bias board for this amplifier is kept at room temperature and the power dissipation of the amplifier itself is small. In Figure 4.4, the room temperature gain of the amplifier and the noise temperature at 1.5 K are given as a function of frequency. The noise temperature is measured by connecting a variable temperature 50 Ω chip-resistor to the input of the amplifier and measuring the noise power at the amplifier output as a function of load temperature. This technique is explained in greater detail later in this chapter.

Following the cryogenic first stage IF amplifier are two Miteq 0.1-8 GHz amplifiers. The noise temperature of the third stage amplifier is ~ 300 K. A 3 dB attenuator is used at the output of the cryogenic amplifier in order to minimize any oscillations that might occur in the IF amplifier chain. The three amplifiers put together have about ~ 80-90 dB of gain.

4.2.6 Signal Detection

The IF signal from the HEB is detected at room temperature after amplification using a HP 8593E 9 kHz - 22 GHz spectrum analyzer. The spectrum analyzer is used when the device is operating as a mixer. When the output noise of the device is to be measured, only an LO signal is applied and the noise power emitted in the IF band is measured. The noise power is measured using a Schottky diode detector with a

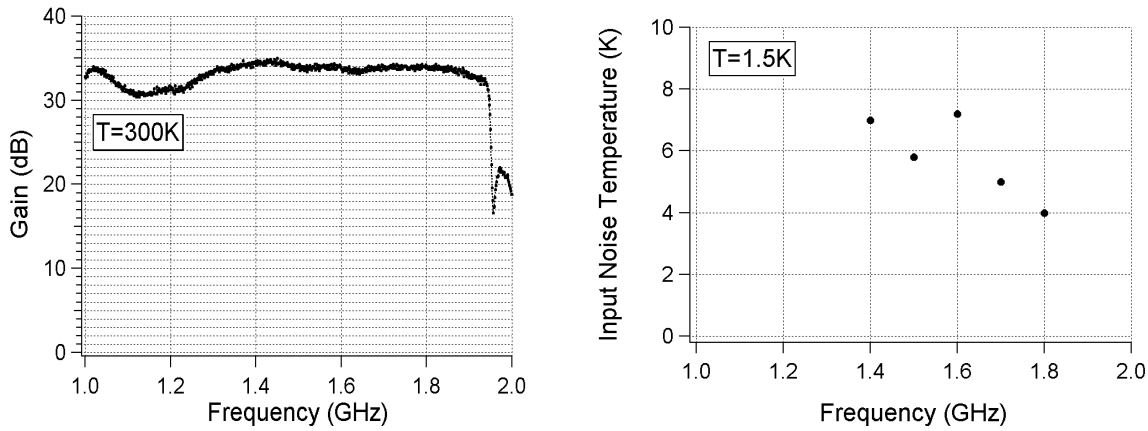

Figure 4.4: Gain and input noise temperature of the 1.1-1.9 GHz cryogenic amplifier and isolator.

sensitivity of 1 mV/μW of input power. Diodes detectors manufactured by Herotek (Sunnvale, CA) and Krytar were used. The particular Herotek detector used is fitted with BNC connectors and is not mechanically stable to motion of the cable attached to it, and adds jitter to the noise measurement. The Krytar diode detector is fitted with K type 2.9 mm connectors and works well up to 40 GHz.

4.3 DC Setup

4.3.1 DC Bias Supply

A very simple biasing scheme is used in the HEB experiments. A room temperature passive voltage bias circuit is used, as shown in Figure 4.5. The DC bias electronics are those used by Burke (1997). They are separated into two boxes, the

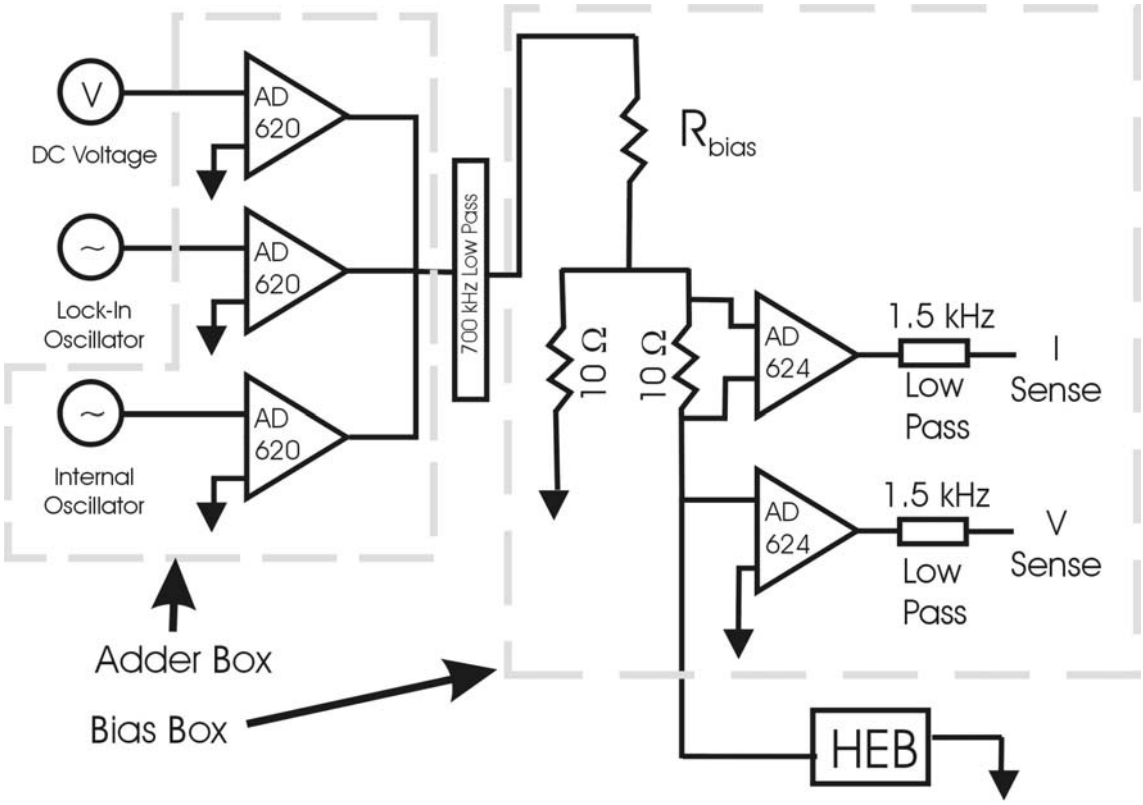

Figure 4.5: Schematic of HEB bias circuit. The gain of the AD624 amplifiers is adjustable from 1-1000, and the AD620 are used with unity gain.

'adder' and the 'bias' box. Each box is in an aluminum enclosure to minimize high frequency pick up. No optical isolation amplifiers are used to separate the ground of the bias supply and the cryostat. All pieces of electrical equipment and the cryostat are grounded to a central water line to minimize 60 Hz noise. The adder box combines two external signals and one internal oscillator (0.1 – 1 kHz). In a typical measurement, one external channel is used to supply a DC voltage from a Yokogawa 7651 DC source (Newnan, Georgia) and the other channel takes the oscillator output of a lock-in amplifier. The internal oscillator is used to display the I-V curve on an oscilloscope. The

Yokogawa DC voltage can be computer controlled to bias at a certain point on the I-V curve or to sweep out the entire curve point by point. The lock-in signal is used when measuring dV/dI or the R vs. T characteristic. These three voltage signals are combined using AD 620 operational amplifiers in a summing configuration. The 'bias' box takes the output of the 'adder' and passes it through the bias resistor R_b which is used to set the range of currents applied to the device. The signal is then divided between two 10 Ω resistors one of which is in series with the device and the other goes directly to ground, establishing the voltage bias with a total 20 Ω load line. The current delivered to the HEB is inferred by measuring the voltage across the 10 Ω resistor in series using an AD 624 differential amplifier. A second differential amplifier connected in parallel with the HEB measures the voltage. HP 34401 digital multi-meters are used to read the output of the differential amplifiers. Several additional resistors are used to set the gains of the sense amplifiers and unity gain buffer amps are also used in several spots in the bias circuit. These details have been omitted from Figure 4.5 for clarity. The DC line to the device is capped with a resistive termination when not connected to the power supply. The bias box is also equipped with a bypass shorting section that allows the output of the electronics to pass through a 10 kΩ potentiometer which is slowly adjusted from its maximum resistance to its minimum, and then shorted to bypass it from the circuit. This is done when connecting the bias supply to the HEB to prevent any voltage spikes. Care is also taken to ground the needle of the wire bonder when making contacts to the device to also avoid voltage spikes.

4.3.2 Low Pass Filtering

Filtering is implemented in the bias electronics and at low temperatures inside the cryostat. Between the 'adder' box and 'bias' box a 700 kHz low pass pi filter is used. On the readout section of the bias box, 1.5 kHz RC low pass filters are used. The bias cable between the bias box and the top feed-through of the cryostat is made using semi-rigid coax and terminated with 1.9 MHz low pass Minicircuits (Brooklyn, NY) filters to minimize external noise. Semi-rigid coax is used all the way to the HEB itself in the cryostat. At the 0.22 K stage, a stainless steel powder filter is used. The filter is constructed by wrapping about 1 m of thin Cu magnet wire insulated with heavy armored polythermaleze around a Teflon post. The wire is soldered to a crimp style SMA connector and pressed into the cylindrical metal body of the filter. The Teflon post is then removed. Stainless steel powder is filled in about 60% the cavity and epoxy is used to fill it to the top. A light vacuum is applied to the connector equipped side to pull the epoxy down through the stainless powder. The bare end of the wire is soldered to a second crimp style SMA connector that is pressed into the filter body to complete the assembly. The filter is allowed to dry for a few days and cycled thermally in liquid nitrogen several times to ensure all its contacts are intact. In Figure 4.6 the transmission vs. frequency of one these powder filters after about 20 liquid helium cool downs is plotted.

4.4 Calibrations

4.4.1 IF Chain Gain and Noise

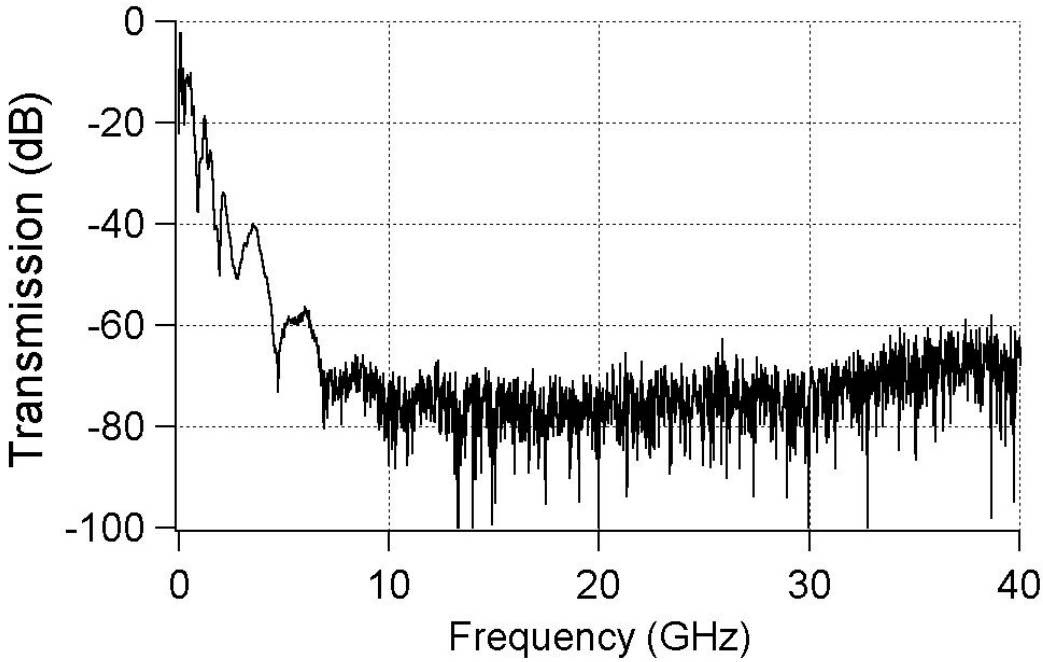

Figure 4.6: Transmission vs. frequency of a stainless steel power filter. This curve was taken after about ~ 20 thermal cycles from 300K to 0.22 K.

The HEB in the normal state is used as a Johnson resistor to calibrate the IF chain. For a HEB with R= 50 Ω, the noise power coupled to the amplifier is k_BTB, where B is the bandwidth and $T > T_c$ is the temperature of the HEB. The measured output power at the end of the IF chain is measured as a function of HEB temperature, as plotted in Figure 4.7. Adjusting the base temperature varies the HEB temperature. The slope of the measured power is equal to k_BBG_{IF}, where G_{IF} is the net gain of the IF chain, including cable losses. The x-intercept is equal to $(-T_{amp}/BG_{IF})$, where T_{amp} is the input noise temperature of the IF chain. It is assumed that this noise is dominated by the noise of the

first stage amplifier. Once the IF gain and noise temperature are determined, the output noise power from the HEB at its operating point is easily expressed in absolute units. This calibration procedure has been repeated in every measurement run.

4.4.2 Calibration of Coupled RF Power

The transmission of the microwave lines at room temperature is measured using a vector network analyzer. This measurement is used to estimate the microwave power delivered to the mixer block as any given frequency. The transmission of the high frequency lines in plotted in Figure 4.8. The RF/LO channel has couplers and attenuators to insure no 300K radiation is coupled to the device. Having many connectors, cable segments, and bends accounts for some of the structure seen in the transmission curve. The transmission of a high frequency line used to couple in broadband signals from room temperature is also plotted in Figure 4.8. There are no attenuators or directional couplers in this line, as it is not necessary to block radiation from room temperature! This channel consists of a Cu semi-rigid line straight from 300 K to the 4.2 K vacuum can, and its transmission curve has less structure. The drop off in transmission above ~ 34 GHz is due to the cutoff in the Krytar –3dB divider/combiner.

At low temperatures, the HEB itself is used to map out any resonances in the microwave lines. The power necessary to suppress the critical current to half its maximum value is noted at a frequency where the power coupling is reasonably flat. The cable attenuation at this frequency is used as an absolute calibration point. As the

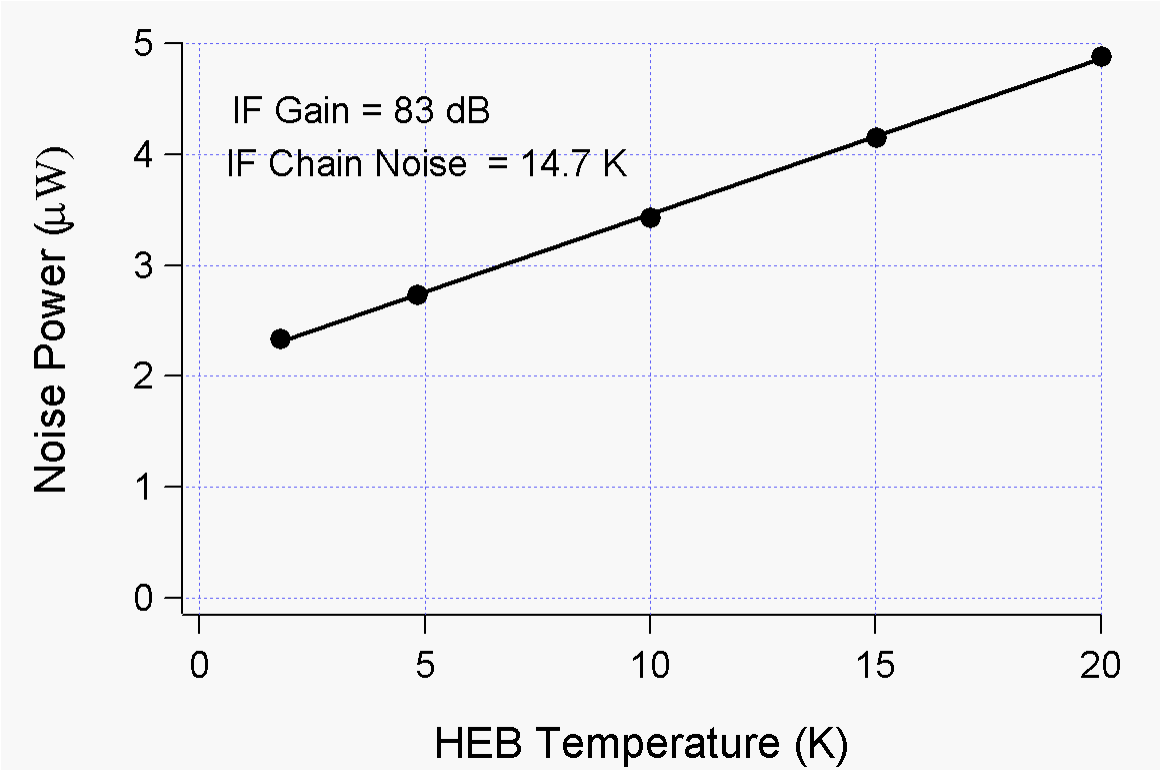

Figure 4.7: Plotted here is the measured output noise power measued in a 50 MHz band centered at 1.5 GHz on a Schottky diode as a function of temperature. A HEB with R ~ 50 Ω is used as Johnson noise source. The net IF gain and noise temperature are extracted for this particular configuration of components are indicated on the plot.

microwave frequency is changed, the power needed to maintain the critical current at half its value changes, and thus gives an indication of the change in transmission. The difference in applied power is used to calibrate the coupling away from the absolute calibration point. This allows for the estimation of the conversion efficiency of the mixer block and LO power delivered to the mixer block in absolute units. The accuracy of this method is estimated to be roughly a couple of dB. All the measurements in this

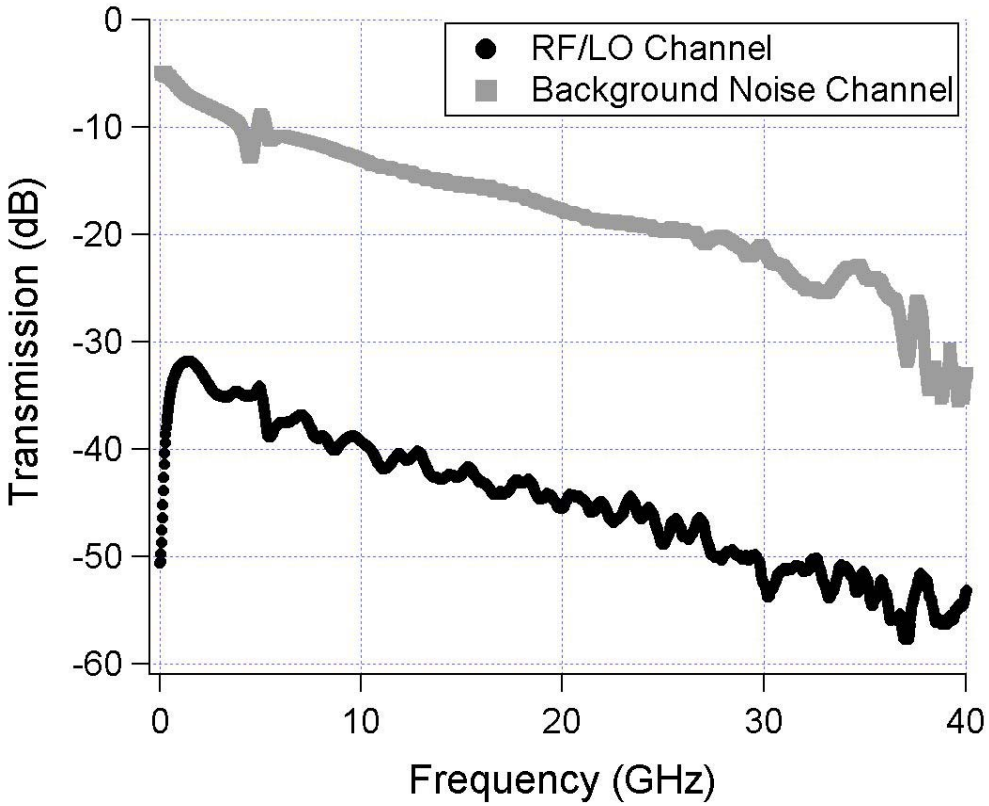

Figure 4.8: Transmission as a function of frequency of the high frequency lines in the cryostat.

thesis have been calibrated using this method. The cable transmission is measured after every run to make sure there are no changes in the transmission properties and to account for any changes in the configuration of microwave components. The cable transmission was stable from run to run. With the conversion efficiency and output noise, the mixer's noise can be calculated.

Chapter V: DC Characterization

In this chapter, the R vs. T and I-V curves in the absence of radiation power are discussed. The R vs. T curves are measured using lock-in amplifiers by applying a small oscillating signal to the mixer and reading out the differential voltage and current. An excitation current of ~ 0.2 μA is used at a frequency of 111 Hz. Corrections for thermally induced offset voltages are made when the HEB is in the superconducting state since V = 0 can be determined by using the odd symmetry of the I-V curve. This ensures that the lock-in excitation is centered about V = 0. The temperature is changed at a rate of ~ 1 mK/sec to ensure that the device temperature and cryostat cold stage temperature have sufficient time to equilibrate. This is confirmed by measuring the R vs. T curve both when heated from base temperature to above T_c and when cooling down from above T_c down to base temperature. Both curves are identical. Any lead resistance has been subtracted from the R vs. T curves. To generate I-V curves, a DC voltage is swept over the desired voltage range in 1000 steps. Whenever there is hysteresis present, the sweep direction is indicated. The I-V curves for the different HEBs reflect the basic features of the R vs. T curves.

For Al devices, there is a resistance drop at T_c but the resistance does not go to R = 0, though R = 0 is generally expected for a superconductor at low temperatures. Even at $T \ll T_c$, a residual resistance is still present. This behavior is observed when the contact pads are in the normal state. It is believed that in this situation superconductivity is suppressed in the microbridge ends, effectively giving a microbridge that is superconducting in the center with edges that are in the normal state. The coherence

length of Al is large, and the thick normal contacts suppress any superconducting material underneath them and the edges of the bridge. When the contacts are made superconducting themselves, the residual resistance vanishes.

The Al HEB I-V curves have two branches: 'superconducting' and 'resistive'. In zero applied magnetic field the entire HEB, the microbridge and the adjacent contact pads, is superconducting. The 'superconducting branch' of the I-V curve is a constant voltage line at V = 0 and represents resistance free transport across the device. When a current larger than the critical current of the microbridge is passed through the HEB, the I-V switches to the 'resistive branch'. At voltages several millivolts above the switching voltage, the I-V is linear as the microbridge is fully normal, though the contact pads are still superconducting. A different I-V curve is observed when a magnetic field is applied. In this case, the contact pads and the ends of the microbridge are normal. The 'superconducting branch' of the I-V now has finite slope since the superconducting center of the microbridge is now connected in series with two resistive areas at the ends. The I-V switches to the 'resistive branch' when sufficient current is passed through the HEB and at voltages above the switching point, the entire structure is in the normal state.

In contrast to the Al devices, the Nb and Nb-Au HEBs have a coherence length that is shorter than the microbridge thickness, and the normal contacts do no fully suppress the superconducting parts underneath them. Thus superconductivity is not suppressed in the ends of the microbridge. At temperatures well below T_c, no residual resistance is observed, at least to an accuracy of less than an Ohm. With a field applied, the T_c of the Nb microbridge decreases. Small features develop in the R vs. T when a field is applied; these are not well understood at present. However, the overall shape of

the R vs. T curves is the same. The I-V curves again have a 'superconducting branch' and a 'resistive branch'. The features are similar to those of the Al curves with no magnetic field applied.

5.1 Al HEB

5.1.1 Al HEB R vs. T

To understand the Al R vs. T curves, we have to carefully describe which parts of the device are superconducting under what conditions. Let us start with the case when no magnetic field is applied. A cartoon of the device geometry is given in Figure 5.1. The device has a superconducting microbridge with a given resistivity. The microbridge has wide contact pads made of the same resistivity Al immediately next to it. The thickness of these thin contact pads is the same as that of the microbridge, 13-17 nm. This geometry results from using the angle deposition technique described in Chapter III. On top of the thin contact pads are thick layers of Al, Ti, and Au. Normal metals are indicated as cross-hatched areas in Figure 5.1. The thickness of the thick 63 nm Al layer is comparable to or larger than the superconducting coherence length. As a result, the Ti and Au layers above it do not drive it fully normal but rather suppress its T_c down to about ~ 0.6 K. The R vs. T transition for these devices consequently has two drops in resistance. At the T_c of the microbridge, the resistance drops to some finite value and appears to remain constant. Above T = 0.6 K, the thick contacts pads are still in the normal state and suppress superconductivity in the thin contact pads and the microbridge.

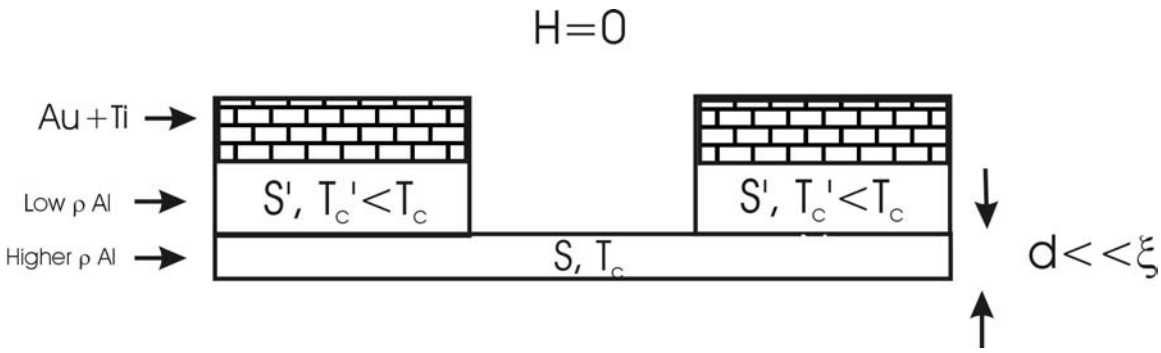

Figure 5.1: The structure of the Al HEB with no applied magnetic field. The cross-hatched area is normal metal and the white sections are superconducting. The critical temperature of the contact pads is $T_c' \sim 0.6$ K. The microbridge has $T_c \sim 1.4 - 2.3$ K.

This results from the thickness of the thin contacts being much smaller than the superconducting coherence length. As the temperature is lowered below the transition temperature of the thick contact pads, the device resistance drops to zero. In Figure 5.2, the R vs. T characteristic in the absence of a magnetic field is shown for Device F. This is the highest resistivity device measured, and it therefore has the highest microbridge T_c. For this device, there is the greatest separation in T_c between the microbridge ($T_c \leq 2.3$ K) and the contact pads ($T_c \sim 0.7$ K). Lower resistivity bridges also have two transitions, but they are much closer to each other in temperature. The thick contact pads have a normal state resistance of 1-2 Ω at maximum, so the residual resistance seen above the transition temperature of the contacts pads must be primarily due to the microbridge. The JPL manufacturing process is designed to avoid interface contamination between the layers, so we anticipate that these interfaces do not add to the resistance.

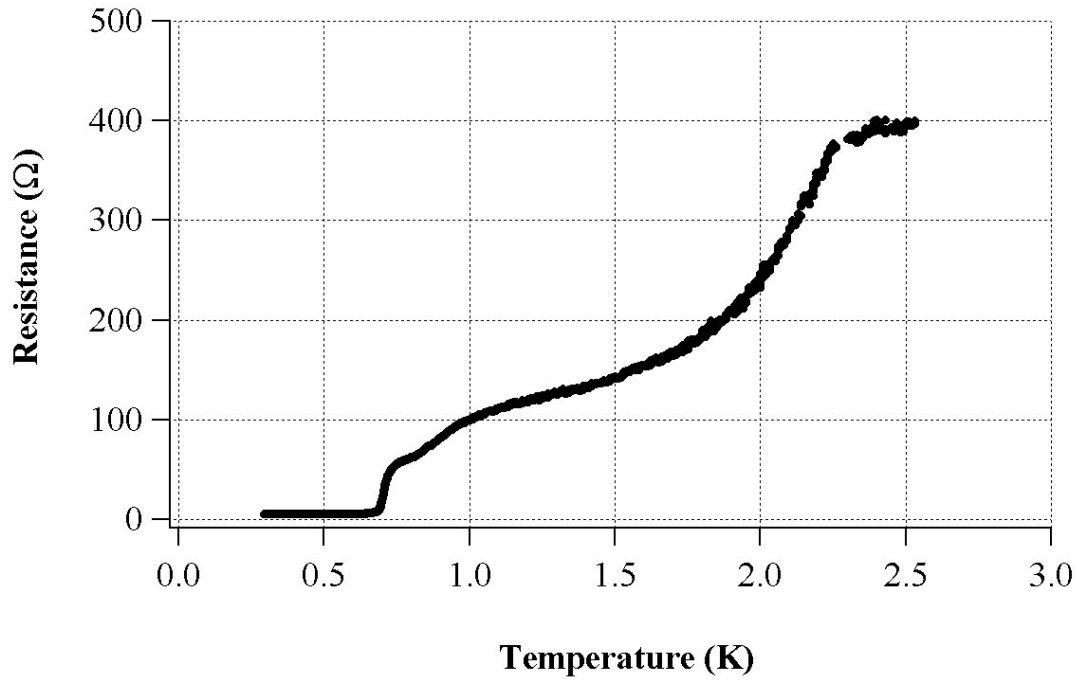

Figure 5.2: R vs. T curve for Device F. The transition temperature of the center of the microbridge is ~ 2.3 K. The contact pads become superconducting at T < 0.7 K, and the device resistance drops to zero.

The qualitative explanation for the residual resistance in the microbridge has to do with the normal-superconducting proximity effect. For very large normal-metal-superconductor contacts, the energy gap reaches its maximum value at a distance approximately equal to ξ, the superconducting coherence length. The superconducting energy gap is zero in the normal sections. In essence, the HEB is a small superconducting section contacted between large normal metals. Over some length in the microbridge, the gap evolves to its maximum value at the bridge center and then drops off to zero at the bridge ends. For short microbridges, the gap does not evolve to

the maximum value observed in bulk superconductors. In fact, for very short devices the microbridge does not become superconducting at all. The resistance in the bridge ends is thus assumed to be due to the suppression of the gap in these areas. However, the resistance observed implies that much more than one or two coherence lengths of the total microbridge length are in the normal state. In the present case, the gap doesn't evolve to its bulk value anywhere in the microbridge. Thus, a more precise calculation is needed to predict what the resistance should be in this geometry.

To test the proximity effect hypothesis, several experiments were done. The first set of measurements was performed to test if that the residual resistance observed above T_c of the contact pads persists to much lower temperatures, if the contact pads are non-superconducting. With the contact pads superconducting, the residual resistance is only present for temperatures > ~ 0.6 K. A small magnetic field was applied perpendicular to the HEB to drive the contacts into the normal state. With a magnetic field, the device configuration is illustrated in Figure 5.3. The field suppresses superconductivity in the thick Al pads. Since the thick pads have a suppressed T_c relative to the microbridge and the thicker Al film can be treated as a type I material (Van Duzer and Turner, 1981), the pads have ~ 4-5 times lower critical field than the microbridge. With sufficient applied field, the thick contacts are driven normal and the microbridge T_c is depressed by a few tenths of a Kelvin. The thick normal Al contacts then suppress superconductivity in the thin contact pads and the edges of the microbridge. The R vs. T curves for Device G are given in Figure 5.4, with and without a magnetic field applied. In zero field, two transitions are observable, similar to Device F in Figure 5.2. For an applied field of 0.05 T, the transition of the contact pads is no longer present. However, the resistance is still

slowly decreasing even at the lowest measured temperature. At this value of the applied field, superconductivity in the contacts is not fully suppressed, and the transition temperature of the contacts pads is probably decreased below 0.22 K. Applying a higher magnetic field shows the resistance does indeed reach a constant value at 0.22 K.

In order to verify that the observed residual resistance in Figure 5.4 is not the result of some magnetic interactions in the microbridge, the R vs. T curves of devices with thick Ti/Au normal contacts are presented in Figure 5.5. These devices do not have thick Al in the contacts, and are thus always in the normal state without applying a magnetic field. The data in Figure 5.5 is that of P. Echternach. Mixing measurements were not made on this batch of normal pad devices since all the structures were electrostatically damaged at JPL during fabrication, with the exception of the bridges

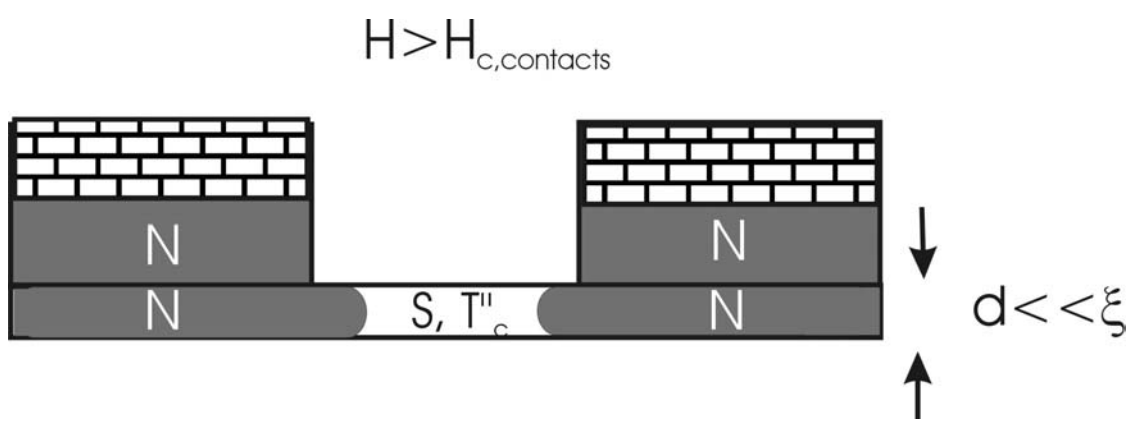

Figure 5.3: The structure of the Al HEB with an applied magnetic field. The hatched area is normal-metal. The dark gray areas have been driven into the normal state by a combination of the magnetic field and the proximity effect. The T_c of the microbridge is slightly reduced by the magnetic field to $T_c'' \sim 1K$.

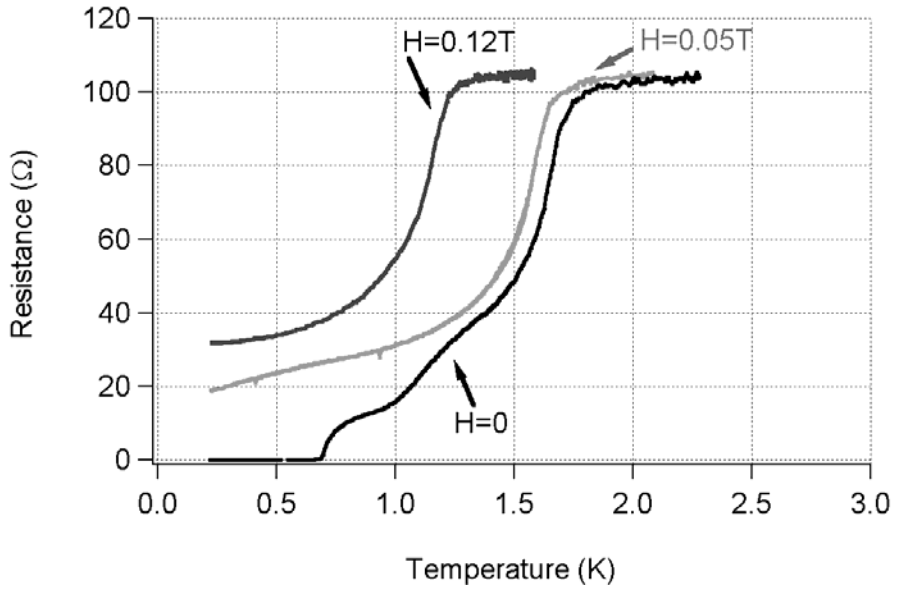

Figure 5.4: R vs. T curve for Device G with and without a magnetic field applied.

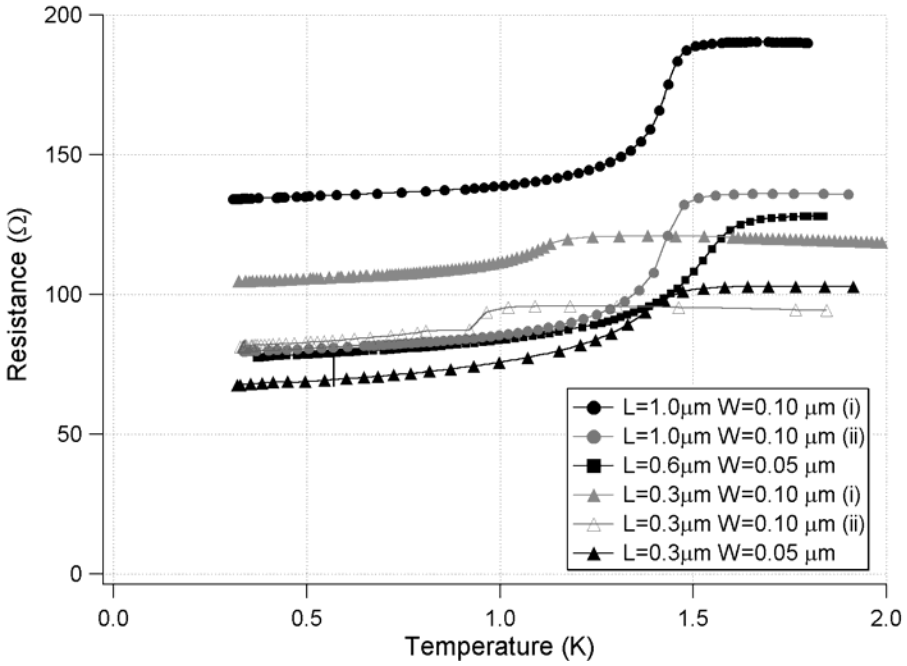

Figure 5.5: R vs. T curves for Al HEB mixers with thick Ti/Au contacts. No magnetic filed has been applied and these contact pads are always in the normal state These data were taken by P. Echternach, JPL.

reported on. These bridges were test structures and did not have appropriate coupling structures for high frequency measurements. We see from the normal contact pad devices, the R vs. T curves are nearly identical in shape to the data in Figure 5.4 where a magnetic field is used. There is a difference in that the transition temperature of the microbridge is higher for the device with normal pads since no field is applied. Applying a magnetic field to the devices with superconducting contacts forces the contacts into the normal state and slightly depresses T_c of the microbridge. Finally, R vs. T curves were measured without any microwave lines connected to make sure no thermal noise was suppressing superconductivity in the bridges. A conjecture had been made that the residual resistance was the result of noise in the setup suppressing a small critical current in the microbridge (Devoret, 2000). Only one powder filtered DC line was used to contact the device. Our experience is that the powder filters attenuate high frequency radiation very effectively, and detection of a critical current much smaller than 1 μA should be possible. In these measurements, no change in the R vs. T curve was observed as compared to when the microwave components were present. It is therefore unlikely that external noise is suppressing superconductivity in the microbridge.

The residual resistance at low temperatures appears to originate from the microbridge and is only present when the contacts are in the normal state. If the edges of the microbridge are in the normal state, there should be no superconducting transition at all, for short enough bridges. To verify this hypothesis, devices with nearly the same resistivity but different bridge lengths were studied. The R vs. T curves for Devices B,D,E and G are presented in Figure 5.6. A magnetic field of 0.12 T is applied to all of these devices to put the contacts into the normal state. Device B is the shortest of the

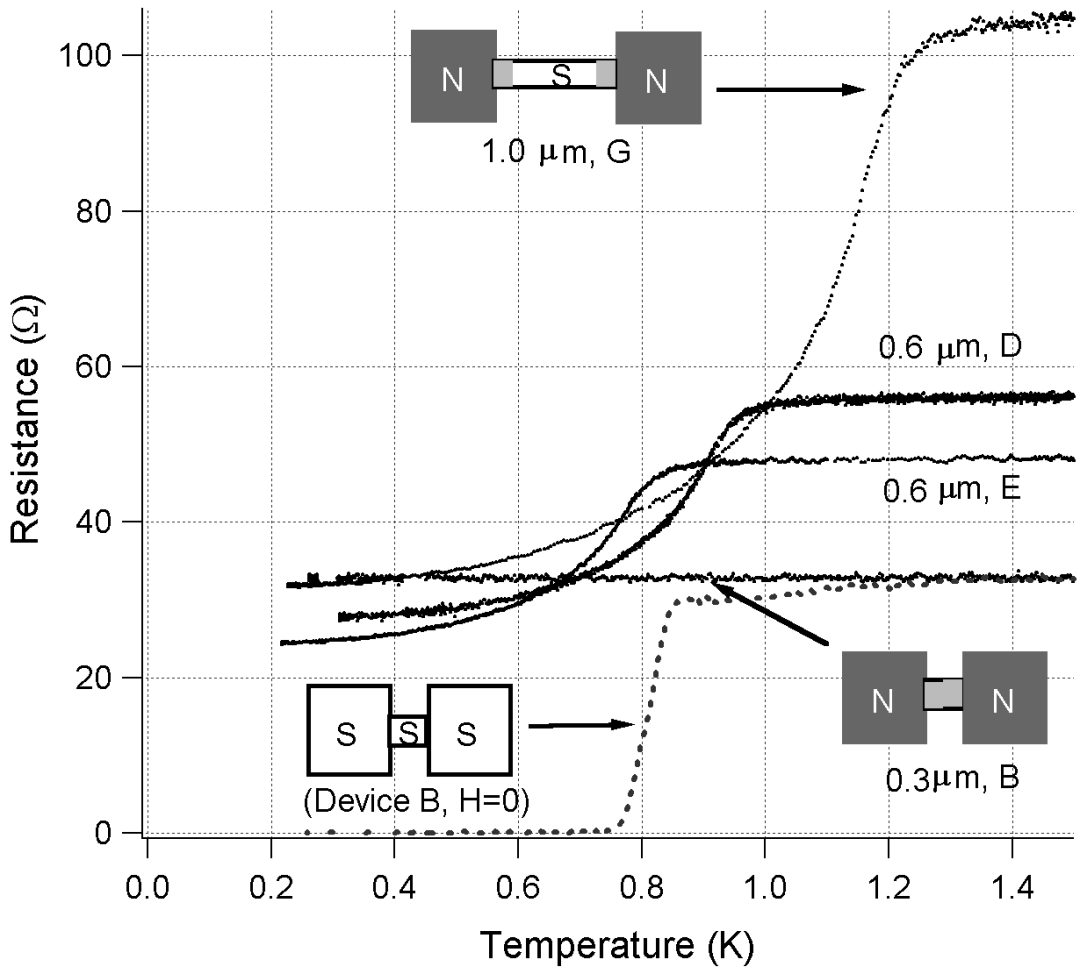

Figure 5.6: The R vs. T curves with H=0.12 T for Devices B,D,E and G which have nearly the same resistivity. Device B has no superconducting transition when the contacts are normal. The dashed line is the R vs. T curve for Device B with no applied field. The cartoons illustrate the resistive areas in the bridge. For Device G with normal pads, the resistive edges are shaded gray and account for the residual resistance at low temperature. For Device B with normal contacts, the whole bridge is resistive. In the case where a magnetic field is not applied to Device B, the contacts are superconducting. There is no proximity effect and the microbridge is superconducting.

four, and this device has no superconducting transition. For this resistivity, the minimum length to observe superconductivity appears to be ~ 0.3 μm. The R vs. T for Device B is also shown with no field applied for reference, and a superconducting transition is clearly present when the contacts are superconducting. Devices with L = 0.1 and 0.2 μm also do not exhibit superconductivity in the microbridge unless the contact pads are superconducting.

Devices with different resistivity have different residual resistances, even for the same normal state resistance. Since it is postulated that the gap is suppressed in the ends, one can further conjecture that the length over which this suppression occurs is proportional to the coherence length. The zero temperature coherence length determines the length over which the gap reaches it maximum in a bulk N-S boundary, and it is likely a similar length, but a multiple of the coherence length, is the appropriate quantity to consider for the present geometry. To test this idea, the 'resistive length' of the microbridge is calculated and then divided by the zero temperature coherence length. The device resistance for every Al HEB is first divided by the normal state resistance. This quantity is then multiplied by the length of the device to obtain the 'resistive length'. The coherence length is calculated from an experimental measurement of the upper critical magnetic field using (Tinkham, 1996),

$$H_{c2} = \frac{\Phi_0}{2\pi\xi^2} \tag{5.1}$$

where Φ_0 is the flux quantum. H is applied perpendicular to the substrate; the value of $\xi(0)$ is less than the bridge width, W ~ 0.1 μm, so formula 5.1 may be used. Since the

widths of the Al HEB are larger than the coherence length, the upper critical field measured in the bridges agrees reasonably well with that measured for much larger thin films of the same material (P. Echternach, 2000). For Device D, $\xi(0) \sim 50$ nm. For the highest resistivity microbridge, Device F, $\xi(0) \sim 22$ nm. The 'resistive length' of the microbridge is plotted as a function of temperature is Figure 5.7 for all 9 Al HEB devices. The data in this plot are a combination of different measurements. For some devices, the full R vs. T curve was measured with and without a field. For other devices, the resistance was measured only at certain temperature, with and without a field. For some of the earliest devices, a magnet was not available, and data only for temperatures above the critical temperature of the contact pads are listed. At low temperatures, the 'resistive length' appears to plateau at ~ 6-7 $\xi(0)$. Data for the devices shown in Figure 5.5 are not included in Figure 5.7 because values for the mean free path are not available. Rough estimates can be made from the resistivity which shows reasonable agreement with the rest of the curves in Figure 5.7, but the experimental values are needed for a quantitative comparison since the mean free path varies quite easily in Al films from batch to batch depending on preparation conditions. The curves in Figure 5.7 suggest that the length of the normal region at each end of the microbridge in the Al devices is ~ 3-3.5 $\xi(0)$, experimentally observed over variation of a factor of ~ 6-7 in resistivity.

Resistance in a superconductor has been experimentally measured in many experiments dealing with thin superconducting films deposited onto normal-metal contacts (Harding et al., 1974). The normal metal contacts can be measured prior to the deposition of the superconductor, and any additional resistance measured with the superconductor present must be due to the superconductor itself. Krahenbuhl and Watts-

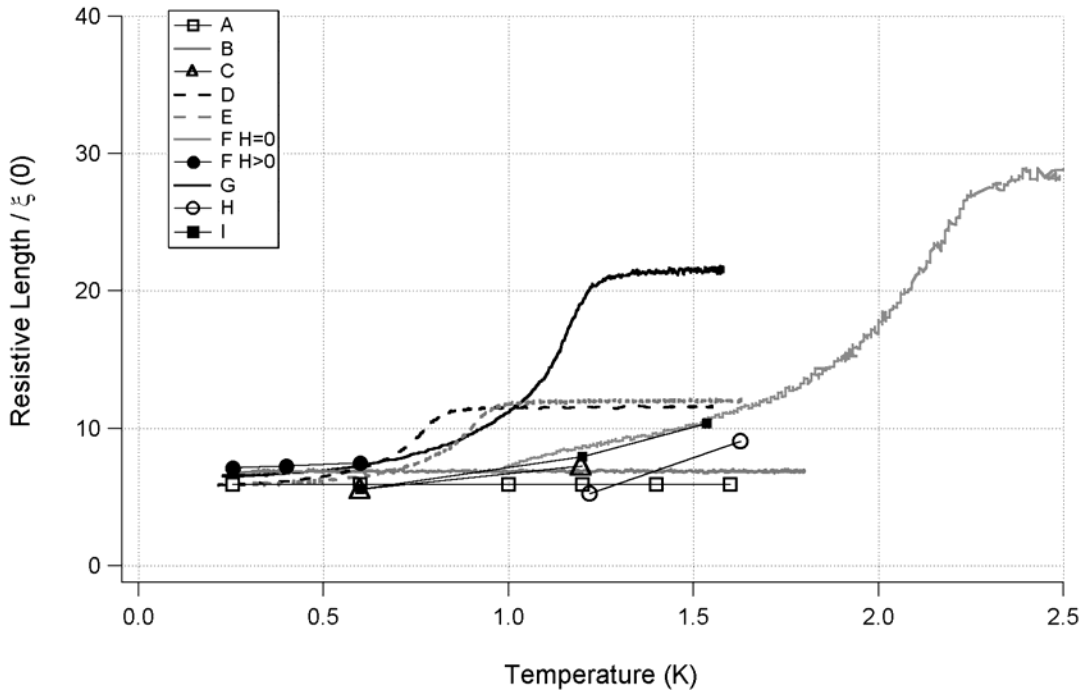

Figure 5.7: The resistive length of the microbridge expressed in units of the zero temperature coherence length as function of temperature for Al microbridges. Above T_c, the resistive length is equal to the length of the microbridge divided by the coherence length.

Tobin (1979) have proposed a theory based on a kinetic equation approach that seems to fit their experimental data well. More recently, Liniger (1993) calculated the minimum length of a one-dimensional superconducting wire to be superconducting using Ginzburg-Landau theory. This prediction is strictly valid in the vicinity of T_c. For a more accurate calculation of the residual resistance at low temperatures, the Usadel equations have to solved self-consistently to yield position dependent quantities such as the gap, density of states, etc in the HEB geometry. Using this information, the distance single excitations

travel in the superconductor before being converted to pairs is obtained. This distance gives the resistive fraction of the microbridge. Initial calculations have been made by Verbruggen et al. (2001) that predict a residual resistance well below T_c in Al HEBs. Further theoretical work on this subject will undoubtedly be significant in the design of small mesoscopic devices consisting of superconductors. In the present context, the proximity effect suppression has two direct consequences for mixer performance. The minimum length places an upper limit on the IF bandwidth. For longer devices, the residual resistance decreases the fractional drop in resistance at T_c, and thus limits the operating range of the device, making the HEB easier to saturate. These effects will be discussed in detail in the later chapters.

5.1.2 Al HEB I-V Curves

The shape of the I-V curve for an Al HEB depends on whether or not a magnetic field is applied. In the absence of an applied magnetic field, both the microbridge and contacts are superconducting. In Figure 5.8 the I-V curve for Device F at T = 0.25 K is plotted as a solid black line, without a magnetic field applied. At V = 0, the device is uniformly at T = 0.25 K which is below T_c of the structure and the entire structure is superconducting. The current flowing through the device is increased until the critical current (~ 3 μA) is reached. The V = 0 branch is called the 'superconducting branch'. After the critical current is exceeded, the I-V switches to the "resistive branch" at finite voltages. At higher voltages (> 1 mV in Figure 5.8), the I-V becomes linear. At these voltages, the microbridge has been driven completely into the normal state. In the

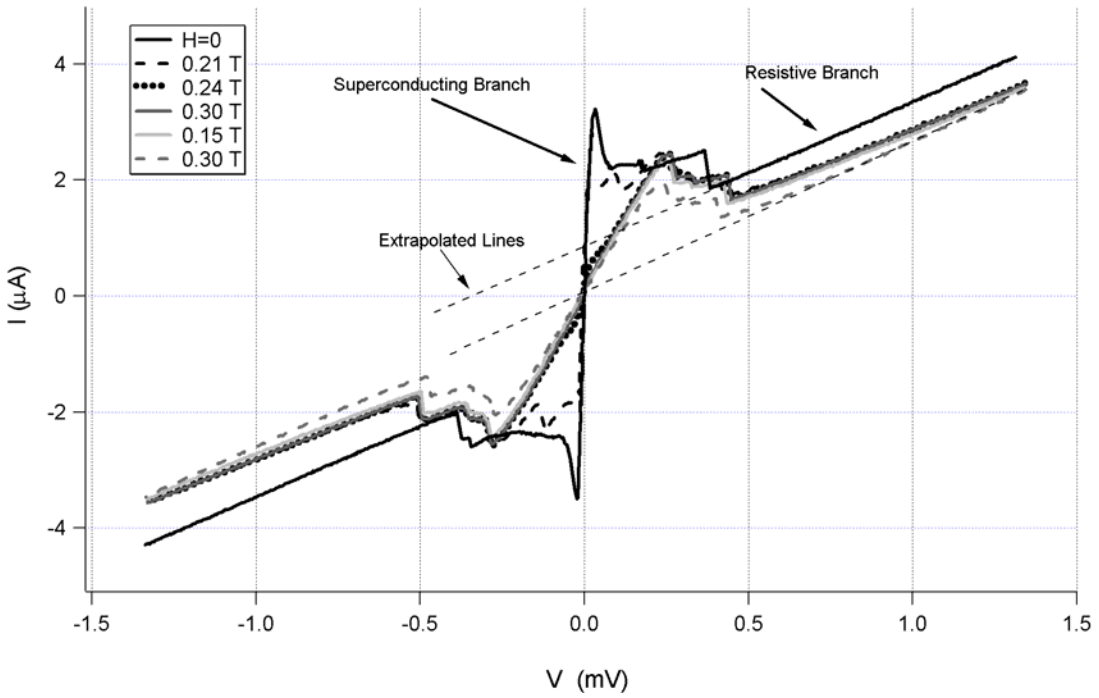

Figure 5.8: I-V curves for Device F at T=0.25 K in different applied magnetic fields.

absence of a magnetic field, the pads are most likely still superconducting since their critical current is much larger than that of the microbridge. This is supported by the presence of 'excess current' when the linear part of the I-V is linearly extrapolated down to V = 0. The intercept is not at the origin, and this might result from Andreev reflection from the superconducting pads (Blonder et al., 1982).

With a magnetic field applied, the situation is different. The contact pads are in the normal state. The I-V curves as a function of increasing magnetic field are also given in Figure 5.8. In finite field, the 'superconducting branch' of the I-V characteristic now has a finite slope. The structure can be thought of as having the center part of the microbridge superconducting with the edges normal, hence the finite slope. After the

critical current is exceeded for the central part of the microbridge, the entire structure goes normal. This can be inferred by extrapolating the linear part of the I-V at V > 1 mV back to V=0. This time the line does cross the origin, and the structure is likely a simple resistor at these voltages.

A similar trend is observed for the I-V curves in zero applied field at different temperatures. At temperatures < 0.6 K, the contacts are superconducting and the description given above for the I-V in zero applied field with T = 0.25 K is valid. With T > 0.6 K, the I-V curves resemble the case of finite field at T = 0.25 K. At temperatures close to T_c of the microbridge, the critical current of the center section of the microbridge begins to decrease, as expected. The I-V curves at different temperatures for Device F are given in Figure 5.9.

5.2 Nb HEBs in a Magnetic Field

5.2.1 Nb HEBs in Magnetic Field, R vs. T

In the absence of an applied field, Devices J and K have T_c ~ 5.5 K. As a perpendicular magnetic field is applied, T_c decreases. The R vs. T curves for both Devices J and K are shown in Figure 5.10 as a function of magnetic field. Typically, the R vs. T of the Nb HEB mixers studied have a large drop in resistance at T_c of the microbridge and a very small change in resistance at the T_c of the contact pads, which is slightly lower (typically ~ 0.5 K lower) than that of the microbridge. Similar to the Al HEB, the thin Nb film which forms the microbridge extends underneath the Au contacts,

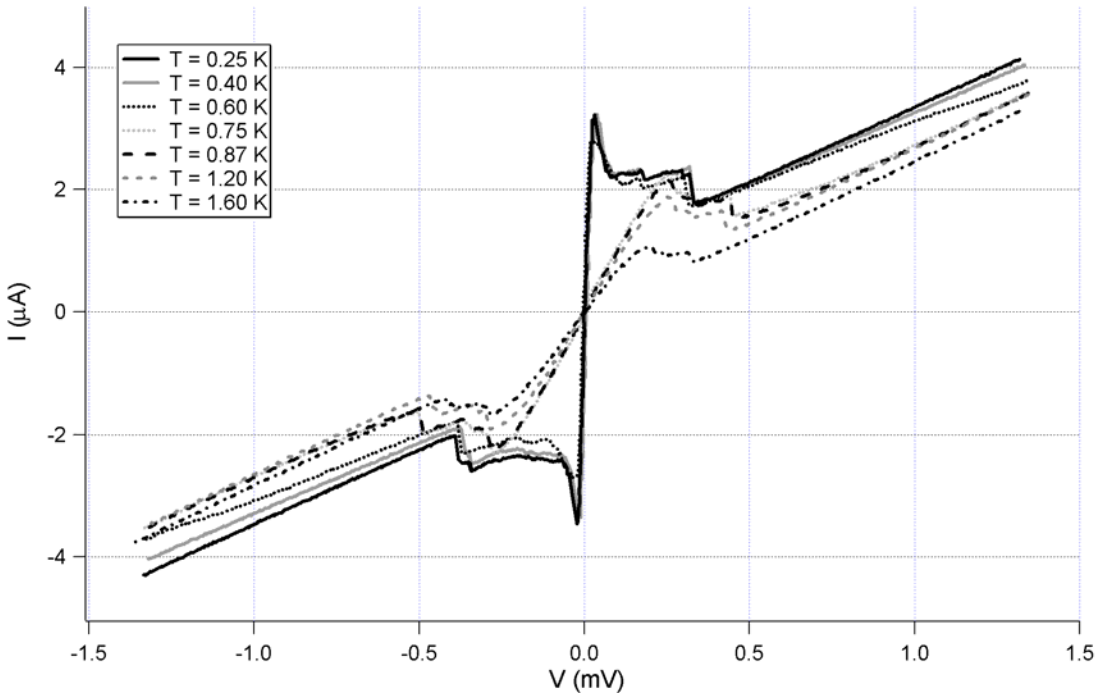

Figure 5.9: I-V curves for Device F at different bath temperatures with no applied magnetic field.

see Figure 5.11. The thick Au on top of the thin Nb contacts suppresses T_c of the contacts, but does not drive them completely normal because the thickness of the thin Nb is greater than ξ (~ 3-5 nm). The coherence length is estimated from data for the mean free path, ~ 1 nm (Gershenzon et al., 1988). This is the opposite case to Al HEBs where the thickness of the microbridge and thin contact pads is much smaller than the coherence length. The resistance of the contact pads is typically a few Ω at most, and it is often difficult to observe their transition in the R vs. T curve. In Fig. 5.10, the transition of the contacts is barely visible.

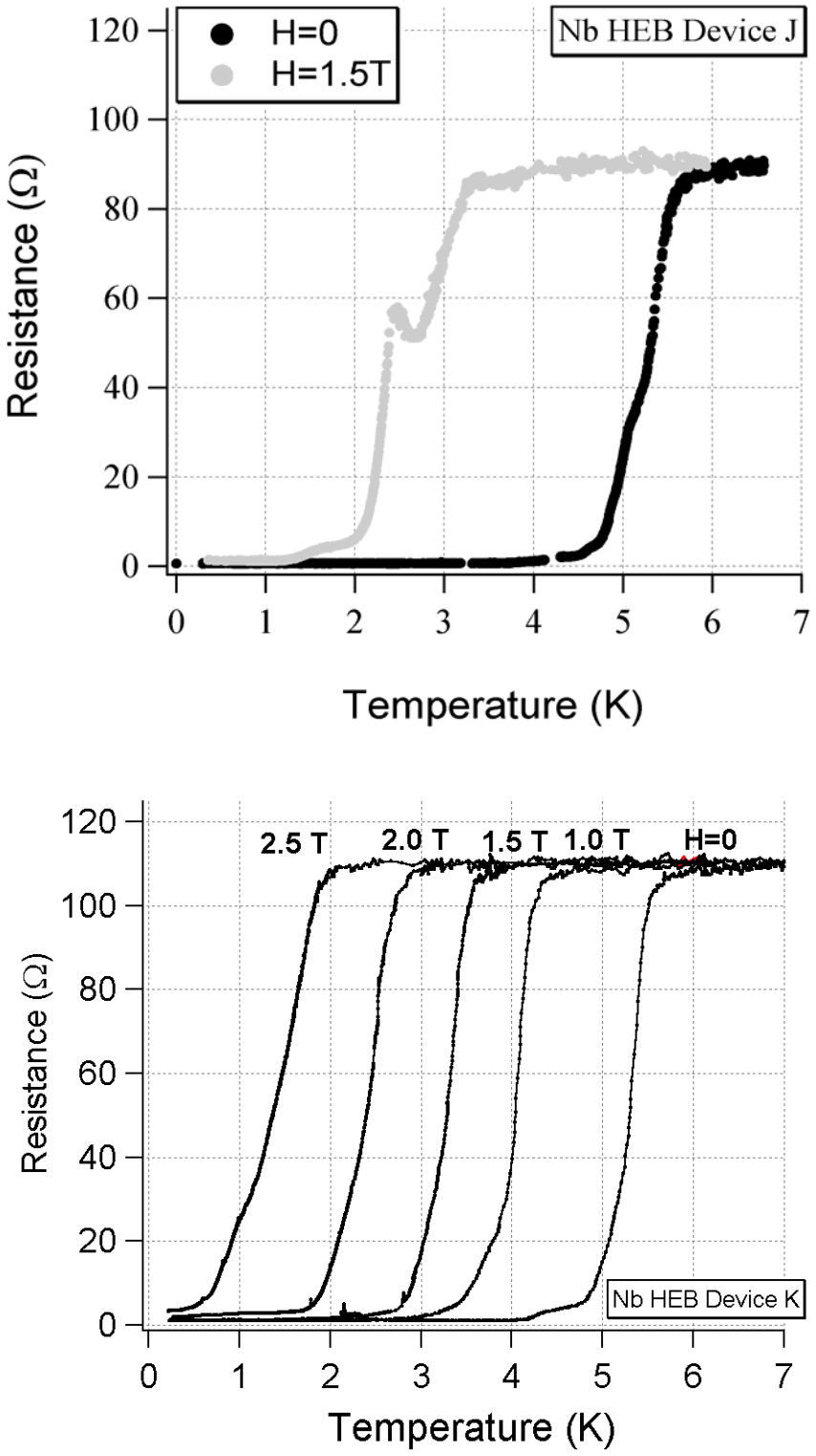

Figure 5.10: R vs. T curves for Nb devices J and K in different applied magnetic

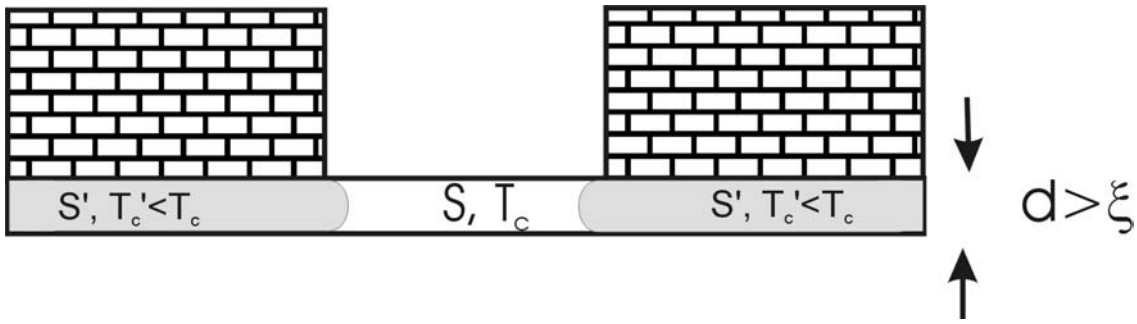

Figure 5.11: The structure of the Nb HEB with no magnetic field applied. The hatched areas are the normal Au pads. The light gray represents areas of Nb where the presence of the Au pads has reduced T_c down to T_c', ~ 0.5 K lower than T_c.

For an applied field of 1.5 T, we observe for Device J a decrease in T_c by nearly a factor of 2. Additionally we see the development of a bump in middle of the R vs. T curve which is not a measurement artifact. The curve was measured with a very small excitation current, very slow changes in the temperature, and while biasing at V = 0. The feature occurs when ramping the temperature up or down. A small bump in the R vs. T is also seen at zero applied field. The origin of the feature is not understood, and it does not occur in the other Nb device measured. For Device K, different applied magnetic fields up to 2.5 T are used to obtain a T_c as low as 1.4 K. For the high magnetic field, the transition actually begins to get broader and appears to have small additional bumps. Overall, the transitions look like that of Nb at 5.5 K but with a reduced T_c. In Table 5.1, the values of the magnetic fields used and the correspond T_c s are listed for both Devices J and K.

Nb HEB Device	L (μm)	H (T)	T_c (K)	I_c (T=0.25K) (μA)
J	0.16	0	5.2	105.0
		1.5	2.4	11.0
K	0.24	0	5.3	100.0
		1.0	4.0	12.0
		1.5	3.3	7.0
		2.0	2.4	3.8
		2.5	1.4	0.5

Table 5.1: Nb HEB critical temperatures for different applied magnetic fields.

5.2.2 Nb HEBs in a Magnetic Field, I-V Curves

The I-V curves for Device J and K are given in Figure 5.12 for different applied magnetic fields. The curves have a 'superconducting branch' in which the microbridge and the adjacent thin Nb contacts are superconducting at V = 0. After the critical current is exceeded, the I-V switches to the 'resistive branch' and the microbridge is driven normal. The thin Nb pads are superconducting in zero applied field. The I-V at high voltages (>1 mV) can be extrapolated back to the V = 0 and it does not cross the origin, suggesting that the pads are superconducting. As a note, the I-V is plotted in Figure 5.12a up to +/- 3 mV to show the structure close to V = 0. The I-V is linear well up

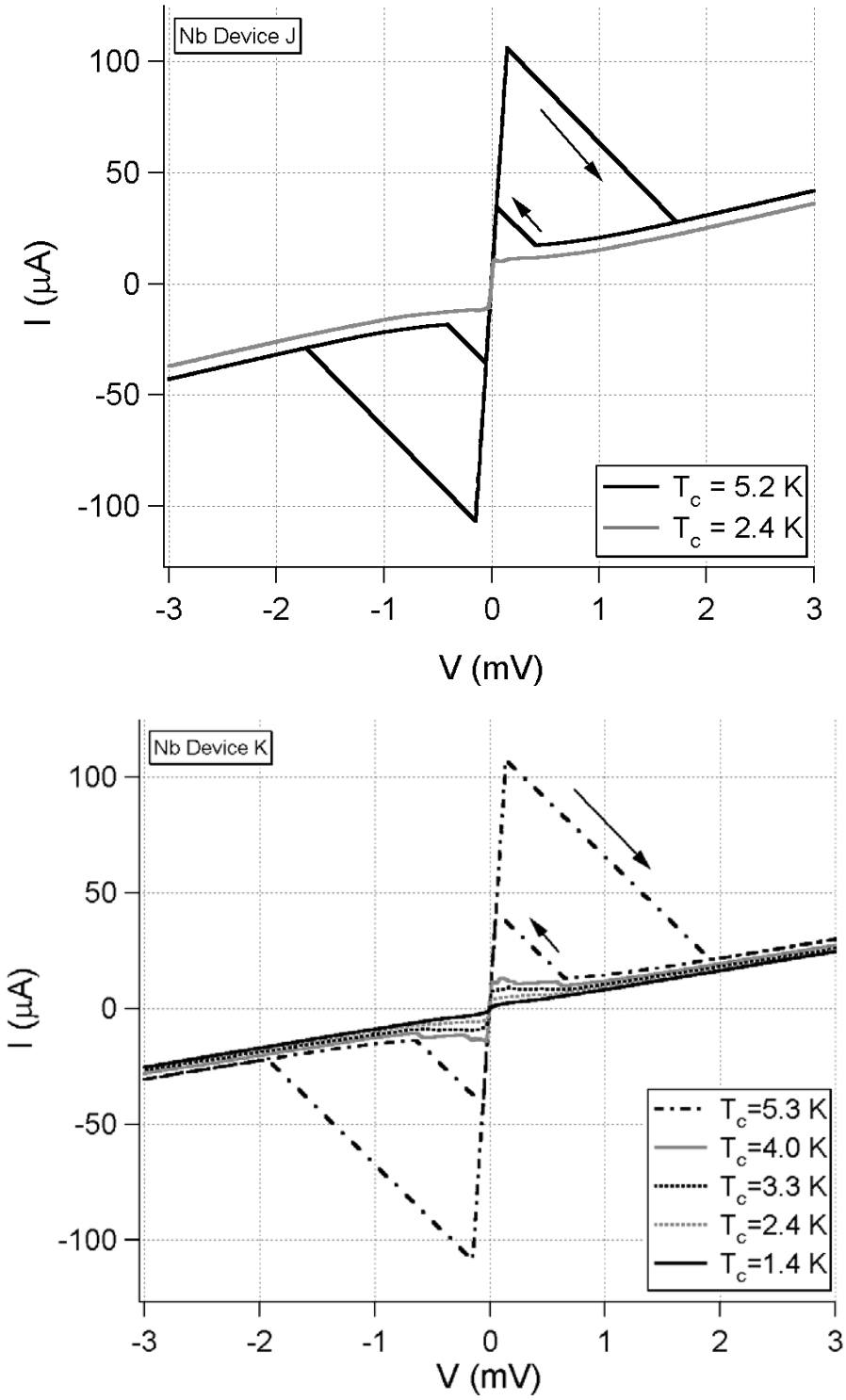

Figure 5.12a: I-V curves for Nb Devices J and K for different values of T_c plotted from –3 mV to + 3 mV.

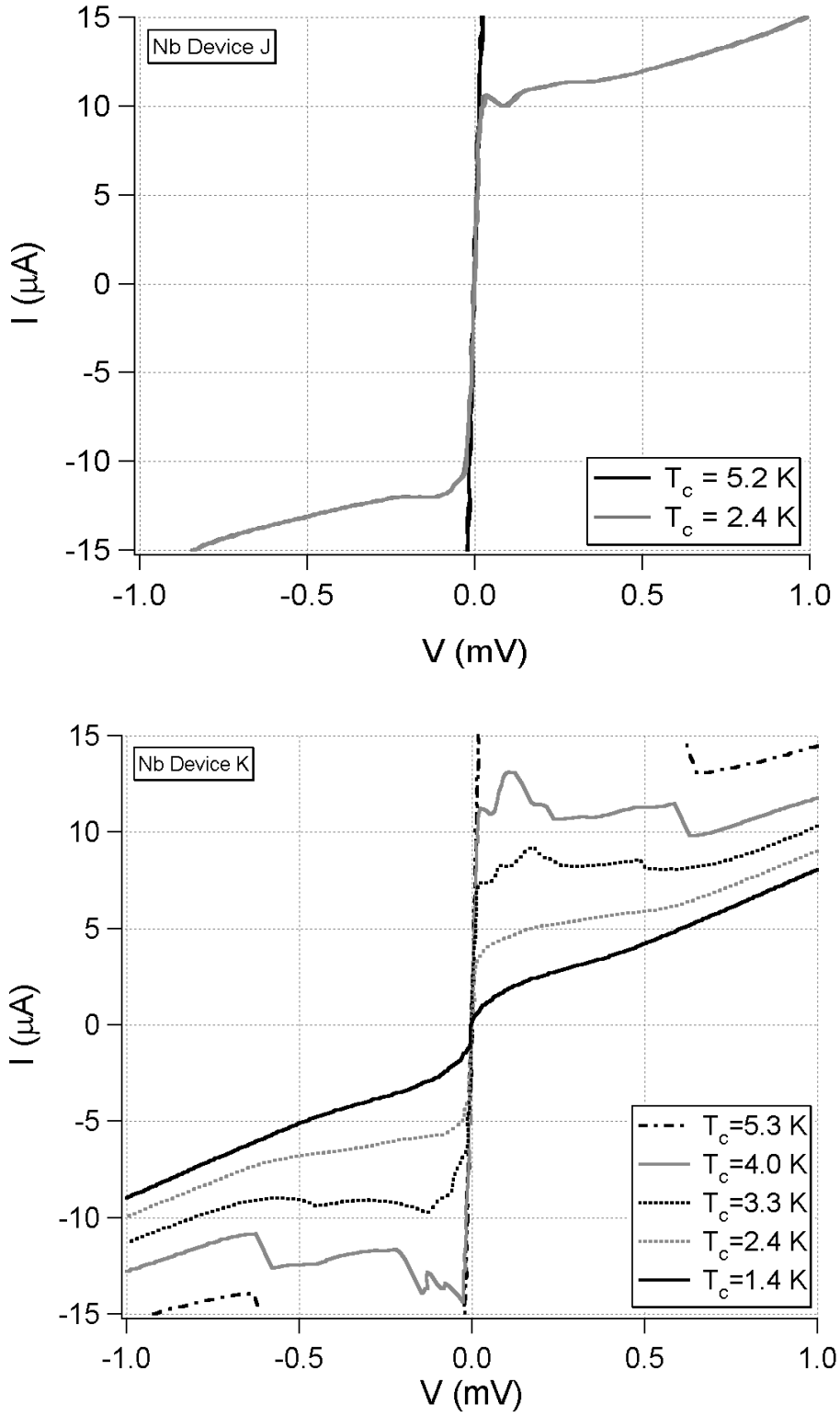

Figure 5.12b: I-V curves for Nb Devices J and K for different values of T_c plotted from –1 mV to + 1mV.

to 6 mV and the extrapolation technique still yields a non-zero y intercept for zero applied field. Thus the thick Au pads do not drive the thin Nb pads normal. For high magnetic fields, extrapolating the I-V back to V = 0 does yield a zero y-intercept. Presumably, the high magnetic field has suppressed superconductivity in the thin Nb contacts. The T_c of the thin Nb pads is lower than that of the microbridge, and the magnetic field suppresses the thin pads more strongly than the bridge.

As T_c is lowered, the critical current (I_c) also decreases. Since the bath temperature is much smaller than T_c, the measured critical current is taken to be approximately equal to I_c (T = 0), the maximum critical current. For Device K at H = 2.5T, I_c is only 0.5 μA. This is considerably smaller than comparable Al devices with similar critical temperature that have about 10 times the critical current. The magnetic field is thus able to form a lower temperature superconductor out of Nb, but it drastically lowers the critical current, and the devices are barely superconducting at the highest fields. This information is not discernable in the R vs. T characteristic since it is measured with a very small excitation current. The mixing performance of the Nb devices in high magnetic field is poor, and it is likely that this is due to the fact that these devices are only weakly superconducting in this regime. With high magnetic field applied, a vortex state is likely fully established in the Nb, and the critical current is not determined by the Ginzburg-Landau depairing current, but rather by the depinning force. Additional magnetic effects might also be present (Huebener et al., 1975).

5.3 Nb-Au HEB

5.3.1 Nb-Au HEB, R vs. T

The R vs. T curve for Nb-Au Device L is plotted in Figure 5.13. Unlike Nb Device K at 2.5 T, the R vs. T characteristic for Device L does not have any strange bumps. The resistance of the device drops from the normal state value to zero at $T_c = 1.6$ K, without any applied magnetic field. Additionally, compared to Device K with a 2.5 T field applied, the Nb-Au HEB exhibits a much sharper transition. The only new feature in the Nb-Au R vs. T is that there is a considerable rounding of the curve right at the onset of the transition. It is possible that since the microbridge thickness is larger than the coherence length of Nb, different parts in the microbridge have different critical temperature. Clearly for a very thick microbridge, the areas very far away from the Au normal layer will be unaffected by it. The T_c of a bilayer N-S film depends on many parameters, such as the transparency of the interface between the normal and superconducting parts. None of these parameters has been carefully studied in this thesis, and will be a topic of future research. What factors are important in obtaining a sharp transition, and how sensitive the device T_c is to the deposition conditions needs to be investigated in detail. What has been established is this work is that thin film Nb HEB mixers that would normally have a $T_c \sim 5$-6 K can be made to have a T_c as low as 1.6 K by the presence of a thin Au layer on top of the microbridge. Presumably, a thinner Au layer will yield a device with a higher T_c and with no Au layer, the original Nb HEB will be attained.

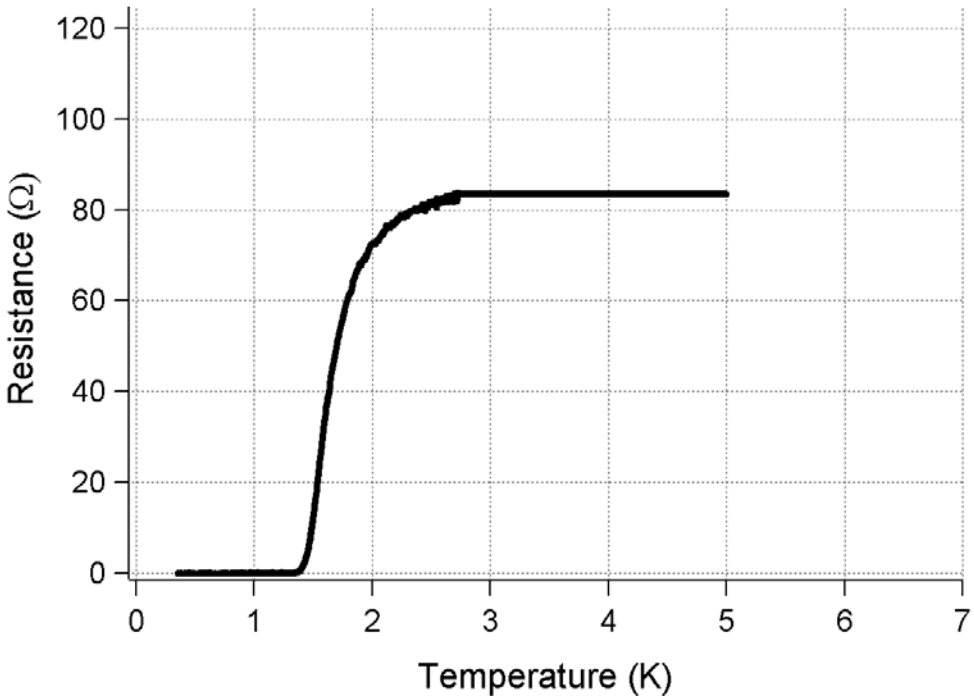

Figure 5.13: R vs. T curve for Nb-Au Device L. No magnetic field is needed to lower T_c for these devices. The thin Au layer on top of the Nb microbridge suppresses its T_c from ~ 5-6 K down to 1.6 K in this particular case.

5.3.2 Nb-Au I-V

The I-V curves for Device L have the same basic shape as the Nb I-V curves described in Section 5.2.2. There are again two braches. At V = 0 there is a 'superconducting branch' with zero resistance. Any discernable resistance on the I-V on the 'superconducting branch' is due to the resistance of the DC wiring since a two wire measurement is used to obtain the I-V curves. With sufficient applied power, the critical

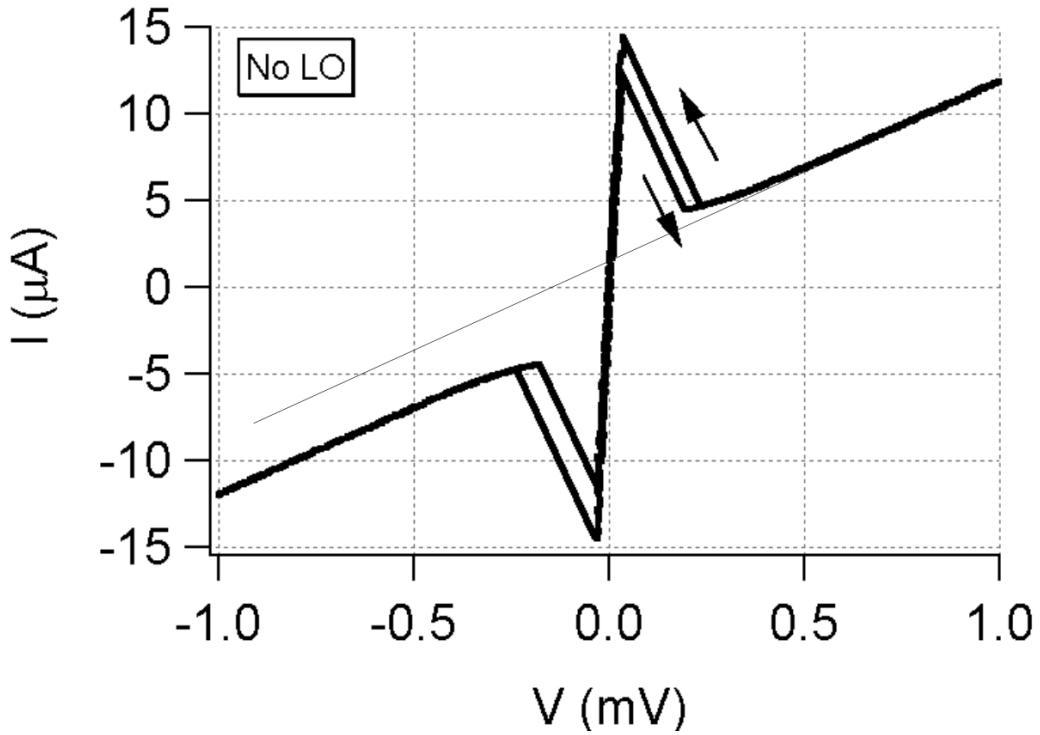

Figure 5.14: I-V curve for Nb-Au Device L.

current is exceeded and the I-V switches to the 'resistive branch'. The I-V curve for Device L is given in Figure 5.14. Like the Nb devices, the thin Nb pads underneath the thick Au are superconducting. This is suggested by 'excess current' on the I-V at high bias voltage. The structure of the device is the same as described in Figure 5.11, the Au pads do not drive the Nb underneath normal because the Nb film thickness is less its coherence length. What is very different in the Nb-Au I-V curves from the Nb data in a high magnetic field is the critical current. For Nb-Au Device L, $I_c(0)$ is 14 μA, which is considerably larger than that of Device K with H = 2.5 T.

Chapter VI: P_{LO} & Conversion Efficiency

In this chapter, measurements of the I-V curves with LO power applied and the conversion efficiency as a function of bias voltage are discussed. The LO power needed for optimum conversion efficiency is an important parameter for THz mixers since the maximum power of solid state sources is currently limited to μW. The conversion efficiency itself is one of the two quantities that are needed to quantify the mixer input noise, which is a measure of mixer sensitivity. The output noise that will be discussed in the Chapter VIII will be referred to the mixer input using the conversion efficiency obtained in this chapter.

The first step in measuring the mixer conversion efficiency is to record the I-V curves with LO power applied. These curves are then used to identify a range of stable bias voltages where the mixer can be operated. When microwave radiation is applied to the Al mixers, two different modes of operation are observed. If the Al HEB contacts are superconducting, then Josephson junction behavior is observed. Shapiro steps develop at voltages $V = nhf_{LO}/2e$ in the I-V curve, especially in the shortest Al microbridges. Upon applying a magnetic field, the contacts pads become normal and Josephson effects are not evident. Applying LO power heats the device and the I-V curves resemble data taken at higher temperatures without radiation. Specifically, the critical current of the 'superconducting' branch decreases with increasing LO power until the microbridge becomes fully normal. For the Nb and Nb-Au HEBs, no Josephson-junction-like behavior is observed since they do not have thick superconducting contact pads and the device length is much longer than the superconducting coherence length. Applying LO

power only heats the mixer and reduces the critical current. In Al HEBs measured with a magnetic field, due to the normal microbridge edges, there is a finite resistance on the I-V curve at low bias voltages. Therefore, there are two possible regions on the I-V where the HEB can be biased. The best conversion efficiency is measured in the 'resistive', higher voltage branch. For Nb and Nb-Au HEBs, no conversion is observed at V = 0 since the device is superconducting and its resistance does not change with power.

Once a set of LO pump powers are chosen for a given device, the conversion efficiency is measured at each bias point on the I-V. The RF signal power is kept at least 20 dB below the LO power to ensure mixer linearity. Several different values of the LO power are sampled to locate the point of maximum conversion efficiency. The LO power which yields the maximum conversion efficiency will be referred to as the optimum LO power. For all the HEB mixers measured, the maximum conversion efficiency is of order –10 dB. There are three situations in which poorer conversion is measured. If the bath temperature is close to the microbridge T_c, then smaller conversion efficiency is observed. This is to be expected since operating at high bath temperatures reduces the amount of LO power that can be applied to the mixer and the conversion efficiency correspondingly decreases. Conversion efficiency is less than –10 dB in devices that have a normal state resistance much larger than 50 Ω. These devices are not impedance matched to the IF readout circuitry nor to the RF input, and only a fraction of the power is effectively coupled. Finally, for Nb Device K, poor conversion efficiency is measured when a magnetic field greater than 1.5 T is applied to the sample. The mixer is only weakly superconducting when T_c is lowered below 3.3 K. We discuss this later.

Along with experimental measurements, numerical simulations are performed to obtain theoretical curves for the mixer quantities described above. Namely, the pumped I-V curves and the conversion efficiency as a function of bias voltage are calculated. In the simulations, the entire length of the microbridge is treated as having a uniform T_c and a very narrow superconducting transition. This is sufficient to accurately describe the optimum conversion efficiency and associated LO power of the devices studied, and both of these assumptions will be relaxed in later chapters to study other effects. The numerical predictions agree well with the experimentally obtained values.

Using both the experimental data and the numerical calculations, the optimum LO power is studied as a function of HEB mixer T_c. The optimum LO power is proportional to T_c^2 when $T_b << T_c$, as predicted. Data from this work suggest that the optimum LO power for a diffusion-cooled HEB mixer with 50 Ω normal resistance is ~ 0.7 nW • T_c^2 at low bath temperatures. For very wide transitions, the simulations predict that this power increases.

6.1 Al HEB

6.1.1 I-V curves with LO power

Different behavior is observed when LO power is applied to the Al HEB depending on whether the contact pads are in the normal state or are superconducting. When the contact pads are superconducting, the device exhibits Josephson junction behavior. The junction is formed because the two large superconducting pads are

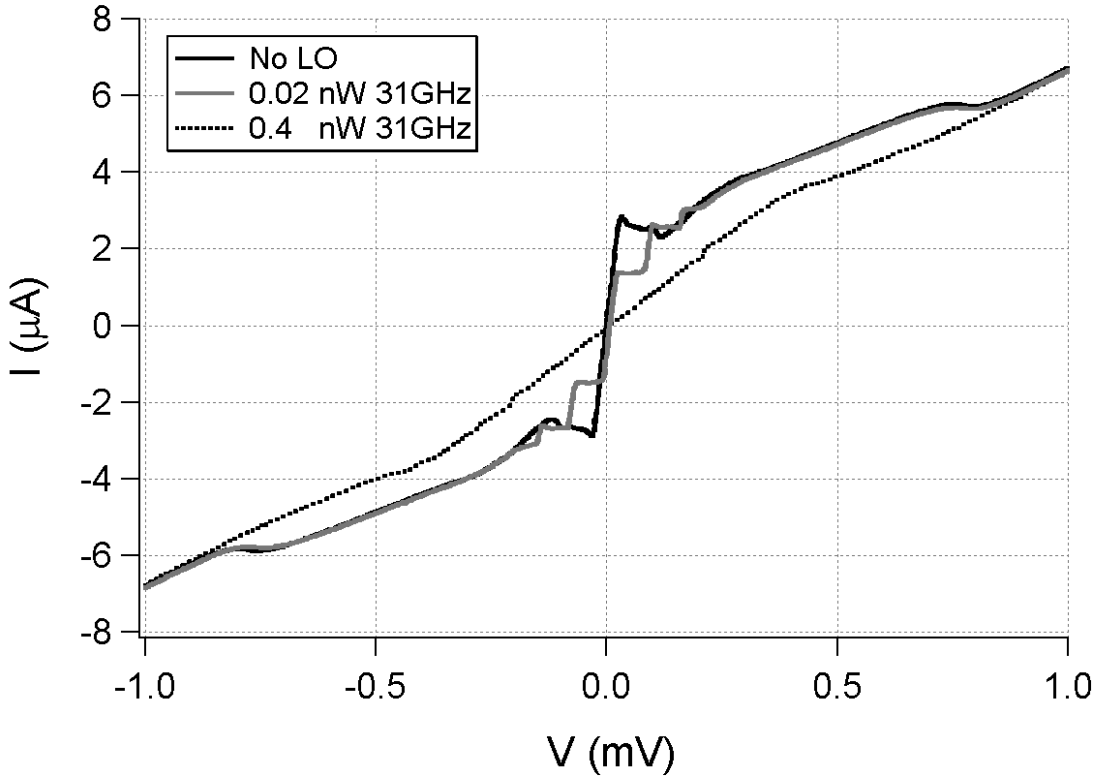

Figure 6.1: Pumped I-V curves for Device C (L = 0.3 μm) in zero magnetic field. Shapiro steps are clearly visible. The bath temperature is 0.25 K.

connected through a weak link, the microbridge. Cooper pairs can diffuse from one contact pad to the other through the microbridge. For short microbridges, the I-V curve develops Shapiro steps when it is 'pumped' with LO power. In Figure 6.1 the I-V curves for a 0.3 μm long HEB, Device C, are presented with and without P_{LO} applied at T_b = 0.25 K. The solid black curve on the graph is the I-V with no LO power. It is similar to the Al I-V described in the last chapter with a 'superconducting' and 'resistive' branch. Applying a small amount of LO power induces constant current steps that have a voltage spacing of ~ 60 μV. For this experiment, the LO frequency is 31 GHz. The predicted

size for Shapiro steps is hf / 2e, which for the LO applied is 64 μV. This is in good agreement with the observed steps. For 0.02 nW LO power, there is excess current observed in the I-V, and this suggests that the contacts are superconducting. For large LO power, 0.4 nW, the device is heated close to the transition temperature of the contacts pads. In the dotted black curve in Figure 6.1, the 'superconducting' branch develops finite resistance and the step features are absent, indicating that contacts are normal or nearly normal. Similarly, if the bath temperature is increased above 0.6 K, the transition temperature of the contacts, no steps are observed on the I-V. For longer microbridges, the steps are not readily observable in the I-V. In Figure 6.2, the pumped I-V curves for a 1.0 μm long HEB, Device G, are plotted at T_b = 0.25 K. With LO power applied, no steps can be seen in the I-V curve. Applying LO power appears to only heat the device and the critical current decreases accordingly. This is understandable since the pairs have to travel coherently a longer distance in this case. The 0.3 μm long device is ~ 6 $\xi(0)$ long where as the 1.0 μm device is nearly 20 $\xi(0)$. Coherence is probably lost in the majority of the Cooper pairs as they traverse the length of the 1.0 μm bridge. In the 0.6 μm microbridges, small steps are observed in the pumped I-V curves when the contacts are superconducting, at T < 0.6 K.

In light of the observed Josephson junction behavior, mixing measurements presented are those made with a magnetic field applied or with the bath temperature above the critical temperature of the contact pads. For the L = 1 μm devices, although the pumped I-V curves do not have strong signatures of Josephson coupling, there are often peaks in the output noise which are very likely due to Josephson coupling. Therefore, only data with normal state contact pads will be discussed for these devices.

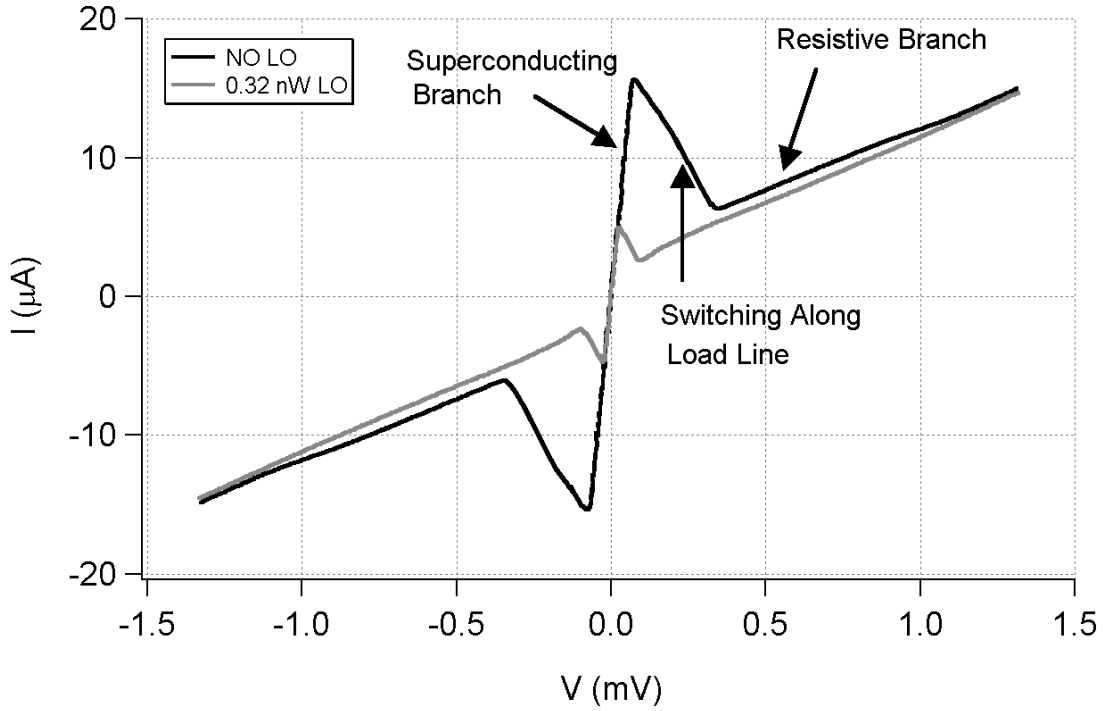

Figure 6.2: Pumped I-V curves for Device G (L = 1.0 μm). No Shapiro steps are observable. The bath temperature is 0.22 K.

Different values of P_{LO} are used to find the optimum operating conditions for each device. In Figure 6.3, the pumped I-V curves for several LO powers applied to Device D are plotted. The data is taken in the presence of a 0.05 T magnetic field. The contact pads are thus normal, and for this Al device approximately ½ the total bridge length is always in the normal state due to normal ends. With increasing LO power, the 'superconducting' branch becomes smaller, indicating that the critical current of the superconducting center of the microbridge is decreasing.

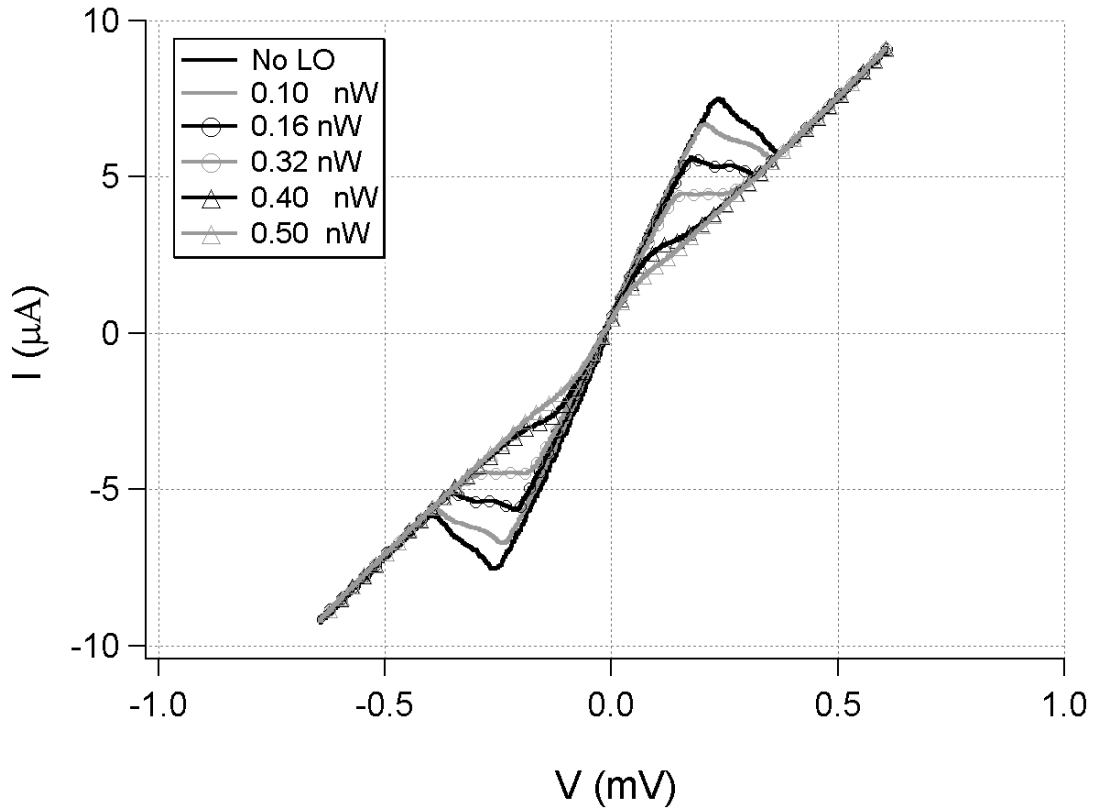

Figure 6.3: I-V with different applied LO powers for Device D.

6.1.2 Conversion Efficiency

The Al HEB mixers are optimized for best conversion efficiency. It will be shown later that the output noise of these mixers varies weakly with LO power. The mixer noise therefore depends more significantly on conversion efficiency. Three parameters affect the conversion efficiency: the magnetic field, the LO power, and the bias voltage. The purpose of the magnetic field is to suppress superconductivity in the contacts. Typically, the smallest field needed to achieve this task is applied. Sometimes, however, if a sufficiently large field is not applied, the contacts can still be weakly

superconducting. Noise measurements are a sensitive probe of this. For this reason, mixing measurements are made with a few different values of the magnetic field. Once the field is fixed, the conversion efficiency is measured at different bias voltages for several LO powers. The RF signal power is kept at least 20 dB smaller than the LO power in the conversion measurements. Also, mixer linearity is checked in each device by increasing the RF signal power by 6 dB in single dB increments. If the IF signal increases proportionally to the increase in RF signal, the mixer is taken to be operating without saturation.

In Figures 6.4a and 6.4b the conversion efficiency as a function of bias voltage is presented for Device D for two different magnetic fields. For each value of the magnetic field, only the data corresponding to the optimum LO power is plotted. No data points for the conversion efficiency are given for bias points where the I-V curve has high differential resistance (eg. V ~ 150-250 μV in Figure 6.4a). It is not possible to maintain a stable bias point in this region. One sign that instability is present is a complex set of peaks in the IF signal. When the HEB is biased at a stable operating point, the IF signal is a single sharp line. For example in the top panel of Figure 6.5, a 500 MHz IF signal is shown when biasing at a stable point in the I-V. In contrast, if the bias point is shifted to a 'flat' section of the I-V curve, multiple sidebands are seen. Additionally, a variety of lower frequency oscillations (~ 10's MHz) are sometimes also observed. If the IF signal is not sampled fast enough, the conversion efficiency measured at one of the unstable bias points does not appear to be oscillating in time. The measured conversion in this case represents an average value as the device rapidly switches between different bias points. Thus it is important to study the IF signal in a wide spectral range to ensure that

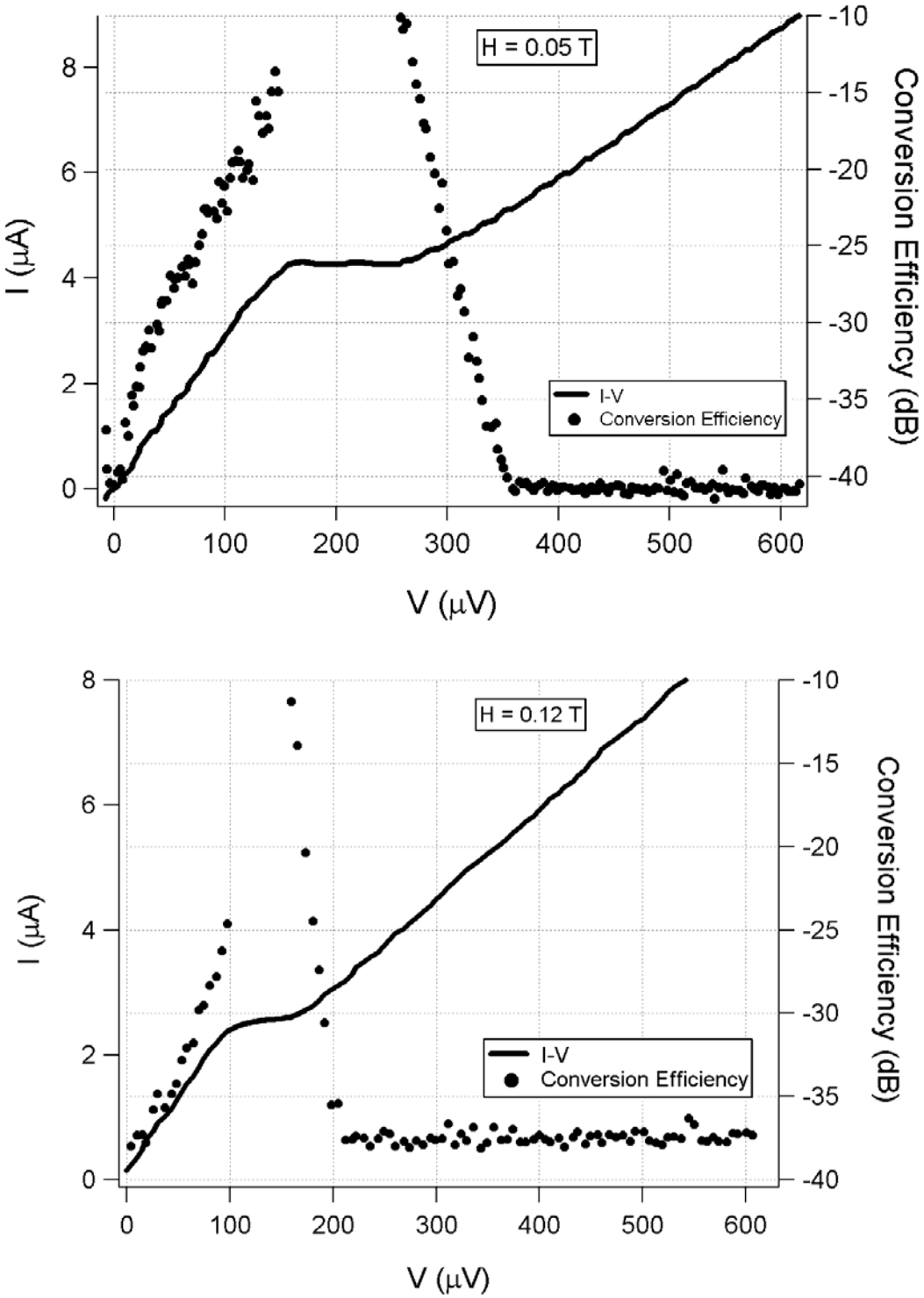

Figure 6.4: (a, top) Pumped I-V (0.32 nW) and conversion efficiency for Device D with H=0.05T. (b, bottom) Pumped I-V (0.13 nW) and conversion efficiency for Device D with H=0.12T.

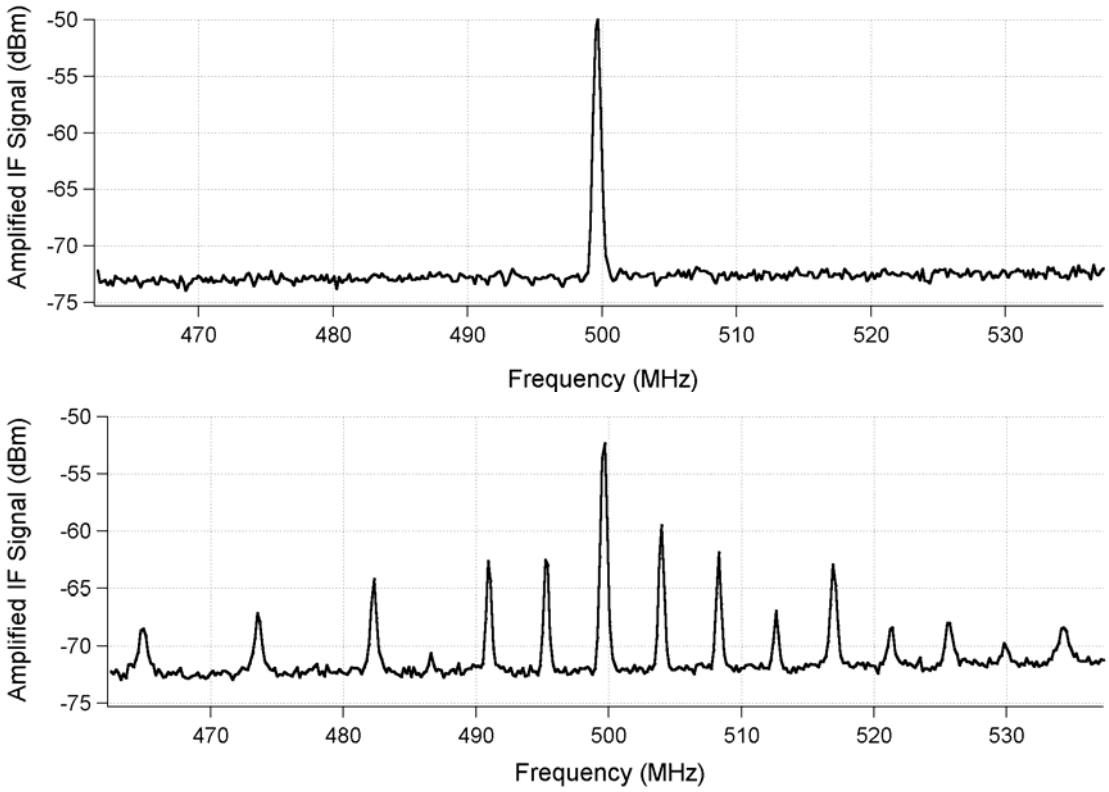

Figure 6.5: A 500 MHz IF line when biasing at a stable point on the I-V curve (top) and an unstable point (bottom).

only the expected heterodyne response is present. Consequently, plots in this thesis will often have some sections removed to ensure that data only for stable bias points is reported. In the conversion efficiency data in Figure 6.4, there is a mixing signal observed in the 'superconducting' branch of the I-V curve. Conceptually, this can be thought of as a size modulation at the IF of the normal regions at the ends of the microbridge. In the R vs. T curves for Al HEBs in a magnetic field, the residual resistance varies slowly at temperatures well below T_c of the microbridge. Biasing at low bias voltages likely corresponds to heating the HEB to this section of the R vs. T curve.

The sharpest part of the transition is near its onset, and biasing on the 'resistive' branch corresponds to an HEB operating point on this section of the R vs. T. In the microwave experiments described here, the IF signal in the 'resistive' branch is always larger. In both magnetic fields used for Device D, the maximum conversion efficiency is approximately –10 dB. There is, however, a difference in the noise performance that is discussed later.

The behavior of all the Al devices is similar to the examples presented above. The conversion efficiency and the operating conditions used in the measurement are listed in Table 6.1. The conversion efficiency is a function of IF, and has a roll off determined by the thermal relaxation time of hot electrons in the microbridge. The –3dB IF bandwidth of the mixers is determined by measuring the IF dependence of the conversion efficiency. This is used to calculate the conversion efficiency at IF = 0. The conversion efficiency reported in Table 6.1 is the IF = 0 value calculated from the measured conversion efficiency and IF bandwidth, discussed in the next chapter. For some of the earlier data runs, a magnetic field was not available and the HEB was kept at a bath temperature above T_c of the contacts, and thus close to T_c of the microbridge. This accounts for the poor conversion efficiency of Devices C and H. Device F is not well impedance matched to the Z ~ 50 Ω IF amplifier, and this can account for its conversion efficiency being poorer than that of the other devices of the same length. Devices A and B do not exhibit a superconducting transition when the contacts are normal. Superconductivity is suppressed in the entire microbridge due to the proximity effect.

Al HEB Device	L (μm)	T_b (K)	H (T)	T_c (K)	P_{LO} (nW)	Conversion Efficiency (IF=0, dB)
A	0.2	-	-	-	-	-
B	0.3	-	-	-	-	-
C	0.3	1.2	0	1.6	0.10	-27
D	0.6	0.22	0.12	0.8	0.32	-11
E	0.6	0.25	0.12	0.9	0.50	-8
F	0.6	0.25	0.30	1.6	0.40	-15
G	1.0	0.22	0.12	1.2	0.32	-10
H	1.0	1.2	0	1.6	0.10	-31
I	1.0	---	---	---	---	---

Table 6.1: Conversion efficiency for Al HEB mixers. For Devices A and B, no superconducting transition is observed in the microbridge when the contacts are in the normal state.

6.2 Nb HEB in a magnetic field

6.2.1 I-V Curves with LO power

The I-V curves for the Nb HEB mixers are simpler in shape than the Al curves. As LO power is applied to the device, the temperature of the device increases and the critical current decreases. No Shapiro steps are observed in these devices. There are two factors that contribute to this. First, the thin Nb contact pads are only weakly

superconducting and thus the HEB does not resemble a constriction type Josephson junction. Also, the length of the shortest device measured (Device J) is > 30 $\xi(0)$. Thus, even if the contact pads were made of thick Nb, the length of the microbridge is prohibitively long for pair tunneling. In Figure 6.6, the pumped I-V curves for Nb Device J are plotted at T_b = 0.22 K. The two sets of curves in the figure correspond to zero applied magnetic field (T_c ~ 5.3 K) and 1.5 T applied field (T_c ~ 2.4 K). In the case of zero applied field, for the largest LO power applied, there is still a small critical current present. Applying a slightly greater LO power can suppress this critical current and give an I-V that is fully smooth. In this case, LO power alone is sufficient to establish a 'hot spot' in the microbridge and no constant voltage 'superconducting' branch on the I-V is observed at V=0. This regime has been called the 'overpumped' regime in past Nb experiments. In the 'overpumped' case, the conversion efficiency is 3 dB or so lower than the optimum value. However, the noise performance is better since the output noise in this case is typically smaller (Burke et al., 1999). For the case of lower T_c devices, the output noise is small in magnitude and does not change very much from the optimum conversion operating regime to the 'overpumped' case. The decrease in conversion, on the other hand, results in a degradation of the noise performance. Furthermore, the 'overpumped' regime is difficult to identify. Many I-V curves have smooth features to start with, and it difficult to compare an 'overpumped' I-V at one value of the applied magnetic field with another. As a result, in this thesis the Nb devices are always optimized for conversion efficiency. This allows for the comparison of mixing properties at different magnetic fields, especially if the maximum conversion efficiency is the same.

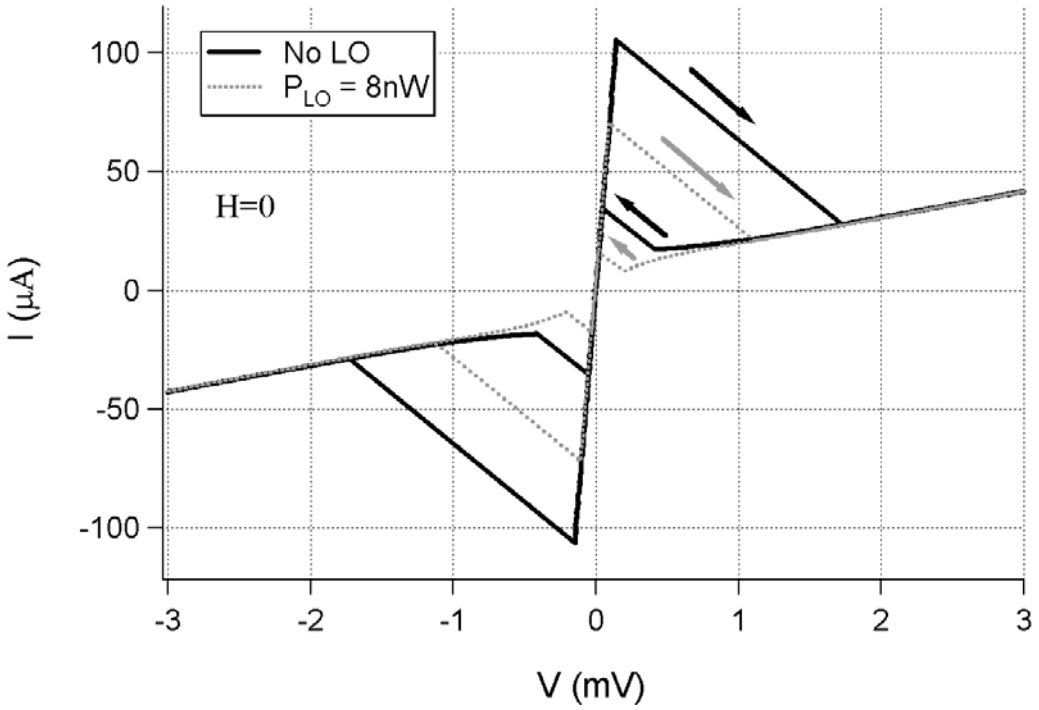

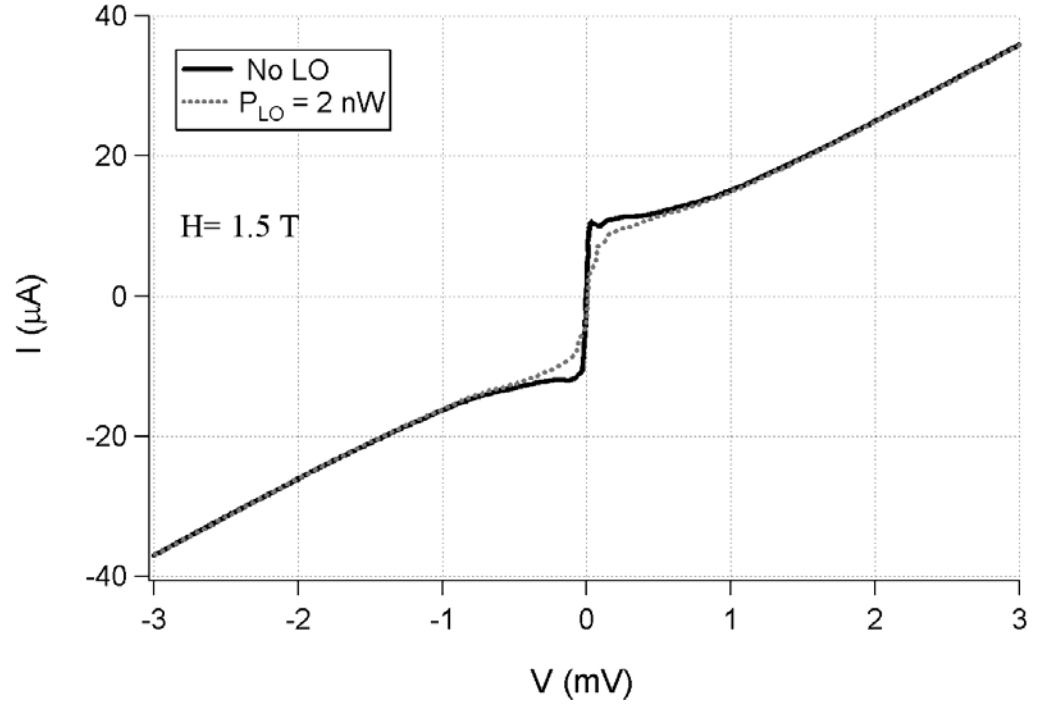

Figure 6.6: (a, top) I-V curves with LO power for Nb Device J in zero magnetic field and (b, bottom) a 1.0 T field. The bath temperature is 0.22 K.

6.2.2 Conversion Efficiency

The conversion efficiency for the Nb devices is a function of the applied magnetic field, the LO power, and the bias voltage. The purpose of applying a magnetic field to the Nb HEBs is to reduce their T_c. At each value of the magnetic field, the conversion efficiency as a function of bias voltage is measured for different LO powers. Once the LO power and bias point corresponding to the optimum conversion efficiency is found, the magnetic field is varied to change the device T_c and the procedure is repeated. Regions of unstable operation are determined; no mixing data for these areas are reported.

In Figure 6.7, the conversion efficiency as a function of bias voltage is presented for Device J. Similar to the I-V curves in Figure 6.6, two cases are considered. This first is with zero applied field and the second with a 1.5 T magnetic field. The conversion efficiency is measured at IF = 1.0 GHz. At both values of T_c, it is possible to obtain a conversion efficiency of ~ -9 dB. With T_c = 2.4 K, however, the conversion efficiency varies more strongly with bias voltage. This is a general trend in lower T_c devices. As the T_c is lowered, the conversion efficiency depends more strongly on bias voltage. This topic will be discussed in detail in Chapter IX where saturation effects are discussed.

The conversion efficiency vs. bias curves are all similar to the data presented in Figure 6.7. A summary of mixer performance for both Nb Devices J and K is presented in Table 6.2. For Device K, it is possible to obtain the same conversion efficiency measured in zero field only for low to intermediate magnetic fields strengths. For T_c = 2.4 and 1.4 K, the conversion efficiency begins to degrade. The performance at T_c = 1.4

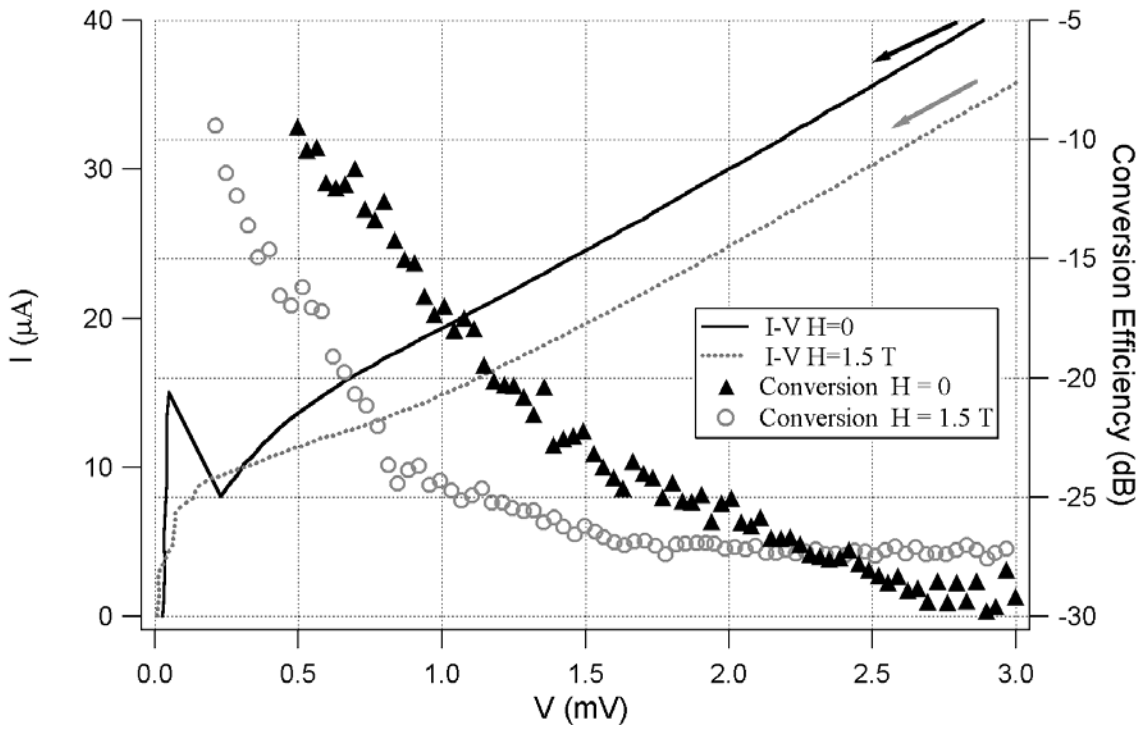

Figure 6.7: Conversion efficiency and pumped I-V curves for Device J with and without a magnetic field. The conversion efficiency is measured at IF=1.0 GHz and T_b = 0.22 K.

K is very poor for Device K, with the conversion efficiency 9 dB lower than the value measured at T_c = 5.3 K. The applied LO power is reported as ~ 0.4 nW in this case, although comparable conversion is observed for smaller LO powers as well. In this regime, Device K exhibits low conversion over a broad range of LO powers. With the magnetic field equal to 2.0 T and 2.5 T, Device K is weakly superconducting and

Nb HEB Device	H (T)	T_c (K)	P_{LO} (nW)	Conversion Efficiency (IF=0, dB)
J	0	5.2	8.0	-9
	1.5	2.4	2.0	-9
K	0	5.3	5.0	-11
	1.0	4.0	3.0	-11
	1.5	3.3	2.0	-11
	2.0	2.4	1.0	-15
	2.5	1.4	≤ 0.4	-20
Burke B (Device J)	*0*	*5.2*	*5*	*-11*
Burke C (Device K)	*0*	*5.3*	*8*	*-10*

Table 6.2: Nb HEB conversion efficiency for different applied magnetic fields. The bath temperature is 0.22K in all cases. The last two rows are values reported in Burke (1997) for Devices J and K in zero magnetic field.

performance is poor. The mixing results obtained for both Nb devices in zero magnetic field are very close to those originally measured by Burke several years ago (1997) for the same devices, also listed in Table 6.2.

6.3 Nb-Au HEB

6.3.1 I-V Curves with LO Power

The pumped I-V curves for Nb-Au Device L resemble those of Nb HEBs in zero magnetic field. Applying LO power heats the device and reduces the critical current. If enough power is applied, an 'overpumped' I-V curve can be obtained which is smooth and without a V = 0 'superconducting' branch. The 'overpumped' case has neither the best conversion efficiency nor the lowest noise temperature. In Figure 6.8, the I-V curves for Device L are presented for a range of different LO powers. No magnetic field is applied in these measurements. The bath temperature is 0.22 K, which is well below the device T_c of 1.6 K.

6.3.2 Conversion Efficiency

The conversion efficiency is measured as a function of bias voltage for several different LO powers. The maximum conversion of η (IF = 0) = –12.5 dB is obtained with an LO power of 2.0 - 2.5 nW. In Figure 6.9, the conversion efficiency is plotted versus bias voltage with a LO power of 2.5 nW. This is a substantially higher LO power than that applied to Nb Device K with a 2.5 T field. The Nb-Au HEB is not weakly superconducting. In fact, the critical current of 15 μA is about 30 times larger than that of Nb Device K at T_c = 1.4 K. The performance of Device L is summarized in Table 6.3.

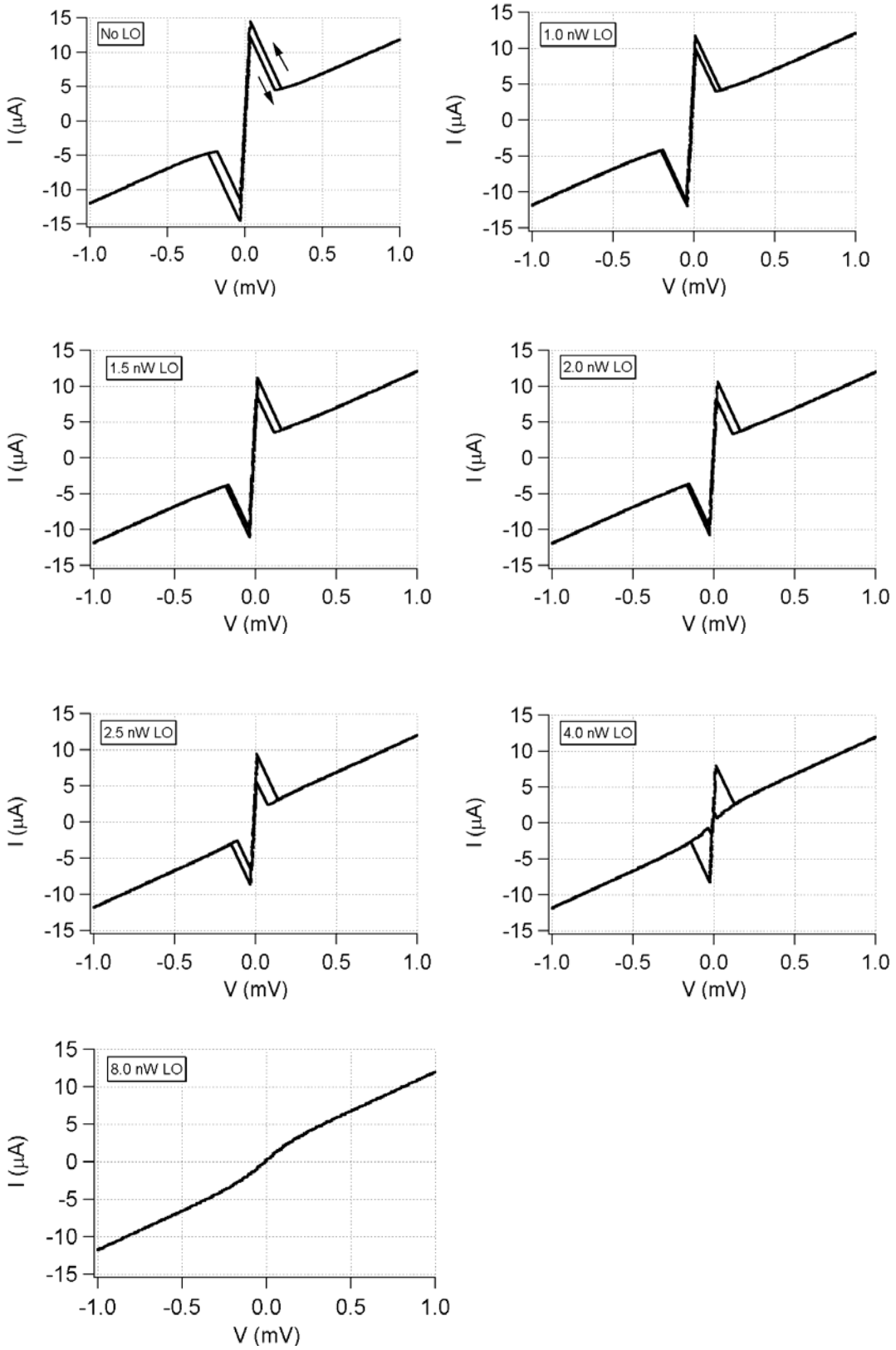

Figure 6.8: I-V curves for Nb-Au Device L with different applied LO powers.

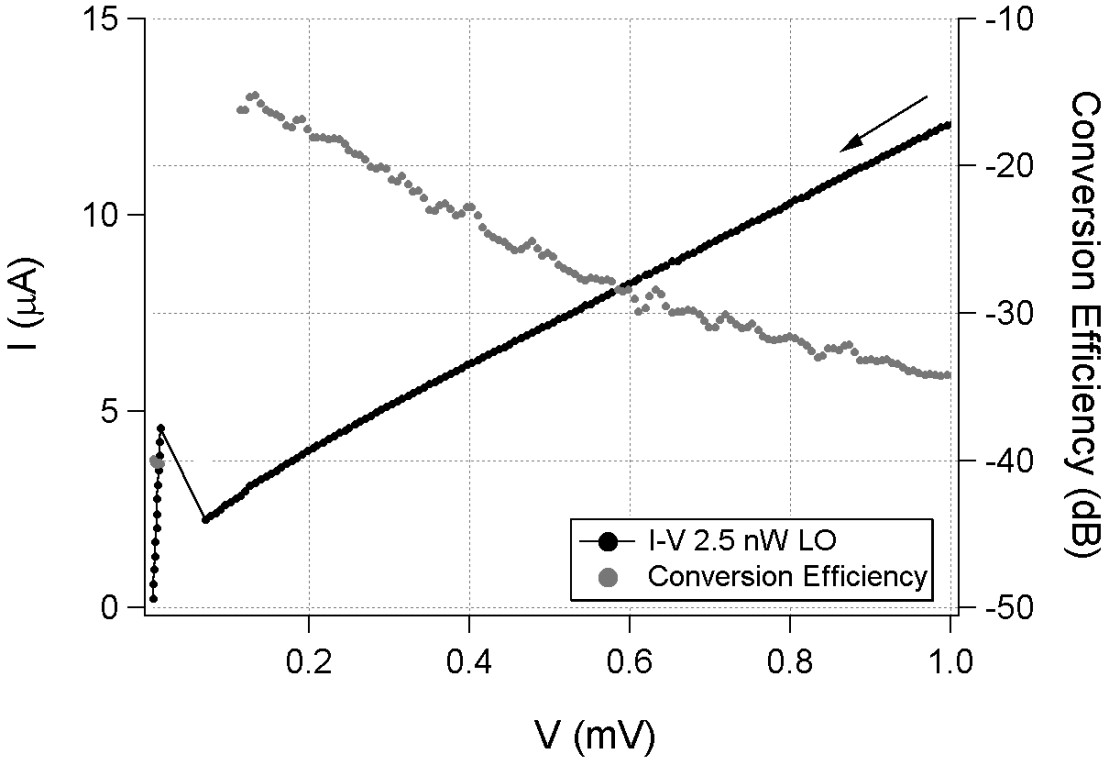

Figure 6.9: Conversion efficiency as a function of bias voltage for Nb-Au Device L. The conversion efficiency is measured at IF = 1 GHz at a bath temperature of 0.22K.

Nb-Au HEB Device	H (T)	T_c (K)	P_{LO} (nW)	Conversion Efficiency (IF=0, dB)
L	0	1.6	2.0-2.5	-11

Table 6.3: Nb-Au HEB conversion efficiency.

6.4 Numerical Simulations

Using the frequency domain model described in Chapter II, numerical simulations are used to predict the LO power needed to obtain optimum conversion for mixers with different values of T_c. In this section, the R vs. θ that is entered into the model is the same across the full length of the bridge. The presence of normal edges for Al mixers does not significantly affect the maximum attainable conversion efficiency. Rather, the normal edges diminish the bias voltage range over which optimum conversion is observed. The model is adjusted to account for normal edges when calculating the saturation power in Chapter IX. The width of the transition is taken to be ~ 0.1 K at all values of T_c. Later this condition will be relaxed to determine how a larger transition width affects mixer performance. In the simulations, the HEB resistance is 50 Ω and the bath temperature is 0.22 K.

Similar to the actual experiment, the first step is to calculate the I-V curves with LO power. In Figure 6.10, the simulated I-V curves for a T_c = 1.0 K HEB are plotted. Lacking a mechanism for calculating the critical current of the device, the I-V curves for small LO powers diverge at V = 0. However, the model is valid in the 'resistive' branch of the I-V and for 'overpumped' I-V curves. The I-V curves display the general features observed in experiment, and the LO power necessary to completely drive the HEB normal agrees reasonably well with the data presented. With the pumped I-V curves, the conversion efficiency as a function of bias voltage can be calculated. In Figure 6.11, the calculated conversion efficiency for a T_c = 1.0 K HEB with 0.5 nW of LO power applied is given. The model does not distinguish between stable and unstable regions of bias. As

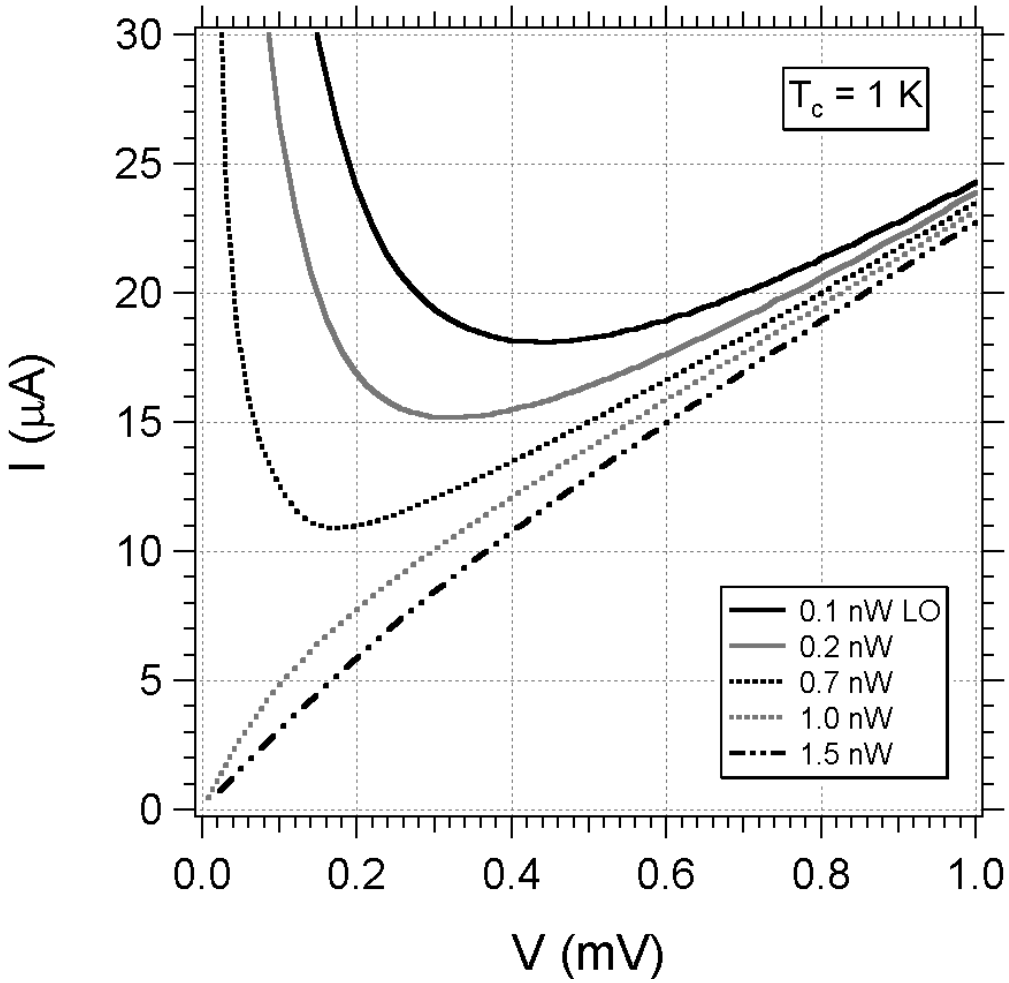

Figure 6.10: Calculated pumped I-V curves for a 1.0 K T_c HEB.

such, the conversion efficiency can be of order unity or greater where the differential resistance is very large or negative. To define an operating regime that more accurately represents the stable bias points accessible with the present experimental setup, a cutoff is placed on the lowest allowable bias voltage. This cutoff is determined from the curvature of the I-V curve, which can be expressed in terms of the self-heating parameter α_0.

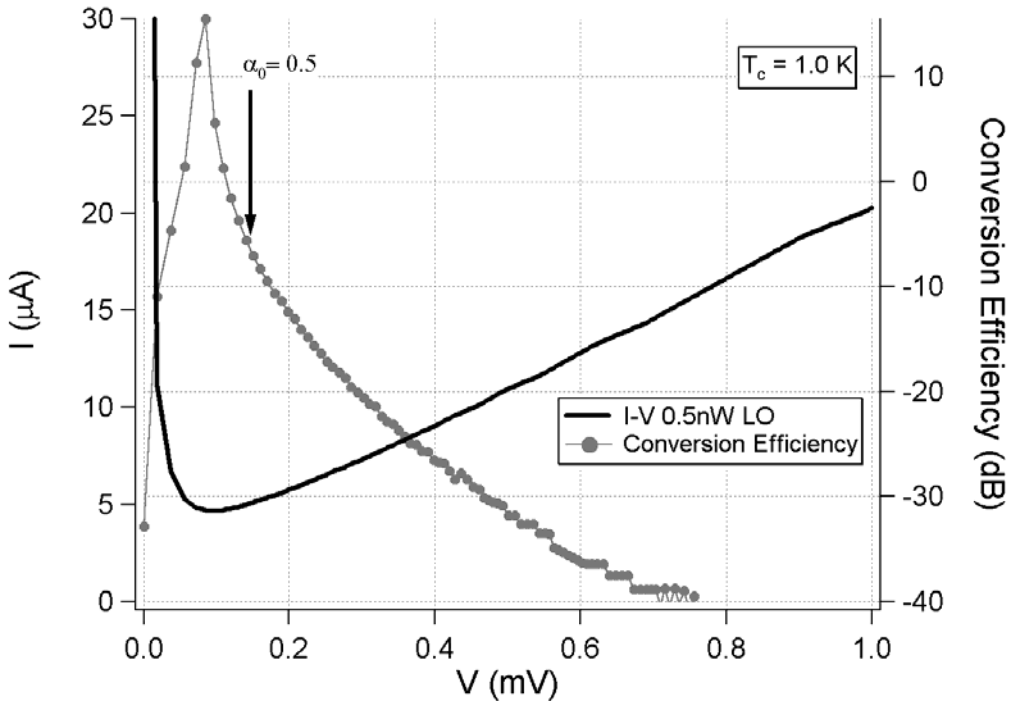

Figure 6.11: Calculated conversion efficiency vs. bias voltage for a 1.0 K T_c HEB. The LO power is 0.5 nW, and the bath temperature is 0.22 K. The arrow indicates the voltage where the self-heating parameter is equal to 0.5. Bias voltages to the left of the arrow are not considered.

Given a particular I-V curve, this parameter can be calculated (Ekstrom et al., 1995) using

$$\alpha_0 = \frac{\frac{dV}{dI} - \frac{V}{I}}{\frac{dV}{dI} + \frac{V}{I}} . \tag{6.1}$$

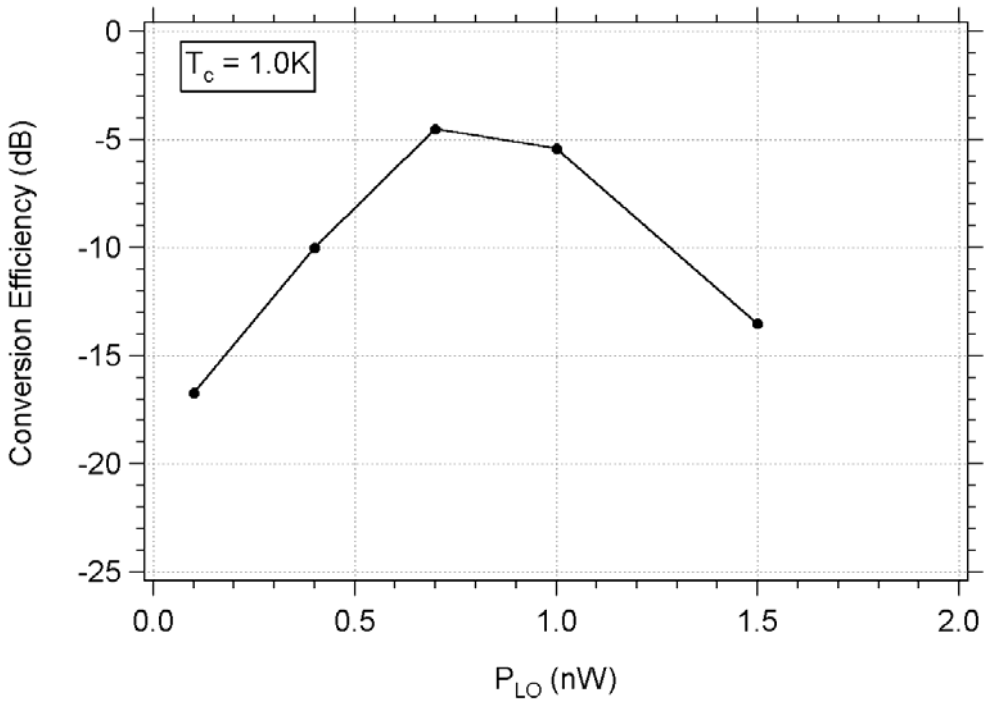

Figure 6.12: Calculated maximum conversion efficiency vs LO power for a 1.0 K T_c HEB.

At high bias voltages, α_0 is nearly zero. As the bias voltage is decreased to the drop-back point, its value increases and approaches 1. In the present experiments, α_0 typically never exceeds 0.5. For values larger than 0.5, some type of instability is observed. For the numerical simulations, bias voltages that correspond to a α_0 value greater than 0.5 are treated as unstable. In Figure 6.11, the cutoff voltage is indicated with an arrow. For 'overpumped' I-V curves, the self-heating parameter typically does not go above 0.5 and all bias points are considered valid.

Having specified which bias points are relevant, the maximum conversion efficiency for each LO power can be determined. In Figure 6.12, the maximum conversion for the T_c = 1.0 K HEB with a narrow transition width is plotted as a function of LO power. The conversion efficiency peaks for a certain LO power, similar to the actual experimental data. The limit on α_0 restricts the maximum mixer conversion efficiency to values of ~ -6 to –8 dB. These predicted values are still a little higher than values obtained experimentally, but nevertheless are a reasonable approximation. The optimum LO power is then calculated for each value of T_c.

6.5 Optimum LO Power vs. T_c

From the experimental data in sections 6.2-6.3, the optimum LO power can be extracted for each type of HEB mixer measured. To compare the values from different devices, the LO power is 'normalized' to that needed for an ideal 50 Ω HEB. From the prediction in Chapter II, the LO power is proportional to 1/R. A 100 Ω device should in theory require ½ the LO power a 50 Ω would if all other parameters were equal. From the experimental values of the LO power, the 'normalized' LO power is obtained by multiplying by 50 Ω /R. In Figure 6.13, the normalized LO power is plotted as a function of mixer T_c. The Al mixers are lumped together as having an optimum LO power of ~ 0.5 nW with ~ 1 K T_c. For Nb Device K, the data points with T_c = 2.4 and 1.4 K are excluded from the plot. Mixer performance is poor in these regimes due to the strong magnetic field. Such performance would not necessarily be observed in HEB mixers that do not require a magnetic field and have T_c ~ 1.5 – 3 K. Also in Figure 6.13, the

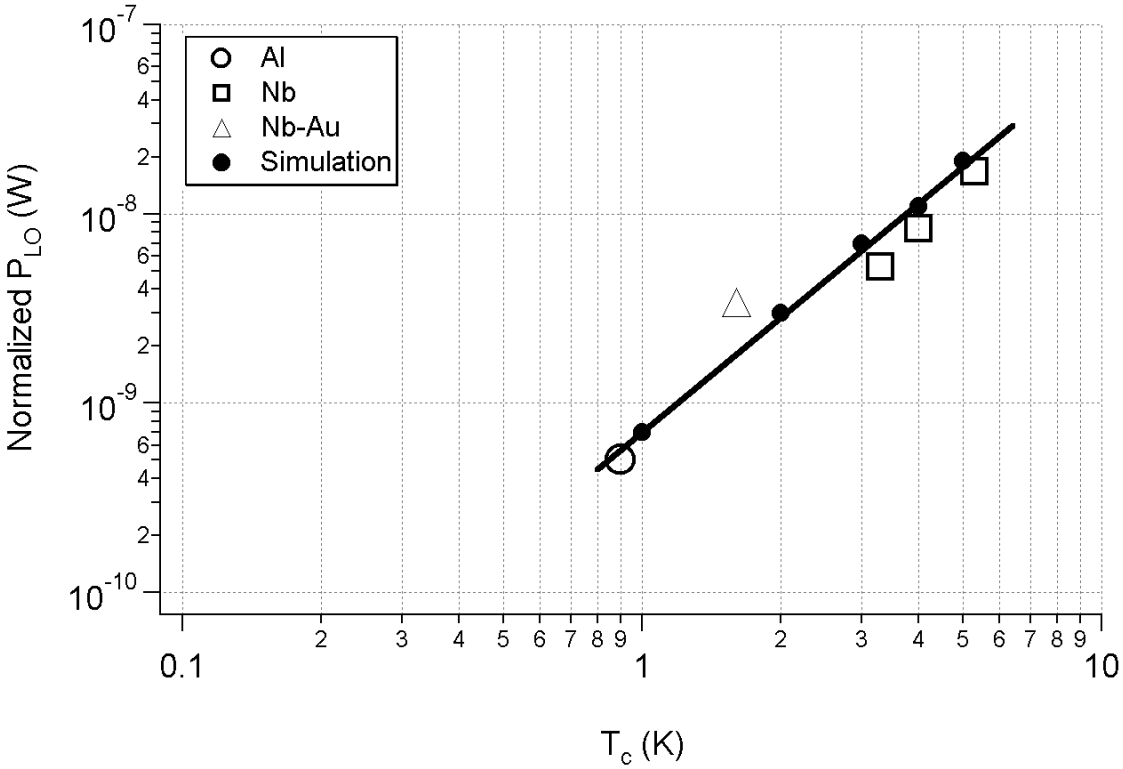

Figure 6.13: Normalized LO power as a function of mixer T_c. The open markers are experimental points and the dark circles with the fitting line are the simulated values.

optimum values of the LO power obtained through the numerical simulations are plotted. The simulations agree quite well with the experimental values of the LO power. Thus for a 50 Ω diffusion-cooled HEB operated with $T_b << T_c$, the LO power is predicted to be,

$$P_{LO} \approx (0.7 \tfrac{nW}{K^2}) \bullet T_c^2 . \tag{6.2}$$

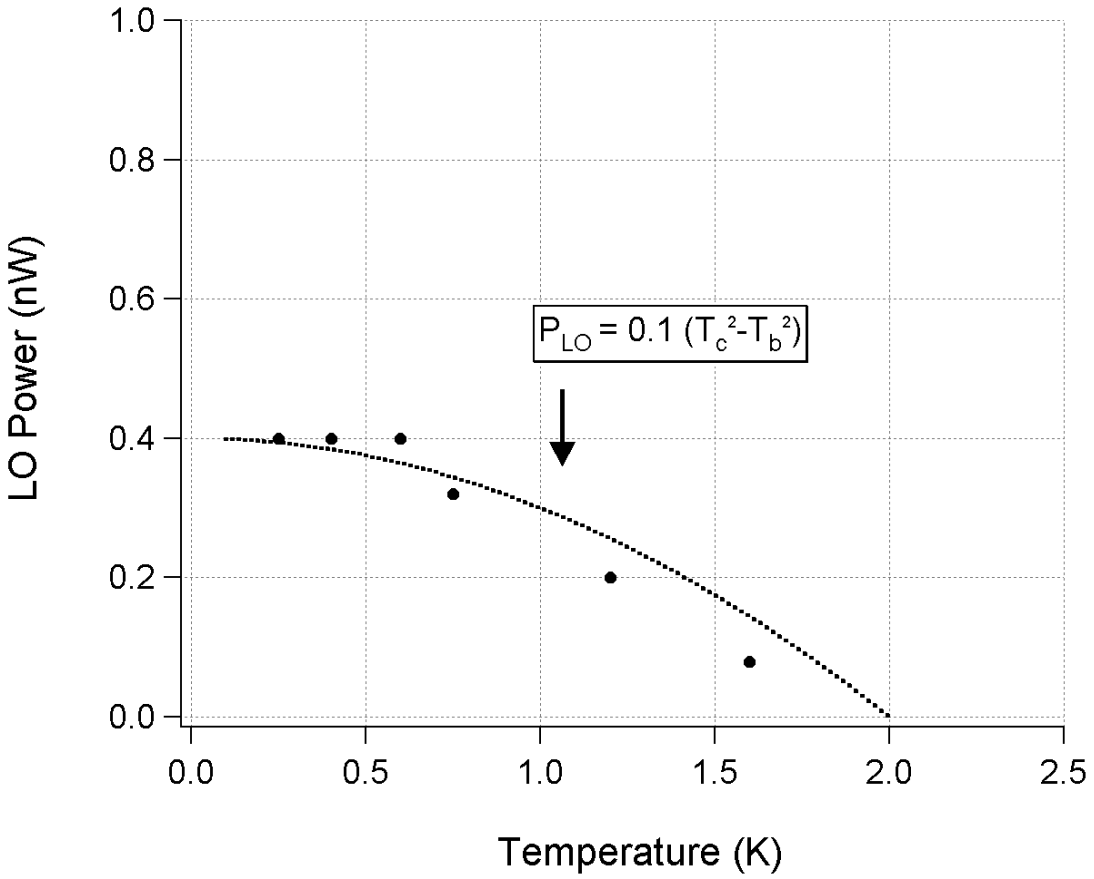

Figure 6.14: LO power vs. bath temperature for Al HEB Device F. The device resistance is 387 Ω and the coefficient on the fitted line has to be adjusted to compare with the value predicted in Equation 6.2. The normalized coefficient is 0.77 which agrees well with the 0.7 prefactor in Equation 6.2.

The LO power scales as T_c^2 as predicted in Chapter II. The numerical coefficient is approximately a factor of two smaller than the rough analytical prediction of Equation 2.63, using the room temperature value of the Lorenz coefficient. Experimental values of the Lorenz constant often differ from the predicted value. For temperatures below the Debye temperature, the Lorenz constant actually decreases (Kittel, 1996). As such, the

agreement with the analytical prediction is reasonably good. Finally, the dependence of the LO power on bath temperature was measured for Device F and the predicted (T_c^2-T_b^2) dependence is observed. This data is plotted in Figure 6.14. When $T_b << T_c$, then the LO power is proportional to T_c^2, and is given by Equation 6.2.

Chapter VII: IF Bandwidth

For practical THz receivers, the mixer element needs to be able to effectively detect an IF signal of a few GHz. This is due to the fact that current THz LO sources cannot be tuned easily, and astronomical observing time is limited. For a given observing run, it is important to be able to study a wide enough frequency window at once rather than a narrow one which would require patching together many scans to obtain one spectrum and such a procedure would be time consuming. In this chapter, measurements of the conversion efficiency as a function of IF are discussed, and values for the IF bandwidth are given. The IF where the conversion efficiency decreases by 3 dB from its maximum value is called the IF bandwidth.

Measuring the conversion efficiency as a function of the IF, and fitting the data to a single time constant roll off determines the bandwidth. This yields the effective bolometer time constant. In combination with information about the device operating point, the relaxation time constant for the electron temperature is calculated. Experimentally obtained values for the relaxation time are compared to calculated diffusion times, and agreement with the diffusion-cooling model is good. The data show that the IF bandwidth is proportional to D/L^2. With the Al mixers, this length scaling is observed but with an upper limit for the bandwidth. This results from the minimum length for a superconducting microbridge imposed by the proximity effect in a N-S-N structure.

In the absence of any limits due to the proximity effect, the thermal relaxation rate sets the IF bandwidth ($f_{-3dB} \sim 1/\tau_\theta$). When the IF is much larger than $1/\tau_\theta$, then the electron temperature cannot be modulated at that frequency. Here, poor conversion results. Using Equation 2.46, the conversion efficiency can in general be expressed in terms of its IF = 0 value and a single time constant τ_{eff},

$$\eta(\omega_{IF}) = \eta(0)\frac{1}{1+(\omega_{IF}\tau_{eff})^2}. \tag{7.1}$$

The effective time constant is equal to the thermal relaxation time of hot electrons in the microbridge, τ_θ, with a few modifications resulting from electro-thermal feedback. Self-heating in the device is included using the parameter α_0. It is necessary to also take into account the stabilizing effect of the passive voltage bias at the IF. Both factors combine to give the following relation, which was previously derived in Equation 2.43,

$$\tau_{eff} = \frac{\tau_\theta}{1+\alpha_0\frac{R-R_L}{R+R_L}}. \tag{7.2}$$

If the IF load resistance is equal to the HEB resistance then the observed time constant is the actual thermal relaxation time. The product $\alpha_0\frac{R-R_L}{R+R_L}$ is simply denoted as α.

In the experiments, τ_{eff} is obtained from the measured frequency dependence of the conversion efficiency and Equation 7.1. Keeping the LO frequency fixed, the RF

power is adjusted at each frequency to maintain a constant power input to the mixer using the procedure described in Chapter IV. The converse, keeping the signal frequency fixed and varying the LO frequency, was also done with nearly the same accuracy. The first method was used to ensure that the I-V did not change shape with LO frequency, and because the LO power in the setup can only be adjusted in 1 dB steps. The bias conditions used are those that yield maximum conversion efficiency. Biasing at a different spot on the I-V curve can increase the bandwidth, although this results in a loss in conversion efficiency and sensitivity (Floet et al., 2000). For diffusion-cooled mixers, there is no degradation of conversion efficiency if ones uses a large IF bandwidth because the bandwidth can be increased by decreasing the length of the bridge or increasing the diffusivity, with no predicted change of conversion efficiency. In Figure 7.1, the conversion efficiency of Al Device H is plotted as a function of IF. The solid line represents a fit to the data using Equation 7.1. For this device, the IF bandwidth is 1.2 GHz. The effective time constant is therefore 133 ps.

From the effective time constant, the thermal time constant τ_θ can be calculated using Equation 7.2. The self-heating parameter is obtained using the values of the resistance and differential resistance at the operating point and Equation 6.1. Assuming an IF load resistance of 50 Ω, α is then calculated. The effective time constant is not very different from the thermal time for devices whose normal state resistance is not very large, typically less than ~ 100 Ω. In these devices, the device resistance at the operating point is close to 50 Ω.

The experimental value of the thermal time constant can then be compared to the predicted diffusion time. In all the devices studied, the dominant mode of cooling hot

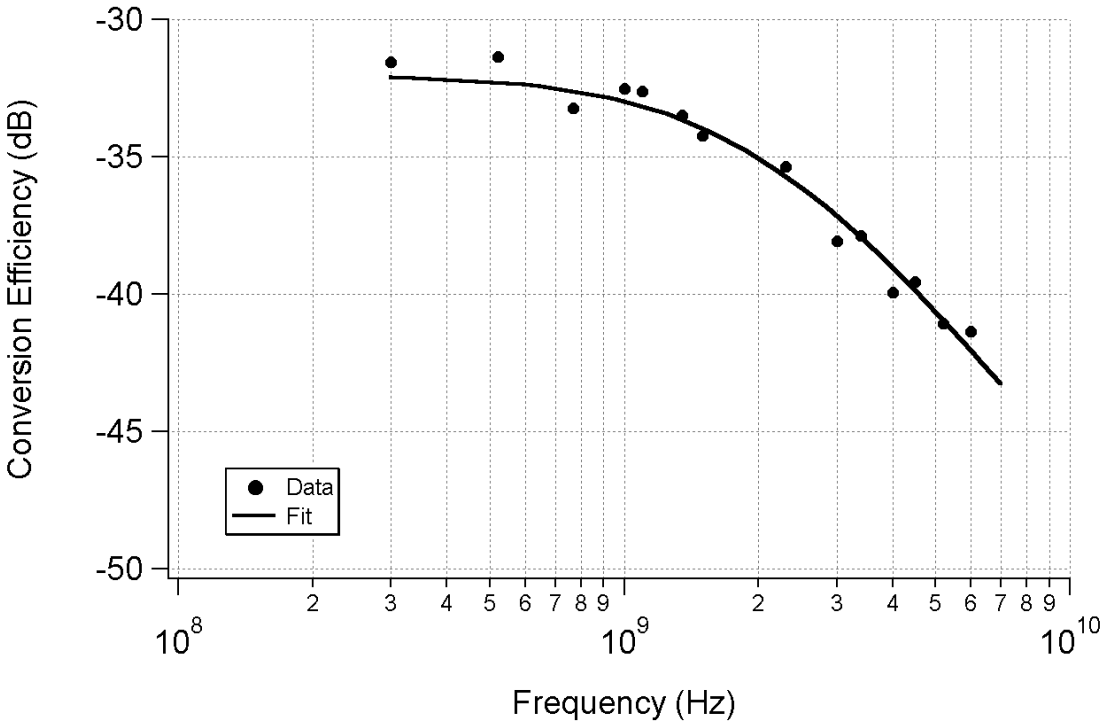

Figure 7.1: Conversion efficiency as a function of IF for Al Device H.

electrons is out diffusion through the contacts. Derived in Chapter II, the average diffusion time for hot electrons in the HEB is,

$$\tau_{diff} = \frac{L^2}{\pi^2 D}. \tag{7.3}$$

Estimating the diffusion time requires knowledge of the diffusion constant. The diffusion constant is measured using the derivative of the upper critical magnetic field with temperature evaluated at T_c. In a normal metal, $D = \frac{1}{3} v_F \ell$ where v_F is the Fermi velocity and ℓ is the mean free path (Kittel, 1996). Using Equation 5.1, the upper critical

magnetic field is related to the coherence length. In a dirty superconductor, the following BCS equations connect the coherence length with the mean free path,

$$\xi(0) = 0.85(\xi_0 \ell)^{1/2}$$
$$\xi_0 = \frac{\hbar v_f}{\pi \Delta(0)}, \Delta(0) = 1.76\, k_b T_c. \tag{7.4}$$

The diffusion constant is thus related to the upper critical field slope through (Gordon and Goldman, 1986),

$$D = \frac{-(4ck_b / \pi e)}{\left.\frac{d(H_{c2})}{dT}\right|_{T_c}}. \tag{7.5}$$

The upper critical field is measured as a function of temperature and approximated as a line near T_c to calculate D. In Figures 7.2a and 7.2b, H_{c2} is plotted as a function of T for Al Device E and Nb-Au Device L. With the diffusion constant and the device length, the diffusion time is calculated. In Table 7.1, the measured IF bandwidth and calculated relaxation times are listed for some Al HEBs and Nb-Au device L. For Al Devices C and H the diffusion constant was not measured but inferred from measurements on devices of comparable resistivity. The data for Nb devices J and K is not listed because the diffusion constant was not measured. The thermal time is in good agreement with the predicted diffusion time. In Figure 7.3, the experimental thermal relaxation time is plotted as a function of the calculated diffusion time. A line of unity slope would

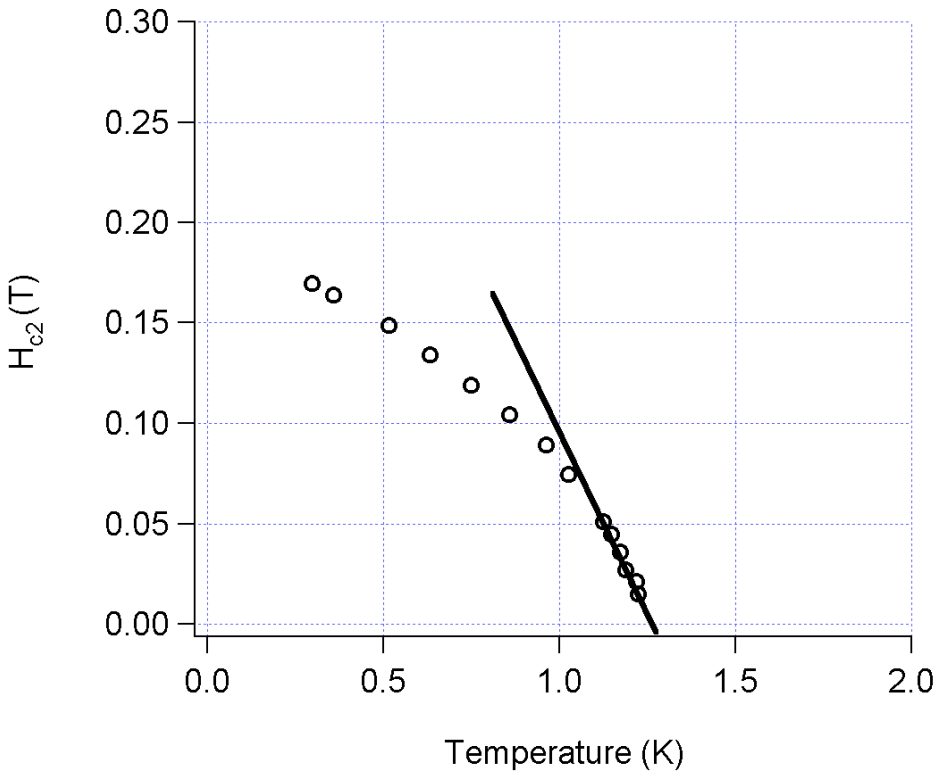

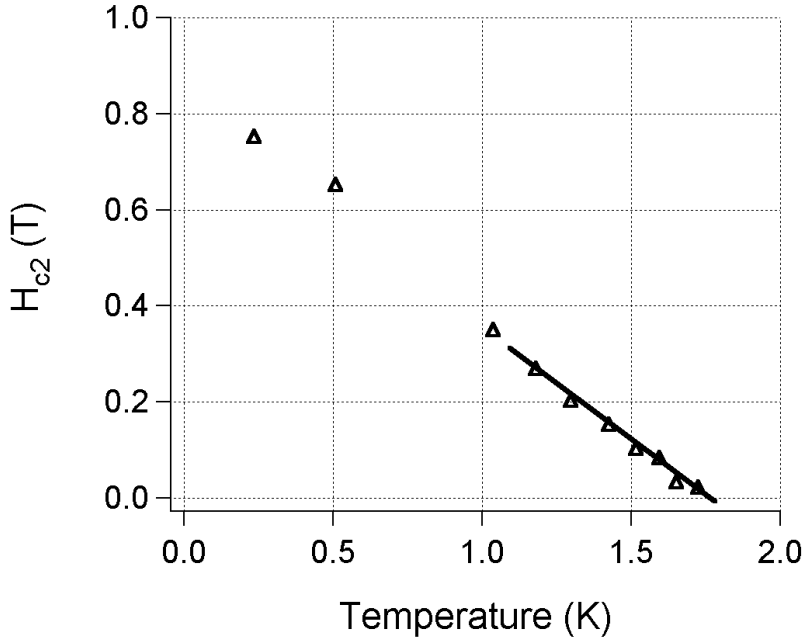

Figure 7.2: Critical magnetic field for Device E (top) and for Device L (bottom) as a function of temperature.

Device	IF BW (GHz)	τ_{eff} (ps)	R (Ω)	dV/dI (Ω)	α_0	α	τ_θ (ps)	L (μm)	D (cm^2/s)	τ_{diff} (ps)
Al -C	6	27	115	169	.19	.075	30	0.3	2.5	36
Al – E	3 +/- 1	53	40	89	.38	-.044	51	0.6	3.5	104
Al – F	2	80	260	750	.49	.33	106	0.6	2.9	125
Al – H	1.2	133	234	353	.13	.20	150	1.0	4.4	230
Nb-Au – L	1.2	133	39	70	.29	-.037	128	0.48	1.3	180

Table 7.1: IF bandwidth for Al HEB mixers C,E,F,H and Nb-Au device L.

indicate perfect agreement with calculations. We see that the thermal relaxation time is proportional to L^2, as expected for diffusion cooling. In contrast, devices based on phonon cooling would have a relaxation time that is independent of length.

In the present work, we have shown that the diffusion cooling prediction, Equation 7.3, is valid for devices other than Nb where L, D, and T_c have been varied. As demonstrated in Figure 7.3, the diffusion cooling model correctly predicts the IF bandwidth for Al and Nb-Au HEB mixers with $T_c < 5$ K. Previous work on $T_c \sim 5$-6 K diffusion-cooled Nb HEBs has demonstrated a $1/L^2$ dependence for the IF bandwidth (Burke et al., 1999). These devices had approximately the same T_c and D. The Al devices measured have both different length and diffusivity. For example, Devices E and F have the same length but different diffusion constant. Devices C and F have different lengths but similar diffusion constants. Nb-Au Device L is a different material than Al or pure Nb. Its diffusivity is approximately that of a Nb device but with a much lower T_c.

The bandwidths of Nb Devices J and K were also measured. The results were comparable to Burke's original data (1997) and unchanged upon applying a field. All these devices exhibit a relaxation time that is consistent with Equation 7.3. Consequently, the IF bandwidth of a diffusion-cooled HEB mixer depends only the diffusion constant and the length, and not explicitly on device T_c, so long as end effects (see below) are not significant.

Since the IF bandwidth is proportional to $1/L^2$, shorter devices have broader bandwidths. However, the microbridge length cannot be decreased without bound. For very short Al microbridges with normal contacts, no superconducting transition is observed. Thus, the minimum length for superconductivity places a maximum limit on the IF bandwidth for a true N-S-N HEB. Furthermore, the bridge length needs to be a little larger than this minimum length or otherwise the devices are only weakly superconducting and have poor conversion efficiency. Based on the Al mixing measurements, the minimum length for superconductivity appears to be ~ 6-7 $\xi(0)$. Let us assume the shortest microbridge length is 10 $\xi(0)$ to have a mixer with good conversion. The IF bandwidth can be calculated using Equation 7.3, expressing the diffusion constant in terms of $\xi(0)$ using Equation 7.4. If the estimate of the minimum length from the Al measurements holds true for other materials, then the maximum IF bandwidth is,

$$\text{Max IF Bandwidth} = (8\ \text{GHz}/\text{K}) \bullet T_c . \tag{7.6}$$

This result only depends on T_c since ξ^2 and D are both proportional to the mean free path ℓ. A limit on the bandwidth is only observed with Al HEB mixers with normal contacts.

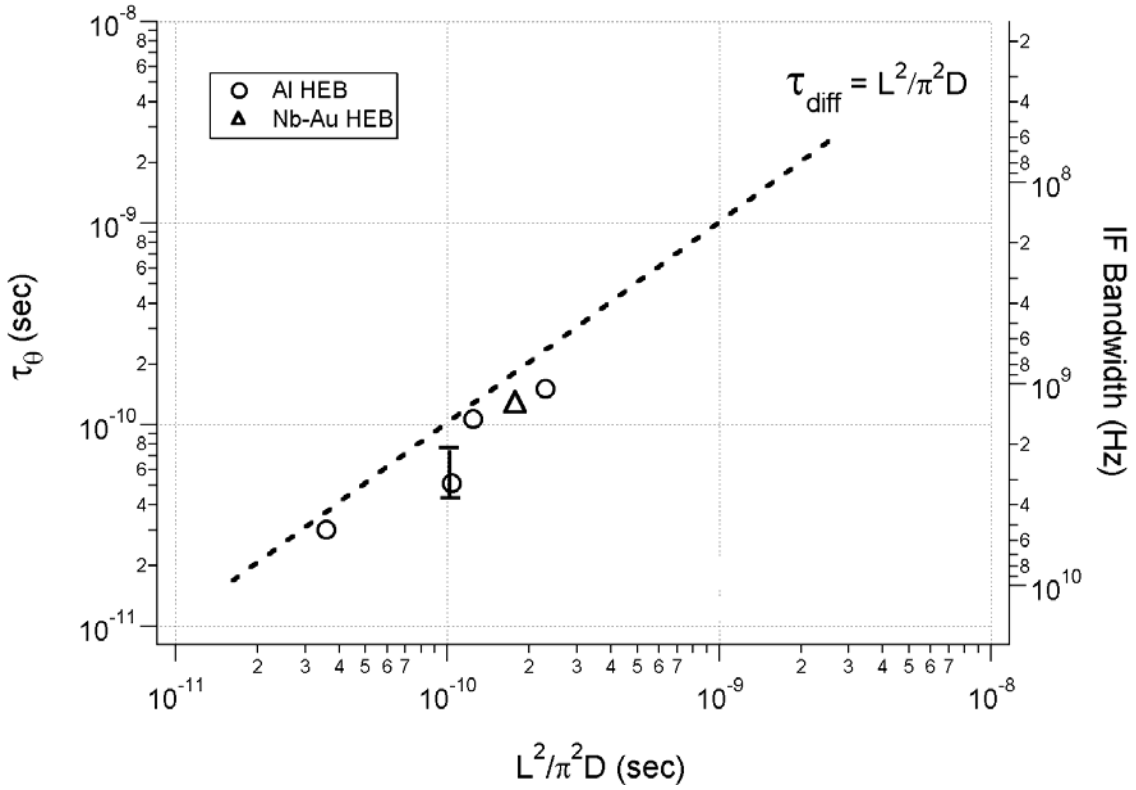

Figure 7.3: Thermal relaxation time and IF bandwidth as a function of calculated diffusion time.

For example, Device B never becomes superconducting. From a simple diffusion time calculation, this device should have an IF bandwidth of ~ 10.5 GHz. Devices with weakly superconducting contacts are not subject to this limit since they do not have any normal edges at the ends of the microbridge. The Nb and Nb-Au HEBs both fit into this category. The Nb film thickness in these samples is larger than the superconducting coherence length, and the normal pads do not induce resistance in the microbridge edges. Also, even if the Nb and Nb-Au devices had purely normal contacts, the maximum bandwidth would be greater than 10 GHz, which is more than sufficient for practical

applications. From the point of view of IF bandwidth, it is advantageous to have a HEB with slightly superconducting contacts. It is not clear, however, if superconducting contacts affect the noise performance. This is discussed in the next chapter.

Chapter VIII: Mixer Noise

Mixer input noise is a measure of the ultimate sensitivity of a heterodyne system since the equivalent noise power at the input determines how weak a signal the mixer can detect. In the microwave measurements, the mixer noise of the HEB is calculated from the output noise power and the conversion efficiency. The output noise is the noise power of the mixer measured in the IF band with LO power applied, and dividing by the conversion efficiency yields an input noise figure. Typically, the noise power per unit bandwidth at the mixer input is divided by k_b and expressed as a temperature. The mixer noise temperature (T_M) can therefore be thought of as the temperature of an ideal Johnson resistor at the mixer input with an output power of k_BT per unit bandwidth, the usual expression in the Rayleigh-Jeans limit. If the energy associated with quantum zero point fluctuations (hf/2) become a significant contribution to the mixer noise, then the Callen-Welton expression is needed to equate power and temperature (Kerr et al., 1997), though this is not the case in the present work.

Two experimental quantities are needed to calculate T_M – the conversion efficiency and T_{output}. In Chapter VI, the conversion efficiency is presented in Tables 6.1-6.3. Data for the mixer output noise is presented in this chapter, and used in combination with the results of Chapter VI to obtain T_M. The mixer output noise is measured between 1 and 2 GHz in a frequency window that is 5 % of the IF. Typically, measurements are made in a ~ 50 MHz wide band near 1 GHz and a ~ 75 MHz wide band near 1.5 GHz. Care is taken when choosing the IF to ensure that noise from spurious signals originating

from wireless communication equipment does not affect the measurement. The noise power is detected on a diode detector. Noise measurements are made as a function of bias voltage with the optimum LO power for conversion applied. Similar to the plots of conversion efficiency versus bias voltage in Chapter VI, the output noise is measured as a function of bias voltage. T_M is obtained by dividing the T_{output} by twice the conversion efficiency. The factor of two is inserted to obtain a double sideband noise temperature, which is then readily comparable to other mixer technologies.

T_M is observed to be approximately proportional to T_c. Devices with lower T_c have a lower noise temperature. Al HEB mixers have the lowest T_c and the lowest noise of all the devices measured. Nb-Au mixers with $T_c = 1.6$ K have the next lowest mixer noise. For the Nb HEBs in a magnetic field, a decrease in mixer noise is observed only for applied fields up to 1.5 T. Although the output noise temperature decreases with increasing magnetic field in all cases, operating with $H > 1.5$ T reduces the conversion efficiency and the mixer noise degrades. Variation is seen from device to device in noise temperature, and the fabrication details that affect HEB performance have not been fully characterized yet. Using data for the noise temperature seen on average in the microwave studies, T_M is approximately 25 times T_c.

In Chapter II, T_M is predicted to be proportional to T_c when thermal fluctuations dominate. In typical operation, the thermal fluctuation noise is larger than Johnson noise. However, there is a discrepancy between the theoretical prediction and the experimental results with respect to the constant of proportionality. The theory predicts that that T_M should be $\sim 8/\pi$ times T_c. Experimentally, however, the mixer noise temperature is ~ 10 times larger than this prediction. This difference cannot be explained through

experimental error. The output noise temperature is measured to better than 1 K accuracy and for the conversion efficiency, a maximum error of 2 – 3 dB is possible. To have agreement between theory and experiment, the error in the conversion efficiency measurement would have to be 8 dB. In light of this discrepancy, numerical simulations are used to predict the thermal fluctuation noise, entertaining the possibility that a fully distributed element model might yield better agreement with the experimental data. The results of the numerical simulations also predict a noise temperature only a few times larger than T_c. Thus, either the theoretical models do not accurately account for the magnitude of the thermal fluctuation noise or there are other temperature dependent noise sources present.

8.1 Al HEB

The output noise temperature of an Al HEB at the operating point is typically less than 10 K. In Figure 8.1, the output noise is plotted as a function of bias voltage for Al Device D. The conversion efficiency for this same device was discussed in Section 6.2. The maximum output noise is measured under the same conditions that yielded the maximum conversion efficiency. Data for two different operating magnetic fields are given in Figure 8.1. The maximum conversion efficiency in both fields is nearly the same, -10 dB for 0.05 T and -11 dB when 0.12 T is applied. The output noise is, however, quite different. For the larger applied field, the output noise is approximately 13 K lower. For Device D, it is likely that the 0.05 T field is not sufficient to fully

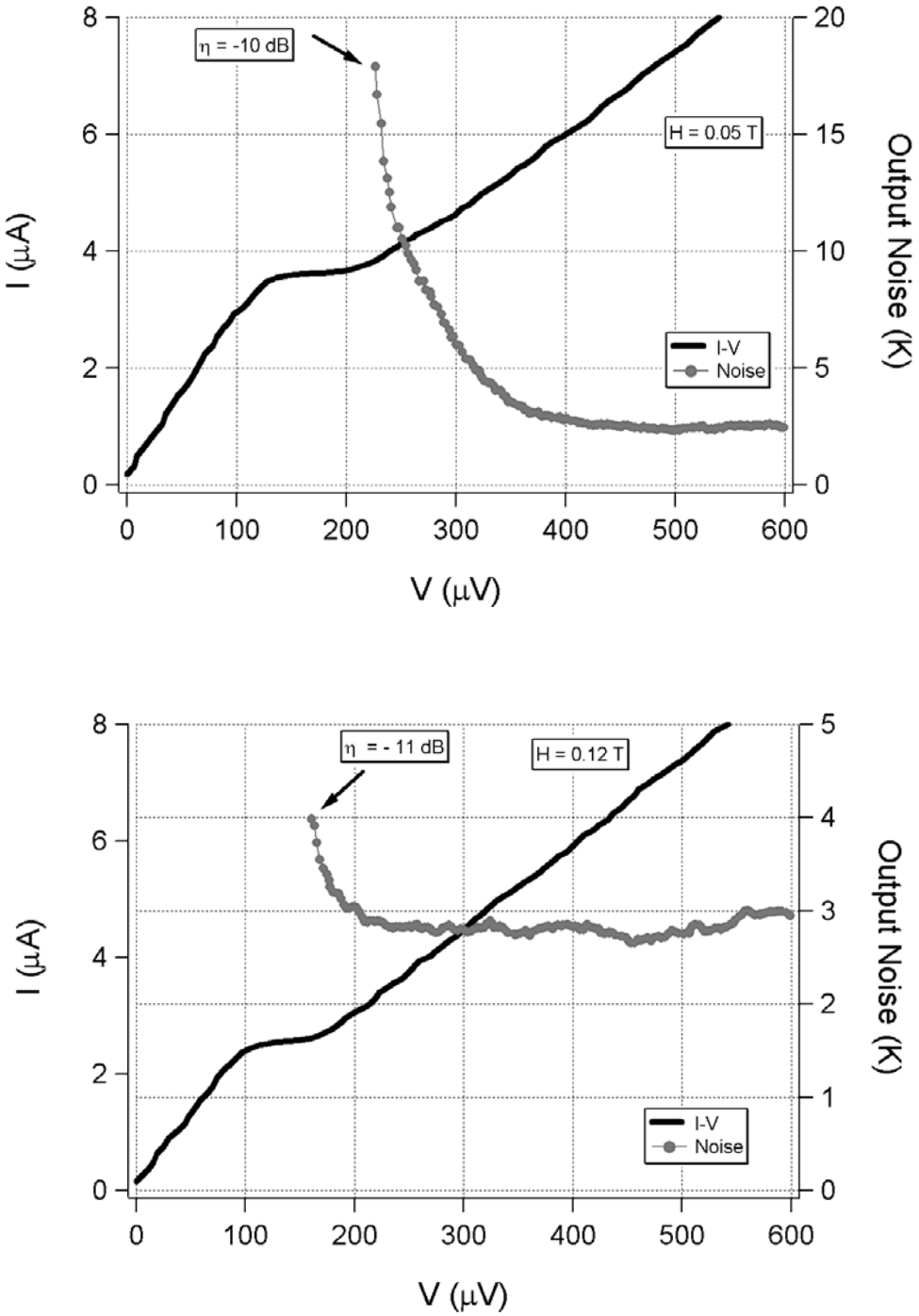

Figure 8.1: Output noise temperature as a function of bias voltage for Device D. The upper plot is for H = 0.05 T and the lower one for H = 0.12 T.

suppress the Josephson effect. With no applied field, the output noise displays peaks that are ~ 100 K or more in amplitude with a spacing in voltage of hf/2e. Once superconductivity in the contact pads has been suppressed, the output noise does not vary strongly with magnetic field so long as T_c is not significantly suppressed. For the H = 0.12 T case, the double sideband mixer noise temperature of Device D is 25 K.

Data for the mixer noise of other Al HEBs is given in Table 8.1. All the values listed are those measured in a magnetic field. The value of T_M reported is measured at IF = 1 or 1.5 GHz. For all the HEBs measured in this thesis, the IF conversion bandwidth is larger than 1 GHz. Only the L = 1.0 μm Al devices and Nb-Au Device L have a conversion bandwidth that is comparable to 1 GHz. The noise bandwidth for a HEB, as discussed in Chapter II, is larger than the conversion bandwidth $1/(2\pi\tau_\theta)$. As a result, the noise temperature measured for Device G at IF = 1.5 GHz is nearly the same as that

Al HEB Device	L (μm)	T_b (K)	H (T)	T_c (K)	Conversion Efficiency (dB) (IF =1 or 1.5 GHz)	T_{output} (K)	T_M (K,DSB)
D	0.6	0.22	0.12	0.8	-11	4	25
E	0.6	0.25	0.12	0.9	-8	1.3	4
F	0.6	0.25	0.30	1.6	-16	1.6	32
G	1.0	0.22	0.12	1.2	-12	13.3	105

Table 8.1: Mixer noise for Al HEB mixers. A magnetic field is used to drive the contact pads into the normal state.

measured at 500 MHz. Consequently, no adjustments have been made in T_M to extract a IF = 0 value for any of the mixers. The noise temperatures of Devices G and E and anomalously large and small, respectively, when compared to other devices. For Al HEBs with $T_c \sim 1$ K, T_M is approximately 20 – 30 K, DSB.

8.2 Nb HEBs in a Magnetic Field

Similar to the Al measurements, the output noise is measured as a function of bias voltage for the Nb mixers. In Figure 8.2, output noise data is shown for Nb Device J. In

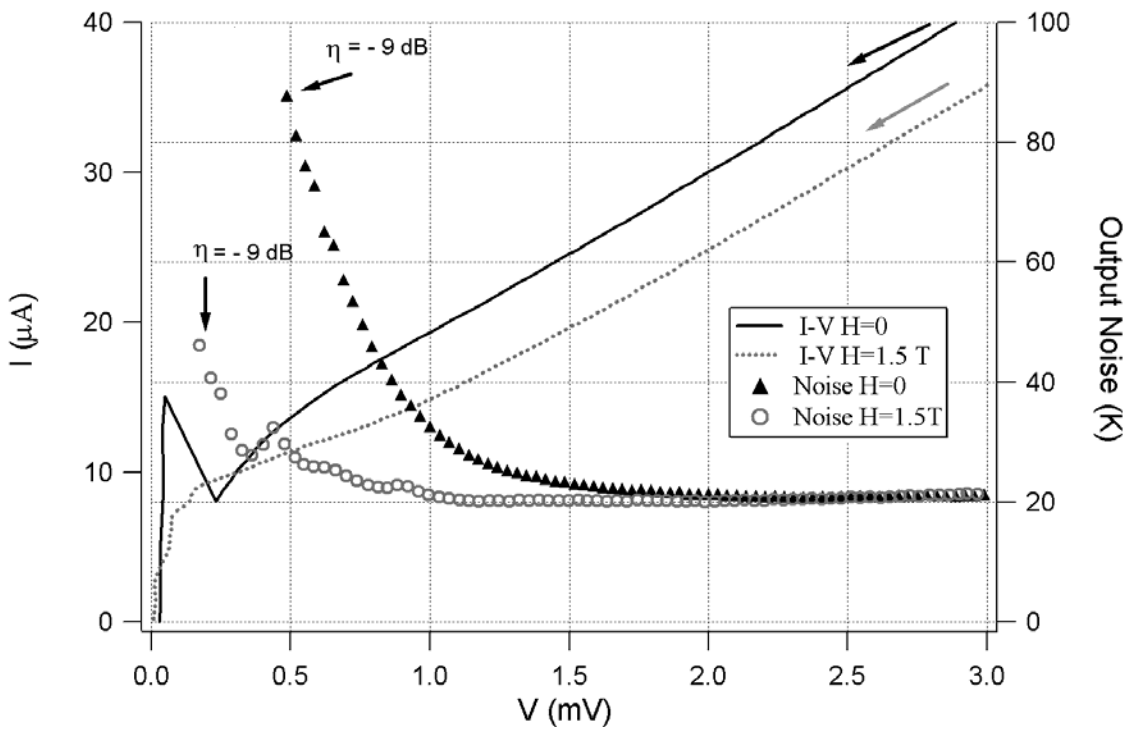

Figure 8.2: Output noise temperature as a function of bias voltage for Nb Device J for H = 0 and H = 1.5 T.

Chapter VI, a conversion efficiency of –9 dB was reported for this device in both zero magnetic field (T_c = 5.2 K) and H = 1.5 T (T_c = 2.4 K). The output noise plotted in Figure 8.2 is measured with the same LO power applied as used in the conversion measurement. At the bias point where the conversion is –9 dB, the output noise decreases from 88 K to 46 K as T_c is lowered from 5.2 to 2.4 K. Since the conversion is the same in both cases, the mixer noise temperature also drops proportionally from 390 K, DSB to 171 K, DSB. For Device K, a similar drop in mixer noise is observed from 160 K, DSB to 88 K, DSB when T_c is reduced from 5.3 K to 3.3 K. Therefore, T_M for Nb HEBs decreases nearly linearly with T_c as T_c is lowered to approximately down to ~ 3 K.

Further reduction in T_c requires applying a stronger magnetic field. For field strengths greater than 1.5 T, the linear drop in mixer noise is no longer observed. As a function of magnetic field, the output noise of the Nb mixers always decreases with increasing field. In Figure 8.3, the output noise for Device K is plotted as a function of T_c. At each value of T_c, the output noise is measured at the point of best conversion. For T_c = 5.3, 4.0, and 3.3 K, this is –11 dB. Poorer conversion is observed for T_c = 2.4 and 1.4 K, and hence T_M is higher for these operating conditions even though the output noise is smaller. In Figure 8.4, T_M is plotted for both Devices J and K as a function of T_c. The technique of applying a magnetic field to reduce T_c of Nb HEBs appears to yield a maximum reduction of ½ in T_M. The noise temperature of Device K is typical of a Nb HEB operated for optimum conversion efficiency for comparison with the other mixers discussed. Thus the Nb HEB has T_M ~ 160 K, DSB which can at best be reduced to 88 K, DSB. The noise properties of both Nb devices are summarized in Table 8.2.

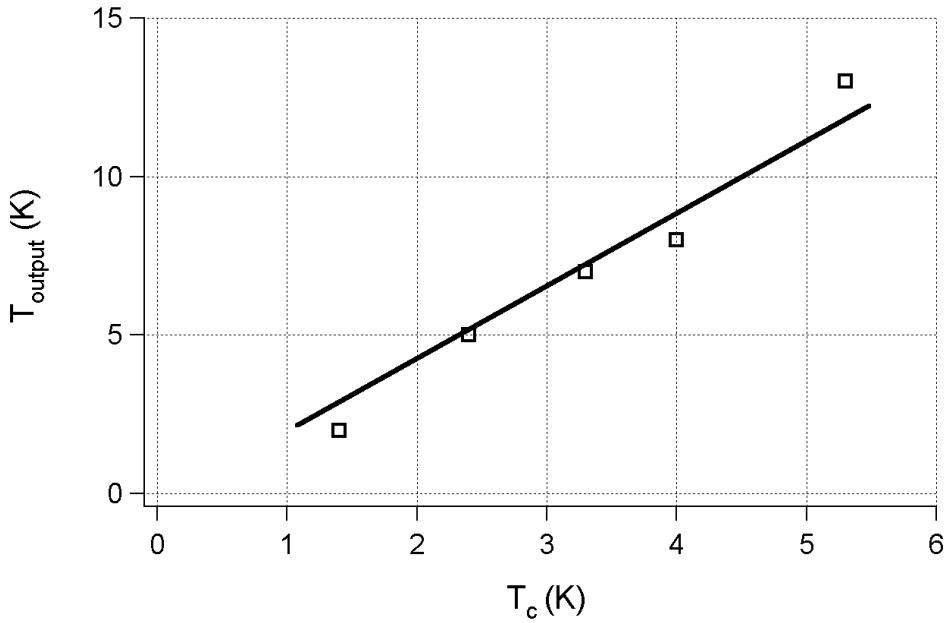

Figure 8.3: Output noise for Device K as a function of T_c. The output noise is measured at the point of maximum conversion for each value of T_c.

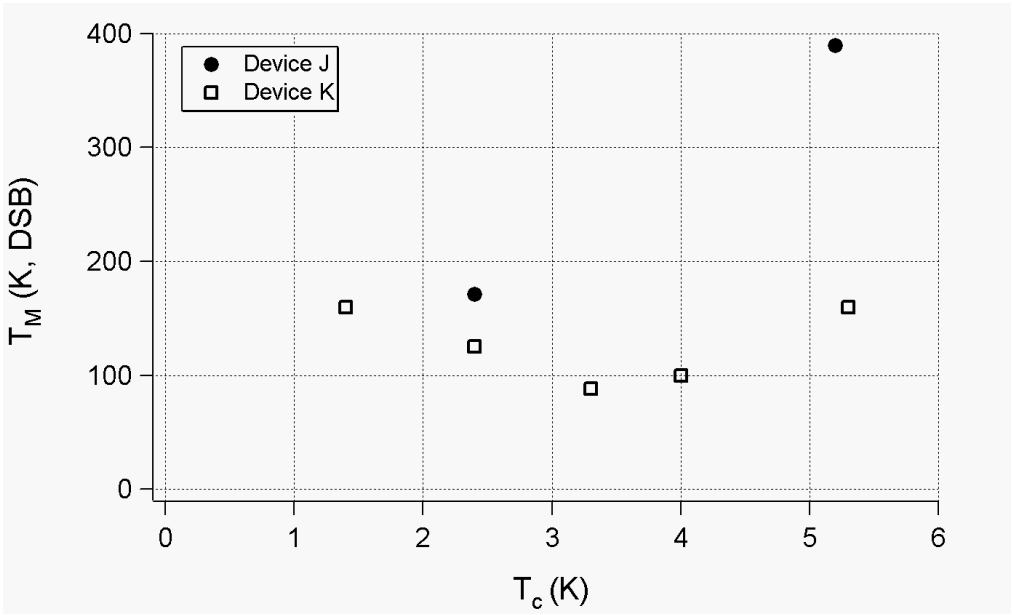

Figure 8.4: Mixer noise temperature for Devices J and K as a function of T_c.

Nb HEB Device	L (μm)	T_b (K)	H (T)	T_c (K)	Conversion Efficiency (dB) (IF =1 or 1.5 GHz)	T_{output} (K)	T_M (K,DSB)
J	0.16	0.22	0	5.2	-9	88	390
			1.5	2.4	-9	46	171
K	0.24	0.22	0	5.3	-14	13	160
			1.0	4.0	-14	8	100
			1.5	3.3	-14	7	88
			2.0	2.4	-17	5	125
			2.5	1.4	-22	2	160

Table 8.2: Mixer noise for Nb HEB mixers measured in a magnetic field.

8.3 Nb-Au HEB

The output noise as a function of bias voltage for Device L is plotted in Figure 8.5. At the operating point with maximum conversion efficiency, the output noise is 3.3 K at IF = 1.5 GHz. Dividing by twice the conversion efficiency at the same IF gives a mixer noise temperature of 47 K, DSB. The noise data is summarized in Table 8.3. T_M for Nb-Au with T_c = 1.6 K is lower than that achievable with pure Nb in zero field or any finite field. It is not lower than that of Al devices. The real advantage of Nb-Au mixers

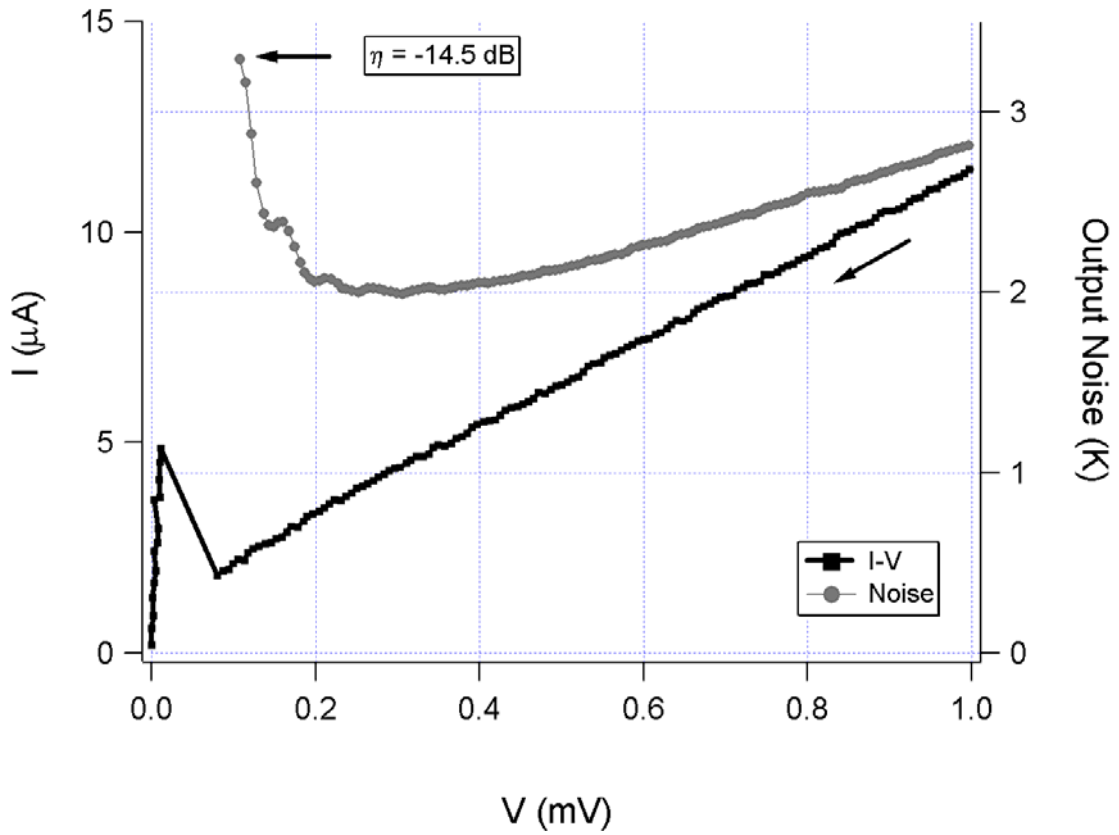

Figure 8.5: Output noise as a function of bias voltage for Nb-Au Device L.

over Al HEBs will be discussed in the next chapter where saturation effects are described.

Nb-Au HEB Device	L (μm)	T_b (K)	H (T)	T_c (K)	Conversion Efficiency (IF =1 or 1.5 GHz)	T_{output} (K)	T_M (K,DSB)
L	0.48	0.22	0	1.6	-14.5	3.3	47

Table 8.3: Mixer noise for Nb-Au Device L.

8.4 Numerical Simulations of Thermal Fluctuation Noise

In Figure 8.6, the typical mixer noise temperature of the three types of HEBs measured is presented as a function of T_c. The experimental values of the mixer noise temperature plotted in Figure 8.6 are considerably larger than predicted by the analytical model. Numerical calculations were carried out to obtain better agreement with the experimental data. Output noise due to thermal fluctuations is calculated at various bias points in the calculated conversion efficiency vs. bias voltage curves in Section 6.4. Using the output noise and the conversion efficiency, the mixer noise is predicted. T_M is calculated for different bias voltages corresponding to a conversion efficiency ranging from –8 dB to –15 dB. The procedure is repeated for T_c = 1, 3, 5, 7 and 10 K. In Figure 8.7, the calculated values of T_M are plotted as a function of T_c. The different traces represent different bias voltages that result in different conversion efficiencies. In all

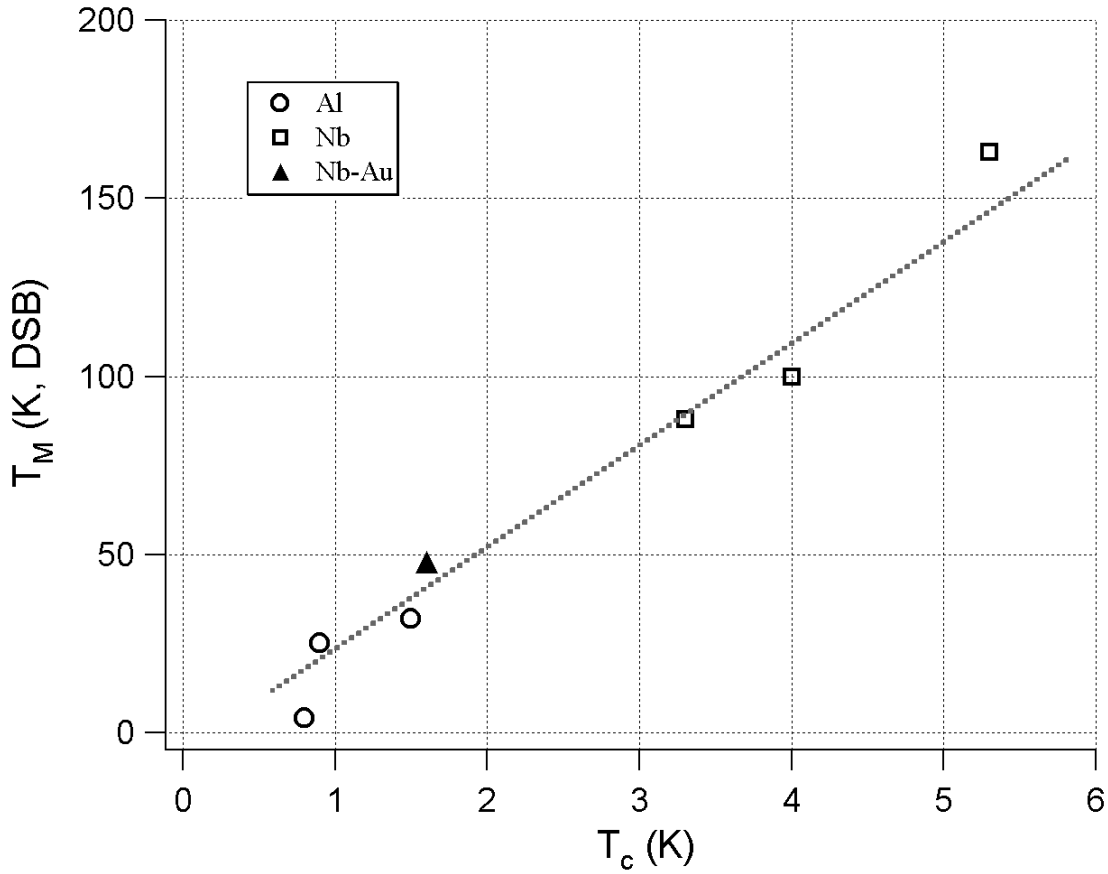

Figure 8.6: Mixer noise temperature as a function of T_c typical of Al, Nb in a magnetic field, and Nb-Au mixers. Data for Devices G, J, and K with H > 1.5 T are not included.

cases, the contribution of thermal fluctuations scales linearly with T_c. For conversion efficiency ~ -8 to – 10 dB, comparable to experimental values, the calculated output noise is much smaller than observed in experiment. The magnitude of the noise temperature is still much smaller than observed experimentally, even if operating with poor conversion efficiency. Consequently, it is not understood at present why the experimentally inferred noise temperature is much larger than predicted.

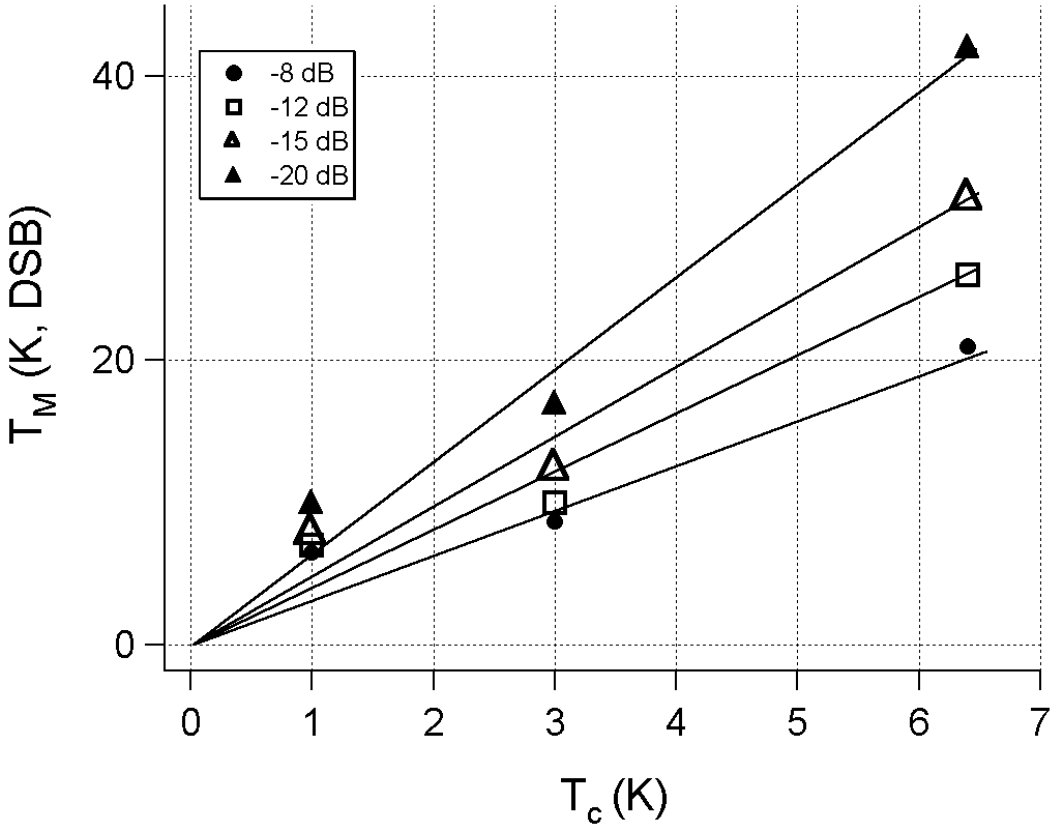

Figure 8.7: Calculated mixer noise temperature as a function of HEB T_c. Shifting the bias voltage away from the optimum operating point to obtain lower conversion efficiency generates the different traces. The deviations from linearity at T_c = 1 K are due in part to a lack of resolution in the calculated data near the operating point.

8.5 Excess Noise

The disagreement between predictions of the HEB noise temperature based on thermal fluctuations and Johnson noise and actual experimental results suggest that other

possible noise sources should be considered. The existence of noise in excess of thermal fluctuation and Johnson noise has been shown with Nb HEBs (Burke et al., 1998) in measurements of the output noise as a function of IF. According to theory, the thermal fluctuation component of the output noise should significantly decrease when the IF is much larger than $1/\tau_\theta$, leaving only Johnson noise. Burke et al. found that at high frequencies, the output noise is frequency independent but its magnitude is many times larger than that of Johnson noise. The origin of this excess noise is not known, although it must be mentioned here that the magnitude of Johnson noise predicted by the present theory assumes equilibrium conditions which validate the use of classical equipartition and the fluctuation-dissipation theorem. The HEB is not a simple resistor in thermodynamic equilibrium at a fixed temperature, and a more rigorous treatment is needed to accurately describe Johnson noise in such a device. Additionally, in the present work it has been shown that the structure of the HEB is more complicated then simply a N-S-N structure. As such, the presence of superconductivity in the contacts may have an effect on the noise performance. For example, in L = 1 μm Al devices, greater output noise is observed when the contacts are in the superconducting state. In these devices, no signs of Josephson conductivity are present and the mechanism giving rise to this additional noise is worthy of further study. It is possible that the excess noise observed in the Nb measurements is due to the contacts being superconducting. Devices with fully normal contacts can be designed in a couple of different ways. For one, the wide contacts pads can be ion milled at an angle to reduce their thickness relative to the microbridge. When thick normal-metal is deposited on top of them, they should be forced into the normal state by the proximity effect. Additionally, patterning only a

narrow microbridge and contacting it directly with thick normal metal contacts can avoid wide contacts all together. This requires more sophisticated lithography than used to produce the devices tested, but is possible with current equipment. To accurately model the noise performance of HEB mixers, further work is needed to better understand the noise mechanisms in a HEB mixer.

Chapter IX: Saturation Effects

In any receiver, the RF signal to be studied is accompanied by background noise from various sources. Background noise is generated from radiation from objects in the sky and from thermal radiation from different parts of the receiver. Performance degrades in any mixer if the input noise power is too large. A large input power heats the mixer and shifts it from optimum operating conditions. In the microwave measurement setup, care is taken to reduce thermal background noise through the use of cryogenic attenuators and other microwave components. Additionally, mixing measurements are made using a RF signal power that is at least two orders of magnitude smaller than the LO power. Therefore, the mixing data presented up to now does not exhibit any saturation effects.

If, on the other hand, a large noise background is present, then two modes of saturation – input saturation and output saturation – are possible. Saturation at the input port typically occurs when the background noise power becomes a sizable fraction of the LO power. In this case, the noise power heats the device and reduces the LO power needed to heat the HEB to the most sensitive part of the R vs T curve. But lowering the LO power reduces the conversion efficiency and thus increases the mixer noise. Background noise can also be down-converted in frequency by the mixer to generate a noise voltage at the IF. If this noise voltage is large enough, it can shift the bias point far enough away from the optimum point so that the average mixer performance is poorer.

Both input and output saturation effects are due to RF power absorption that result in a degradation of mixer performance.

It is important to characterize the input noise power needed to saturate the HEB since background noise is present with the signal. HEB mixers with lower T_c saturate more easily. This motivates the concept of an optimum T_c. Using the data presented up till now, the best performance should seen in devices with the lowest possible T_c since these would have the lowest mixer noise and require the least LO power. However, since saturation effects exist, T_c cannot be lowered indefinitely. For low enough T_c, background noise is sufficient to result in an increase in mixer noise due to saturation, and offset any improvements achieved by lowering T_c. It is also observed that if the edges of the microbridge are normal due to proximity effects, then saturation effects are stronger. For this reason Al mixers are not practical for most applications. However, Nb-Au devices with $T_c \sim 2$ K do not exhibit strong proximity effects and have a T_c slightly higher than Al. It will be shown that a Nb-Au device with this T_c should work well in most astronomical applications. Another nice feature about these devices is that the mixer T_c, in principle, can be easily tuned in the Nb-Au material system, allowing for the use of devices with higher T_c in applications with a larger noise background noise. Approximations are made for the noise power that results in saturation effects as a function of T_c. These relations can be used as a guideline for deciding the optimum mixer T_c for a given application.

9.1 Input (RF) Saturation

When background noise is incident on the HEB, it heats the electrons in the microbridge. Applying the optimum LO power in conjunction with the background radiation 'overpumps' the mixer. One way to see this is to think of the HEB as being biased at the sharpest part of the R vs. T transition when no background radiation is present. The LO power needed to achieve this bias condition is the optimum LO power. In the presence of background noise, the operating point shifts to a higher temperature and a larger mixer noise temperature is obtained since dR/dT is smaller. The LO power can be decreased to bias again at the sharpest point of this transition, but this does not recover the lowest mixer noise since $T_M \propto 1/P_{LO}$. Even though the mixer operating point is on the sensitive part of the R vs. T curve, a smaller LO power is applied and the noise temperature is higher. To estimate how sensitive the mixer is to input saturation, the dependence of T_M on P_{LO} has to be investigated. In Figure 9.1, T_M for Al Device F and Nb-Au device L are plotted as a function of LO power. There is a range of LO power centered around the optimum value for which T_M does not change greatly. For larger deviations in LO power, the noise temperature increases. For Nb-Au Device L, the LO power can be ~ 2 – 4 nW with T_M ~ 50 K. As a design guide, we can postulate that an increase in noise temperature is observable when the LO power is decreased by 20% from the optimum value. Nb-Au has a wider operating range but typically a 1 dB (20%) decrease in P_{LO} does have some appreciable effect on T_M. Therefore, the background noise power at which input saturation occurs is approximated as 0.2 $P_{LO.}$ Using the results of Chapter VI, this corresponds to

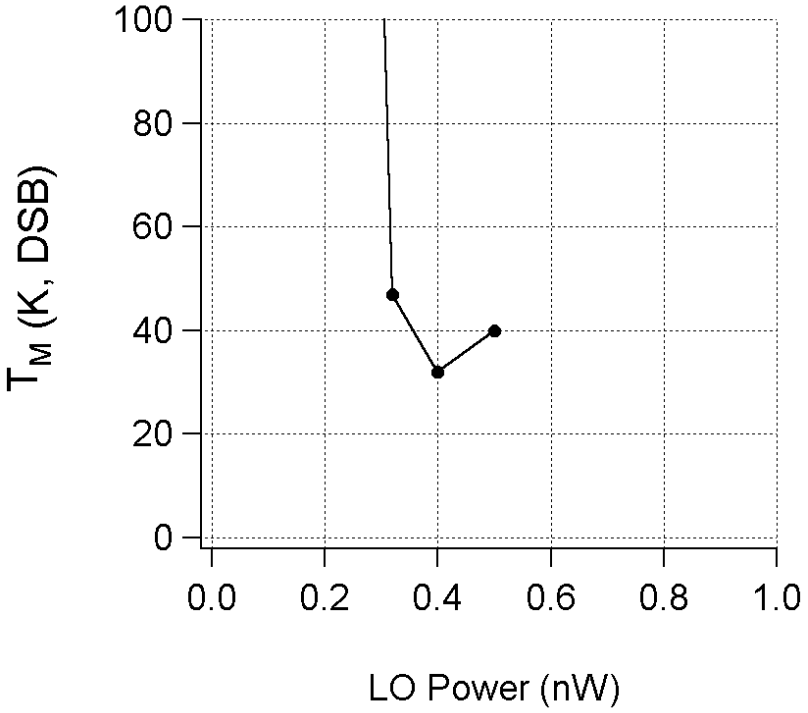

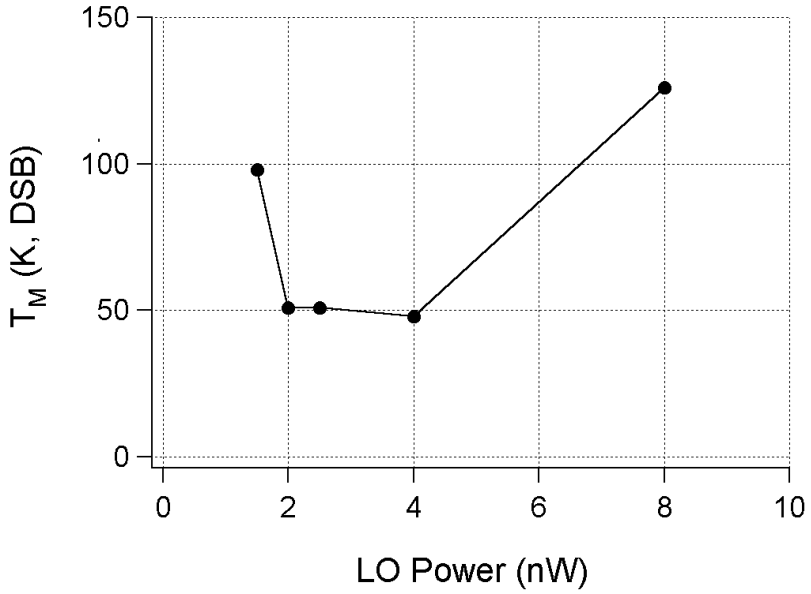

Figure 9.1: Mixer noise temperature as a function of LO power for (top) Al Device F and (bottom) Nb-Au Device L.

$$P_{sat}^{input} = 0.2\ P_{LO} = (0.14\,\tfrac{nW}{K^2})\ T_c^2\ . \tag{9.1}$$

A bath temperature much lower than T_c is assumed.

Equation 9.1 can used to estimate the maximum temperature of the input background radiation if the input bandwidth is known. The background noise power is equal to $k_b T_{back} B_{RF}$, where T_{back} is the temperature of the incident radiation and B_{RF} is the input bandwidth of the mixer. With a 200 GHz input bandwidth, the maximum input load temperature is

$$T_{back}^{MAX} = (50K^{-1})\ T_c^2\ . \tag{9.2}$$

The background sky noise temperature in many applications is approximately 130 K. Therefore Nb-Au with $T_c \sim 1.6 - 2K$ should not exhibit input saturation, according to Equation 9.2. If the performance achieved with Device L can be reliably achieved, then the situation is even better since for this particular device, the LO power can be shifted by almost 3 dB without degradation in T_M and 1 dB shift is used to obtain Equation 9.2. For a 1 K mixer, on the other hand, a very narrow input bandwidth is needed to avoid input saturation.

9.2 Output (IF) Saturation

Output saturation is also a heating effect that moves the mixer operating point away from the sharpest part of the resistive transition. The source of saturation in this case is background noise that is down-converted in frequency by the mixer. This down-

converted noise has two effects. First, it adds noise in the IF band which directly increases the mixer output noise. This is easy to understand and is always present regardless of whether or not the mixer is saturated. A more complicated effect results from the noise voltage generated at the IF. If this noise voltage swing is large, the mixer will sample regions of poor conversion efficiency. On average, therefore, the mixer will operate with lower than optimum conversion efficiency, and a higher mixer noise temperature. This effect has been well characterized for SIS mixers (Tucker and Feldman, 1985). To characterize how large a noise voltage is required to observe output saturation, it is necessary to know how the conversion efficiency and mixer noise vary as a function of bias voltage. In Figure 9.2, the conversion efficiency and mixer noise of Nb-Au Device L is plotted a function of bias voltage. A quantity called ΔV_{-3dB} is defined to quantify the variation of mixer performance with voltage. For conversion efficiency, $\Delta V_{-3dB,\eta}$ is the voltage shift from the optimum bias voltage that results in a 3 dB decrease in conversion efficiency. Similarly, for the mixer noise temperature, $\Delta V_{-3dB,\, T_M}$ is the bias voltage shift that results in a factor of 2 increase in T_M. Both of these quantities are graphically indicated in Figure 9.2. The mixer noise temperature degrades over a wider voltage range than the conversion efficiency. This is the case since T_M is a ratio of the output noise and conversion efficiency, both of which decrease with increasing bias voltage. For the purpose of defining an input noise power which results in output saturation, $\Delta V_{-3dB,T_M}$ is too large a voltage swing to consider. The mixer noise has significantly increased if the noise voltage generated from background noise is $\Delta V_{-3dB,T_M}$. A more realistic estimate for the onset of output saturation can be made by using $\Delta V_{-3dB,\eta}$, which is typically a factor of 2-3 times smaller. If the bias voltage swing from the

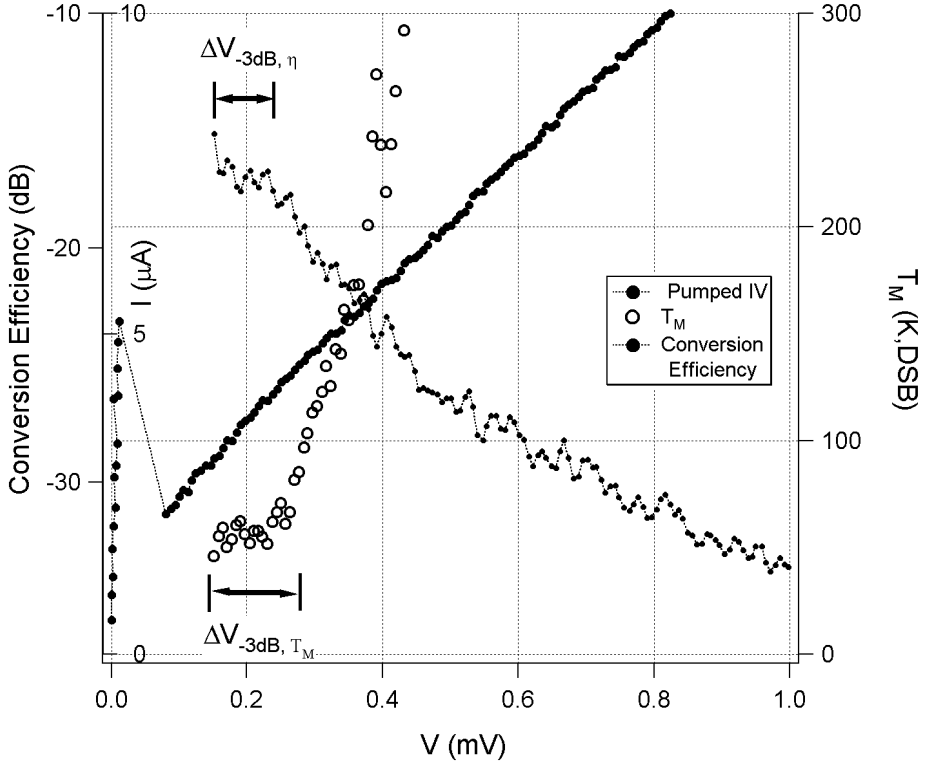

Figure 9.2: Conversion efficiency and mixer noise temperature for Nb-Au device L as a function of bias voltage. The voltage range over which both of these quantities degrade by a factor of two is also indicated.

noise background is ~ $\Delta V_{-3dB,\eta}$, then the average conversion efficiency will be ~ 1.5 dB lower than the optimum value and a ~ 20% increase in mixer noise should be observed. For T_M, this is only considering the degradation due to shifting the bias voltage and not including the effect of the direct increase in output noise. The input noise power that results in output saturation is equal to the power which generates a peak to peak noise voltage at the IF equal to $\Delta V_{-3dB,\eta}$,

$$P_{sat}^{input} \sim \frac{\left(\frac{0.7}{2}\Delta V_{-3dB,\eta}\right)^2}{R}\frac{1}{\eta}. \tag{9.3}$$

The factor of 0.7/2 is used to convert between a rms value of the voltage and a peak to peak value. The conversion efficiency is inserted in Equation 9.3 to infer the saturation power to the mixer input.

To compare the saturation power of mixers with different T_c, the dependence of $\Delta V_{-3dB,\,\eta}$ on T_c is needed. In Figure 9.3, the experimental values of ΔV_{-3dB} are plotted for both the conversion efficiency and mixer noise. Both quantities exhibit a linear dependence on T_c. Also in Figure 9.3, the results of the numerical simulations are plotted. Using the simulated conversion efficiency and mixer noise calculated in Chapters VI and VIII, ΔV_{-3dB} for both quantities is easily obtained. The optimum operating point is taken to be the bias voltage that yields –8 dB conversion efficiency. $\Delta V_{-3dB,\,\eta}$ is therefore the voltage shift over which the conversion efficiency drops to -11dB. Similarly, the mixer noise temperature at the bias voltage with η = -8 dB is taken to be the minimum, and $\Delta V_{-3dB,\,T_M}$ is the voltage shift which results in a doubling of T_M. Agreement with experiment for the conversion efficiency data is much better than for mixer noise. The simulations predict that the mixer noise should fall off over a much wider voltage range than is experimentally observed. This discrepancy is perhaps another indication that the actual noise behavior of HEB mixers is more complicated than predicted by the simple classical treatment of thermal fluctuations. From Figure 9.3, $\Delta V_{-3dB,\eta}$ is approximately equal to 30 μV/K multiplied by T_c. This result can be

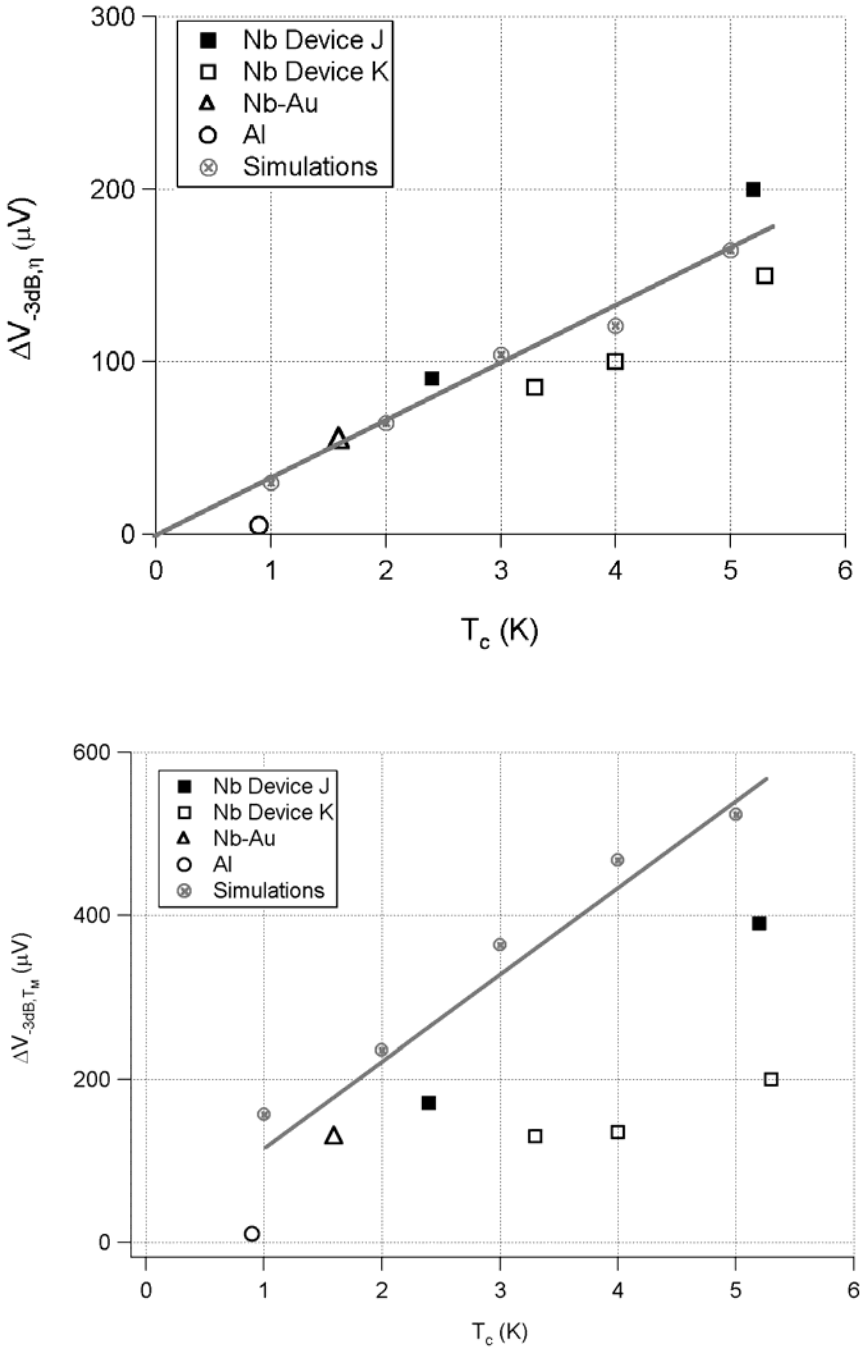

Figure 9.3: Experimental and simulated values for (top) $\Delta V_{-3dB,\eta}$ and (bottom) $\Delta V_{-3dB,T_M}$ as a function of mixer T_c. The solid line is a linear fit to the simulation data. No proximity effects have been included in this calculation.

substituted into Equation 9.3. Estimating the device resistance to be 50 Ω and η = - 10 dB gives

$$P_{sat}^{output} = 27 \frac{pW}{K^2} T_c^2 . \tag{9.4}$$

A maximum load temperature that can be incident upon the mixer before output saturation is observed is estimated using the IF bandwidth. The maximum noise bandwidth that is down-converted is 2 times the IF bandwidth. A typical value of the IF bandwidth needed in receivers is 4 GHz. The maximum background noise temperature is then,

$$T_{background}^{MAX} = (240K^{-1})\, T_c^2 . \tag{9.5}$$

Nb-Au devices therefore should experience no output saturation even with a T_c as low as 1.6 K. Al devices with $T_c \sim 1$ K should not output saturate either. For Al mixers with normal edges, this is not the case. Equation 9.5 is calculated assuming that $\Delta V_{-3dB,\,\eta}$ is 30 μV at T_c = 1K. The actual value is ~ 5-10 μV. This reduces the maximum load temperature by a factor of 10 or so to 24 K, which is very small and an Al mixer would easily saturate due to background noise.

The cause of the very narrow operating range for Al HEBs is related to the edges of the microbridge being normal. Since the resistance drop at T_c is only a fraction of the total resistance, only a small section of the R vs. T curve has areas where optimum performance can be achieved. As a result, shifting the bias voltage even by 10 μV moves

the bias point off the sensitive part of the transition. Numerical simulations are used to model this effect. For the ends of the microbridge, the resistivity is modeled as being independent of temperature and equal to the normal state value. A superconducting transition at T_c is used to describe the center of the microbridge. Several different lengths of the normal edges are used in the calculation. In Figure 9.4, three types of R vs. T curves used in the calculations are shown. The one in dark black models the entire bridge as having a superconducting transition, and the resistance drops to zero below T_c. The other two curves consider the case when 35 % and 50 % of the total bridge remains normal because of the proximity effect. An experimental R vs. T curve for Device D is also plotted. The experimental curve is most similar to the case when half the device remains normal below T_c. The conversion efficiency as a function of bias voltage is calculated for each of the three simulated R vs. T curves. From this data, $\Delta V_{-3dB,\,\eta}$ is extracted. In Figure 9.5, $\Delta V_{-3dB,\,\eta}$ obtained from the simulations is shown as a function of mixer T_c. The three traces again represent cases where the microbridge is fully superconducting and has two different residual resistances. As a larger fraction of the microbridge remains normal, $\Delta V_{-3dB,\,\eta}$ decreases. For the 50% normal case, $\Delta V_{-3dB,\,\eta} \sim$ 10 μV for T_c = 1 K. This is in good agreement with the experimental data for Al. Therefore, the incident power resulting in output saturation is significantly smaller for a N-S-N HEB in which the normal microbridge edges comprise a sizable fraction of the total device length.

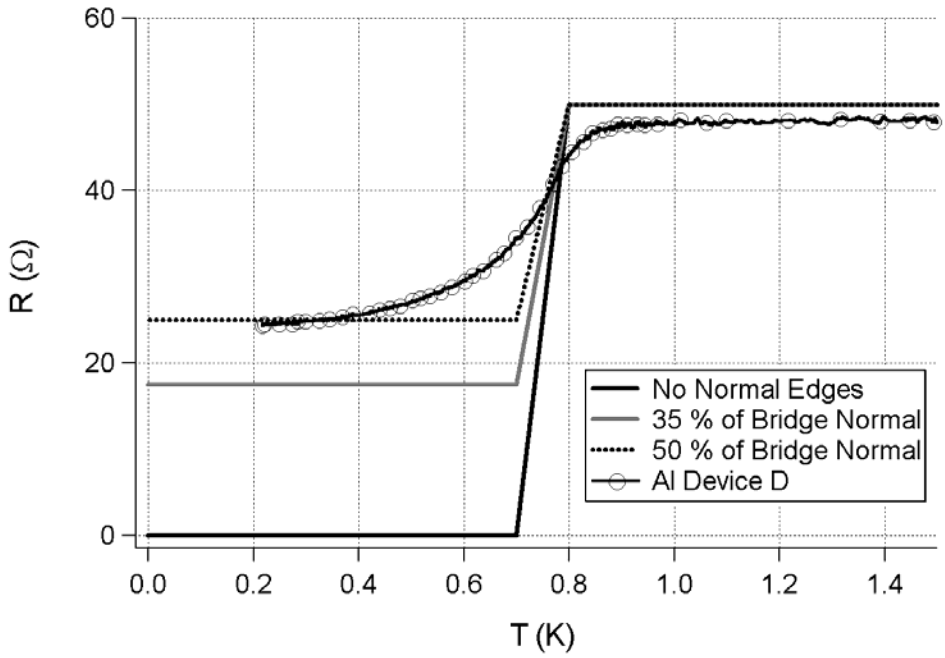

Figure 9.4: R vs. T curves used in the numerical simulations and the R vs. T curve for Al Device D with H=0.12 T.

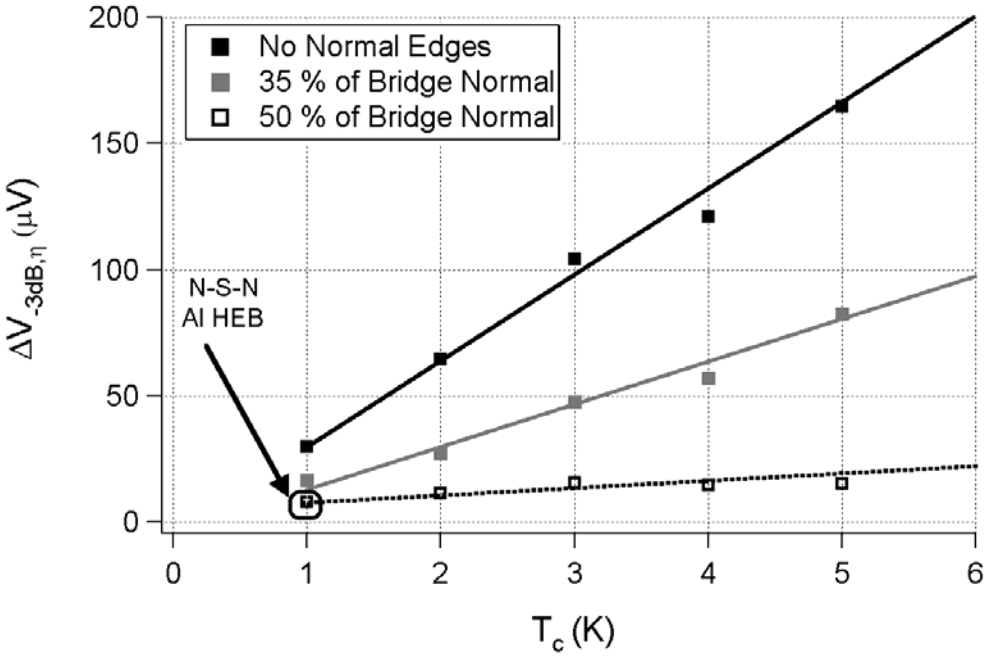

Figure 9.5: Calculated values for $\Delta V_{-3dB,\,\eta}$ as function of T_c for different normal fractions of the microbridge.

9.3 Observing Saturation

In order to test the formulas obtained for the noise power that results in saturation effects, we measured the mixer conversion efficiency when a broadband noise signal is combined with the monochromatic RF signal. The power of the background noise signal is controllable, and it is therefore possible to identify at what noise power level the conversion efficiency degrades. We placed a commercial 2.4 mm 50 Ω termination on the input port of a 26.5-40 GHz high gain amplifier to generate the broadband noise. The frequency window through which there is good transmission is from 26.5-34 GHz due to the upper frequency cutoff of the 3dB couplers. Device D was chosen for the saturation measurements since it has an IF bandwidth of ~ 4 GHz. Choosing 30 GHz for the LO frequency ensures that nearly all the broadband noise will be down-converted by the mixer. In Figure 9.6, the I-V curves for Device D with and without noise power added are shown. For small noise power, the I-V curves look approximately the same. When large powers are applied, the critical current decreases and the mixer is 'overpumped'. The maximum measured conversion efficiency is plotted as a function of incident noise power in Figure 9.7. A decrease in conversion efficiency is observed for incident powers as small as 3-10 pW. This power is more than 30 times smaller than the LO power, so the drop in conversion efficiency is very likely due to output saturation. At much higher incident powers, the poor performance is due to a combination of input and output saturation. For 10 pW of input noise power, the corresponding background noise temperature is 90 K. Therefore output saturation is seen for this Al device when the background noise temperature is 90 K or higher.

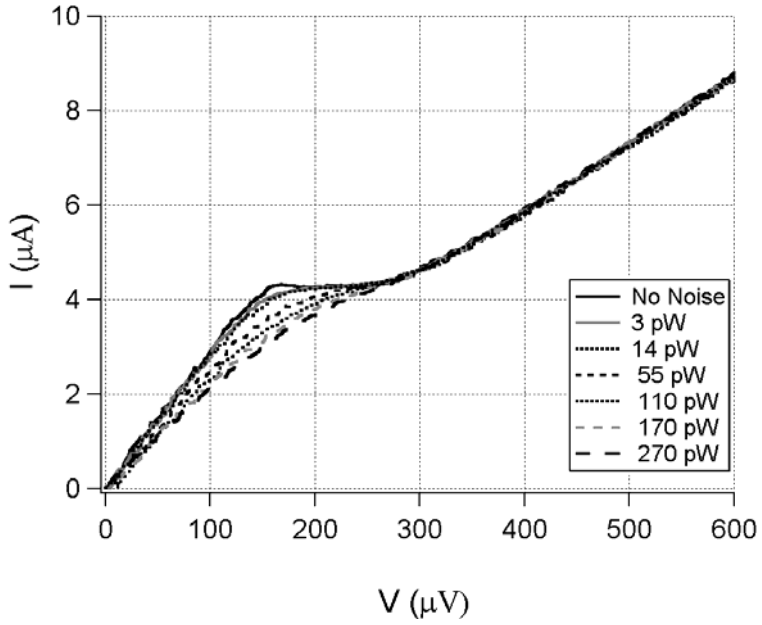

Figure 9.6: I-V curves for Device D as a function of applied noise power at the mixer input. All the curves have 0.32 nW of LO power applied.

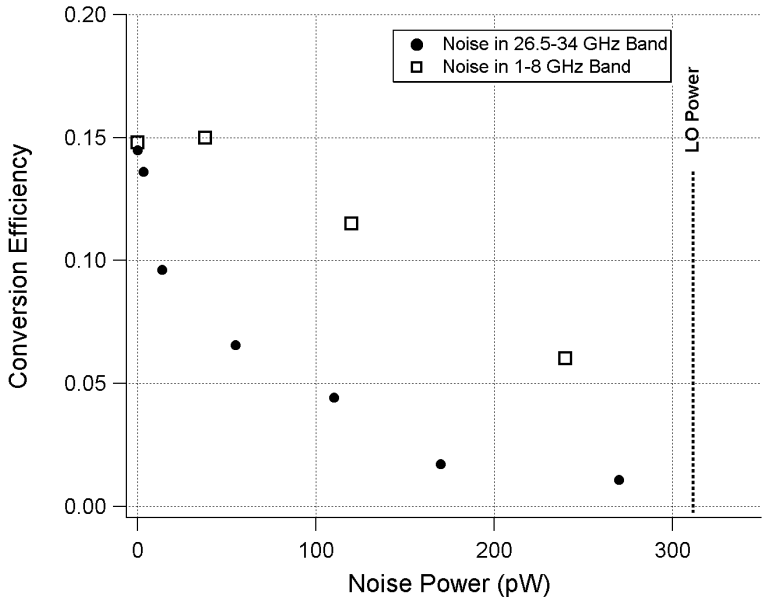

Figure 9.7: Conversion efficiency as a function of applied noise power for Device D. The DC bias voltage is ~ 280 μV. Noise power is applied in either the 26.5-34 GHz band or the 1-8 GHz band.

To try to simulate input saturation and to separate input and output saturation effects, we applied noise at lower frequencies also. The frequency of the noise generator was lowered to 1-8 GHz using a different HEMT amplifier with a termination as the noise source. In the simple mixing model, most of the noise power in this case is not down-converted to the IF since the LO frequency is 30 GHz and the IF bandwidth is 4 GHz. In Figure 9.7, the conversion efficiency in the presence of 1-8 GHz noise is also shown. The conversion efficiency now drops at much higher incident noise powers. A noticeable drop is seen at ~ 100 pW which is approximately 30% of the LO power. This effect is most likely due to input saturation and is in good agreement with the saturation criterion discussed in Section 9.1. Finally, the LO power is reduced with 170 pW of noise power applied to see if the conversion efficiency can be restored. The I-V curves for different LO powers with a constant applied noise power are presented in Figure 9.8. Decreasing the LO power does yield an I-V curve similar to case when no noise power is applied. However, the conversion efficiency, as expected, does not recover. The conversion data is plotted in Figure 9.9. With the saturation experiments, both input and output saturation effects have been observed and occur at approximately the predicted input noise power levels. Therefore, the relations for maximum input noise power can be used as a guide in choosing mixer T_c so as to avoid saturation effects.

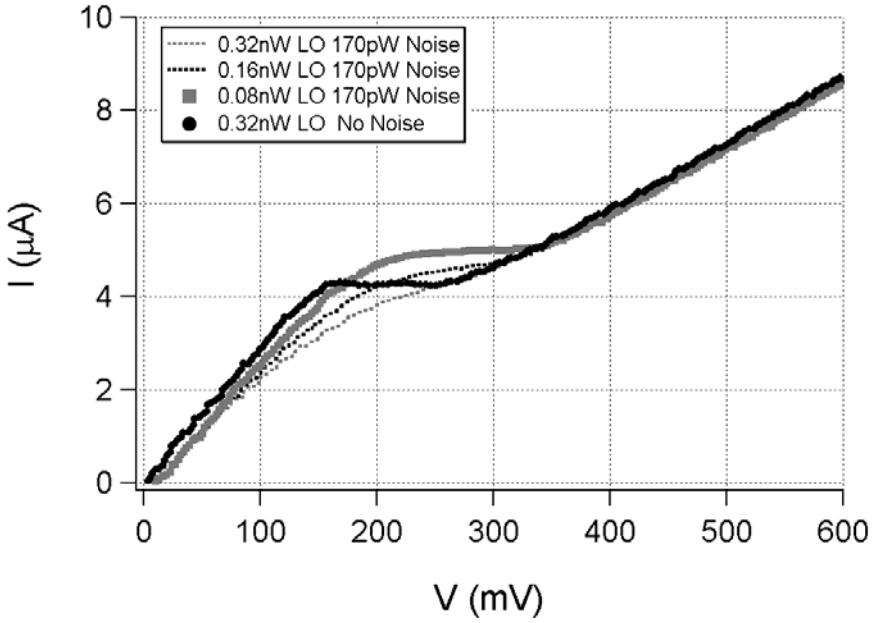

Figure 9.8: I-V curves for Device D as a function of LO power. All the curves have an applied noise power of 170 pW in the 26.5-34 GHz band.

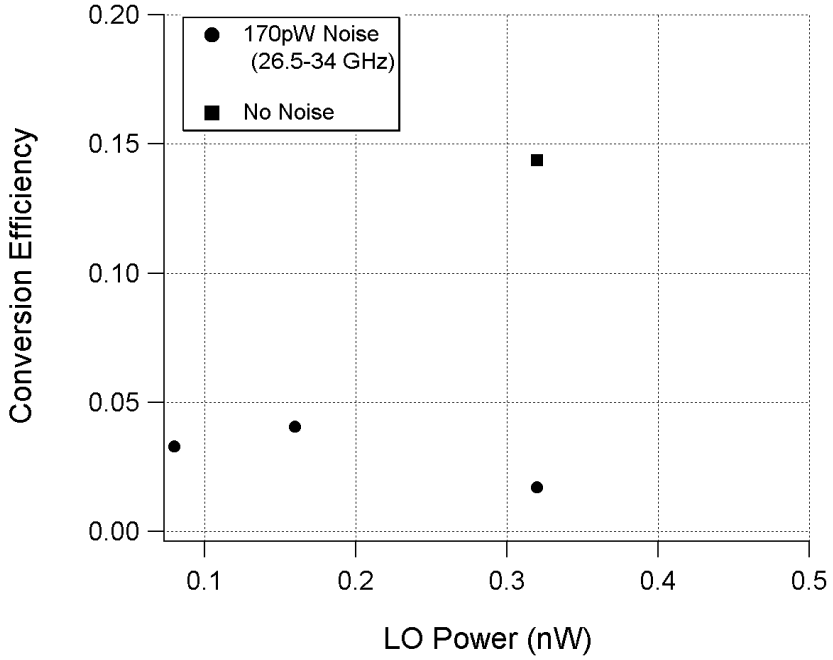

Figure 9.9: Conversion efficiency as a function LO power for Device D, with and without a noise background added.

Chapter X: Dependence on ΔT_c

Up to this point, we have assumed that the mixer transition width ΔT_c is << T_c. The simplification was used in Chapter II to derive simple relations for mixer performance as a function of T_c. In the numerical simulations, narrow transitions widths have also been used until now. The theoretical predictions in the limit of a narrow transition width yield a mixer noise temperature and an operating voltage range (ΔV_{-3dB}) that scale with T_c when operating in the region of best conversion. The LO power is proportional to T_c^2 at low bath temperatures. The transition width does not enter these formulas. From the experimental data, these mixer properties were indeed shown to scale with T_c as predicted.

In this chapter, mixer performance at a fixed T_c and its dependence on T_c are studied for different values of ΔT_c. Similar to the simulations already presented in previous chapters, the numerical model is used to calculate the conversion efficiency, mixer noise, LO power, and ΔV_{-3dB}. The value of ΔT_c was taken to be ~ 0.1 T_c in all the previous simulations. In the present set of calculations, ΔT_c / T_c is varied from 0.02 to 1.5. Using this data, an upper limit for ΔT_c / T_c is approximated. For normalized transition widths up to this upper limit, no significant performance degradation is observed. Also, the simple scaling predictions are also still observed. The transition widths for nearly all the HEB mixers studied are less than or equal to this maximum calculated transition width.

When the width of the superconducting transition becomes large, the conversion efficiency decreases. The parameter α_0 characterizes the operating regime of the mixer

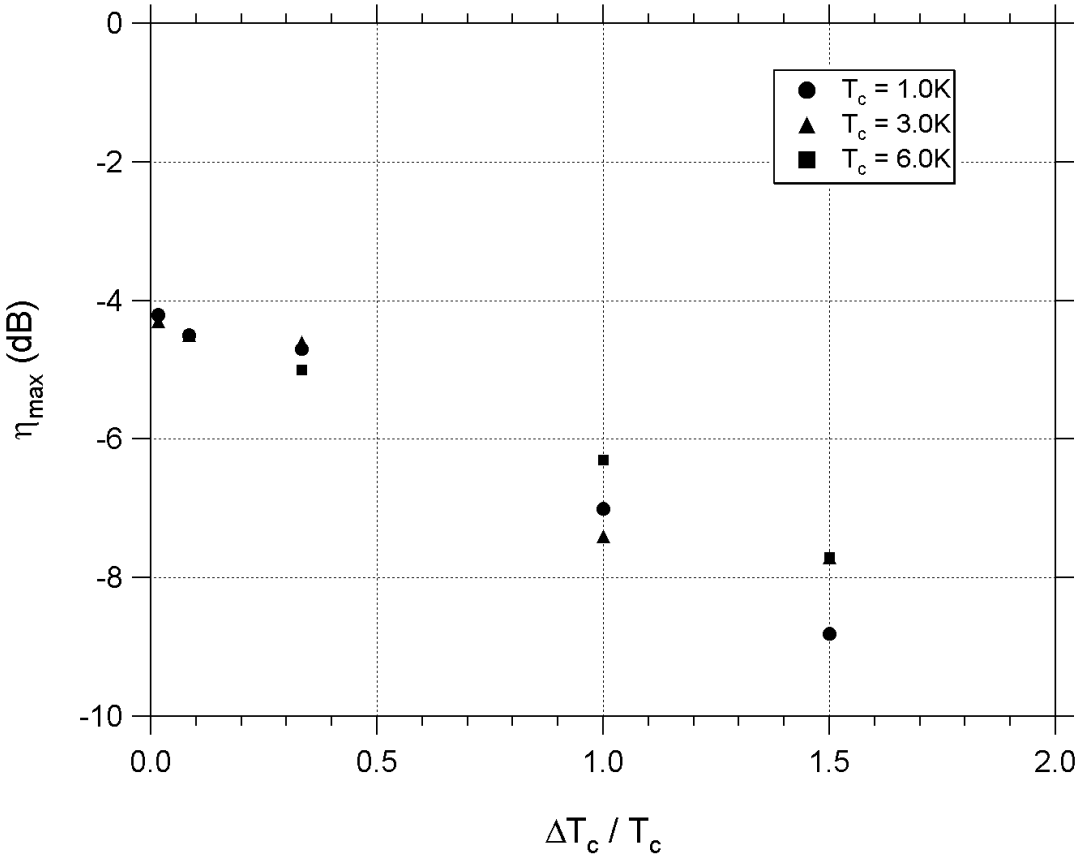

Figure 10.1: Calculated conversion efficiency as a function of transition width.

since the conversion efficiency is proportional to α_0^2 (Equation 2.46). The quantity dR/dT is smaller for wide transitions and the parameter α_0 also decreases as the transition width is increased. The detailed dependence of α_0 on ΔT_c is a bit complicated. For narrow widths, increasing the bias current can compensate for a slight broadening of the transition. However, for very wide widths, α_0 does decrease. In Figure 10.1, the calculated maximum conversion efficiency is plotted as a function of ΔT_c / T_c. For each data point, the LO power has been optimized for conversion efficiency. Three different

values of T_c are chosen, 1 K, 3 K, and 6 K. For each T_c, different widths are sampled. From Figure 10.1, the conversion efficiency does not decrease significantly if $\Delta T_c / T_c$ is less than 1/3. For larger ratios, the conversion efficiency is several dB lower than the optimum value. A similar plot to Figure 10.1 is made for the devices measured. The transition width for the experimental data is defined using the total resistance drop at T_c, ΔR. The onset of the transition is the point where the device resistance is R_N - 0.1 ΔR, where R_N is the resistance above T_c. The temperature at which the resistance is R_N - 0.9 ΔR is taken to be the end of the transition. This definition is useful for comparing devices that have a finite resistance below T_c, namely the Al mixers, and Nb devices that simply drop in resistance from R_N to 0 at T_c. In Figure 10.2, the conversion efficiency for Devices D,E,G, K, and L are plotted as a function of $\Delta T_c/T_c$. All the devices in the figure have a conversion efficiency of ~ -10 dB, with the exception of Nb Device K with H = 2.0 and 2.5 T (indicated with a circle in Figure 10.2). Mixers with ~ -10 dB conversion have $\Delta T_c / T_c$ less than or equal to ~ 0.4. The experimental data agree well with the prediction that no decrease in conversion should be seen if $\Delta T_c / T_c$ is about 1/3 or less. Nb Device K operated with a high field has a much broader transition than in zero field, and also has significantly poorer conversion efficiency. In addition to a broad transition, Nb Device K in a high field has a small critical current compared to both Nb-Au and Al mixers. Typically, poor conversion is observed in mixers with an unpumped critical current of less than ~ 4-5 μA.

Having defined a range of transition widths over which no significant degradation in conversion efficiency is observed, we have to verify if the mixer properties scale with T_c in this range. So far, we have discussed the dependence of T_M, P_{LO}, and ΔV_{-3dB} on T_c.

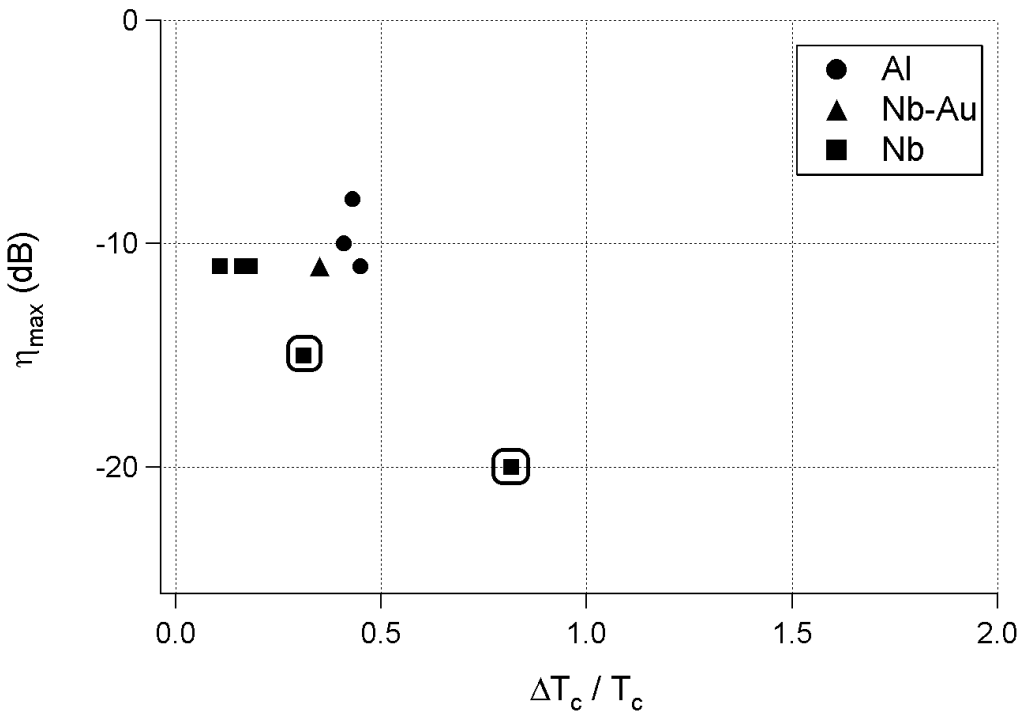

Figure 10.2: Experimental values of the conversion efficiency as a function of the transition width. The two Nb data points with circles are for Device K with H = 2.0 (left) and 2.5T (right). The conversion efficiency is poor and the transitions are broad with a high field applied.

The numerical model is not well suited for studying the noise temperature in the case of very broad transitions. When the conversion efficiency decreases for the case of large ΔT_c, the mixer noise is no longer dominated by thermal fluctuations. Johnson noise becomes non-negligible. Since the model only treats thermal fluctuation noise, it cannot predict the dependence of T_M on T_c when Johnson noise has to be considered. However, it is possible to verify that the mixer noise temperature due to thermal fluctuations is proportional to T_c for $\Delta T_c / T_c < 0.33$, where no significant decrease in conversion

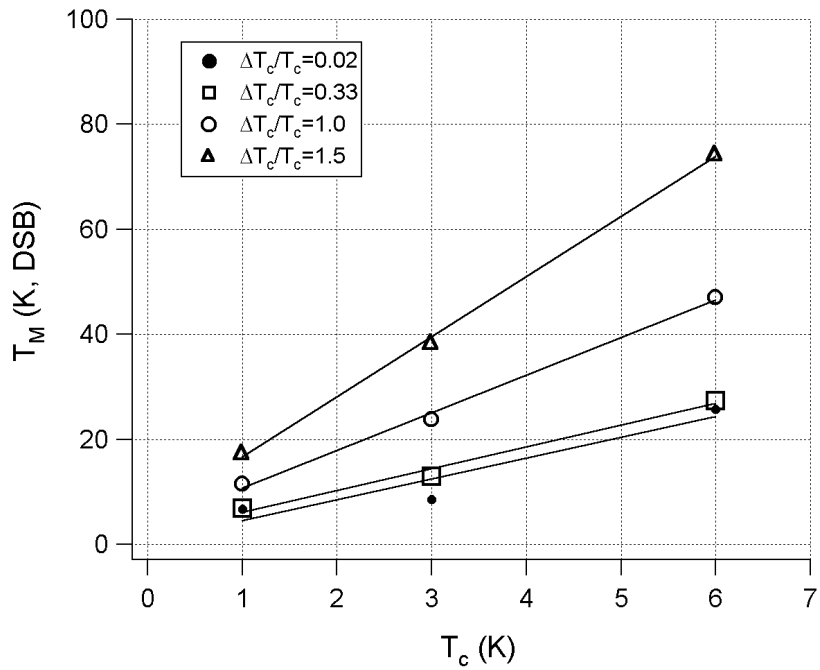

Figure 10.3: Calculated mixer noise temperature due to thermal fluctuations only as a function of T_c. The different traces are different transition widths.

efficiency is expected from the narrow transition value. The model does in fact predict this linear dependence, and is shown in Figure 10.3. For the LO power, no change is also observed up to ΔT_c / T_c ~ 0.33. Finally, the operating voltage range over which the conversion efficiency drops by 3 dB – $\Delta V_{-3dB,\ \eta}$ – is also nearly constant over the same range of transition widths. This data is presented in Figure 10.4. Therefore, mixers with ΔT_c / T_c < 0.33 should perform well and the scaling predictions explored in this thesis should be valid. This range of transition widths is readily achievable with current fabrication processes.

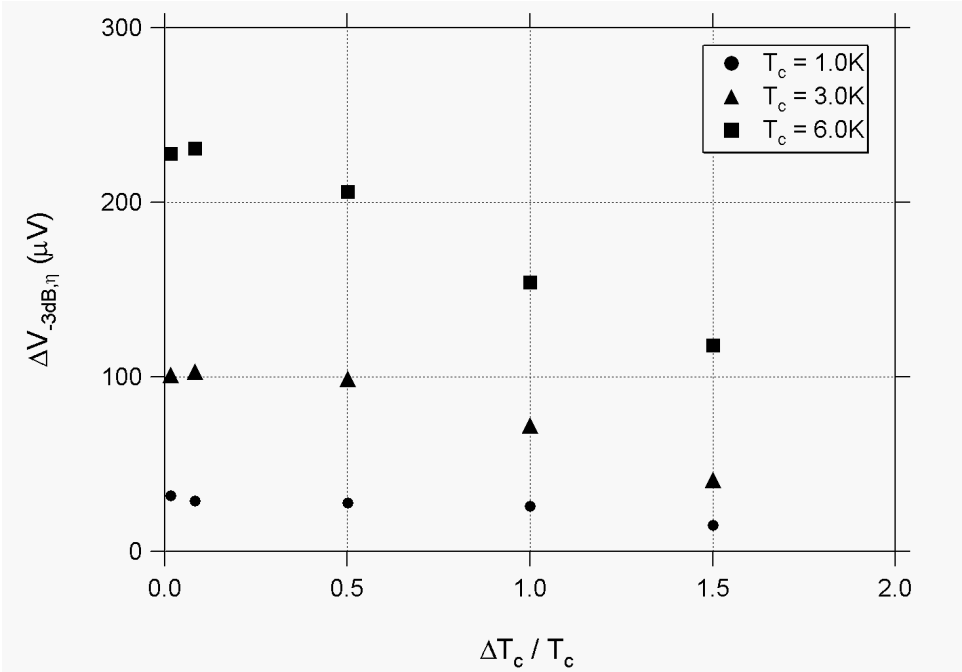

Figure 10.4: Calculated values for $\Delta V_{-3dB,\eta}$ as a function of transition width. The three traces are for different values of mixer T_c.

Chapter XI: JPL Al HEB Measurements

HEB mixers are being developed for astronomical applications in THz frequency heterodyne receivers. The microwave measurements presented in this thesis, through an exploration of the underlying device physics in HEBs, are intended to be a guide for the development of these receivers. A true test of the feasibility of low T_c diffusion-cooled mixers requires testing at THz frequencies in both laboratory experiments and in actual receivers. Receivers based on Nb-Au mixer technology are currently being developed for use in ground-based observatories. No tests of these mixers at frequencies greater than 30 GHz have been performed yet. As for Al devices, mixing measurements at f ~ 600 GHz have been carried out at JPL (Skalare et al., 2001). The results of the JPL measurements do not agree in certain aspects with the microwave data. The conversion efficiency measured at 600 GHz is lower than that measured at 30 GHz by 10 dB or greater. For operation at similar bias conditions, the approximate absolute conversion efficiency at 600 GHz is less than –20 dB.

A recent theory has predicted that Al HEBs should not work well at high frequencies (Semenov and Gol'tsman, 2000). This work cites the absence of inelastic electron-electron interactions as the cause of poor performance at f ~ THz. Since the LO frequency is much larger then the energy gap, the incoming radiation will produce very high-energy single particle excitations. In the absence of inelastic scattering, energy exchange between these single particles does not occur. High energy excitations are not effective in suppressing the superconducting energy gap, and therefore a large LO power would be needed to put the mixer into the operating state. Devices that do not have

inelastic scattering must be very short and of low resistivity. From the experimental results presented, such devices cannot be superconducting if they are contacted with normal pads. As a result, the predictions in Semenov and Gol'tsman (2000) are for the most part not relevant for Al HEB mixers. Additionally, one of the main predictions of this theory is that $P_{LO} > \mu W$ for Al mixers. This increase of LO power is not observed in the 600 GHz measurements. The output power of the LO sources used in these measurements is ~ 100 μW, and the estimated maximum power coupled to the device is less than 200 nW (Skalare et al., 2001). Also, poor conversion is measured in devices with L = 1 μm which are clearly longer than estimates of the inelastic length. Therefore, it is unlikely that the discrepancy in conversion efficiency between the 30 GHz and 600 GHz data is due to the absence of inelastic scattering in the microbridge.

A possible reason for poor performance at 600 GHz is saturation. The 600 GHz setup uses quasi-optical techniques to couple radiation to the mixer. Background radiation levels that impinge on the mixer are much higher in the quasi-optical setup than in the microwave setup. In the latter, cryogenic attenuators are used to reduce the thermal background noise power by almost three orders of magnitude. It is possible that the additional thermal background radiation of the 600 GHz setup saturates the Al devices. Input saturation is not likely since this would require significantly heating the electrons in the microbridge and would change the apparent T_c of the mixer. The R vs. T curves of the Al devices measured in the 600 GHz setup and the 30 GHz setup are similar. Output saturation, on the other hand, is possible. In the microwave measurements, ~ -10 dB conversion is observed for Al devices, but only over a very narrow bias voltage range. A noise voltage of 5-10 μV is sufficient to degrade the

conversion efficiency by 3 dB. To reduce the noise background, thin films of absorber have been placed on cold internal mirrors and on the lower temperature shields of the cryostat. These films should act as attenuators, in much the same way coaxial attenuators are used in the 30 GHz setup. However, the initial results of these measurements do not show an improvement in conversion efficiency.

The difference in conversion efficiency measured in the low and high frequency measurements is not completely understood. It is possible that output saturation is the cause, though further work is needed to verify this. In any event, based just on our own 30 GHz results, we find that output saturation will be a problem in any practical receiver based on Al mixers. Nb-Au mixers, on the other hand, should be able tolerate a larger noise background than Al. Nb mixers with $T_c \sim 5$- 6 K clearly can work in a quasi-optical setup (Wyss et al., 1999). Tests of Nb-Au mixers with varying T_c at THz frequencies are essential for characterizing the lowest T_c mixer that is practical for use in receivers.

Chapter XII: Conclusions

The goal of this work has to been to improve the performance of diffusion-cooled HEB mixers through a reduction in their T_c. At the start of this research, Nb diffusion-cooled mixers with $T_c \sim 5$- 6 K had been successfully tested at both 20 GHz and at THz frequencies. Two major improvements were anticipated in lower T_c mixers, a reduction in mixer noise and in LO power. Both of these predictions have been successfully verified. In addition to performance improvements, limitations arising from lowering T_c, which had not been anticipated, have also been characterized. HEB mixers with lower T_c are more prone to saturation effects. Additionally, materials with a long coherence length, such as Al, exhibit a suppression of superconductivity in the ends of the microbridge in the presence of large normal-metal contact pads. The proximity effect causes the edges of the microbridge to be in the normal state. For these devices, only a fraction of the normal state resistance drops at T_c, making it possible to operate the mixer in only a narrow range of input power. Very short devices do not become superconducting at all and this limits the minimum length for a HEB with normal contacts. Such a limitation on the device length imposes an upper limit on the IF bandwidth. At the conclusion of this work, a more balanced pictured has emerged regarding low T_c HEB mixers. The initial ideas about lowering mixer noise and LO power were indeed correct, but T_c cannot be lowered indefinitely. Saturation effects limit the utility of very low T_c mixers. Therefore, the idea of an optimum mixer T_c has evolved with this work. For most applications from 1-3 THz, a T_c of 2K is predicted to be optimum. Mixers with $T_c = 2$ K

should have 2-3 times lower noise and 4-9 times smaller LO power than Nb devices, yet should not exhibit saturations effects.

Among the benefits of lowering T_c is an improvement in noise temperature. Mixer noise is observed to be proportional to T_c. Al devices have the lowest noise temperature of all the devices tested, and Nb in zero magnetic field the highest. Al mixers have a DSB mixer noise temperature of ~ 20 – 30 K with T_c ~ 1 K. Nb HEBs have a DSB mixer noise > 100 K with T_c ~ 5 – 6 K. Devices with critical temperature in between these values have a noise temperature between 20 and ~ 100 K. Specifically, T_M is approximately equal to 25 times T_c. This result agrees with the scaling predicted by theory in that T_M is predicted to be proportional to T_c when the dominant noise source is thermal fluctuation noise. However, the magnitude of the observed noise is larger than predicted. Understanding this discrepancy is a possible direction for both future theoretical and experimental work. Also, experiments with Nb and Nb-Au devices with fully normal contact pads might also shed light on other possible noise sources. Current devices have weakly superconducting areas next to the microbridge that may be adding to the total noise of the mixer. In spite of this disagreement with theory as to the magnitude of the scaling factor, from the point of view of receiver design, the mixer noise temperature is a linear function of T_c when thermal fluctuations are much larger than any other noise source, such as quantum noise or Johnson noise. Johnson noise will always be small compared to thermal fluctuation when the mixer is operated with maximum conversion efficiency. Current Nb HEBs would have quantum noise larger than thermal fluctuation noise only at frequencies of several THz. Therefore for current applications,

sizable reductions in mixer noise should be possible through the use of mixers with $T_c <$ 5 – 6 K.

In addition to a reduction in mixer noise, the LO power for diffusion-cooled mixers is observed to be equal to (0.7 nW/K^2) • T_c^2 when the bath temperature is much smaller than T_c. Devices with lower LO powers are very useful for actual receivers. Most convenient LO sources at THz frequencies have a limited power output, typically in the μW range. Reducing the LO power requirement of the HEB makes it realistic to consider HEB arrays with currently available LO sources. The dependence of the LO power on T_c^2 is in good agreement with the theoretical prediction.

There are, however, some disadvantages to having a smaller LO power requirement. Devices requiring smaller LO power are easier to saturate at the mixer input. Background noise heats the mixer and shifts it away from optimum operating conditions. From the experimental data, an increase in mixer noise is observed when the background noise power is 20 % of the LO power. Consequently, for a HEB mixer with a transition temperature of T_c, input saturation is expected when the background noise power is ~ (0.14nW/K^2) • T_c^2. Al devices are therefore not practical for most applications since the sky background noise is likely to result in input saturation. On the other hand, a mixer with T_c = 2K should not experience input saturation in the presence of ~ 150 K sky noise and a 200 GHz input RF bandwidth.

In addition to saturating at the mixer input, output saturation is also more likely in very low T_c mixers. Noise voltages resulting from background radiation down-converted to the IF band shift the bias voltage away from the optimum operating point. The bias voltage range over which good mixing is observed is proportional to T_c, and therefore

lower T_c mixers are more susceptible to output saturation. From the experimental results, an input noise power of (27 pW/K^2) • T_c^2 is likely to cause output saturation effects in a HEB mixer with a transition temperature of T_c. For devices with T_c = 2 K, output saturation should not be a problem. Al mixers have an especially narrow operating voltage range. This results from sizable fractions of the microbridge being in the normal state. Output saturation is likely to occur in Al HEB receivers.

The origin of the normal edges for Al HEBs is due to the normal-superconductor proximity effect. The coherence length of Al is much larger than the thickness of the thin Al pads that are adjacent to the microbridge. The normal contacts on top of the thin Al pads suppress superconductivity in the thin pads and in the microbridge edges. It is observed that the length of each normal edge of the microbridge is ~ 3 - 3.5 $\xi(0)$. There are two detrimental effects of these normal edges. First, they reduce the fractional drop of resistance at T_c in devices longer than 7 $\xi(0)$. Therefore, a small shift in bias voltage or LO power moves the operating point off the sensitive section of the R vs. T curve and performance rapidly degrades. Second, very short microbridges never undergo a superconducting transition when the contacts pads are normal. There is therefore a minimum length for the superconducting section of an N-S-N HEB. Microbridges shorter than this length are always completely resistive. This minimum length is many times larger than ξ (0) since ξ (0) determines the length scale of variation of the gap in an semi-infinite N-S boundary of equal size. In the HEB, the normal-metal pads are much larger than the small microbridge. HEB mixers with a length many times longer than the coherence length have an IF bandwidth that is determined by the average diffusion time of hot electrons from the microbridge. For these devices, the measured bandwidth agrees

well with the expression IF BW = $\frac{\pi D}{L^2}$. Shortening the bridge length increases the IF bandwidth. However, since there is a minimum length to observe superconductivity, an upper limit exists for the IF bandwidth. This upper limit depends only on T_c and is (8 GHz/K) • T_c. This is still plenty of bandwidth for planned applications, but does represent a limit previously unappreciated. Nb and Nb-Au devices have a short coherence length and do not exhibit suppression of superconductivity in the bridge ends. This bandwidth limit only applies to N-S-N structures, when all the material adjacent to the microbridge is in the normal state. Materials with a large coherence length therefore experience limits on the IF bandwidth and are more likely to saturate.

The microwave measurements have investigated both the advantages and disadvantages of lower T_c mixers. The key parameters that characterize a diffusion-cooled mixer scale as a power of T_c when the transition width is small. From numerical simulations, the scaling arguments are predicted to be valid when $\Delta T_c < 1/3\ T_c$. In the design of actual receivers, the background radiation level has to be estimated and optimum value of T_c is the lowest one at which saturation is not likely to occur. This represents the lowest mixer noise temperature that can be achieved in the presence of the specified background noise power.

The major experimental task that remains for low T_c HEB mixers consists of testing them at THz frequencies. Nb-Au devices are ideal for this task. In the microwave measurements, T_c = 1.6 K has been investigated and shown to have T_M = 47 K, DSB. The LO power used is ~ 2 nW and the operating voltage range over which T_M remains nearly unchanged is large, tens of μV. Devices with these characteristics should not saturate at high frequencies. Additionally, adjusting the normal metal thickness can

continuously vary the critical temperature of these devices. Testing a set of Nb-Au devices with a range of values of T_c provides a means for experimentally optimizing the HEB for its intended application. Nb-Au mixers have demonstrated state of the art mixer performance at microwave frequencies. Their superb performance and tunability of T_c make then very attractive candidates for future THz applications.

References

Altshuler B.L. and A.G. Aronov, *Sol. State Comm.* **46**, 429 (1983).

Becklin E.E., *Proceedings of the ESA Symposium 'The Far Infrared and Submillimetre Universe'* (Grenoble, France, 15-17 April 1997), p 201.

Blundell R. and C.-Y.E Tong, *Proc. IEEE* **80**, 1702 (1992).

Boonman A.M., A.M.S. Stark, F.F.S. van der Tak, E.F. van Dishoeck, P.B. van der Wal, F. Schafer, G. de Lange, W.M. Laauwen, *Astrophys. J. Lett.* **L63**, 553 (2001).

Bumble B. and H.G. LeDuc, *IEEE Trans. Appl. Supercond.* **7**(2), 3560 (1997).

Burke P.J., Ph.D. thesis, Yale University, 1997.

Burke P.J., R.J. Schoelkopf, D.E. Prober, A. Skalare, B.S. Karasik, M.C. Gaidis, W.R. McGrath, B. Bumble, and H.G. LeDuc, *Appl. Phys. Lett.* **72**, 1516 (1998).

Burke P.J, R.J. Schoelkopf, D.E. Prober, A. Skalare, B.S. Karasik, M.C. Gaidis, W.R. McGrath, B. Bumble, and H.G. LeDuc, *J. Appl. Phys*. **85**, 1644 (1999).

Carslaw H. and J. Jaeger, *Conduction of Heat in Solids*, Oxford University Press, London (1959).

Caves C, *Phys. Rev. D* **26**(8), 1817 (1981)

Ceccarelli C., D.J. Hollenbach, and A.G.G.M. Tielens, *Astrophys. J.* **471**, 400 (1996).

Cherednichenko S., M. Kroug, P. Yagoubov, H. Merkel, E. Kollberg, K.S. Yngvesson, B. Voronov, G. Gol'tsman, *Proceedings of the 11th International Symposium on Space THz Technology* (University of Michigan, Ann Arbor, MI, 2000), p. 219.

de Jong M.J.M., Ph.D. thesis, Leiden University, 1995.

Echternach P.M., H.G. LeDuc, A. Skalare, and W.R. McGrath, *Proceedings of the 10th International Symposium on Space THz Technology* (University of Virginia, Charlottesville, VA, 1999), p. 261.

Echternach P.M., personal communication, 2000.

Ekstrom H., B.S. Karasik, and E.L. Kollberg, *IEEE Trans. Microwave Theory Tech.* **43**(4), 938 (1995).

Floet D.W., J.J.A. Baselmans, and T.M. Klapwijk, *Appl. Phys. Lett.* **73**, 2826 (1998).

Floet D.W., T.M. Klapwijk, J.R. Gao, and P.A.J. de Korte, *Appl. Phys. Lett.* **77**(11), 1719 (2000).

Gaidis M.C., H.M. Pickett, C.D. Smith, S.C. Martin, R.P. Smith and P.H. Siegel, *IEEE Trans. Microwave Theory Tech.* **48**, 733 (2000).

Gershenzon E., M. Gershenzon, G. Gol'tsman, A. Semenov, and A. Sergeev, *JETP Letters* **36**(7), 296 (1982).

Gershenzon E.M., G.N. Gol'tsman, A.I. Elant'ev, B.S. Karasik, and S.E. Potoskuev, *Sov. J. Low Temp. Phys,* **14** (7), 414 (1988).

Gershenzon E., M. Gershenzon, G. Gol'tsman, A.M. Lyul'kin, A. Semenov, and A. Sergeev, *JETP* **70**(3), 505 (1990).

Gordon J.M. and A.M. Goldman, *Phys. Rev. B* **34**, 1500 (1986).

Groppi C., C. Walker, J. Drouet-D'Aubigny, D. Golish, C. Kulesa, A. Hedden, A. Lichtenberger, A. Datesman, and J. Kooi, *Proceedings of the 9th International Conference on THz Electronics* (University of Virginia, Charlottesville, VA, October 2000), to be published.

Harding G.L., A.B. Pippard, F.R.S., and J.R. Tomlinsion, *Proc. R. Soc. London, Ser. A* **340**, 1 (1974).

Heubener R.P., R.T. Kampwirth, R.L. Martin, T.W. Barbee, Jr., and R.B. Zubeck, *J. Low Temp. Phys.* **19**, 247 (1975).

Jackson B., G. de Lange, W.M. Laauwen, J.R. Gao, N.N. Iosad, and T.M. Klapwijk, *Proceedings of the 11th International Symposium on Space THz Technology* (University of Michigan, Ann Arbor, MI, 2000), p. 238.

Jahn R., undergraduate senior project, Yale University, 2001.

Karasik B.S. and A.I. Elantiev, *Proceedings of the 6th International Symposium on Space THz Technology* (California Institute of Technology, Pasadena, CA, 1995), p. 229.

Karasik B.S. and A. I. Elantiev, *Appl. Phys. Lett.* **68**, 853 (1996).

Kaufman M.J., M.G. Wolfire, D.J. Hollenbach, and M.L. Luhman, *Astrophys. J.* **527,** 795 (1999).

Kawamura J., R. Blundell, C.-Y.E. Tong, D.C. Papa, T.R. Hunter, G. Gol'tsman, S. Cherednichenko, B. Voronov, E. Gershenzon, *Proceedings of the 9th International Symposium on Space THz Technology* (Pasadena, CA, 1998), p. 35.

Kawamura J., J. Chen, D. Miller, J. Kooi, J. Zmuidzinas, B. Bumble, H.G. LeDuc, and J.A. Stern, *Appl. Phys. Lett.* **75**, 4013 (1999).

Kerr A.R., M.J. Feldman, and S.-K. Pan, *Proceedings of the 8th International Symposium on Space THz Technology* (Harvard University, Cambridge, MA, 1997), p. 101.

Kittel C., *Introduction to Solid State Physics* 7th Ed., John Wiley and Sons, New York (1996).

Kozhevnikov A.A., Ph.D. thesis, Yale University, 2001.

Krahenbuhl Y. and R.J. Watts-Tobin, *J. Low Temp. Phys.* **35**, 5 (1979).

Liniger W., *J. Low Temp. Phys.* **93**, 1 (1993).

Mather J.C., *Appl. Opt.* **21**(6), 1125 (1982).

Mather J.C., *Appl. Opt.* **23**(18), 3181 (1984).

McGrath W.R., personal communication, 1999.

Mueller E.R., J. Fontanella, R. Henschke, *Proceedings of the 11th International Symposium on Space THz Technology* (University of Michigan, Ann Arbor, MI, 2000), p. 179.

Narayanan G., N.R. Erickson, and R.M. Grosslein, , *Proceedings of the 10th International Symposium on Space THz Technology* (University of Virginia, Charlottesville, VA, 1999), p. 519.

Phillips T.G. and J. Keene, *Proc. IEEE* **80**, 1662 (1992).

Pilbratt G.L., *Proceedings of the IAU Symposium 'The Extragalactic Infrared Background and its Cosmological Implications',* **204** (2000).

Prober D.E., *Appl. Phys. Lett.* **62**, 2119 (1993).

Santhanam P., and D.E. Prober, *Phys. Rev. B* **29**, 3733 (1984).

Schoelkopf R.J., J. Zmuidzinas, T.G. Phillips, H.G. LeDuc, and J.A. Stern, *IEEE Trans. Microwave Theory Tech.* **43**(4), 977 (1995).

Schoelkopf R.J., personal communication, 2000.

Semenov A.D. and G.N. Gol'tsman, *J. Appl. Phys.* **87**(1), 502 (2000).

Skalare A. and W.R. McGrath, *Proceedings of the 10th International Symposium on Space THz Technology* (University of Virginia, Charlottesville, VA, 1999[a]), p. 539.

Skalare A. and W.R. McGrath, *IEEE Trans. Appl. Supercond.* **9**(2), 4444 (1999)[b].

Skalare A., W.R. McGrath, P.M. Echternach, H.G. LeDuc, I. Siddiqi, A. Verevkin, and D.E. Prober, *IEEE Trans. Appl. Supercond.* **11,** 641 (2001).

Sturdivant R., C. Quan, and J. Wooldridge, *IEEE International Microwave Symposium Digest*, **1**, 235 (1996).

Tinkham M., *Introduction to Superconductivity*, McGraw-Hill, New York (1996).

Tucker J.R. and M.J. Feldman, *Rev. Mod. Phys.* **57**, 1055 (1985).

Turek B., personal communication, 2001.

Van Duzer T. and C.W. Turner, *Principles of Superconducting Devices and Circuits*, Elsevier North Holland, New York (1981).

Verbruggen A., T.M. Klapwijk, W. Belzig, and J.R. Gao, *Proceedings of the 12th International Symposium on Space THz Technology* (San Diego, CA 2001), to be published.

Waters J.W., *Proc. IEEE* **80**, 1679 (1992).

Wyss R.A, B.S. Karasik, W.R. McGrath, B. Bumble, and H.G. LeDuc, *Proceedings of the 10th International Symposium on Space THz Technology* (University of Virginia, Charlottesville, VA, 1999), p. 215.

Yngvesson S., personal communication, 2001.